

**LES AND σ -COORDINATE RANS SIMULATIONS OF LABORATORY
SURFACE WAVE BREAKING**

by

Morteza Derakhti

A dissertation submitted to the Faculty of the University of Delaware in
partial fulfillment of the requirements for the degree of Doctor of Philosophy in Civil
Engineering

Winter 2016

© 2016 Morteza Derakhti
All Rights Reserved

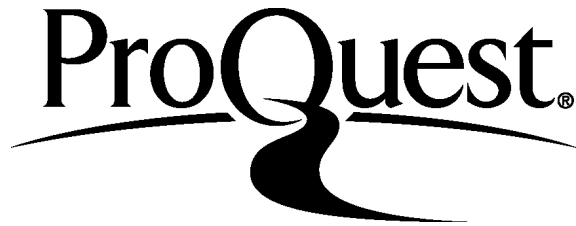
ProQuest Number: 10055801

All rights reserved

INFORMATION TO ALL USERS

The quality of this reproduction is dependent upon the quality of the copy submitted.

In the unlikely event that the author did not send a complete manuscript and there are missing pages, these will be noted. Also, if material had to be removed, a note will indicate the deletion.



ProQuest 10055801

Published by ProQuest LLC (2016). Copyright of the Dissertation is held by the Author.

All rights reserved.

This work is protected against unauthorized copying under Title 17, United States Code
Microform Edition © ProQuest LLC.

ProQuest LLC.
789 East Eisenhower Parkway
P.O. Box 1346
Ann Arbor, MI 48106 - 1346

**LES AND σ -COORDINATE RANS SIMULATIONS OF LABORATORY
SURFACE WAVE BREAKING**

by

Morteza Derakhti

Approved: _____
Harry W. Shenton III, Ph.D.
Chair of the Department of Civil and Environmental Engineering

Approved: _____
Babatunde Ogunnaike, Ph.D.
Dean of the College of Engineering

Approved: _____
Ann L. Ardis, Ph.D.
Interim Vice Provost for Graduate and Professional Education

I certify that I have read this dissertation and that in my opinion it meets the academic and professional standard required by the University as a dissertation for the degree of Doctor of Philosophy.

Signed: _____
James T. Kirby, Ph.D.
Professor in charge of dissertation

I certify that I have read this dissertation and that in my opinion it meets the academic and professional standard required by the University as a dissertation for the degree of Doctor of Philosophy.

Signed: _____
Robert A. Dalrymple, Ph.D.
Member of dissertation committee

I certify that I have read this dissertation and that in my opinion it meets the academic and professional standard required by the University as a dissertation for the degree of Doctor of Philosophy.

Signed: _____
Tian-Jian Hsu, Ph.D.
Member of dissertation committee

I certify that I have read this dissertation and that in my opinion it meets the academic and professional standard required by the University as a dissertation for the degree of Doctor of Philosophy.

Signed: _____
Fabrice Veron, Ph.D.
Member of dissertation committee

ACKNOWLEDGEMENTS

Foremost, I would like to begin with expressing my sincere gratitude to James Kirby for his guidance, insight, enthusiasm, and support during my study as a graduate student at the University of Delaware. I would also like to thank the members of my committee, Tony Dalrymple, Tian-Jian Hsu, and Fabrice Veron. Finally, I acknowledge all the people and friends in the Center for Applied Coastal Research for their support.

TABLE OF CONTENTS

LIST OF TABLES	ix
LIST OF FIGURES	xii
ABSTRACT	xxvii
 Chapter	
1 SUMMARY	1
2 BREAKING-ONSET, ENERGY AND MOMENTUM FLUX IN UNSTEADY BREAKING WAVES	3
2.1 Abstract	3
2.2 Introduction	4
2.3 Model Set-up and Choice of Experimental Conditions	9
2.4 Prediction of the Onset of Wave Breaking	10
2.5 Fractional and Total Losses of Energy Flux	15
2.5.1 Characteristic Wave Group Velocity	21
2.5.2 Nonlinear Wave-wave Interaction Before the Focal/Break Point	25
2.5.3 Parameterization of the Averaged Breaking-induced Wave Energy Dissipation Rate	31
2.6 Fractional and Total Losses of Momentum Flux	39
2.7 Conclusions	40
3 INTERMITTENT BUBBLE TRANSPORT IN THE SURF ZONE	44
3.1 Abstract	44
3.2 Introduction	44
3.3 Model Set-up and Averaging Procedures	48
3.3.1 Model Set-up and Choice of Experimental Conditions	48

3.3.2	Averaging Procedures and Scale Decomposition	49
3.4	Model Validation	52
3.4.1	Free Surface Evolution	53
3.4.2	Spanwise-time-averaged Organized and Turbulent Fields	53
3.5	The Role of the LBTCS in Bubble Transport in the Surf Zone	57
3.5.1	Coherent Structure Definition and Identification	57
3.5.2	Intermittent 3D Bubble Distribution	58
3.5.3	Preferential Accumulation of Bubbles into the LBTCS	59
3.6	Conclusions	69
4	NHWAVE: GOVERNING EQUATIONS, EXACT BOUNDARY CONDITIONS AND TURBULENCE MODELING	77
4.1	Abstract	77
4.2	Introduction	77
4.3	Governing Equations in Conservative Form	80
4.3.1	Continuity and Momentum Equations	81
4.3.2	Scalar Transport Equation	87
4.3.3	Turbulence Model	88
4.4	Surface and Bottom Boundary Conditions	91
4.4.1	Kinematic Boundary Conditions	91
4.4.2	Tangential Stress Boundary Conditions	92
4.4.3	Normal Stress Boundary Condition	96
4.4.4	Neumann-type Boundary Condition for a Scalar Quantity	97
4.4.5	Boundary Conditions for \mathcal{K} and \mathcal{E}	98
4.5	Numerical Method	98
4.5.1	Hydrostatic Velocity Calculation	100
4.5.2	Implicit Non-hydrostatic Velocity Correction	103

4.5.3	Truncation Error Analysis	105
4.6	The Role of Surface Slopes in the Near-surface Velocity and Turbulence Fields	106
4.6.1	Standing Wave in a Closed Basin	106
4.6.2	Two-dimensional Isotropy Test	107
4.6.3	Surf zone Regular Breaking Waves	107
4.7	Conclusions	108
5	WAVE BREAKING IN THE SURF ZONE AND DEEP WATER IN A NON-HYDROSTATIC MODEL	116
5.1	Abstract	116
5.2	Introduction	117
5.3	Mathematical Formulation and Numerical Methods	120
5.4	Depth-limited Breaking Waves on a Planar Beach	120
5.4.1	Regular Breaking Waves	121
5.4.1.1	Time-dependent Free Surface Evolution	122
5.4.1.2	Organized Flow Field	123
5.4.1.3	Turbulence Statistics	124
5.4.2	Irregular Breaking Waves	126
5.4.2.1	Power Spectra Evolution and Integral Breaking-induced Dissipation	127
5.4.2.2	Wave Statistics	129
5.4.2.3	Time-averaged Velocity and \bar{k}	130
5.5	Depth-limited Breaking Waves on a Barred Beach	131
5.5.1	Regular Breaking Waves	131
5.5.1.1	Time-dependent Free Surface Evolution	132
5.5.1.2	Time-averaged Velocity and \bar{k}	133
5.5.2	Irregular Breaking Waves	134
5.5.2.1	Power spectra evolution and integral breaking-induced dissipation	135

5.5.2.2	Wave Statistics	136
5.5.2.3	Time-averaged Velocity and k field	136
5.6	Steepness-limited Unsteady Breaking Waves	137
5.6.1	Time-dependent Free Surface Evolution	138
5.6.2	Integral Breaking-Induced Dissipation	139
5.6.3	Velocity Field	141
5.7	Conclusions	142
BIBLIOGRAPHY		181
Appendix		
A EULERIAN-EULERIAN MULTIPHASE MODELS		191
A.1	Different Numerical Approaches to Turbulent Multiphase Flows	191
A.2	Polydisperse Two-fluid Model	196
A.2.1	The filtered two-fluid equations	196
A.2.2	Interfacial Momentum Exchange	200
A.2.3	Bubble Entrainment Model	201
A.2.4	Subgrid-scale Model	203
A.2.5	Free Surface Tracking	205
A.2.6	Boundary Conditions	206
A.2.7	Numerical Method	207
A.2.8	Reynolds Decomposition of the Resolved Fields	208
B FREE SURFACE DEFINITION CLOSE TO THE BREAK POINT		210
C ESTIMATION OF WAVE ENERGY DISSIPATION DUE TO BREAKING AND NON-BREAKING PROCESSES		213
D INPUT PARAMETERS FOR THE BREAKING WAVES DUE TO MODULATIONAL INSTABILITY		215
E THREE-POINTS FINITE-DIFFERENCE APPROXIMATION IN A NON-UNIFORM GRID		216
F SECOND-ORDER FINITE-DIFFERENCE APPROXIMATION FOR THE PRESSURE AND VELOCITY GRADIENTS IN A NON-UNIFORM GRID		217

LIST OF TABLES

- 2.1 Input parameters for the 2D and 3D simulated cases. (i): [Rapp & Melville \(1990\)](#), $d = 0.6\text{m}$, $d/L_c = 0.3$ intermediate-depth, constant-amplitude packets; (ii): [Drazen et al. \(2008\)](#), $d = 0.6\text{m}$, $d/L_c = 0.3$ intermediate-depth, constant-steepness packets; (iii): [Tian et al. \(2012\)](#), $d = 0.62\text{m}$, $d/L_c = 1.1$ deep-water, constant-steepness packets. Here, d is the still water depth, L_c is the wavelength of the center frequency component of the incident packet f_c , S is the theoretical linear global wave steepness, Δf is the packet band width, x_b and t_b are the predefined, linear theory estimates of location and time of breaking respectively, and N is the number of different wave components in the packet. In constant-steepness packets, each wave component has a different amplitude, $a_i = S/(k_i N)$ such that component steepness $a_i k_i$ is constant with respect to i . In constant-amplitude packets, on the other hand, all the components have the same amplitude, $a_i = a$. [Rapp & Melville \(1990\)](#) defined the global steepness of a constant-amplitude packet as $S = k_c \sum_{i=1}^N a_i = k_c N a$ and, thus, $a = S/(k_c N)$. Different mesh grid densities are: G1 = $(\Delta x = 21.5, \Delta y = 7.0, \Delta z = 7.0)\text{mm}$, G2 = $(\Delta x = 18.3, \Delta z = 5.0)\text{mm}$, G3 = $(\Delta x = 10.0, \Delta z = 5.0)\text{mm}$, and G4 = $(\Delta x = 5.0, \Delta z = 5.0)\text{mm}$ 8
- 2.2 Summary of fractional and total energy and momentum flux loss for the breaking packets. $\overline{\overline{\eta^2}}/\overline{\overline{\eta_1^2}}$ is the fractional loss of the total potential energy, $\overline{\overline{F^E}}/\overline{\overline{F_1^E}}$ and $\int_t \overline{\overline{F^E}}$ are the fractional and total loss of the total horizontal energy flux respectively, $\overline{\overline{I}}/\overline{\overline{I_1}}$ and $\int_t \overline{\overline{I}}$ are the fractional and total loss of the total horizontal wave momentum flux respectively. $\overline{\overline{S_{p1}}}$ is the horizontal momentum flux due to the mean pressure field. $\int_t (2.11)$ and $\int_t (2.13)$ are the commonly used and the proposed estimates of $\int_t \overline{\overline{F^E}}$, respectively. α_1, α_2 and β are defined below (2.12). γ is defined below (2.25). Subscript 1 refers to far upstream of the break point. 24

2.3	Summary of the breaking parameters. S_{s0} is the spectrally-weighted global steepness of the wave packet far upstream of breaking given by (2.19), S is the theoretical linear global steepness of a wave packet defined in §2, k and a are the local wave number and amplitude as defined in Figure 2.1, $\int_t \Delta F_{br}^E$ is the total loss of the total horizontal energy flux due to breaking, T_b and c_b are the breaking wave period and phase speed respectively, and are calculated based on k_b and using linear dispersion relation, ξ is the local dynamic parameter defined in §3 and b is the breaking strength parameter given by (2.18). Subscript b refers to the breaking-onset instant at which a vertical tangent develops near the wave crest, where $t_b^* = -0.2 \sim 0$.	30
3.1	Input parameters for the simulated cases. Here, d_0 is the still water depth in the constant-depth region, H and T are the wave height and period of the cnoidal wave generated by the wavemaker, $(kH)_0 = 2\pi H_0/L_0$ is the corresponding deep water wave steepness of the generated wave, $\xi_0 = s/\sqrt{H_0/L_0}$ is the self similarity parameter, and s is the plane slope.	49
3.2	Input parameters for the experiments which are similar with the simulated cases.	50
3.3	Numerical set-up for the 3D LES cases. * These are the number of the available wave cycles after the simulation reaches a quasi-steady state conditions, which is approximately 15 wave periods after the start of the simulation. Here, superscripts b and nb refer to a simulation with and without the consideration of dispersed bubbles respectively. .	50
5.1	Input parameters for the simulated surf zone regular breaking cases on a planar beach. Here, d_0 is the still water depth in the constant-depth region, H and T are the wave height and period of the cnoidal wave generated by the wavemaker, $(kH)_0$ is the corresponding deep water wave steepness of the generated wave, $\xi_0 = s/\sqrt{H_0/L_0}$ is the self similarity parameter, and s is the plane slope.	122
5.2	Input parameters for the simulated surf zone irregular breaking cases on a planar beach. Here, d_0 is the still water depth in the constant-depth region, $k_p d_0$ and $(k_p H_{rms})_0$ are the dispersion and nonlinearity measure of the incident irregular waves respectively, f_p is the peak frequency of the input signal, $\xi_0 = s/\sqrt{(H_{rms})_0/L_0}$ is the self similarity parameter, $L_0 = g(2\pi)^{-1} f_p^{-2}$, and s is the plane slope.	127

5.3	Input parameters for the simulated depth-limited regular breaking waves on a barred beach. Here, H_0 and L_0 are the deep water wave height and wave length calculated using linear theory, $(kH)_0$ is the corresponding deep water wave steepness of the generated wave, $\xi_0 = s/\sqrt{H_0/L_0}$ is the self similarity parameter, and s is the averaged slope before the bar, assumed as $s \sim 1/12$. For the irregular wave case S2, $H = H_{s0}$ is the deep-water characteristic wave height, $T = T_p$ and $k = k_p$, where p refers to the peak frequency of the incident waves.	132
5.4	Input parameters for the simulated focused wave packets. d is the still water depth, $S = \sum_{i=1}^N a_i k_i$ is the global steepness, N is the number of components in the packet, $a_i k_i$ is the component steepness which is the same for the all components, and the discrete frequencies f_i were uniformly spaced over the band $\Delta f = f_N - f_1$ with a central frequency defined by $f_c = \frac{1}{2}(f_N - f_1)$	139
A.1	Bubble Stokes number for different bubble diameters and turbulence dissipation rates. w_b is the rise velocity of a bubble.	193
C.1	Variation of the breaking strength parameter b given by (2.18) with respect to different grid densities for simulated focused packets. Different meth grid densities are: G2 = $(\Delta x = 18.3, \Delta z = 5.0)$ mm, G3 = $(\Delta x = 10.0, \Delta z = 5.0)$ mm, and G4 = $(\Delta x = 5.0, \Delta z = 5.0)$ mm.	214
D.1	Input parameters for the simulated breaking packets due to modulational instability. Here, $k_0 = 8.23(\text{m}^{-1})$ and $d = 0.55\text{m}$ is the still water depth.	215

LIST OF FIGURES

2.1	Definitions of the local wave parameters. k and a are the local wave number and amplitude respectively. The wave propagates from the left to the right.	11
2.2	Temporal variations of (a, b, c) the normalized local energy density maximum, μ , and (A, B, C) its normalized growth rate, ξ , for different breaking and non-breaking packets. (a, A) intermediate-depth incipient breaking RI (---), spilling breaker RS1 (-·-), plunging breaker RP1 (—); (b, B) intermediate-depth incipient breaking DI (·····), spilling breaker DS1 (---), plunging breaker DP1 (-·-), plunging breaker DP2 (—); and (c, C) deep-water non-breaking packet TN (·····), weak plunging breaker TP1 (---), plunging breaker TP2 (-·-), plunging breaker TP3 (—). Horizontal lines show $\mu = 0.2$ and $\xi = 0.05$. Thick lines in panels (a, A) are the results for RP1(3D).	12
2.3	Temporal variations of the ratio of the potential energy density to the total energy density for (a) RI, (b) RS1, (c) RP1, (d) TN, (e) TP2, (f) TP3; at the locations of E_{max} (—), crest maxima (---), and trough maxima (-·-).	13
2.4	Normalized exact $\overline{\overline{F^E}} / \overline{\overline{F_1^E}}$ (—) and approximated $(\overline{\overline{F^E}} / \overline{\overline{F_1^E}})_{app1} \approx \overline{\overline{\eta^2}} / \overline{\overline{\eta_1^2}}$ (---) averaged horizontal energy flux for intermediate-depth (a) incipient breaking, RI; (b) spilling breaker, RS1; (c) plunging breaker, RP1; and (d) plunging breaker, RP2. Circles are the measured $\overline{\overline{\eta^2}} / \overline{\overline{\eta_1^2}}$ adopted from Rapp & Melville (1990) Figure 11(b). Thick lines are the results for RP1(3D).	16

- 2.5 Normalized averaged energy flux due to dynamic pressure, $\overline{\overline{F_p^E}}/\overline{\overline{F^E}}$ (—), and kinetic energy $\overline{\overline{F_k^E}}/\overline{\overline{F^E}}$ (---) for intermediate-depth (a) non-breaking packet RN; (b) incipient breaking, RI; (c) spilling breaker, RS1; and (d) plunging breaker, RP1. Thick lines are the results for RP1(3D). Here, $\overline{\overline{F_p^E}} = \overline{\int_{-d}^{\eta} [p + \rho g z] u dz}$ and $\overline{\overline{F_k^E}} = \overline{\int_{-d}^{\eta} [\frac{1}{2} \rho u_i^2] u dz}$ 17
- 2.6 Temporal variations of surface elevation for (a) intermediate-depth plunger RP1 and (b) deep-water plunger TP2 at different spatial locations. Different lines show $dx^*/dt^* = C$, where $C = C_E$, energy transport velocity (—), $C = C_{gs}$, spectrally-weighted group velocity (---), and $C = C_{gc}$, group velocity of the center frequency of the wave packet (- · -). Circles show the crest maximum at each spatial location. For clarity, the surface elevation is exaggerated by a factor of 4. 20
- 2.7 Normalized averaged kinetic energy density, $\overline{\overline{E_k^*}}$, (—); and potential energy density, $\overline{\overline{E_p^*}}$, (---) for intermediate-depth (a) non-breaking packet RN; (b) incipient breaking, RI; (c) spilling breaker, RS1; and (d) plunging breaker, RP1. Thick lines are the results for RP1(3D). The results are normalized by a reference value of $\rho^l g k_{s0}^2 S_{s0}^{-2}$, where S_{s0} and k_{s0} are defined in §4.3. 21
- 2.8 Energy transport velocity, C_E , (—) and spectrally-weighted group velocity, C_{gs} (---) for intermediate-depth (a) non-breaking packet RN; (b) incipient breaking, RI; (c) spilling breaker, RS1; and (d) plunging breaker, RP1. Thick lines are the results for RP1(3D). . . 22
- 2.9 Normalized energy transport velocity $C_E^* = (C_E - C_{gs1})/C_{gs1}$ (—), normalized wave asymmetry near the dominant component of the packet $As^* = 0.25As/|As|_{max}$ (· · · · ·), and normalized spectrally-weighted frequency $f_s^* = (f_s - f_{s1})/f_{s1}$ (---) for intermediate-depth (a) non-breaking packet RN; (b) incipient breaking, RI; (c) spilling breaker, RS1; and (d) plunging breaker, RP1. 26

- 2.10 Modulus of the wavelet transform of the non-breaking packet RN (left); and plunging breaker RP1 (right). Contours show $|W_{\langle\eta\rangle}|$, in the range 0.025 to 0.5 with intervals of 0.025. Horizontal dotted lines show the frequency band boundaries of the input packet. — shows the arrival time of the different frequencies based on the linear group velocity. --- shows the arrival time of the wavelet amplitude maximum for the different frequencies. 27
- 2.11 Phase angle $\Theta_{B_{\langle\eta\rangle}}$ of the free surface bispectrum $B_{\langle\eta\rangle}(s_1, s_1, t)$, for the nonbreaking packet RN (---); and plunging breaker RP1 (—) at (a) $x^* = -0.3$; and (b) $x^* = 1.3$. Here, $s_1 = (\theta f_1)^{-1}$, $f_1 = f_c$ is the center frequency, and $\theta = 4\pi/(\omega_0 + \sqrt{2 + \omega_0^2})$ is a constant. . 28
- 2.12 Variations of the breaking strength parameter b with respect to (a) the local wave steepness at breaking-onset $k_b a_b$, and (b) the dynamic diagnostic parameter ξ_b for (open circles) the unsteady dispersive focused breaking packets and (solid circle) the modulated unstable breaking packets; their input parameters are given in Appendix D. Dashed lines are linear fits through the results of the simulated focused packets. 33
- 2.13 Spatial variations of the spectrally-weighted global steepness S_s for (a) intermediate-depth nonlinear packet RN (.....), incipient breaking RI (---), spilling breaker RS1 (-.-), plunging breaker RP1 (—); and (b) deep-water nonlinear packet TN (.....), weak plunging breaker TP1 (-.-), plunging breaker TP2 (---), plunging breaker TP3 (—). 34
- 2.14 Variations of the breaking strength parameter b with respect to (a) the theoretical linear slope of a wave packet $S = \Sigma k_n a_n$; and (b) the initial spectrally-weighted global steepness $S_{s0} = k_{s0} \Sigma a_n$ for the considered focused wave packets (open circles), the simulated spillers due to modulational instability (solid circle), and the weak spilling breaking waves in a wide tank adopted from Allis (2013, Table 8.1) (pluses). The dashed and dotted lines in (a) are given by equation (2.21) and $b = 0.16 (S_{s0} - 0.28)$. The dashed line in (b) was given by Romero et al. (2012). In Allis (2013) the values of $S = \Sigma a_i k_i$ have not been calculated. We assume $S = S_{s0}$ for their cases. 36

2.15	Normalized horizontal momentum flux by waves and turbulence, $\overline{\overline{I^*}}$, (—); mean pressure field, $\overline{\overline{S_p^*}}$, (---); $\overline{\overline{I_{apx}^*}}$ (-.-); and $\overline{\overline{(S_p^*)_{apx}}}$ (.....) for intermediate-depth (a) non-breaking packet RN; (b) incipient breaking RI; (c) spilling breaker RS1; and (d) plunging breaker RP1. Thick lines are the results for RP1(3D). The results are normalized by a reference value of $\rho^l g k_{s0}^2 S_{s0}^{-2}$	38
3.1	Side view of the experimental layout of the simulated cases and coordinate systems. The rectangular mesh is shown some part of the numerical grid.	49
3.2	Snapshots of the free-surface (isosurface of $\psi = 0.5$) evolution the weakly-plunging/spilling case S1 after 23 wave periods after the start of the simulation ($t_b = 46.91s$). Here, x_b is approximately the point of incipient wave breaking, and is defined as the cross-shore location at which a vertical tangent appears near the wave crest.	52
3.3	Spanwise-phase-averaged free surface elevations at different cross-shore locations for the weakly-plunging/spilling case S1. Comparison between --- the simulation and — the corresponding measurements by Ting & Nelson (2011) . Here, $\widehat{\cdot}$ indicates phase averaging over N successive waves after the wave field reaches to a steady state condition, where N is 15 in the simulation, and is 10 the measurements. x_b is approximately the point of incipient wave breaking, and is the cross-shore location at which a vertical tangent appears near the wave crest. No spanwise averaging was involved in the measurement.	54
3.4	Cross-shore variation of the wave height $H = \widehat{\eta}_{max} - \widehat{\eta}_{min}$ for the weakly-plunging/ spilling case S1. Comparison between — the simulation and +++ the corresponding measurements by Ting & Nelson (2011) . $\circ \circ \circ$ show the results for the spilling case of Ting & Kirby (1994)	54
3.5	Spatial distribution of (a) the normalized conditional spanwise-time-averaged, $(P_w^{-1} \overline{\langle k \rangle})^{1/2} / \sqrt{gh}$, and (b) the spanwise-time-averaged, $\overline{\langle k \rangle}^{1/2} / \sqrt{gh}$, turbulent kinetic energy for S1. Thick solid lines show the troughs and the crests levels. Vertical dashed lines show the cross-shore locations of the data-model comparisons shown in Figure 3.6 . Here, $\sigma = (z - \bar{\eta})/h$	55

3.6	Spanwise-time-averaged normalized $(a - f)$ turbulent kinetic energy, $\overline{\langle k \rangle}^{1/2}/\sqrt{gh}$, profiles and $(A - F)$ normalized horizontal velocity, $\overline{\langle u \rangle}/\sqrt{gh}$, (undertow) profiles for the weakly-plunging/spilling case S1 at different cross-shore locations after the initial break point. $\circ \circ \circ$ show measurements of Ting & Kirby (1994) . Here, $\sigma = (z - \bar{\eta})/h$.	56
3.7	Snapshots of the bubble plume (isosurface of $\alpha_b = 0.5\%$) evolution for (right) plunging case P1, and (left) the weakly-plunging/spilling case S1. Here, $t_b = 90.78$ s and $t_b = 46.91$ s for P1 and S1 respectively. .	60
3.8	Snapshots of the evolution of $(a - d)$ LBTCS, blue and red volumes are VS and DBS respectively, and $(A - D)$ bubble plume, opaque and transparent volumes are the isosurfaces of $\alpha_b = 1\%$ and $\alpha_b = 0.2\%$ respectively, for the plunging case P1 underneath the first splash-up. Waves are propagating in the positive x direction, into the paper. .	61
3.9	As in Figure 3.8 except underneath the second splash-up. The box volume shows approximately the location of 3D velocity measurements by Ting & Reimnitz (2015)	62
3.10	Snapshots of the bubble void fraction (%) distribution at $(a - d)$ the mid cross-shore section and $(A - D)$ different along-shore sections for the plunging case P1. Black and blue contours indicate the locations of DBS and VS respectively. Arrows in the right panels show the turbulent velocity vectors at the along-shore sections. For clarity only one-half of the arrows are shown. Arrows at each panel scale accordingly to give a better visibility. The vertical dashed line in each left panel shows the cross-shore location of the corresponding along-shore section shown in the right panel of that row. Horizontal dashed lines in panel c are the vertical elevations of the horizontal sections shown in Figure 3.11	63
3.11	Horizontal distribution of the bubble void fraction (%) at $t_b + t/T = 0.35$ for the plunging case P1 at different vertical elevations shown in Figure 3.10 . (a) $z = 115.5$ mm, (b) $z = 80.5$ mm, (c) $z = 45.5$ mm, and (d) $z = 10.5$ mm. Black and blue contours indicate the locations of DBS and VS respectively. The dashed lines show the cross-shore location of the along-shore sections shown in the right column of Figure 3.10	64

3.12	Snapshots of the evolution of $(a - d)$ LBTCs, blue and red volumes are VS and DBS respectively, and $(A - D)$ bubble plume, opaque and transparent volumes are the isosurfaces of $\alpha_b = 05\%$ and $\alpha_b = 0.1\%$ respectively, for the weakly-plunging/spilling case S1 underneath the first splash-up. Waves are propagating in the positive x direction.	65
3.13	As in Figure 3.10 except for the weakly-plunging/spilling case S1.	66
3.14	Horizontal distribution of the bubble void fraction (%) at $t_b + t/T = 0.85$ for the weakly plunging/spilling case S1 at different vertical elevations shown in Figure 3.13. (a) $z = 136.5\text{mm}$, (b) $z = 94.5\text{mm}$, (c) $z = 52.5\text{mm}$, and (d) $z = 10.5\text{mm}$. Black and blue contours indicate the locations of DBS and VS respectively. The dashed lines show the cross-shore location of the along-shore sections shown in the right column of Figure 3.13.	67
3.15	Snapshots of the spatial distribution of the dynamic pressure in $(a - d)$ the plunging case P1 and $(A - D)$ the weakly plunging/spilling case S1. Black and blue contours indicate the locations of DBS and VS respectively. Arrows in the right panels show the turbulent velocity vectors at the along-shore sections. For clarity only one-half of the arrows are shown. Arrows at each panel scale accordingly to give a better visibility. The reference value is $0.01\rho g$	70
3.16	Snapshots of the spatial distribution of the dynamic pressure gradient in the $(a - d)$ vertical and $(A - D)$ spanwise directions in the plunging case P1. Black and blue contours indicate the locations of DBS and VS respectively. The reference value is ρg	71
3.17	Snapshots of the spatial distribution of the dynamic pressure gradient in the $(a - d)$ vertical and $(A - D)$ spanwise directions in the weakly plunging/spilling case S1. Black and blue contours indicate the locations of DBS and VS respectively. The reference value is ρg	72
3.18	Snapshots of the spatial distribution of (a) drag, (b) lift and (c) virtual mass forces in the vertical direction per unit volume of the liquid in the weakly plunging/spilling case S1. Black and blue contours indicate the locations of DBS and VS respectively. Arrows show the corresponding vector force at the along-shore sections. Arrows at each panel scale accordingly to give a better visibility. The reference value is $0.01\rho g$	73

3.19	Snapshots of the spatial distribution of (a) drag, (b) lift and (c) virtual mass forces in the spanwise direction per unit volume of the liquid in the weakly plunging/spilling case S1. Black and blue contours indicate the locations of DBS and VS respectively. Arrows show the corresponding vector force at the along-shore sections. Arrows at each panel scale accordingly to give a better visibility. The reference value is $0.01\rho g$	74
3.20	Snapshots of the spatial distribution of the total interfacial forces per unit volume of the liquid in the (a – d) vertical and (A – D) spanwise directions in the weakly plunging/spilling case S1. Black and blue contours indicate the locations of DBS and VS respectively. The reference value is $0.01\rho g$	75
3.21	Spatial distribution of the conditional time-averaged bubble void fraction (%) for the weakly plunging/spilling case S1, (a) inside the VS $\overline{\langle\alpha_b\rangle}_{VS}$, (b) inside the DBS $\overline{\langle\alpha_b\rangle}_{DBS}$, (c) $P_w^{-1}\overline{\langle\alpha_b\rangle}$ in the 3D simulation. Panel (d) gives the corresponding conditional time-averaged bubble void fraction $P_w^{-1}\overline{\langle\alpha_b\rangle}$ for the corresponding 2D simulation. Blue solid lines show trough and crest elevations. Here, $\sigma = (z - \bar{\eta})/h$	76
4.1	Spatial distribution of the long-time-averaged velocity field under a standing wave in a closed basin. Comparison between NHWAVE results with 10 vertical levels using the (a) exact and (b) old boundary conditions.	110
4.2	Time variation of the normalized wave-averaged potential energy of a standing wave in a closed basin. Comparison between NHWAVE results with (circle symbols) 3, (+ symbols) 5 and (diamonds symbols)10 vertical levels using the (solid lines) exact and (dashed lines) old boundary conditions.	111
4.3	Snapshots of the two-dimensional free surface locations generated by the evolution of an initial two dimensional Gaussian hump at (a, A) $t - t_0 = 0.1s$, (b, B) $t - t_0 = 1.5s$, and (c, C) $t - t_0 = 9.9s$. (a, b, c) show the plan view, while (A, B, C) show the corresponding 3d view.	112
4.4	Cross sections of the two-dimensional free surface locations shown in figure 4.3(b, B), at (solid line) $x = 0$, (dashed line) $y = 0$ and (dotted line) $x = y$	113

4.5	Snapshots of the turbulent kinetic energy, $k(\text{m}^2/\text{s}^2)$, distributions under the spilling periodic surf zone breaking waves. Comparison between NHWAVE results with 10 vertical levels using the $(a - e)$ new and $(A - E)$ old model. Here, $x = 0$ corresponds to the cross-shore location at which $d = 0.38$ as in Ting & Kirby (1994)	114
4.6	Time-averaged normalized turbulent kinetic energy, $\sqrt{k/gh}$, profiles at different cross-shore locations under the spilling periodic surf zone breaking waves. Comparison between NHWAVE results with 10 vertical levels using the new model with (solid lines) RNG-based, (dotted-dashed lines) standard $k - \epsilon$ and (dashed lines) the old model. Here, $x^* = x - x_b$, is the horizontal distance from the break point; and $h = d + \bar{\eta}$, where d is the still water depth and $\bar{\eta}$ is the wave set-up/set-down.	115
5.1	Experimental layout of Ting & Kirby (1994) . Vertical solid lines: the cross-shore locations of the velocity measurements for TK1. Vertical dashed lines: the cross-shore locations of the velocity measurements for TK2.	144
5.2	Cross-shore distribution of crest and trough elevations as well as mean water level for the surf zone (a,A) spilling breaking case TK1 and (b,B) plunging breaking case TK2. Comparison between NHWAVE results with 4 σ levels (dashed lines), 8 σ levels (dotted-dashed lines), 16 σ levels (solid lines) and the measurements of Ting & Kirby (1994) (circle markers). In panels (A) and (B), $x^* = x - x_b$ represents the horizontal distance from the break point.	145
5.3	Phase-averaged free surface elevations for the surf zone spilling breaking case TK1 at different cross-shore locations before and after the initial break point $x^* = 0$. Comparison between NHWAVE results with 4 σ levels (dashed lines), 8 σ levels (dotted-dashed lines) and the measurement (thin red solid lines).	146
5.4	Phase-averaged free surface elevations for the surf zone plunging breaking case TK2 at different cross-shore locations before and after the initial break point $x^* = 0$. Comparison between NHWAVE results with 4 σ levels (dashed lines), 8 σ levels (dotted-dashed lines) and the measurement (thin red solid lines).	146

5.5	Phase-averaged normalized horizontal velocities for the surf zone spilling breaking case TK1 at about 5 cm above the bed (z^* is the distance from the bed), at different cross-shore locations before and after the initial break point $x^* = 0$. Comparison between NHWAVE results with 4 σ levels (dashed lines), 8 σ levels (dotted-dashed lines), 16 σ levels (thick solid lines) and measurements (thin red solid lines).	147
5.6	Phase-averaged normalized horizontal velocities for the surf zone plunging breaking case TK2 at about 5 cm above the bed (z^* is the distance from the bed), at different cross-shore locations before and after the initial break point $x^* = 0$. Comparison between NHWAVE results with 4 σ levels (dashed lines), 8 σ levels (dotted-dashed lines), 16 σ levels (thick solid lines) and measurements (thin red solid lines).	148
5.7	Time-averaged velocity field, $\bar{\mathbf{u}}$, for the surf zone spilling breaking case TK1. NHWAVE results with (a) 4 σ levels, (b) 8 σ levels, and (c) 16 σ levels. Dash lines show the crest $\langle \eta \rangle_{max}$ and trough $\langle \eta \rangle_{min}$ elevations. Colors show \bar{u}/\sqrt{gh} .	149
5.8	Time-averaged normalized horizontal velocity (undertow) profiles for the surf zone spilling breaking case TK1 at different cross-shore locations before and after the initial break point, $x^* = 0$. Comparison between NHWAVE results with 4 σ levels (dashed lines), 8 σ levels (dotted-dashed lines), 16 σ levels (solid lines) and the measurements (circle markers).	150
5.9	Time-averaged normalized horizontal velocity (undertow) profiles for the surf zone plunging breaking case TK2 at different cross-shore locations before and after the initial break point, $x^* = 0$. Comparison between NHWAVE results with 4 σ levels (dashed lines), 8 σ levels (dotted-dashed lines), 16 σ levels (solid lines) and the measurements (circle markers).	151
5.10	Snapshots of the turbulent kinetic energy, $k(\text{m}^2/\text{s}^2)$, distribution for the surf zone spilling breaking case TK1. NHWAVE results with (a – e) 4 σ levels and (A – E) 8 σ levels.	152
5.11	Phase-averaged k time series for the surf zone spilling breaking case TK1 at (a – f) ~ 4 cm and (A – F) ~ 9 cm above the bed at different cross-shore locations before and after the initial break point, $x^* = 0$. Comparison between NHWAVE results with 4 σ levels (dashed lines), 8 σ levels (dotted-dashed lines), 16 σ levels (thick solid lines) and the measurement (thin red solid lines)	153

5.12	Phase-averaged k time series for the surf zone plunging breaking case TK2 at $(a - f) \sim 4$ cm and $(A - F) \sim 9$ cm above the bed at different cross-shore locations after the initial break point, $x^* = 0$. Comparison between NHWAVE results with 4 σ levels (dashed lines), 8 σ levels (dotted-dashed lines), 16 σ levels (thick solid lines) and the measurement (thin red solid lines)	154
5.13	Time-averaged normalized k field, $\sqrt{k/gh}$, for the surf zone spilling breaking case TK1. NHWAVE results with (a) 4 σ levels, (b) 8 σ levels, and (c) 16 σ levels. Dash lines show the crest $\langle \eta \rangle_{max}$, mean $\bar{\eta}$ and trough $\langle \eta \rangle_{min}$ elevations.	155
5.14	Time-averaged normalized k profiles for the surf zone spilling breaking case TK1 at different cross-shore locations before and after the initial break point, $x^* = 0$. Comparison between NHWAVE results with 4 σ levels (dashed lines), 8 σ levels (dotted-dashed lines), 16 σ levels (solid lines) and the measurements (circle markers). . . .	156
5.15	Time-averaged normalized k profiles for the surf zone plunging breaking case TK2 at different cross-shore locations before and after the initial break point, $x^* = 0$. Comparison between NHWAVE results with 4 σ levels (dashed lines), 8 σ levels (dotted-dashed lines), 16 σ levels (solid lines) and the measurements (circle markers). . . .	157
5.16	Experimental layout of Bowen & Kirby (1994) . Vertical solid lines: the cross-shore locations of the free surface measurements.	158
5.17	Experimental layout of Mase & Kirby (1992) . Vertical solid lines: the cross-shore locations of the free surface measurements.	158
5.18	Power spectral density evolution, $S(f)$ ($\text{cm}^2.\text{s}$), for the random breaking cases, (a) BK with $f_p = 0.225\text{Hz}$, (b) MK1 with $f_p = 0.6\text{Hz}$, and (c) MK2 with $f_p = 1.0\text{Hz}$ at different cross-shore locations. Comparison between NHWAVE results with 4 σ levels (dashed lines), 8 σ levels (thick solid lines) and the corresponding measurements (circles). Here, d is the still water depth, and d_b is the still water depth at $x = x_b$ ($d_b \sim 20.5\text{cm}$ for BK and $d_b \sim 12.5\text{cm}$ for MK1 and MK2). The solid lines show an f^{-2} frequency dependence.	159

5.19	Cross-shore variation of different Second- and third-order wave statistics for (a) BK, (b) MK1 and (c) MK2. Comparison between NHWAVE results with 4 σ levels (dashed lines), 8 σ levels (solid lines) and the corresponding measurements (circles). Here, N_w is the number of waves detected by the zero-up crossing method, $H_{0.1}$ and $T_{0.1}$ are the averaged height and period of the one-tenth highest waves in the signal, H_{m0} , T_{m02} are the characteristic wave height and period based on the power spectra of the signal, $\text{Skewness} = \overline{\eta^3} / (\overline{\eta^2})^{3/2} > 0$ is the normalized wave skewness, and $\text{Asymmetry} = \overline{\mathcal{H}(\eta)^3} / (\overline{\eta^2})^{3/2} < 0$ is the normalized wave asymmetry. The results shown in (a) and (c) has the same label as in (b).	160
5.20	Time-averaged velocity field, $\bar{\mathbf{u}}$, for the surf zone irregular breaking case MK2. NHWAVE results with (a) 4 σ levels and (b) 8 σ levels. Dash lines show $H_{rms} + \bar{\eta}$. Colors show \bar{u} / \sqrt{gh}	161
5.21	Time-averaged normalized k field, $\sqrt{k/gh}$, for the surf zone irregular breaking case MK2. NHWAVE results with (a) 4 σ levels and (b) 8 σ levels. Dash lines show $H_{rms} + \bar{\eta}$	161
5.22	Experimental layout of Scott et al. (2004) . Vertical thick solid lines: the cross-shore locations of the velocity measurements. Vertical thin solid lines: the cross-shore locations of the free surface measurements.	162
5.23	(a) Cross-shore distribution of the wave height, $H = \langle \eta \rangle_{max} - \langle \eta \rangle_{min}$, and (b) mean water level, $\bar{\eta}$, for the surf zone regular breaking waves on a barred beach case S1. Comparison between NHWAVE results with 4 σ levels (dashed lines), 8 σ levels (dotted-dashed lines) and the measurements of Scott et al. (2004) (circle markers). Vertical lines: the cross-shore locations of the velocity measurements shown in Figure 5.22	162
5.24	Phase-averaged free surface elevations for the surf zone regular breaking waves on a barred beach case S1 at different cross-shore locations before and after the bar. Comparison between NHWAVE results with 4 σ levels (dashed lines), 8 σ levels (dotted-dashed lines) and the measurement (thin red solid lines).	163

5.25	Time-averaged velocity field, $\bar{\mathbf{u}}$, for the surf zone regular breaking waves on a barred beach case S1. NHWAVE results with (a) 4 σ levels, and (b) 8 σ levels. Dash lines show the crest $\langle \eta \rangle_{max}$ and trough $\langle \eta \rangle_{min}$ elevations. Colors show \bar{u}/\sqrt{gh} . Vertical lines: the cross-shore locations of the velocity measurements shown in Figure 5.22.	164
5.26	Time-averaged normalized horizontal velocity (undertow) profiles for the surf zone regular breaking waves on a barred beach case S1 at different cross-shore locations before and after the bar. Comparison between NHWAVE results with 4 σ levels (dashed lines), 8 σ levels (dotted-dashed lines), and the measurements at two different longshore locations (open and solid circle markers). Red lines at (c) show the results 3m seaward of the corresponding measurement location.	165
5.27	Time-averaged normalized k field, $\sqrt{k/gh}$, for the surf zone regular breaking waves on a barred beach case S1. NHWAVE results with (a) 4 σ levels, and (b) 8 σ levels. Dash lines show the crest $\langle \eta \rangle_{max}$, mean $\bar{\eta}$ and trough $\langle \eta \rangle_{min}$ elevations. Vertical lines: the cross-shore locations of the velocity measurements shown in Figure 5.22.	166
5.28	Time-averaged normalized k profiles for the surf zone regular breaking waves on a barred beach case S1 at different cross-shore locations before and after the bar. Comparison between NHWAVE results with 4 σ levels (dashed lines), 8 σ levels (dotted-dashed lines), and the measurements (circle markers). Red lines at (c) show the results 3m seaward of the corresponding measurement location.	167
5.29	Power spectral density evolution, $S(f)$ ($m^2.s$), for the random breaking on a barred beach case S2 at different cross-shore locations. Comparison between NHWAVE results with 4 σ levels (dashed lines), 8 σ levels (thick solid lines) and the corresponding measurements (circles). The solid lines show f^{-2}	168
5.30	Cross-shore variation of different Second- and third-order wave statistics for the random breaking on a barred beach case S2. Comparison between NHWAVE results with 4 σ levels (dashed lines), 8 σ levels (solid lines) and the corresponding measurements (circles). The definitions are the same as in Figure 5.19.	169
5.31	Time-averaged velocity field, $\bar{\mathbf{u}}$, for the random breaking on a barred beach case S2. NHWAVE results with (a) 4 σ levels and (b) 8 σ levels. Dash lines show $H_{rms} + \bar{\eta}$. Colors show \bar{u}/\sqrt{gh}	170

5.32	Time-averaged normalized horizontal velocity (undertow) profiles for the random breaking on a barred beach case S2 at different cross-shore locations before and after the bar. Comparison between NHWAVE results with 4 σ levels (dashed lines), 8 σ levels (dotted-dashed lines), and the measurements (circle markers). Red lines at (c) show the results 3m seaward of the corresponding measurement location.	171
5.33	Time-averaged normalized k field, $\sqrt{k/gh}$, for the random breaking on a barred beach case S2. NHWAVE results with (a) 4 σ levels and (b) 8 σ levels. Dash lines show $H_{rms} + \bar{\eta}$	172
5.34	Time-averaged normalized k profiles for the random breaking on a barred beach case S2 at different cross-shore locations before and after the bar. Comparison between NHWAVE results with 4 σ levels (dashed lines), 8 σ levels (dotted-dashed lines), and the measurements (circle markers). Red lines at (c) show the results 3m seaward of the corresponding measurement location.	173
5.35	Snapshots of the free surface evolution during active breaking for the intermediate depth breaking case, RM1. Comparison between NHWAVE results with 8 σ levels (thick solid lines) and the VOF-based model (thin solid lines). The free surface time series at the locations indicated by vertical dashed lines are shown in Figure 5.36.	174
5.36	Time series of the free surface evolution for the intermediate depth breaking case, RM1 at (a) before and (b) after the break point ($x^* = 0$). Comparison between NHWAVE results with 8 σ levels (solid lines) and the corresponding measurements of Rapp & Melville (1990) (circles).	175
5.37	Time series of the free surface evolution at different x locations for the deep water breaking case, T1. Comparison between NHWAVE results with 8 σ levels and the horizontal resolution of $\Delta x = 10\text{mm}$ (dotted dashed lines) and the measurement of Tian et al. (2012) (solid lines).	176

5.38	Normalized time-integrated potential energy density, $\overline{\overline{E_p}}$, for the intermediate depth breaking case, RM2. Comparison between the corresponding measurements (circles) and NHWAVE results with (a) 8 σ levels and (b) 16 σ levels, using different horizontal resolutions of $\Delta x = 23\text{mm}$ (solid lines), $\Delta x = 10\text{mm}$ (dashed lines) and $\Delta x = 5\text{mm}$ (dashed-dotted lines).	177
5.39	Energy density spectrum evolution, $S(f)$ ($\text{cm}^2.\text{s}$) for the deep water breaking case, T1. Comparison between NHWAVE results with 8 σ levels using $\Delta x = 10\text{mm}$ (thick solid lines) and $\Delta x = 5\text{mm}$ (dashed lines) as well as the measurements of Tian et al. (2012) (solid lines). Vertical dotted lines indicate the frequency range of the input packet.	178
5.40	Normalized ensemble-averaged velocities for RM1 using 8 σ levels (dashed lines) and 16 σ levels (solid lines) at $x^* = 0.6$, $z^* = -0.025$. The circles are the measurements of the corresponding case adopted from Rapp & Melville (1990) , Figure 41.	179
5.41	Normalized low-pass filtered velocities for RM1 using 8 σ levels (dashed lines) and 16 σ levels (solid lines), at (a,c) $x^* = 0.15$ and (b,d) $x^* = 0.60$ at different elevations. The circles are the measurements of the corresponding case adopted from Rapp & Melville (1990) , Figure 42.	179
5.42	(a, d) Spatial distribution of the normalized mean current, \mathbf{u}_c^* ; (b, e) normalized horizontal-averaged mean current in the streamwise direction, \widehat{u}_c^* and (c, f) normalized accumulative horizontal-averaged mass flux, \widehat{M}^* , in the breaking region for RM1. (a-c) NHWAVE results with 8 σ levels and (d-f) LES/VOF results by Derakhti & Kirby (2014a)	180
A.1	Different approaches to turbulent multiphase flows. Their applicability is separated in terms of timescale and length-scale ratios. Figure taken from Balachandar & Eaton (2010) figure 1.	192
B.1	Snapshots of the spatial variations of the air-water interface (—) and the calculated $\eta(t, x)$ (—) for the intermediate-depth plunging breaker DP1. The resolution density is $G3 = (\Delta x = 10.0, \Delta z = 5.0)\text{mm}$	211

B.2	Spatial variations of the normalized exact, $2\overline{E_p}/\rho^l g$, (—) and approximated, $\overline{\eta^2}$, (—) time-averaged potential energy density for the intermediate-depth plunging breaker DP1. The resolution density is G3 = ($\Delta x = 10.0, \Delta z = 5.0$)mm. Vertical dashed lines show $x^* = -0.2$ and $x^* = 0.5$	212
C.1	Calculation of the total loss of the horizontal wave energy flux due to breaking and non-breaking processes. The reference value is the total horizontal wave energy flux far upstream of the break point, $\int_t \overline{F_1^E}$.	214

ABSTRACT

This dissertation presents a three-dimensional (3D) numerical study of the turbulent bubbly flow in surface breaking waves, from steepness-limited unsteady breaking in deep water to depth-limited breaking in the surf zone. Because of available computational resources, the whole range of the relevant scales can not be resolved in a single high resolution framework. Instead, two different frameworks are chosen to study the relevant physics from small scales through field scales. In the first framework, a Volume-of-Fluid (VOF) based Eulerian-Eulerian polydisperse two-fluid model (Ma et al. 2011, Derakhti & Kirby 2014b) is used to study breaking-induced energy dissipation (chapter 2), bubble entrainment and liquid-bubble interaction (Derakhti & Kirby 2014b) in unsteady whitecaps as well as large-scale turbulent coherent structures and their interaction with dispersed bubbles in the surf zone (chapter 3). A 3D non-hydrostatic wave-resolving σ -coordinate framework is chosen as the lower-resolution framework. We derive a new set of equations, in conservative form, describing the kinematics and dynamics of continuous and dispersed phases in a multiphase mixture in a surface- and terrain-following σ -coordinate system, together with exact surface and bottom boundary conditions for the velocity and dynamic pressure fields as well as a Neumann-type boundary condition for scalar fluxes (chapter 4). The model capability and accuracy to reproduce the evolution of the free surface, velocity and vorticity fields and breaking-induced dissipation under regular and irregular breaking waves from surf zone to deep water is examined in detail (chapter 5).

Chapter 1

SUMMARY

Surface wave breaking is a complex two-phase flow phenomenon that has an important role in numerous environmental processes, such as air-sea transfer of gas, momentum and energy, acoustic underwater communications, optical properties of the water column as well as nearshore mixing and morphodynamics ([Melville 1996](#)). Wave breaking is a highly dissipative process, limiting the height of surface waves. It is also a source of turbulence, which enhances transport and mixing in the ocean surface layer. It entrains a large volume of air which rapidly evolves into a distribution of bubble sizes, which interact with liquid turbulence and organized motions. In shallow water and nearshore regions, this process becomes even more complicated when the bottom effect and sediment alter the flow field. In the surf zone, large-scale breaking-induced turbulent coherent structures (LBTCS), for example obliquely descending eddies, are responsible for intermittent sediment and bubble transport. Although these intermittent LBTCS play significant role in the transport of dispersed bubbles and sediment under individual breaking waves in a localized/short-term manner, long-term transport of dispersed particles and passive tracers are highly dependent on the structure of organized motions and their evolution.

This dissertation presents a three-dimensional (3D) numerical study of both short-term and long-term breaking-induced processes, from steepness-limited unsteady breaking in deep water to depth-limited breaking in the surf zone. The work is broken into four chapters. Each chapter is written to be freestanding and thus has its own abstract, introduction, and literature review relevant to the topic followed by a discussion of the results and the corresponding conclusions.

Because of available computational resources, the whole range of the relevant scales can not be resolved in a single high-resolution framework. Instead, two different frameworks are chosen to study the relevant physics from small-scales through field-scales. In the first framework, a Volume-of-Fluid (VOF) based Eulerian-Eulerian polydisperse two-fluid model (Ma et al. 2011, Derakhti & Kirby 2014b) is used to study breaking-induced energy dissipation (chapter 2), bubble entrainment and liquid-bubble interaction (Derakhti & Kirby 2014b) in unsteady whitecaps as well as LBTCS and their interaction with dispersed bubbles in the surf zone (chapter 3). In this framework, turbulence is modeled using a large-eddy simulation (LES). The model accounts for momentum exchange between dispersed bubbles and liquid phase as well as bubble-induced dissipation. A 3D non-hydrostatic wave-resolving σ -coordinate framework is chosen as the lower-resolution framework. We derive a new set of equations, in conservative form, describing the kinematics and dynamics of continuous and dispersed phases in a multiphase mixture in a surface- and terrain-following σ -coordinate system, together with exact surface and bottom boundary conditions for the velocity and dynamic pressure fields as well as a Neumann-type boundary condition for scalar fluxes (chapter 4). The model capability and accuracy to reproduce the evolution of the free surface, velocity and vorticity fields and breaking-induced dissipation under regular and irregular breaking waves from surf zone to deep water is examined in detail (chapter 5). As opposed to the VOF/LES framework, the free surface is a single-valued function of horizontal location, and detailed near-surface processes during active breaking, such as turbulence generation and air entrainment, can not be resolved in this lower-resolution framework. Due to computational efficiency, however, this framework can be used to study long-term, $O(\text{days})$, and large-scale, $O(100m \approx 10km)$, breaking wave-driven circulation as well as transport of fine sediment and small, persistent bubbles.

Chapter 2

BREAKING-ONSET, ENERGY AND MOMENTUM FLUX IN UNSTEADY BREAKING WAVES

2.1 Abstract

Breaking waves on the ocean surface transfer energy and momentum into currents and turbulence. What is less well understood, however, is the associated total loss of wave energy and momentum flux. Further, finding a robust and universal diagnostic parameter that determines the onset of breaking and its strength is still an open question. [Derakhti & Kirby \(2014b\)](#) have recently studied bubble entrainment and turbulence modulation by dispersed bubbles in isolated unsteady breaking waves using large-eddy simulation. In this chapter, a new diagnostic parameter $\xi(t)$ is defined based on that originally proposed by [Song & Banner \(2002\)](#), and it is shown that, using a threshold value of $\xi_{th} = 0.05$, the new dynamic criteria is capable of detecting single and multiple breaking events in the considered packets. In addition, the spatial variation of the total energy and momentum flux in intermediate- and deep-water unsteady breaking waves generated by dispersive focusing is investigated. The accuracy of estimating these integral measures based on free surface measurements and using a characteristic wave group velocity is addressed. It is found that the new diagnostic parameter just before breaking, ξ_b , has a strong linear correlation with the commonly used breaking strength parameter b , suggesting that ξ_b can be used to parameterize the averaged breaking-induced dissipation rate and its associated energy flux loss. It is found that the global wave packet time and length scales based on the spectrally-weighted packet frequency proposed by [Tian et al. \(2010\)](#), are the reasonable estimations of the time and length scales of the carrier wave in the packet close to the focal/break point. A global wave steepness, S_s , is defined based on these spectrally-weighted scales, and its

spatial variation across the breaking region is examined. It is shown that the corresponding values of S_s far upstream of breaking, S_{s0} , have a strong linear correlation with respect to b for the considered focused wave packets. The linear relation, however, can not provide accurate estimations of b in the range $b < 5 \times 10^{-3}$. A new scaling law given by $b = 0.3(S_{s0} - 0.07)^{5/2}$, which is consistent with inertial wave dissipation scaling of [Drazen et al. \(2008\)](#), is shown to be capable of providing accurate estimates of b in the full range of breaking intensities, where the scatter of data in the new formulation is significantly decreased compared with that proposed by [Romero et al. \(2012\)](#). Furthermore, we examine nonlinear interactions of different components in a focused wave packet, noting interactive effect on a characteristic wave group velocity in both non-breaking and breaking packets. Phase locking between spectral components is observed in the breaking region as well, and subsequently illustrated by calculating the wavelet bispectrum.

2.2 Introduction

The breaking of ocean surface gravity waves [Figures 2](#) in a number of different environmental processes including air-sea exchange of heat, momentum and energy, underwater optics and acoustics, and upper ocean mixing ([Melville 1996](#)). During active breaking, the process may be characterized as a two-phase turbulent flow with a complex interface, involving a wide range of temporal and spatial scales. For practical use in large-scale wave modeling, the onset of breaking and subsequent integral measures of the process, such as total loss of wave energy and momentum flux, need to be parameterized using available pre-breaking information.

For many decades, considerable attention has been paid to find a robust and universal methodology to predict the onset of steepness-limited unsteady breaking waves ([Song & Banner 2002](#), [Wu & Nepf 2002](#), [Banner & Peirson 2007](#), [Tian et al. 2008](#)). There are several important reviews on the topic of wave breaking ([Banner & Peregrine 1993](#), [Melville 1996](#), [Duncan 2001](#), [Kiger & Duncan 2012](#)). Recently, [Perlin et al. \(2013\)](#) have reviewed the latest progress on prediction of geometry, breaking onset, and

energy dissipation of intermediate- and deep-water breaking waves. The predictive parameters involved can be categorized as (i) geometric, (ii) kinematic, and (iii) dynamic criteria. As summarized in [Perlin et al. \(2013, §3\)](#), one of the most reliable criteria which can distinguish between breaking packets from those that do not break is the dynamic criterion proposed by [Song & Banner \(2002\)](#). They proposed a dimensionless parameter, $\delta(t)$, to measure the growth rate of the local wave energy density, given by

$$\delta(t) = \frac{1}{\omega_c} \frac{D\langle\mu\rangle}{Dt}, \quad \mu = \frac{E_{max}k^2}{\rho^l g}, \quad (2.1)$$

where $\omega_c = 2\pi f_c$ is a characteristic angular frequency (e.g. , taken as the initial angular frequency of the center component of the dispersive packet), D/Dt represents the total derivative following the wave group, μ is the dimensionless local wave energy density, E_{max} is the maximum local wave energy density given in §3, k is the local wave number, ρ^l is the liquid density, and g is the gravitational acceleration. Here, the averaging procedure denoted by $\langle \rangle$ was proposed by [Song & Banner \(2002\)](#) to remove the large oscillation of μ , involving the determination of the upper and lower envelopes of μ as described in [Song & Banner \(2002, Appendix B\)](#). [Song & Banner \(2002\)](#) found that this dynamically-based mean growth rate of the local energy density maximum along a wave packet had a common threshold value of $[1.4 \pm 0.1] \times 10^{-3}$ associated with the initiation of breaking. As pointed out by [Perlin et al. \(2013\)](#), the calculation of the time-averaged local wave energy density $\langle\mu\rangle$ is nontrivial, and, thus, the application of the criterion, e.g. , in phase-resolving nonlinear wave prediction models, may be limited. A modified version of (2.1), which removes the required post-processing procedure in the calculation of $\langle\mu\rangle$, is defined in §3 and is tested for the packets considered here.

In addition to a selected pre-breaking diagnostic parameter, the accurate estimation of total loss of wave energy and momentum flux is needed to find a robust parameterization for the breaking strength, e.g. , the averaged breaking-induced wave energy dissipation rate. During the last three decades, laboratory experiments have

been conducted for the estimation and parameterization of total energy and momentum flux losses and their rates (Duncan 1983, Rapp & Melville 1990, Banner & Peirson 2007, Drazen et al. 2008, Tian et al. 2010, 2012). The most up-to-date review may be found in Perlin et al. (2013, §4). Inherent difficulties associated with the measurement of an instantaneous velocity field during an active breaking event make direct estimates of energy and momentum flux in a breaking region impractical. The common practice is to approximate energy and momentum flux through surface elevation measurements taken at fixed locations upstream and downstream of a break point, using a wave theory (usually linear theory) and a simple control volume analysis to obtain estimates of total fluxes (e.g., see Rapp & Melville 1990, §2.4).

Because numerical computations based strictly on inviscid, irrotational flow theory can not proceed beyond the onset stage of breaking, a post breaking flow field becomes unavailable. As summarized by Perlin et al. (2013, §6), most two-phase viscous numerical simulations for steepness-limited breaking waves are limited to the evolution of a periodic unsteady wave train having relatively low Reynolds numbers ($\sim 10^4$) and short wave lengths ($< 0.3m$). An exception is noted in recent work by Derakhti & Kirby (2014b). Examining bubble entrainment and turbulence modulation by dispersed bubbles in isolated unsteady breaking waves generated by dispersive focusing (with the same scale as in the previous laboratory experiments), they used an Eulerian-Eulerian polydisperse two-fluid model to performed large-eddy simulation (LES), together with a dynamic Smagorinsky sub-grid formulation for turbulence closure. As opposed to direct numerical simulations, the dissipative scales of the process as well as liquid-bubble interaction were sub-grid scale and were modeled using the available closure models, which is an inherent limitation in any LES study.

In this paper, we present direct estimates of total energy and momentum flux in unforced intermediate- and deep-water unsteady breaking waves generated by dispersive focusing. Both spilling and plunging breaking packets are considered. The accuracy of estimating these integral measures based on free surface measurements and using a characteristic wave group velocity is examined in detail. In addition, we

examine nonlinear interactions of different frequency components in a focused wave packet as well as interaction effects on a characteristic wave group velocity both in non-breaking and breaking packets. Phase locking between spectral components is observed in the breaking region as well, and subsequently illustrated by calculating the wavelet bispectrum.

Beside dispersive energy focusing, other mechanisms such as modulational instability (Benjamin & Feir 1967, Melville 1982) and wind-forcing (Grare et al. 2013, Smit et al. 2014) can induce wave breaking. Although some of the available estimates of the non-dimensional breaking strength parameter, b , in the field (Thomson et al. 2009, Smit et al. 2014) are comparable to those in spillers due to dispersive energy focusing (Drazen et al. 2008, Tian et al. 2010), most of the field estimations of b (Phillips et al. 2001, Gemmrich et al. 2008, 2013) tend to be more consistent with the observed b values in weak spillers due to modulational instability (Banner & Peirson 2007, Allis 2013). Here, we briefly establish that the present model is capable of capturing breaking waves due to modulational instability. A more detailed evaluation of this class of weak breaking events will appear in a separate paper.

In §2.3, the model set-up and choice of experimental data are explained. Results for breaking-onset prediction, energy and momentum flux are presented in §2.4, §2.5 and §2.6, respectively. Conclusions are given in §2.7.

Table 2.1: Input parameters for the 2D and 3D simulated cases. (i): [Rapp & Melville \(1990\)](#), $d = 0.6\text{m}$, $d/L_c = 0.3$ intermediate-depth, constant-amplitude packets; (ii): [Drazen et al. \(2008\)](#), $d = 0.6\text{m}$, $d/L_c = 0.3$ intermediate-depth, constant-steepness packets; (iii): [Tian et al. \(2012\)](#), $d = 0.62\text{m}$, $d/L_c = 1.1$ deep-water, constant-steepness packets. Here, d is the still water depth, L_c is the wavelength of the center frequency component of the incident packet f_c , S is the theoretical linear global wave steepness, Δf is the packet band width, x_b and t_b are the predefined, linear theory estimates of location and time of breaking respectively, and N is the number of different wave components in the packet. In constant-steepness packets, each wave component has a different amplitude, $a_i = S/(k_i N)$ such that component steepness $a_i k_i$ is constant with respect to i . In constant-amplitude packets, on the other hand, all the components have the same amplitude, $a_i = a$. [Rapp & Melville \(1990\)](#) defined the global steepness of a constant-amplitude packet as $S = k_c \sum_{i=1}^N a_i = k_c N a$ and, thus, $a = S/(k_c N)$. Different mesh grid densities are: G1 = ($\Delta x = 21.5, \Delta y = 7.0, \Delta z = 7.0$)mm, G2 = ($\Delta x = 18.3, \Delta z = 5.0$)mm, G3 = ($\Delta x = 10.0, \Delta z = 5.0$)mm, and G4 = ($\Delta x = 5.0, \Delta z = 5.0$)mm.

∞

Case no.	S	f_c (s ⁻¹)	$\Delta f/f_c$	t_b (s)	x_b (m)	N	Mesh resolution	Domain size (m)	Exp.
RN	0.150	0.88	0.73	20.5	8.5	32	G2,G3	(22.0,0.8)	(i)
RI	0.256	0.88	0.73	20.5	8.5	32	G2,G3	(22.0,0.8)	(i)
RS1	0.278	0.88	0.73	20.5	8.5	32	G2,G3	(22.0,0.8)	(i)
RP1	0.352	0.88	0.73	20.5	8.5	32	G2,G3	(22.0,0.8)	(i)
RP1(3D)	0.352	0.88	0.73	20.5	8.5	32	G1	(17.0,0.77,0.63)	(i)
RP2	0.388	0.88	0.73	20.5	8.5	32	G2,G3	(22.0,0.8)	(i)
DI	0.30	0.88	0.75	20.5	8.8	32	G2,G3	(22.0,0.86)	(ii)
DS1	0.32	0.88	0.75	20.5	8.8	32	G2,G3	(22.0,0.86)	(ii)
DP1	0.42	0.88	0.75	20.5	8.8	32	G2,G3	(22.0,0.86)	(ii)
DP2	0.46	0.88	0.75	20.5	8.8	32	G2,G3	(22.0,0.86)	(ii)
TN	0.256	1.7	0.824	25.0	7.0	128	G3,G4	(16.0,0.8)	(iii)
TP1	0.410	1.7	0.824	25.0	7.0	128	G3,G4	(16.0,0.8)	(iii)
TP2	0.576	1.7	0.824	25.0	7.0	128	G3,G4	(16.0,0.8)	(iii)
TP3	0.742	1.7	0.824	25.0	7.0	128	G3,G4	(16.0,0.8)	(iii)

2.3 Model Set-up and Choice of Experimental Conditions

A detailed description of the polydisperse two-fluid model used here as well as boundary conditions are given in Appendix A. Here, the incident wave boundary condition and model set-up are discussed briefly.

All model simulations are performed with the model initialized with quiescent conditions. An incident wave packet is then generated at the model upstream boundary. The input wave packet was composed of N sinusoidal components of steepness $a_i k_i$, $i = 1, \dots, N$ where a_i and k_i are the amplitude and wave number of the i th frequency component. Based on linear superposition and by imposing that the maximum η occurs at x_b and t_b , the total surface displacement at the incident wave boundary $x = 0$ is given by

$$\eta(0, t) = \sum_{i=1}^N a_i \cos[2\pi f_i(t - t_b) + k_i x_b], \quad (2.2)$$

where f_i is the frequency of the i th component, and x_b and t_b are the predefined, linear theory estimates of location and time of breaking, respectively (e.g. see [Rapp & Melville 1990](#), §2.3). The discrete frequencies f_i were uniformly spaced over the band $\Delta f = f_N - f_1$ with a central frequency defined by $f_c = 1/2(f_N + f_1)$. Different theoretical global steepness, $S = \sum_{i=1}^N a_i k_i$, and bandwidth, $\Delta f / f_c$, lead to spilling or plunging breaking, where increasing S and/or decreasing $\Delta f / f_c$ increases the breaking intensity (See [Drazen et al. \(2008\)](#) for more details). Free surface displacements and velocities for each component are calculated using linear theory and then superimposed at $x = 0$.

The input packet parameters as well as mesh resolutions and domain sizes for cases considered here are summarized in Table 3.1. The convergence study may be found in [Derakhti & Kirby \(2014a\)](#). The model parameters for a polydisperse bubble phase are chosen as summarized in [Derakhti & Kirby \(2014b, Table 4\)](#).

For non-breaking cases, t_b and x_b are used as the reference for the time and x direction respectively. For breaking packets, the references for time and x direction are t_{ob} and x_{ob} , respectively. For plunging breakers, t_{ob} and x_{ob} are the time and location

at which the falling jet hits the undisturbed forward face of the wave. For spilling breakers, on the other hand, t_{ob} and x_{ob} are the time and location at which a vertical tangent develops near the wave crest. Normalized horizontal position and time can then be written as

$$x^* = \frac{x - x_{ob}}{L_{s0}}, \quad t^* = \frac{t - t_{ob}}{T_{s0}}, \quad (2.3)$$

where L_{s0} and T_{s0} are the characteristic length and time scales of the carrier wave in the packet far upstream of the focal/break point, and are calculated based on the spectrally-weighted frequency of the wave packet f_s given by

$$f_s = \frac{\sum f_i |\mathcal{F}_i|^2 \Delta f_i}{\sum |\mathcal{F}_i|^2 \Delta f_i}, \quad (2.4)$$

where, \mathcal{F}_i and f_i are the discrete Fourier transform and the frequency of the i th component of the wave train, respectively. Δf_i is the frequency difference between components, which is constant here. The characteristic wave length L_s and period T_s , hereafter called spectrally-weighted wave length and period, are calculated based on f_s and using the linear dispersion relation. [Tian et al. \(2010\)](#) found that this choice of the characteristic wave parameters provided the best data collapse for their wave packets. We also found that the corresponding length and time scales of the carrier wave in the packet close to the focal/break point are predicted more accurately by this choice of the characteristic parameters compared with those of the center frequency of the wave packet, especially for our deep-water packets. For constant-amplitude packets we have $f_{s0} \approx f_c$, and thus $L_{s0} \approx L_c$ and $T_{s0} \approx T_c$, where subscript c indicates the center frequency component of the wave packet.

2.4 Prediction of the Onset of Wave Breaking

Avoiding the post-processing procedure in (2.1), we define the normalized growth rate of the time-dependent $\mu = E_{max} k^2 / \rho^l g$ as

$$\xi(t) = \frac{1}{\omega_{s0}} \frac{D\mu}{Dt}, \quad (2.5)$$

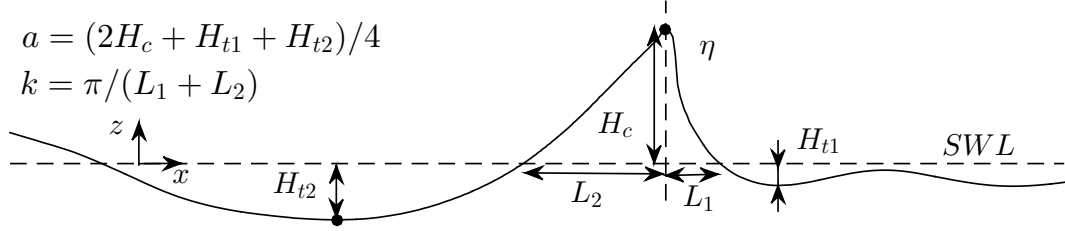


Figure 2.1: Definitions of the local wave parameters. k and a are the local wave number and amplitude respectively. The wave propagates from the left to the right.

where $\omega_{s0} = 2\pi f_{s0}$ is the pre-breaking characteristic wave angular frequency, and k is the local wave number calculated based on two consecutive zero-crossings adjacent to the breaking crest (see Figure 2.1) as suggested by Tian et al. (2008). Here, E_{max} is the time-dependent, non-horizontally averaged local maximum of the ensemble-averaged depth-integrated total energy density $E(t, x)$ along the wave group given by

$$E(t, x) = \left\langle \int_{-d}^{\eta} \frac{1}{2} \rho u_i^2 dz \right\rangle + \left\langle \int_{-d}^{\eta} \rho g z dz \right\rangle + \frac{1}{2} \rho^l g d^2 = E_k + E_p \quad (2.6)$$

where $i = 1, 2, 3$ refers to the x, y and z directions respectively; $\rho = \alpha \rho^l$ is the mixture density, and α is liquid volume fraction; d is the still water depth, z is the vertical distance to the still water level (positive upward), E_k is the ensemble-averaged depth-integrated kinetic energy density, and E_p is the ensemble-averaged depth-integrated potential energy density. Hereafter, $\langle \cdot \rangle$ indicates ensemble averaging and is approximated by spanwise averaging as in Derakhti & Kirby (2014b, §2.8). No spatial averaging is employed in the 2D simulations.

Figure 2.2 shows that, in all the intermediate- and deep-water breaking packets considered here, the corresponding values of ξ before breaking, say $-0.5 < t^*$, exceed an approximate threshold value of $\xi_{th} = 0.05$. In the incipient breaking packets RI and DI, it is seen that $\xi_{max} \sim 0.05$, also supporting the selection of $\xi_{th} = 0.05$ as a maximum normalized growth rate of the local wave energy density maximum for the

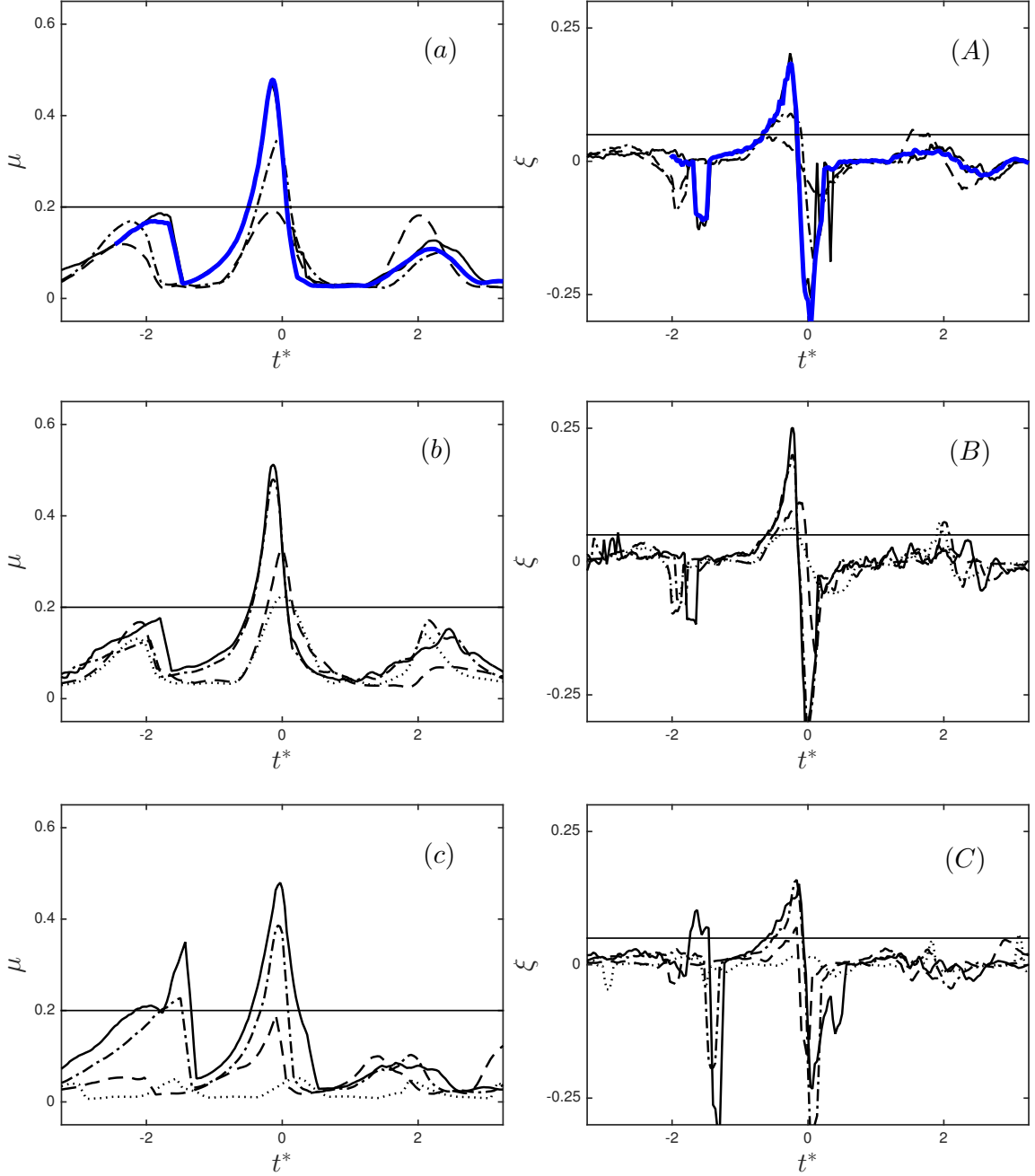


Figure 2.2: Temporal variations of (a, b, c) the normalized local energy density maximum, μ , and (A, B, C) its normalized growth rate, ξ , for different breaking and non-breaking packets. (a, A) intermediate-depth incipient breaking RI (---), spilling breaker RS1 (-·-), plunging breaker RP1 (—); (b, B) intermediate-depth incipient breaking DI (·····), spilling breaker DS1 (---), plunging breaker DP1 (-·-), plunging breaker DP2 (—); and (c, C) deep-water non-breaking packet TN (·····), weak plunging breaker TP1 (---), plunging breaker TP2 (-·-), plunging breaker TP3 (—). Horizontal lines show $\mu = 0.2$ and $\xi = 0.05$. Thick lines in panels (a, A) are the results for RP1(3D).

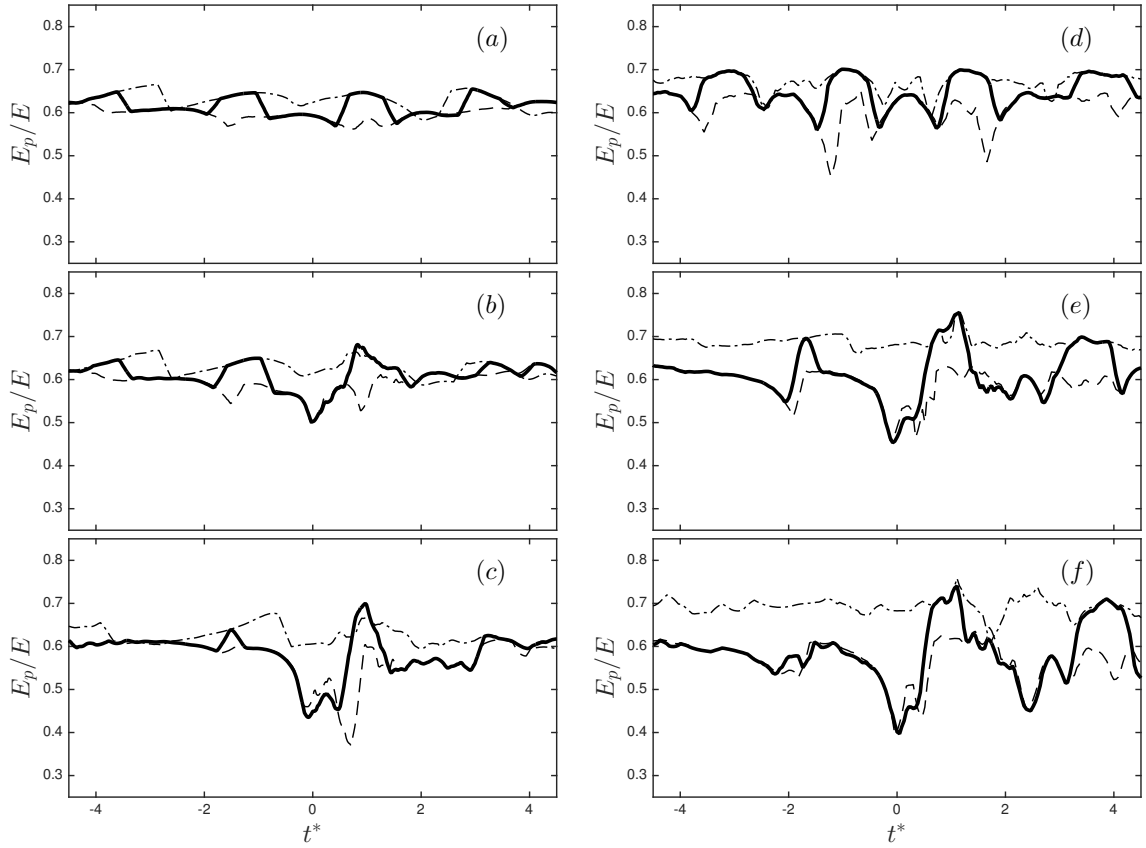


Figure 2.3: Temporal variations of the ratio of the potential energy density to the total energy density for (a) RI, (b) RS1, (c) RP1, (d) TN, (e) TP2, (f) TP3; at the locations of E_{max} (—), crest maxima (---), and trough maxima (- · -).

non-breaking packets. The exceedance of the threshold value $\xi_{th} = 0.05$ at $t^* \approx -1.5$ for the deep-water packet with multiple plungers TP3 is because of the preceding weaker breaking wave in the packet before the main breaker at $t^* = 0$, observed both in the simulation and the corresponding measurement by [Tian et al. \(2012\)](#). Thus, the criterion is capable of detecting multiple breaking events in a wave group. [Figure 2.2](#) also shows that $\mu > 0.2$ at which $\xi > \xi_{th}$ in all breaking packets except the deep-water weak plunging breaker TP1. For the intermediate-depth plunging breaking case RP1, comparing the results of the two-dimensional (2D) and the three-dimensional (3D) simulations, shown in panel (A) with thin and thick solid lines respectively, we may conclude that the 2D simulation captures the evolution of ξ fairly accurately.

The evaluation of E_{max} needs the spatio-temporal variation of both the free surface and velocity field. Although the free surface locations are easy to measure, the velocity field may not be available especially in in-situ measurements. Thus, the estimation of E_{max} based only on the free surface information is of potential interest. [Figure 2.3](#) shows that the location of E_{max} switches between the crest maxima and trough maxima before and after the focal/break point both in the intermediate- and deep-water packets. However, it is always on the crest maxima close to the focal/break point, say $-1 < t^* < 0$, at which ξ goes beyond the threshold value of 0.05. As S increases, the location of E_{max} occurs at the crest maxima more frequently. In addition, increasing S results in decreasing the E_p/E ratio at the crest maxima and in increasing the E_p/E ratio at trough maxima; a similar trend can be seen in [Tian et al. \(2008, Figure 11\)](#). Thus, we may estimate $E_{max} \approx E_p^{cm}/\lambda$ before the break point, where $E_p^{cm} = \frac{1}{2}\rho^l g z_{max}^2$ is the local potential energy density at the crest maxima and $\lambda = E_p/E_{max}$, shown by thick solid lines in [Figure 2.3](#), varies from ≈ 0.6 for $t^* < -1$ down to ≈ 0.5 at breaking-onset.

2.5 Fractional and Total Losses of Energy Flux

The ensemble- and time-averaged depth-integrated horizontal energy flux of a 2D wave packet per unit crest length over the time $t = t_1 \rightarrow t_2$, $\overline{\overline{F^E}}$, can be written as

$$\overline{\overline{F^E}}(x) = \frac{1}{t_2 - t_1} \int_{t_1}^{t_2} \left\langle \int_{-d}^{\eta} \left[\frac{1}{2} \rho u_i^2 + p + \rho g z \right] u dz \right\rangle dt, \quad (2.7)$$

where $\overline{(\)}$ hereafter refers to ensemble and time averaging, p is the pressure, and the rest of variables were defined in the text below (2.6). For simplicity, hereafter the term ‘‘averaged’’ is used to represent ensemble- and time averaging and depth-integration. We choose $t_1 = 0$ and $t_2 = 40.0$ s to cover the entire signal. For breaking packets, although (2.7) represents the averaged horizontal wave energy flux before and far downstream of the break point ($x^* < 0$ and $x^* > 1$), the breaking-induced current and turbulent motions contribute partially to the averaged energy flux for $0 < x^* < 1.0$. Our main interest is estimating the total loss of wave energy flux after the breaking region, and thus such a decomposition close to the break point has not been applied.

The spatial variations of $\overline{\overline{F^E}}$ are shown in Figure 2.4 (solid lines) for different packets. Most of the energy flux loss occurs within one wavelength downstream of the break point, $0 < x^* < 1$, while the rate of loss is larger close to the break point. The app2Arent loss before $x^* = 0$ in panel (d) is due to a weaker preceding breaking event in the packet. For breaking packets, the contribution of the kinetic energy flux, $\overline{\overline{F_k^E}} = \overline{\overline{\int_{-d}^{\eta} \left[\frac{1}{2} \rho u_i^2 \right] u dz}}$, to $\overline{\overline{F^E}}$ is negligibly small far from the break point, less than 3% of the total flux, but reaches up to $0.15 \overline{\overline{F^E}}$ close to the break point, as shown in Figure 2.5. Consistent with the linear theory prediction, the contribution of $\overline{\overline{F_k^E}}$ to $\overline{\overline{F^E}}$ is negligibly small for the non-breaking packet RN, shown in panel (a).

Under the linear potential flow assumption, it is known that the averaged wave horizontal energy flux and energy density can be related using a group velocity based on the linear dispersion relation. Thus, we define an energy transport velocity for our

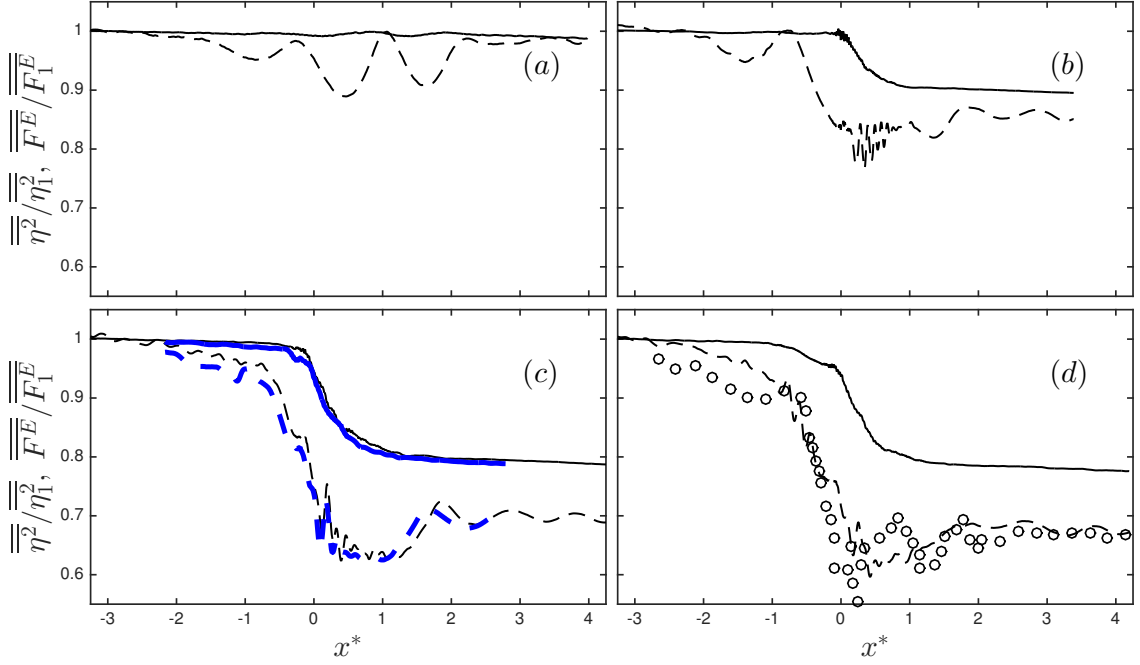


Figure 2.4: Normalized exact $\overline{\overline{F^E}} / \overline{\overline{F_1^E}}$ (—) and approximated $(\overline{\overline{F^E}} / \overline{\overline{F_1^E}})_{app1} \approx \overline{\overline{\eta^2}} / \overline{\overline{\eta_1^2}}$ (---) averaged horizontal energy flux for intermediate-depth (a) incipient breaking, RI; (b) spilling breaker, RS1; (c) plunging breaker, RP1; and (d) plunging breaker, RP2. Circles are the measured $\overline{\overline{\eta^2}} / \overline{\overline{\eta_1^2}}$ adopted from Rapp & Melville (1990) Figure 11(b). Thick lines are the results for RP1(3D).

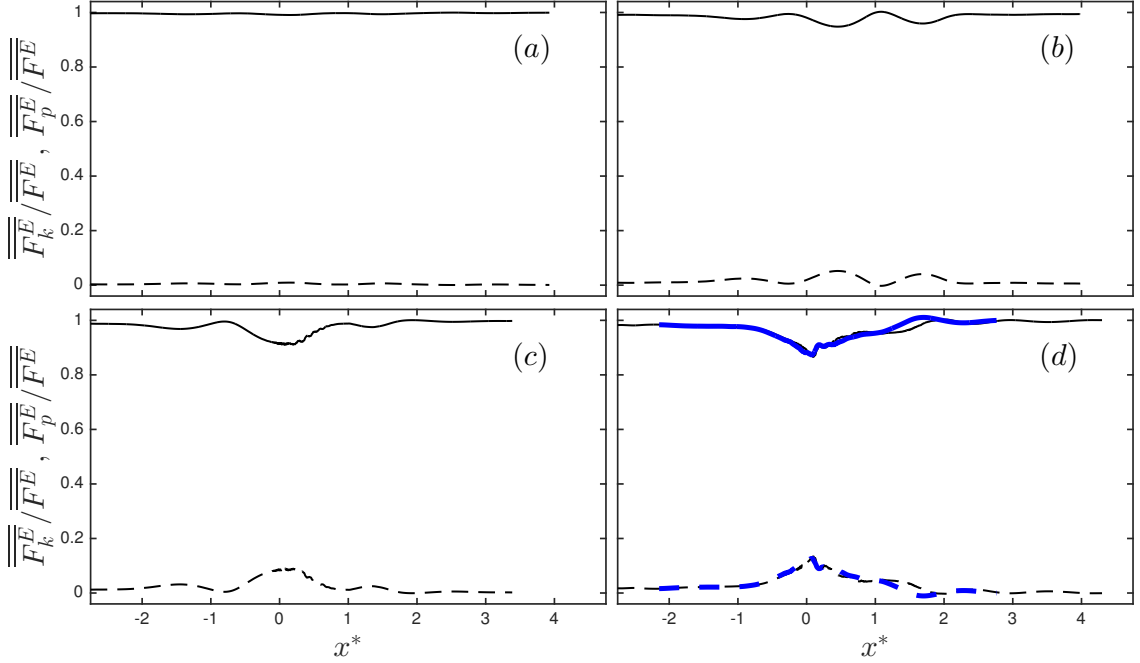


Figure 2.5: Normalized averaged energy flux due to dynamic pressure, $\overline{\overline{F_p^E}}/\overline{\overline{F^E}}$ (—), and kinetic energy $\overline{\overline{F_k^E}}/\overline{\overline{F^E}}$ (---) for intermediate-depth (a) non-breaking packet RN; (b) incipient breaking, RI; (c) spilling breaker, RS1; and (d) plunging breaker, RP1. Thick lines are the results for RP1(3D). Here, $\overline{\overline{F_p^E}} = \int_{-d}^{\eta} [p + \rho g z] u dz$ and $\overline{\overline{F_k^E}} = \int_{-d}^{\eta} [\frac{1}{2} \rho u_i^2] u dz$.

nonlinear and breaking packets as

$$C_E = \overline{\overline{F^E}} / \overline{\overline{E}}, \quad (2.8)$$

where $\overline{\overline{F^E}}$ and $\overline{\overline{E}} = \overline{\overline{E_p}} + \overline{\overline{E_k}}$ are the exact averaged energy flux and density calculated from the simulation results using (2.7) and (2.6), respectively. Strictly speaking, the strong nonlinearity as well as breaking-induced current and turbulent motions, which do not have a dispersion relation, make the linear potential flow assumption invalid, and thus this definition of C_E is different from the theoretical definition of a linear wave group velocity, e.g. , $C_g = \partial\omega/\partial k$ in the breaking region. Far from the break point, however, $C_E \simeq C_g$.

The estimation of potential energy is challenging in regions where a multi-valued surface and/or large bubble void fraction exist. In other words, $\frac{1}{2}\rho^l g \overline{\eta^2}$ is only an approximate measure of the exact averaged potential energy density given by $\overline{\overline{E_p}} = \overline{\int_{-d}^{\eta} \rho g z dz} + \frac{1}{2}\rho^l g d^2$ in the regions of jet formation and subsequent splashes, which are limited in the range $-0.2 < x^* < 0.5$ in our breaking packets. Consistent with experimental studies, we use the $\frac{1}{2}\rho^l g \overline{\eta^2}$ estimation for $\overline{\overline{E_p}}$ only in our approximate formulas. Our methodology to define the free surface location in the regions with a multi-valued surface together with the comparison between $\overline{\overline{E_p}}$ and $\frac{1}{2}\rho^l g \overline{\eta^2}$ are presented in Appendix A. In conclusion, $\frac{1}{2}\rho^l g \overline{\eta^2}$ is a fairly accurate estimation for $\overline{\overline{E_p}}$ except for $-0.2 < x^* < 0.5$.

The total loss of the averaged horizontal wave energy flux in the breaking region can be obtained as $\Delta \overline{\overline{F^E}} = \overline{\overline{F_1^E}} - \overline{\overline{F_2^E}}$, where the subscripts 1 and 2 refer to upstream and downstream of the break point respectively. By assuming that the averaged energy density is equal to twice the averaged potential energy density and using (2.8), we get

$$\Delta \overline{\overline{F^E}} \approx \rho^l g C_{E1} (\overline{\eta_1^2} - \frac{C_{E2}}{C_{E1}} \overline{\eta_2^2}), \quad (2.9)$$

where either the linear group velocity of the center frequency component, C_{gc} , or a

spectrally-weighted group velocity of the wave packet have been previously proposed as an estimation for the characteristic group velocity. Drazen et al. (2008) defined a spectrally-weighted group velocity, C_{gs} , as

$$C_{gs} = \frac{\sum C_{gi} |\mathcal{F}_i|^2 \Delta f_i}{\sum |\mathcal{F}_i|^2 \Delta f_i}, \quad (2.10)$$

where C_{gi} is the linear group velocity of the i th component of the wave train, and the rest of variables were defined in (2.4). They showed that their wave trains propagated at a speed close to this characteristic group velocity. figure 2.6 also demonstrates that both C_E and C_{gs} are reasonable estimators of the travel speed of the wave groups, while C_{gc} significantly underestimates wave group travel speed (see also Tian et al. 2010, Figure 4). In a number of previous experimental studies (Rapp & Melville 1990, Wu & Nepf 2002, Banner & Peirson 2007, Tian et al. 2010, 2012), it has been assumed that $C_{E2} = C_{E1}$. Thus, the total loss of the averaged horizontal wave energy flux and its associated fractional loss may be approximated as

$$(\overline{\Delta F^E})_{app1} \approx \rho^l g C_{gs1} \Delta \overline{\eta^2}, \quad (\overline{\Delta F^E / F_1^E})_{app1} \approx \Delta \overline{\eta^2} / \overline{\eta_1^2}. \quad (2.11)$$

Figure 2.4 shows $\overline{F^E / F_1^E}$ and $(\overline{F^E / F_1^E})_{app1} \approx \overline{\eta^2} / \overline{\eta_1^2}$ for the intermediate-depth incipient breaking RI, spilling breaker RS1, and plunging breakers, RP1 and RP2. First, 2D simulations give fairly reasonable results in terms of the averaged horizontal energy flux and potential energy density variations compared with the corresponding 3D-simulation shown in panel (c) as well as the measurement shown in panel (d), and also provide fairly accurate results compared with the surface measurements by Tian et al. (2012) for deep-water packets (not shown). The app2Arent undulations in $\overline{\eta^2}$ do not exist in $\overline{F^E}$. Because of these undulations, a spatially-averaged value of $\overline{\eta^2}$ over about two meters is used upstream and downstream of the break point to apply (2.11). As summarized in Table 2.2, using (2.11) overestimates the fractional and total loss of the horizontal energy flux by approximately 35% to 70% for our breaking packets.

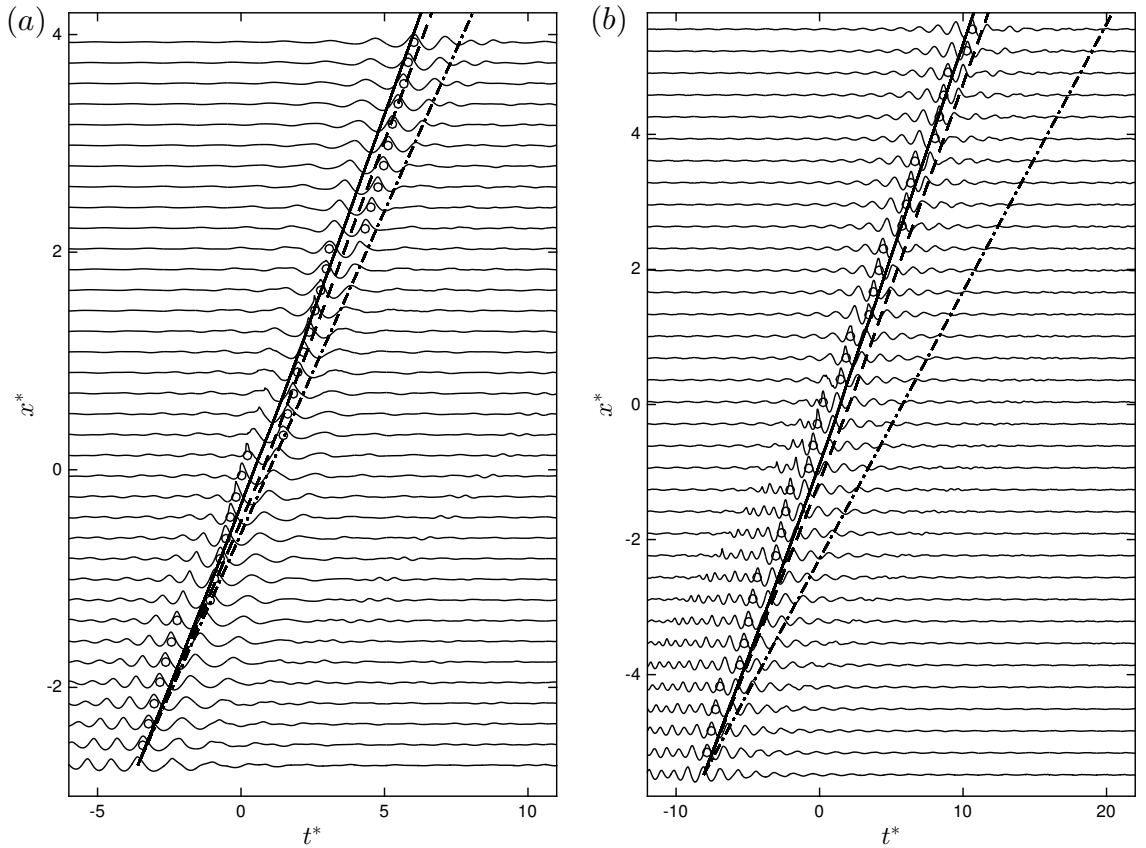


Figure 2.6: Temporal variations of surface elevation for (a) intermediate-depth plunger RP1 and (b) deep-water plunger TP2 at different spatial locations. Different lines show $dx^*/dt^* = C$, where $C = C_E$, energy transport velocity (—), $C = C_{gs}$, spectrally-weighted group velocity (---), and $C = C_{gc}$, group velocity of the center frequency of the wave packet (-·-). Circles show the crest maximum at each spatial location. For clarity, the surface elevation is exaggerated by a factor of 4.

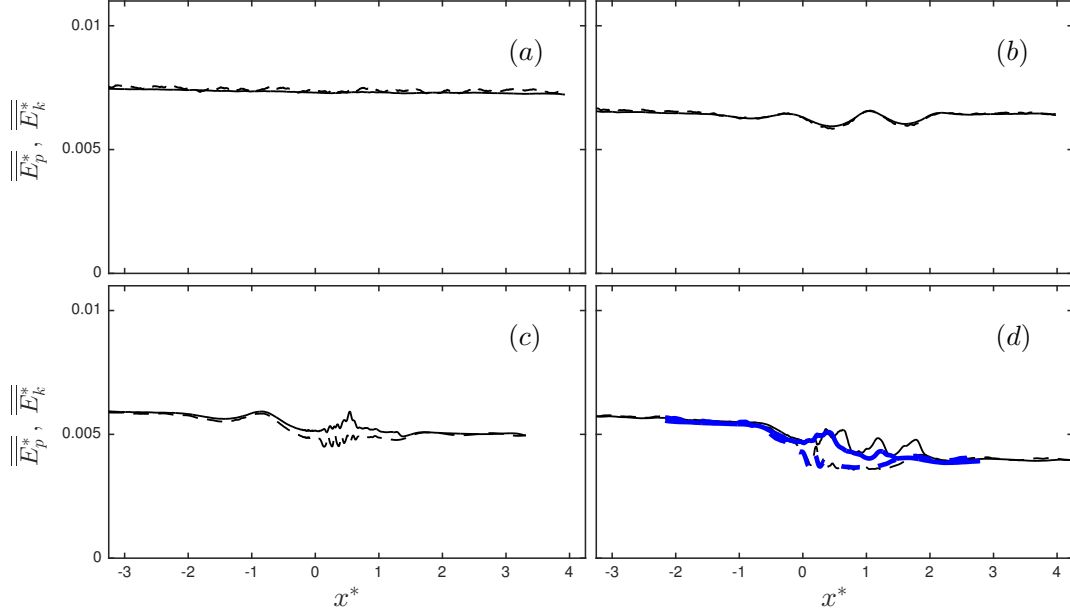


Figure 2.7: Normalized averaged kinetic energy density, $\overline{\overline{E_k^*}}$, (—); and potential energy density, $\overline{\overline{E_p^*}}$, (---) for intermediate-depth (a) non-breaking packet RN; (b) incipient breaking, RI; (c) spilling breaker, RS1; and (d) plunging breaker, RP1. Thick lines are the results for RP1(3D). The results are normalized by a reference value of $\rho^l g k_{s0}^2 S_{s0}^{-2}$, where S_{s0} and k_{s0} are defined in §4.3.

Three main assumptions are involved in (2.11): (i) $\overline{\overline{E}} \approx \rho^l g \eta^2$ is a valid estimation, (ii) using C_{gs} is a sufficient estimate of C_E , and (iii) the change of a selected group velocity through the breaking region may be ignored. As shown in Figures 2.7 and Figure B.2, the first assumption is fairly accurate far from the break point ($x^* < -0.5$ and $x^* > 2$). The other two assumptions will be discussed in the following section.

2.5.1 Characteristic Wave Group Velocity

Figure 2.8 shows the spatial variation of C_E (solid lines) and C_{gs} (dashed lines), calculated using (2.8) and (2.10), for the intermediate-depth non-breaking packet RN, incipient breaking RI, as well as breaking packets RS1 and RP1. C_{gs} is easily computed based on measured free surface time-series, while estimating C_E requires instantaneous velocity and pressure measurement over the entire depth. For all the breaking and

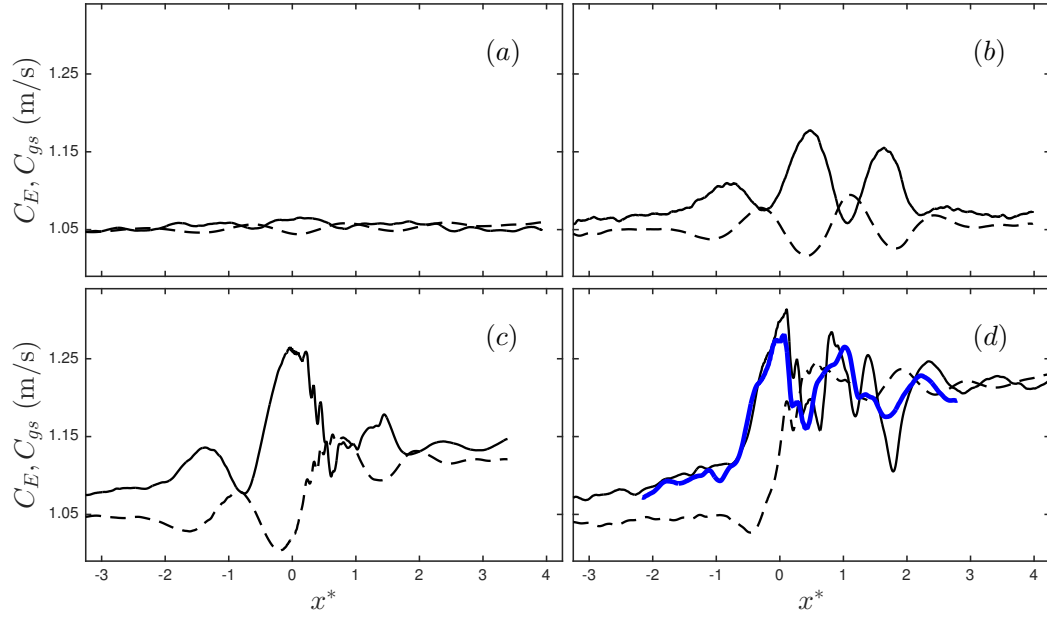


Figure 2.8: Energy transport velocity, C_E , (—) and spectrally-weighted group velocity, C_{gs} (---) for intermediate-depth (a) non-breaking packet RN; (b) incipient breaking, RI; (c) spilling breaker, RS1; and (d) plunging breaker, RP1. Thick lines are the results for RP1(3D).

non-breaking packets, there is a local increase of C_E as the packets approach the focal/break point, where local peaks become relatively smaller as S decreases. Far downstream of the focal/break point, C_E is equal to its value at the upstream of the focal point for the non-breaking packet RN and the incipient breaking RI. For breaking packets, on the other hand, there is an apparent increase after the break point, due to noticeable breaking-induced dissipation of higher frequency components of the packet. This increase of C_E after the breaking region becomes relatively larger as the breaker intensity increases. Tian et al. (2010) also observed a jump about a 5% to 10% increase in C_{gs} after wave breaking for their breaking packets. On the other hand, this jump is not reported by Drazen et al. (2008), who argued that their spectrally-weighted group velocity remains unchanged within their experimental accuracy. Figure 2.8 shows that C_{gs} is a good choice for an energy transport velocity, because it predicts fairly comparable estimates of C_E before and after the breaking region.

Thus, ignoring the change of a selected wave group velocity after breaking region leads to the overprediction of $\overline{\Delta F^E}$ (Table 2.2). We can rewrite (2.9) based on C_{gs} as

$$\overline{\Delta F^E} \approx \rho^l g C_{gs1} (\alpha_1 \overline{\eta_1^2} - \alpha_2 \beta \overline{\eta_2^2}), \quad (2.12)$$

where $\alpha_{1,2} = (C_E/C_{gs})_{1,2}$ and $\beta = C_{gs2}/C_{gs1}$, with $\beta > 1.0$ can be obtained for each specific breaker using free surface measurements. Table 2.2 summarizes the computed values of α_1, α_2 and β for the different breaking packets. By choosing $\alpha_2 = 1.0$, we get

$$(\overline{\Delta F^E})_{apx2} \approx \rho^l g C_{gs1} (\alpha_1 \overline{\eta_1^2} - \beta \overline{\eta_2^2}). \quad (2.13)$$

where $\alpha_1 = \text{Max}(1.0, 0.13(S_{s0} - 0.2) + 1.0)$, obtained based on linear curve fitting. Here, S_{s0} is the spectrally-weighted global steepness of the packet far upstream of breaking as defined in §4.3. The estimated total horizontal wave energy flux losses using (2.13) are also given in Table 2.2. In contrast to $(\overline{\Delta F^E})_{apx1}$, which has at least 35% error, $(\overline{\Delta F^E})_{apx2}$ is more accurate, with errors of less than 5%.

Table 2.2: Summary of fractional and total energy and momentum flux loss for the breaking packets. $\overline{\Delta\eta^2}/\overline{\eta_1^2}$ is the fractional loss of the total potential energy, $\overline{\Delta F^E}/\overline{F_1^E}$ and $\int_t \overline{\Delta F^E}$ are the fractional and total loss of the total horizontal energy flux respectively, $\overline{\Delta\bar{I}}/\overline{\bar{I}_1}$ and $\int_t \overline{\Delta\bar{I}}$ are the fractional and total loss of the total horizontal wave momentum flux respectively. $\overline{S_{p1}}$ is the horizontal momentum flux due to the mean pressure field. \int_t (2.11) and \int_t (2.13) are the commonly used and the proposed estimates of $\int_t \overline{\Delta F^E}$, respectively. α_1, α_2 and β are defined below (2.12). γ is defined below (2.25). Subscript 1 refers to far upstream of the break point.

Case no.	$\frac{\overline{\Delta\eta^2}}{\overline{\eta_1^2}}$ (%)	$\frac{\overline{\Delta F^E}}{\overline{F_1^E}}$ (%)	$\int_t \overline{\Delta F^E}$ (J/m)	\int_t (2.11) (J/m)	\int_t (2.13) (J/m)	α_1	α_2	β	$\frac{\overline{\Delta\bar{I}}}{\overline{\bar{I}_1}}$ (%)	$\frac{\overline{S_{p1}}}{\overline{\bar{I}_1}}$	$\int_t \overline{\Delta\bar{I}}$ (N/m)	γ
RS1	14.0	10.1	5.7	7.6	5.4	1.030	1.016	1.07	12.6	0.21	4.1	1.021
RP1	28.9	19.5	17.8	25.4	18.5	1.035	1.007	1.16	23.7	0.17	12.4	1.063
RP2	31.7	21.7	24.3	33.8	24.05	1.045	1.000	1.20	26.3	0.16	16.8	1.073
DS1	10.7	6.9	8.4	12.9	9.0	1.017	1.000	1.06	7.6	0.26	4.8	1.027
DP1	21.7	15.3	32.0	43.6	31.2	1.037	0.990	1.13	15.9	0.26	17.3	1.056
DP2	28.1	19.9	50.5	67.8	51.8	1.047	0.980	1.16	17.2	0.23	22.6	1.067
TP1	13.3	8.1	0.45	0.7	0.5	1.010	1.015	1.05	13.0	0.10	0.5	0.988
TP2	25.0	16.0	1.6	2.3	1.8	1.031	1.027	1.12	24.6	0.07	1.9	0.979
TP3	30.3	21.5	3.5	4.6	3.7	1.053	1.027	1.16	31.0	0.03	4.0	0.974

2.5.2 Nonlinear Wave-wave Interaction Before the Focal/Break Point

Although C_{gs} captures the main features of C_E , there is a permanent lag between the local peaks of C_{gs} and C_E . In addition, C_{gs} predicts slightly smaller values compared with C_E especially before the break point, consistent with the observation of envelope propagation shown in Figure 2.6 and by Tian et al. (2010, Figure 4). Tian et al. (2010) found that a nonlinear correction to the linear group velocity, used to calculate C_{gs} , had negligibly small effects and argued that this difference should be explained by nonlinear interaction between different wave components rather than the nonlinear correction to the linear group velocity of each wave component.

Figure 2.9 shows that there is an interesting correlation between these local peaks of C_E before the focal/break points (solid lines) and the wave asymmetry of the dominant wave in the packet $A_s(x) = \int_{t_{zu}}^{t_{max}} \eta^3 dt - \int_{t_{max}}^{t_{zd}} \eta^3 dt$ (dotted lines); in which negative asymmetry, indicating waves which are pitched forward, is associated with the increase of C_E and vice versa. Here, t_{zu} and t_{zd} are the associated time of two consecutive zero-crossing $\eta = 0$ before and after the crest maxima at t_{max} . The negative asymmetry can explain the observed energy transfer to the higher frequency components, and the increase of the spectrally-weighted frequency of the packet f_s (dashed lines). Since the higher frequency components have relatively smaller linear group velocities, one may expect the decrease of C_E as f_s increases, as predicted by C_{gs} shown in Figure 2.8 (dashed lines). Surprisingly, C_E considerably increases as f_s increases close to the focal/break points, which is completely an opposite trend compared with that predicted using the linear theory.

In the following we use the continuous wavelet transform to study the spatio-temporal structure and relative phasing of different wave components in the packet. We particularly aim to explain the considerable increase of C_E before the break point $x^* < 0$ as well as the noticeable undulation of C_E in the incipient breaking case RI, as shown in Figures 2.8 and 2.9 (solid lines). Because there is negligibly small breaking-induced dissipation in RI and in $x^* < 0$ for breaking packets, this increase of C_E can only be explained through the nonlinear interaction of different wave components of

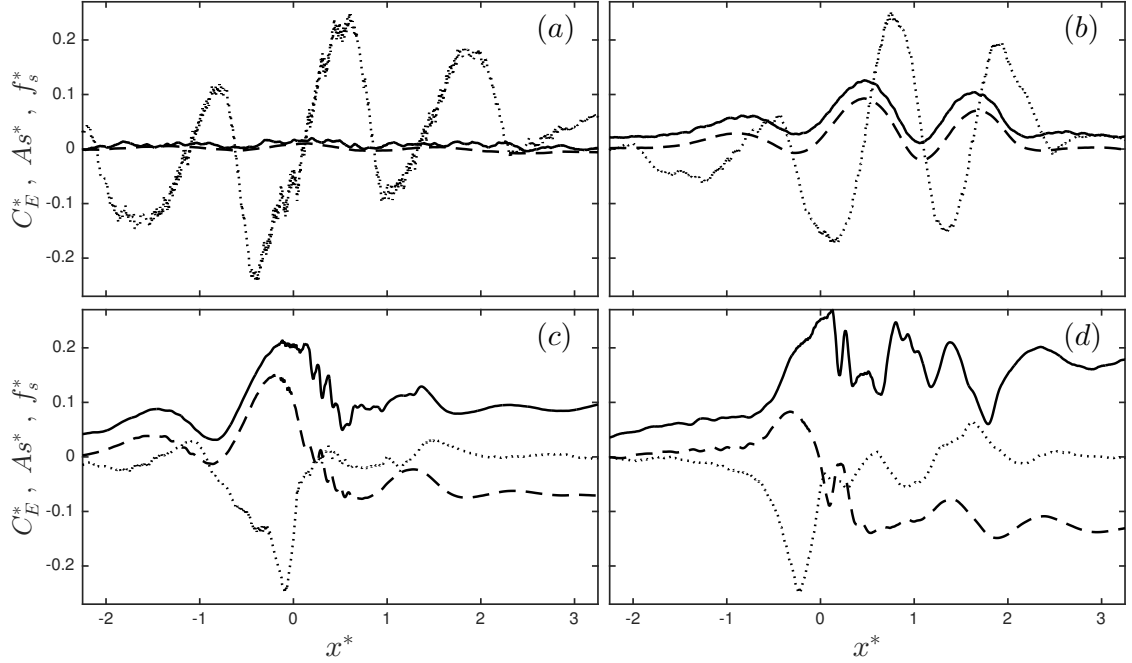


Figure 2.9: Normalized energy transport velocity $C_E^* = (C_E - C_{gs1})/C_{gs1}$ (—), normalized wave asymmetry near the dominant component of the packet $A_s^* = 0.25A_s/|A_s|_{max}$ (·····), and normalized spectrally-weighted frequency $f_s^* = (f_s - f_{s1})/f_{s1}$ (---) for intermediate-depth (a) non-breaking packet RN; (b) incipient breaking, RI; (c) spilling breaker, RS1; and (d) plunging breaker, RP1.

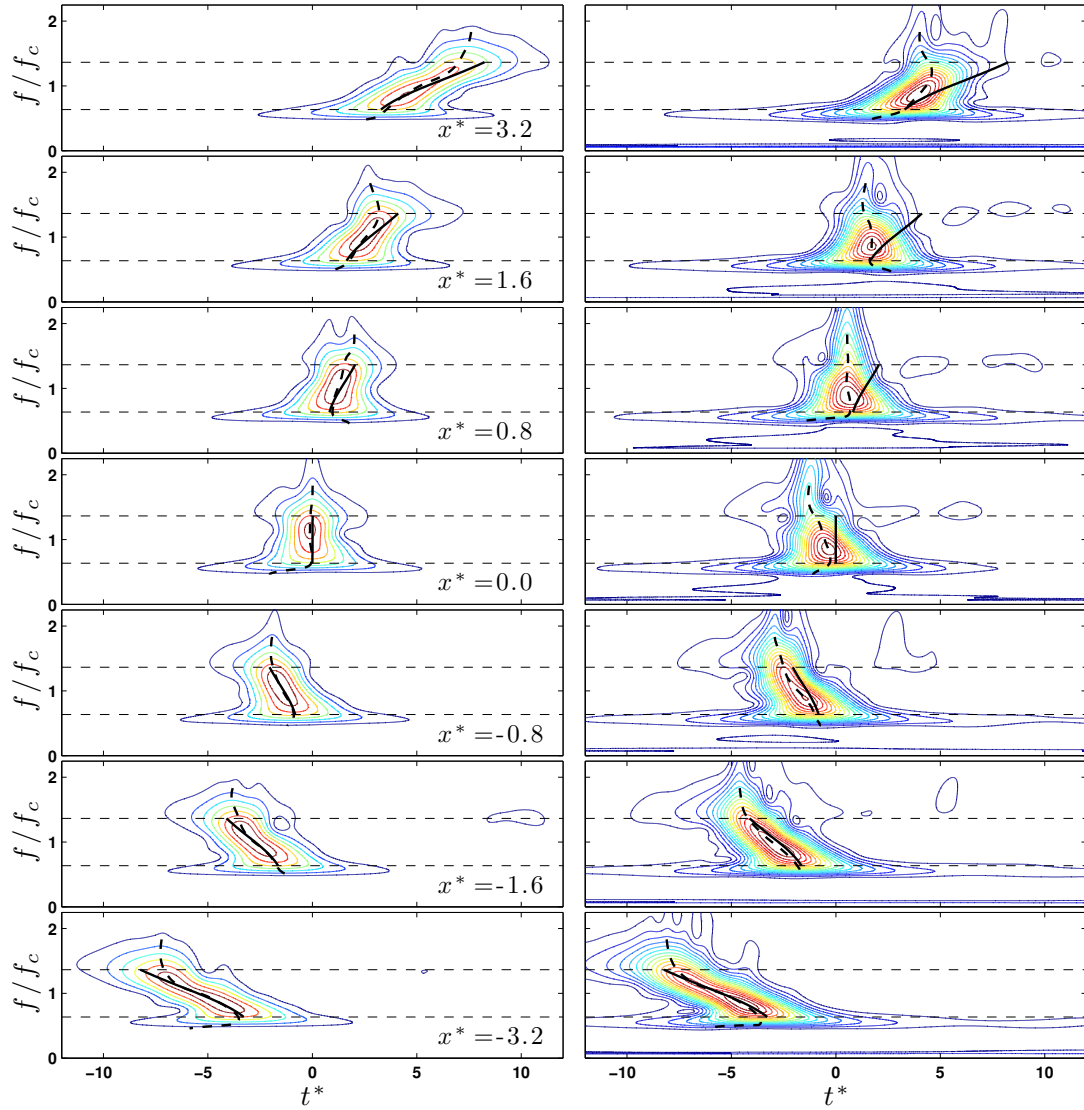


Figure 2.10: Modulus of the wavelet transform of the non-breaking packet RN (left); and plunging breaker RP1 (right). Contours show $|W_{(\eta)}|$, in the range 0.025 to 0.5 with intervals of 0.025. Horizontal dotted lines show the frequency band boundaries of the input packet. — shows the arrival time of the different frequencies based on the linear group velocity. - - - shows the arrival time of the wavelet amplitude maximum for the different frequencies.

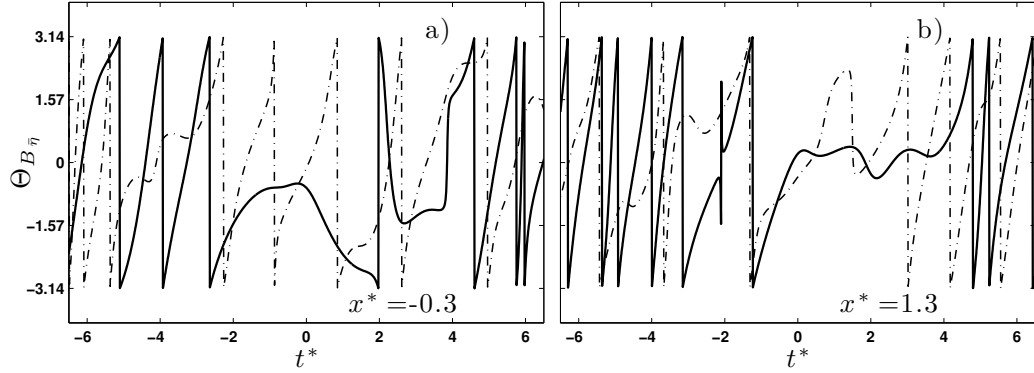


Figure 2.11: Phase angle $\Theta_{B_{\langle\eta\rangle}}$ of the free surface bispectrum $B_{\langle\eta\rangle}(s_1, s_1, t)$, for the nonbreaking packet RN (---); and plunging breaker RP1 (—) at (a) $x^* = -0.3$; and (b) $x^* = 1.3$. Here, $s_1 = (\theta f_1)^{-1}$, $f_1 = f_c$ is the center frequency, and $\theta = 4\pi/(\omega_0 + \sqrt{2 + \omega_0^2})$ is a constant.

the packet.

The continuous wavelet transform $W_{\langle\eta\rangle}$ of a discrete sequence of the free surface time series at certain location, $\langle\eta(t)\rangle$, is defined as the convolution of $\langle\eta(t)\rangle$ with a scaled and translated version of a mother wavelet ϕ ,

$$W_{\langle\eta\rangle}(s, t) = \frac{1}{\sqrt{s}} \int_{-\infty}^{\infty} \langle\eta(\tau)\rangle \phi^*\left(\frac{\tau - t}{s}\right) d\tau \quad (2.14)$$

where t is time, $s = (\theta f)^{-1}$ is the scale factor, $\theta = 4\pi/(\omega_0 + \sqrt{2 + \omega_0^2})$ is a constant, τ is the translation factor, \sqrt{s} is for energy normalization across different scales, and $*$ denotes the complex conjugate. The wavelet kernel adopted here is the Morlet wavelet $\phi(t) = e^{i\omega_0 t} e^{-\frac{t^2}{2}}$ (Farge 1992), where ω_0 is the non-dimensional central frequency of the analyzing wavelet. The wavelet transform is computed in Fourier space to obtain an arbitrary number and distribution of scales.

The modulus of the wavelet transforms of the weakly nonlinear non-breaking packet, RN, and the plunging breaker, RP1, are shown in Figure 2.10. Except the cross-section at $x^* = 0$, all the x locations shown for RP1 are outside of the region in which the surface is multi-valued. In RN, the results follow the linear theory prediction in which all the frequencies in the packet arrive at the predefined focal point, x_b , at

the predefined time, t_b . In addition, energy at each frequency component propagates with its corresponding linear group velocity before and after the focal point, leading to symmetry of the results about $x^* = 0$. In RP1, however, as the packet approaches the break point, nonlinear effects lead to faster propagation of the energy, generating a permanent lead in arrival time relative to the linear prediction. In addition, a phase locking can be seen which starts from near the break point up to $x^* \approx 2$, and nearly all of the frequencies propagate together with the speed close to the linear group velocity of the low frequency components of the packet.

Strictly speaking, phase locking occurs if two frequencies, say f_1, f_2 , are simultaneously present in the signal along with their sum frequency, $f_3 = f_1 + f_2$, with $\Theta_3 = \Theta_1 + \Theta_2 + \text{const.}$, where Θ_i is a corresponding phase of f_i . This phase locking process in the breaking region is further demonstrated by looking at the first higher-order spectrum, or bispectrum, of the wavelet transform near the peak frequency of the wave packet. The bispectrum is defined as

$$B_{\langle\eta\rangle}(s_1, s_2, t) = W_{\langle\eta\rangle}(s_1, t)W_{\langle\eta\rangle}(s_2, t)W_{\langle\eta\rangle}^*(s_3, t), \quad (2.15)$$

with $1/s_1 + 1/s_2 = 1/s_3$ corresponding to addition of frequencies. This analysis tool was first introduced by [Van Milligen et al. \(1995\)](#) in an integrated form with respect to time, $\int_T B_{\langle\eta\rangle}(s_1, s_2, \tau) d\tau$, which was shown to measure the amount of phase locking in the interval T between wavelet components of scale lengths s_1, s_2 and s_3 or equivalently of frequencies f_1, f_2 and f_3 . We set $s_1 = s_2$, then $s_3 = s_1/2$ or $f_1 = f_2 = f_3/2$. Here, s_1 is the corresponding scale for a frequency near the peak frequency of the signal. Note that the bispectrum is a complex number, and its phase represents $\Theta_{B_{\langle\eta\rangle}} = \Theta_1 + \Theta_2 - \Theta_3$. In a decoupled linear system, $\Theta_{B_{\langle\eta\rangle}}$ changes continuously between $-\pi$ to π . In the case of phase locking, however, it becomes constant or nearly so over the interval in which phase-locking is occurring. Figure 2.11 shows $\Theta_{B_{\langle\eta\rangle}}$ corresponding to the center frequency for RN and RP1 at two different x locations. In RP1, phase locking starts upstream of the break point, and lasts for more than two wave periods in the breaking

Table 2.3: Summary of the breaking parameters. S_{s0} is the spectrally-weighted global steepness of the wave packet far upstream of breaking given by (2.19), S is the theoretical linear global steepness of a wave packet defined in §2, k and a are the local wave number and amplitude as defined in Figure 2.1, $\int_t \Delta F_{br}^E$ is the total loss of the total horizontal energy flux due to breaking, T_b and c_b are the breaking wave period and phase speed respectively, and are calculated based on k_b and using linear dispersion relation, ξ is the local dynamic parameter defined in §3 and b is the breaking strength parameter given by (2.18). Subscript b refers to the breaking-onset instant at which a vertical tangent develops near the wave crest, where $t_b^* = -0.2 \sim 0$.

Case no.	S_{s0}	S_{s0}/S	$k_b a_b$	$\int_t \overline{\Delta F_{br}^E}$ (J/m)	k_b (rad/m)	T_b (s)	c_b (m/s)	ξ_b	b
RS1	0.34	1.22	0.36	5.1	4.3	0.97	1.50	0.09	9.1×10^{-3}
RP1	0.46	1.34	0.44	16.3	4.8	0.92	1.42	0.20	40.0×10^{-3}
RP2	0.53	1.37	0.39	18.7	4.4	0.96	1.49	0.14	34.7×10^{-3}
DS1	0.33	1.03	0.36	7.4	3.5	1.09	1.65	0.11	7.3×10^{-3}
DP1	0.47	1.12	0.42	30.5	3.8	1.04	1.60	0.20	37.3×10^{-3}
DP2	0.54	1.17	0.45	48.6	3.8	1.04	1.59	0.25	60.0×10^{-3}
TP1	0.33	0.81	0.32	0.17	12.6	0.57	0.88	0.07	6.8×10^{-3}
TP2	0.48	0.83	0.41	1.18	10.5	0.62	0.97	0.16	29.3×10^{-3}
TP3	0.63	0.85	0.45	2.60	9.7	0.64	1.00	0.15	52.0×10^{-3}

region. In RN, on the other hand, there is not such a strong phase locking and $\Theta_{B(\eta)}$ continuously changes between $-\pi$ to π . The existence of phase locking near the center frequency in RP1, supports the results from the wavelet analysis in a more quantitative sense.

In conclusion, the phase locking of the higher frequency components to the lower frequency components (e.g. , as shown for RP1 Figures 2.10 and 2.11), which have greater linear group velocities, leads to a considerable increase of C_E before the focal/break points in the packets considered here, up to $\approx 30\%$ increase compared with its values upstream of the break point.

2.5.3 Parameterization of the Averaged Breaking-induced Wave Energy Dissipation Rate

Based on scaling arguments, [Duncan \(1983\)](#) showed that the wave energy dissipation rate per unit length of breaking crest, ϵ , can be written in the form

$$\epsilon = b\rho^l g^{-1} c_b^5, \quad (2.16)$$

where b is a breaking strength parameter, and c_b is the phase speed of the breaking wave. Hereafter, the subscript b refers to breaking-onset instant at which a vertical tangent develops near the wave crest ($t_b^* = -0.2 \sim 0$). As described by [Derakhti & Kirby \(2014b, §4.3\)](#), the dissipation rate during active breaking has strong temporal and spatial variations, and thus using a time-invariant b in any formulation like (5.3) may provide an averaged estimate of the energy dissipation rate during active breaking. The averaged wave energy dissipation rate during active breaking can be approximated as

$$\epsilon = \frac{\int_t \overline{\Delta F_{br}^E}}{\tau_b}, \quad (2.17)$$

where $\int_t \overline{\Delta F_{br}^E}$ is the total horizontal wave energy flux loss only due to breaking (see Appendix C), $\tau_b = \alpha_t T_b$ is a time scale related to the active breaking period and is on the order of the breaking wave period T_b , α_t is a constant in the range $0.5 \sim 1.0$. To estimate T_b and c_b , we first estimate the local wave number, k_b , as defined in Figure 2.1. Then, the linear dispersion relation is used to estimate the breaking wave phase speed and period as $c_b = (g/k_b \tanh k_b d)^{1/2}$ and $T_b = 2\pi/k_b c_b$. We found $c_b/c_{s0} = 0.85 \sim 0.90$ in our breaking packets. Because no particular choice of α_t gives the actual time-averaged breaking-induced dissipation rate, we set $\alpha_t = 0.75$ for all cases which is consistent with [Drazen et al. \(2008, Figure 10\)](#). Rearranging (5.3) and using (5.4), the breaking strength parameter is written as

$$b = \frac{g \int_t \overline{\Delta F_{br}^E}}{\rho^l c_b^5 \tau_b}. \quad (2.18)$$

All the breaking parameters for the focused wave packets are summarized in Table 2.3. For a packet with multiple breaking events, e.g. , RP2 and TP3, the given parameters are associated with the strongest breaker of that packet. Figure 2.12 shows the variation of b with respect to the local wave steepness at breaking-onset $k_b a_b$, and to the diagnostic parameter ξ_b for different breaking packets. The solid circles are the corresponding results for the breaking waves due to modulational instability; their input parameters are given in Appendix D. These local parameters can be fairly accurately estimated in phase-resolving nonlinear wave models, such as pseudo-spectral wave models (West et al. 1987, Goullet & Choi 2011, Tian et al. 2012). For our focused wave packets, b linearly decreases as $k_b a_b$ decreases, where $k_b a_b \approx 0.32$ at incipient breaking. This trend does not exist for the spilling breakers due to modulational instability, indicating $k_b a_b$ is not a reliable criterion neither for breaking-onset prediction or parameterization of b . Large values of local steepness, say $k_b a_b > 0.4$, have been also observed by Allis (2013) for their very weak spillers due to modulational instability. In addition, several experimental studies (Wu & Nepf 2002, Allis 2013) showed that local geometric parameters are sensitive to the degree of directionality.

The diagnostic dynamic parameter ξ_b , on the other hand, increases systematically from 0.048 in the weakest spiller due to modulational instability up to 0.25 in the strongest plunger due to dispersive focusing. A linear correlation between b and ξ_b exists as shown in Figure 2.12b, given by

$$b = 0.3(\xi_b - 0.05). \quad (2.19)$$

The threshold value of 0.05 is consistent with the corresponding ξ_b values for our incipient breaking packets. Banner & Peirson (2007) also observed an approximately linear relationship between their diagnostic parameter just prior to wave breaking, δ_b , and b as shown in their Figure (8)b.

The parameterization of b based on a characteristic spectrally-based global steepness of a wave packet is also of an interest, especially for use in wave-averaged

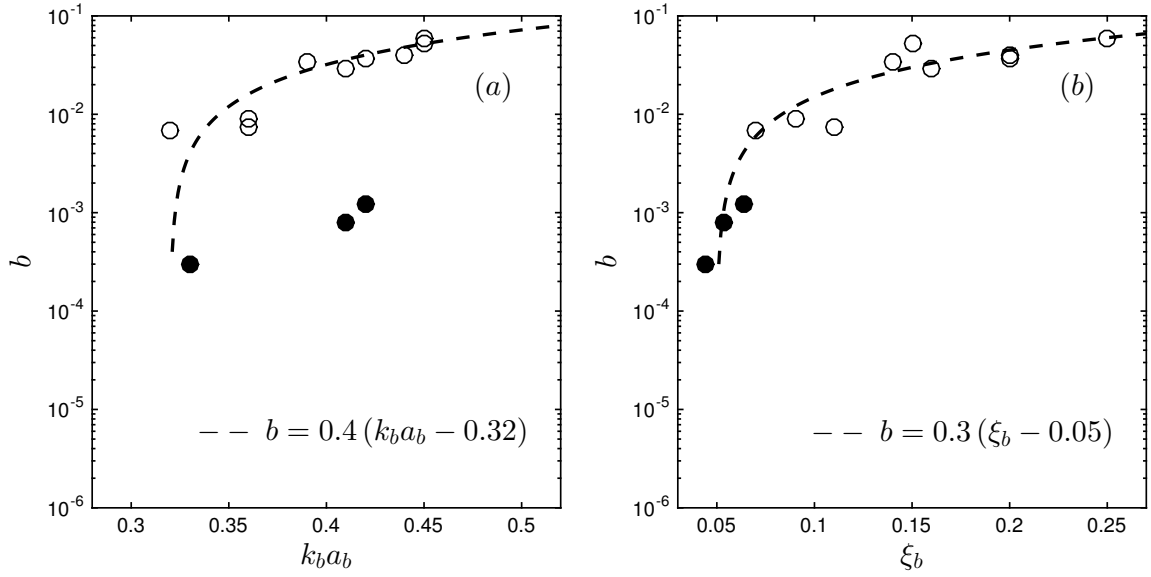


Figure 2.12: Variations of the breaking strength parameter b with respect to (a) the local wave steepness at breaking-onset $k_b a_b$, and (b) the dynamic diagnostic parameter ξ_b for (open circles) the unsteady dispersive focused breaking packets and (solid circle) the modulated unstable breaking packets; their input parameters are given in Appendix D. Dashed lines are linear fits through the results of the simulated focused packets.

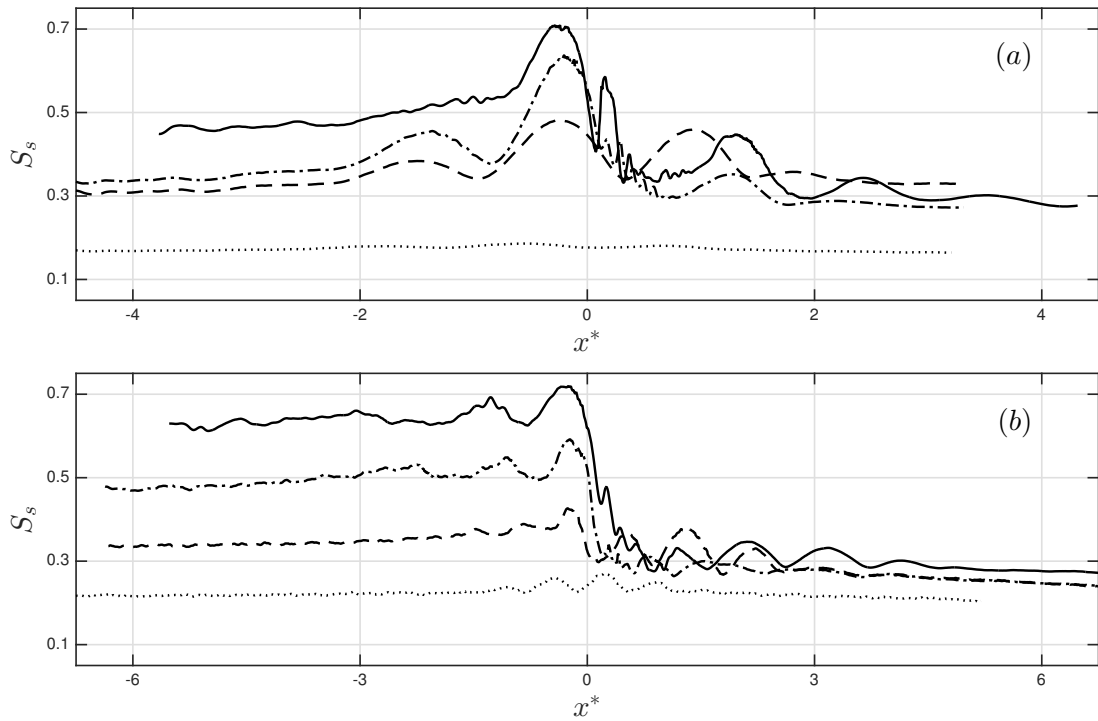


Figure 2.13: Spatial variations of the spectrally-weighted global steepness S_s for (a) intermediate-depth nonlinear packet RN ($\cdots\cdots$), incipient breaking RI ($---$), spilling breaker $RS1$ ($-\cdot-$), plunging breaker $RP1$ ($---$); and (b) deep-water nonlinear packet TN ($\cdots\cdots$), weak plunging breaker $TP1$ ($-\cdot-$), plunging breaker $TP2$ ($---$), plunging breaker $TP3$ ($---$).

models where ξ_b can not be evaluated. Following [Tian et al. \(2010\)](#), we define the spectrally-weighted global steepness of a packet as

$$S_s = k_s \Sigma a_n, \quad (2.20)$$

where, $k_s = 2\pi/L_s$ is the spectrally-weighted wave number and a_n is the Fourier amplitude of the n th component of the wave train. Here, we only consider Fourier components in which $0.25f_{s0} < f_n < 4.0f_{s0}$. [Figure 2.13](#) shows the spatial variation of S_s for different non-breaking and breaking packets. [Figure 2.13](#) shows that S_s has a relatively constant value far upstream of the focal/break point, say $x^* < -3$, hereafter referred to as S_{s0} . We note that S_{s0} can be easily calculated in wave-averaged models based on wave energy spectra. It is seen that S_{s0} for all the dispersive focused breaking packets is greater than $S_{s0} = 0.31$ for the incipient breaking packets RI and DI (not shown). In addition, S_s increases as the packet approaches the break point, consistent with the observations of [Tian et al. \(2010\)](#). Interestingly, the corresponding values of S_s after the breaking region seems to reach below the threshold value of $(S_{s0})_{th} = 0.31$ for all the dispersive focused breaking packets. This universal post-breaking value of S_s could be used as a test for any selected model for the parameterization of the breaking-induced wave energy dissipation in broad-banded deep-water packets.

Available estimates of b in the previous laboratory experiments range over three order of magnitude from $O(10^{-4})$ for gently spillers ([Banner & Peirson 2007](#), [Allis 2013](#)) up to $O(10^{-1})$ for strong plungers ([Melville 1994](#), [Drazen et al. 2008](#), [Tian et al. 2010](#)), see for example [Romero et al. \(2012, Figure 1\)](#). [Figure 2.14](#) shows the variation of b versus the theoretical linear slope of a wave packet S defined in §2 as well as S_{s0} for the considered focused wave packets (open circles), the simulated spillers due to modulational instability (solid circle), and the weak spilling breaking waves in a wide tank by [Allis \(2013\)](#) (pluses). Here, the recent laboratory results of [Allis \(2013\)](#) are used instead of those from [Banner & Peirson \(2007\)](#), because the characteristic global steepness of the wave packets in [Allis \(2013\)](#) were calculated far upstream of

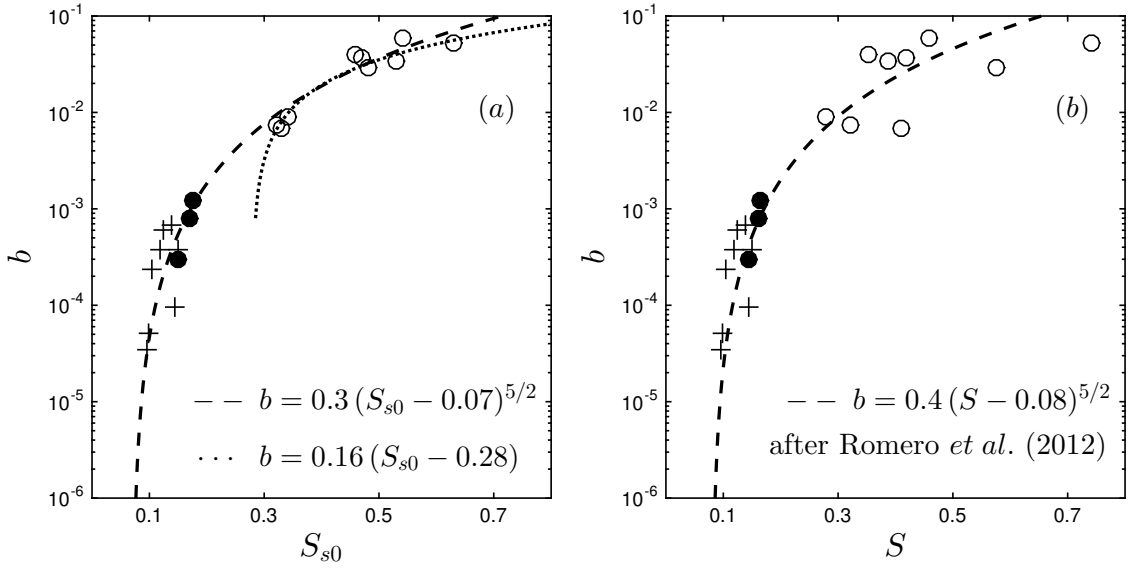


Figure 2.14: Variations of the breaking strength parameter b with respect to (a) the theoretical linear slope of a wave packet $S = \sum k_n a_n$; and (b) the initial spectrally-weighted global steepness $S_{s0} = k_{s0} \sum a_n$ for the considered focused wave packets (open circles), the simulated spillers due to modulational instability (solid circle), and the weak spilling breaking waves in a wide tank adopted from Allis (2013, Table 8.1) (pluses). The dashed and dotted lines in (a) are given by equation (2.21) and $b = 0.16(S_{s0} - 0.28)$. The dashed line in (b) was given by Romero et al. (2012). In Allis (2013) the values of $S = \sum a_i k_i$ have not been calculated. We assume $S = S_{s0}$ for their cases.

the first break, consistent with our calculation of S_{s0} . Note that [Banner & Peirson \(2007\)](#) calculated the characteristic global steepness just before the first break in order to exclude the viscous background losses, which were $O(10^1)$ higher than that in [Allis \(2013\)](#).

For our focused wave packets, $b > 6 \times 10^{-3}$, [Figure 2.14a](#) shows that $b \sim S_{s0}$, consistent with the results in [Tian et al. \(2010, Figure10a\)](#) and the scaling law from [Derakhti & Kirby \(2014b, equation 4.16\)](#). However, a linear correlation does not exist for the weaker breaking packets in which $b < 5 \times 10^{-3}$. [Drazen et al. \(2008\)](#) used an inertial scaling argument indicating that wave energy dissipation depends on a local wave slope to the 5/2 power. Subsequently, [Romero et al. \(2012\)](#) showed that, within the scatter of the experimental data, a relation $b = 0.4(S - 0.08)^{5/2}$ fit the considered laboratory data in the range $8 \times 10^{-5} < b < 9 \times 10^{-2}$. [Figure 2.14](#) shows that using the initial spectrally-weighted global steepness S_{s0} instead of S results in a significant decrease of the scatter of the data. As shown in [Figure 2.14a](#), the new polynomial fit based on inertial scaling is given by

$$b = 0.3 (S_{s0} - 0.07)^{5/2}, \quad (2.21)$$

where [\(2.21\)](#) gives reasonable estimates of b over the full range of different unsteady uni-directional breaking waves. As shown in [Figure 2.13](#), the location at which S_{s0} is evaluated needs to be far upstream of the break point, say $x^* < -3$, to remove the spatial dependency in S_{s0} .

Other relevant physics, such as the effects of the degree of directionality and wind forcing, need to be investigated to apply [\(2.21\)](#) in a real sea state.

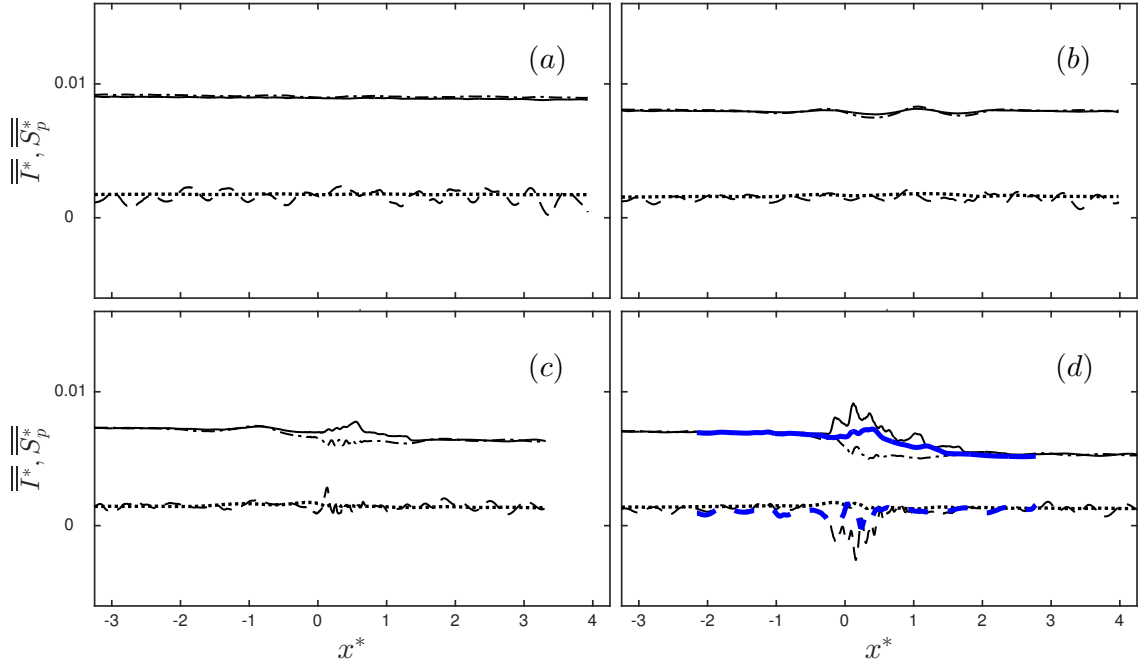


Figure 2.15: Normalized horizontal momentum flux by waves and turbulence, $\overline{\overline{I^*}}$, (—); mean pressure field, $\overline{\overline{S_p^*}}$, (---); $\overline{\overline{I_{apx}^*}}$ (-·-); and $\overline{\overline{(S_p^*)_{apx}}}$ (·····) for intermediate-depth (a) non-breaking packet RN; (b) incipient breaking RI; (c) spilling breaker RS1; and (d) plunging breaker RP1. Thick lines are the results for RP1(3D). The results are normalized by a reference value of $\rho^l g k_{s0}^2 S_{s0}^{-2}$.

2.6 Fractional and Total Losses of Momentum Flux

The averaged horizontal momentum flux of a 2D wave packet per unit crest length over the time $t = t_1 \rightarrow t_2$, $\overline{\overline{F^M}}$ can be written as

$$\overline{\overline{F^M}}(x) = \frac{1}{t_2 - t_1} \int_{t_1}^{t_2} \langle \int_{-d}^{\eta} [(\rho u)u + p] dz \rangle dt. \quad (2.22)$$

By subtracting the static pressure contribution from (2.22), the total excess horizontal momentum flux, also called the radiation stress, can be defined as

$$\overline{\overline{S}} = \overline{\overline{F^M}} - \frac{1}{2} \rho^l g (d + \overline{\eta})^2 = \overline{\overline{I}} + \overline{\overline{S_p}}, \quad (2.23)$$

where $\overline{\overline{I}} = \frac{1}{t_2 - t_1} \int_{t_1}^{t_2} \langle \int_{-d}^{\eta} [(\rho u)u] dz \rangle dt$ represents both the averaged wave horizontal momentum flux and the turbulent Reynolds stress. For a pure wave field, however, $\overline{\overline{I}} \approx \overline{\overline{I}}_{apx} = \rho^l g \overline{\eta}^2 n$ to the second order, where here we define n as the ratio of the characteristic group velocity over the characteristic phase speed of the packet, given by

$$n = C_{gs}/c_s, \quad (2.24)$$

where the c_s is the spectrally-weighted phase speed. Figure 2.15 shows that $\overline{\overline{I}}_{apx}$ accurately predicts $\overline{\overline{I}}$ before and after the breaking region. Thus, the total loss of the wave horizontal momentum flux can be written as

$$\Delta \overline{\overline{I}} \approx \Delta \overline{\overline{I}}_{apx} = \rho^l g n_1 (\overline{\overline{\eta}}_1^2 - \gamma \overline{\overline{\eta}}_2^2), \quad (2.25)$$

where $\gamma = n_2/n_1$. The corresponding γ values for the different cases are summarized in Table 2.2. In addition, $\overline{\overline{S_p}} = \frac{1}{t_2 - t_1} \int_{t_1}^{t_2} \langle \int_{-d}^{\eta} [p] dz \rangle dt - \frac{1}{2} \rho^l g (d + \overline{\eta})^2$ represents the averaged horizontal momentum flux due to the mean pressure field. For a pure wave field, $\overline{\overline{S_p}} \approx (\overline{\overline{S_p}})_{apx} = \rho^l g \overline{\eta}^2 (n - 1/2)$ to the second order. Direct estimates of $\overline{\overline{S_p}}$ (dashed lines) and its corresponding approximate measure $(\overline{\overline{S_p}})_{apx}$ (dotted lines) for non-breaking RN, incipient breaking RI, spilling RS1, and plunging RP1 packets are

shown in Figure 2.15. The results show that $\overline{\overline{S_p}}$ has relatively small change after the breaking region; thus we may assume $\Delta\overline{\overline{S}} \approx \Delta\overline{\overline{I}}$. The loss of wave radiation stress is balanced by the increase of $\overline{\eta}$ after the break point. In intermediate-depth packets the fractional loss of the time-averaged horizontal momentum flux is overpredicted by approximately 11% to 63% by ignoring the change of n after the breaking region, or choosing $\gamma = 1$ in (2.25) (see Table 2.2). In deep-water cases, instead, the fractional loss of the time-averaged potential energy density is close to that of the time-averaged momentum flux, $\Delta\overline{\overline{I}}/\overline{\overline{I}}_1 \approx \Delta\overline{\overline{\eta^2}}/\overline{\overline{\eta_1^2}}$.

2.7 Conclusions

A continuum polydisperse two-fluid model described in Derakhti & Kirby (2014b) was used to study the breaking-onset prediction as well as the spatial variations of total energy and momentum flux in laboratory-scale intermediate- and deep-water unsteady breaking waves generated by dispersive focusing. We should remark that all the following conclusions may not be directly applicable to other types of breaking waves such as steepness-limited breaking waves due modulational instability. Also, the absolute values may need to be tested for a wider range of breaking scales. Here, we briefly establish that the present model is capable of capturing breaking waves due to modulational instability. A more detailed evaluation of this class of weak breaking events will appear in a separate paper. The main conclusions are summarized as follows.

(a) *Breaking-onset prediction:* Avoiding the post-processing procedure in the dimensionless parameter originally proposed by Song & Banner (2002) given by (2.1), we defined a new diagnostic parameter, $\xi(t)$, as the normalized growth rate of the time-dependent local energy density maxima along the wave packet given by $\xi(t) = \omega_{s0}^{-1} D\mu/Dt$, where $\mu = E_{max}k^2/\rho^l g$. The threshold value of $\xi_{th} = 0.05$ was found as the maximum value of ξ for the non-breaking and incipient breaking packets. It was shown that, the new dynamic criterion is capable of detecting a single or multiple breaking events in a packet. Noting different length scales, depth regime, and packet types (see Table 1) of the considered cases, the dynamic criterion with the threshold value of

$\xi_{th} = 0.05$ seems to be universal at least for steepness-limited unsteady breaking waves generated by dispersive focusing.

(b) *Fractional and total losses of horizontal wave energy flux:* It was shown that the widely used formulas $\Delta\overline{\eta^2}/\overline{\eta_1^2}$ and $(\Delta\overline{F^E})_{apx1} \approx \rho^l g C_{gs1} \Delta\overline{\eta^2}$ overpredict both fractional and total losses of horizontal wave energy flux by approximately 35% to 70% for our breaking packets, due to the neglect of the increase of the characteristic group velocity after the breaking region. A new simple formulation was proposed to improve the prediction of the averaged horizontal wave energy flux as $(\Delta\overline{F^E})_{apx2} \approx \rho^l g C_{gs1} (\alpha_1 \overline{\eta_1^2} - \beta \overline{\eta_2^2})$, in which $\alpha_1 = \text{Max}(1.0, 0.13(S_{s0} - 0.2) + 1.0)$, obtained based on linear curve fitting. Here, $\beta = C_{gs2}/C_{gs1}$ can be obtained based on free surface measurements upstream and downstream of the break point. The β varied between 1.05 for weak spilling breakers to 1.2 for strong plunging breakers in the simulated cases.

(c) *Characteristic wave group velocity:* The energy transport velocity, defined as $C_E = \overline{F^E}/\overline{E}$, was compared with the spectrally-weighted linear group velocity C_{gs} , defined by [Drazen et al. \(2008\)](#). In general, C_{gs} is an appropriate choice for a characteristic group velocity, because (i) it is an easily computable quantity using only free surface time series, and (ii) it provides fairly accurate estimates of C_E before and after the breaking region. However, we showed that the local peaks of C_{gs} and C_E were 180° out of phase near the focal/break points. In addition, C_{gs} predicts smaller values compared with C_E , especially before the break point. A strong correlation between a local increase of C_E and the asymmetry of the dominant wave in the packet was observed in both non-breaking and breaking packets, where negative asymmetry (wave pitched forward) led to increase of the spectrally-weighted frequency, f_s , of the packet, and led to a noticeable increase of C_E . This increase of C_E can not be captured using linear wave theory. For example, as f_s increases, C_{gs} decreases which is completely an opposite trend compared with that observed in the results for C_E . It was shown that the phase locking of the higher frequency components to the lower frequency components which have greater linear group velocities led to the considerable increase of

C_E before the focal/break points, up to $\approx 30\%$ increase of C_E compared with its values upstream of the break point. Far downstream of the focal point, C_E returned to its value upstream of the focal point for non-breaking packets. For breaking packets, however, there is a significant increase of C_E after the break point, due to noticeable breaking-induced dissipation of higher frequency components within the wave packet. This increase became relatively larger as the breaker intensity increased.

(d) *Parametrization of the breaking strength parameter b* : As summarized by [Romero et al. \(2012\)](#), the available estimates of b ranges from $O(10^{-4})$ for gently spillers up to $O(10^{-1})$ for strong plungers. In most of the previous experiments, $\overline{\Delta F^E}$ was approximated using $(\overline{\Delta F^E})_{apx1} \approx \rho^l g C_{gs1} \overline{\Delta \eta^2}$. As we explained, using $(\overline{\Delta F^E})_{apx2} \approx \rho^l g C_{gs1} (\alpha_1 \overline{\eta_1^2} - \beta \overline{\eta_2^2})$ the estimation of $\overline{\Delta F^E}$ and the associated b is improved compared with that predicted using $(\overline{\Delta F^E})_{apx1} \approx \rho^l g C_{gs1} \overline{\Delta \eta^2}$. In addition, we found that the initial spectrally-weighted global steepness, S_{s0} , is a preferable parameter compared with the theoretical linear global steepness $S = \sum_{i=1}^N a_i k_i$ for our dispersive focused packets. The new diagnostic parameter at the breaking onset, ξ_b , was shown to have a strong linear dependence with respect to b given by $b = 0.3(\xi_b - 0.05)$. Note that in the present work, the estimated b ranges from 3×10^{-4} up to 0.06. Although ξ_b can not be evaluated in wave-averaged wave models, it can be easily used in wave-resolving nonlinear wave models. A strong linear dependence was also found between b and S_{s0} for the considered focused wave packets, while a large scatter was found between b and S . The linear relation, however, can not provide accurate estimations of b in the range $b < 5 \times 10^{-3}$. A new scaling law given by $b = 0.3(S_{s0} - 0.07)^{5/2}$, which is consistent with inertial wave dissipation scaling of [Drazen et al. \(2008\)](#), is shown to be capable of providing accurate estimates of b in the full range of breaking intensities, $10^{-5} < b < 10^{-1}$, where the scatter of data in the new formulation significantly decreases compared with that proposed by [Romero et al. \(2012\)](#).

(e) *Fractional and total losses of total momentum flux*: Momentum flux due to the mean pressure $\overline{S_p}$ was shown to have relatively small change after the breaking region, and, thus, $\overline{\Delta S} \approx \overline{\Delta I}$. We showed that total wave momentum flux, \overline{I} , could be

accurately estimated as $\overline{I}_{apx} = \rho g \overline{\eta^2} n$ upstream and far downstream of the break point, where we defined $n = C_{gs}/c_s$. In intermediate-depth breaking packets, total fractional loss of horizontal momentum flux was approximately 11% to 63% overpredicted by ignoring the change of n after the breaking region, or choosing $\gamma = n_2/n_1 = 1$ in (2.25). In deep-water cases, on the other hand, the fractional loss of the averaged potential energy density was close to that of the averaged horizontal wave momentum flux.

Chapter 3

INTERMITTENT BUBBLE TRANSPORT IN THE SURF ZONE

3.1 Abstract

[Derakhti & Kirby \(2014a,b\)](#) have recently studied bubble entrainment and turbulence modulation by dispersed bubbles in isolated unsteady breaking waves along with extensive model verifications and convergence tests. In this chapter, we use the model of [Derakhti & Kirby \(2014b\)](#) to examine the role of large-scale breaking-induced turbulent coherent structures (LBTCS) in the three-dimensional (3D) intermittent transport of dispersed bubbles in the surf zone. The relative importance of preferential accumulation of dispersed bubbles in coherent vortex cores is investigated. It is shown that the 3D distribution of the bubble plume is highly correlated with that of the LBTCS, with high bubble void fraction regions located closer to the part of the vortex cores with negative turbulent vertical velocity. Near-bed bubble void fractions greater than 5% have been observed in the plunging case considered here.

3.2 Introduction

Surface wave breaking is of considerable importance to air-sea interactions, acoustic underwater communications, optical properties of the water column, and upper ocean/surf zone dynamics. Wave breaking is a highly dissipative process, representing an important source of turbulence in the ocean surface layer. Air is entrained and rapidly evolves into a distribution of bubble sizes, hereafter referred to as a bubble plume, which interacts with liquid turbulence and organized motions. Bubble plume kinematics and dynamics are the basis for evaluating the effects of dispersed bubbles on the environmental and technical processes mentioned above ([Thorpe 1995](#), [Melville 1996](#)).

The breaking process can be divided into two stages; (i) the generation of bubbles in the vicinity of the free surface due to cavity break up, and (ii) the later distribution of entrained bubbles in the water column by LBTCs and organized motions. An examination of the former is beyond the scope of this study, and the reader is referred to [Kiger & Duncan \(2012\)](#), who reviewed the most recent progress on the air-entrainment mechanisms in plunging jets and breaking waves. Due to a need to understand air-sea interaction processes in the upper ocean layer, investigating air entrainment and bubble distribution in steepness-limited breaking waves is advanced compared to depth-limited surf zone breaking waves. Thus, to summarize the relevant literature, we review field and experimental studies of bubble void fraction in both deep-water and surf zone breaking waves. Then we discuss the relevant numerical studies.

In the past few decades, several theoretical and experimental studies ([Thorpe & Humphries 1980](#), [Thorpe 1982](#), [Baldy 1988](#), [Hwang et al. 1990](#), [Leifer & De Leeuw 2006](#), [Leifer et al. 2006](#)) have described the characteristics of the bubble distribution in breaking wind waves. In summary, the bubble plume characteristics, including spatial distributions of time-averaged bubble void fraction and its size spectrum, have been shown to be different in the near surface zone, say $z > -H_s$, compared with those in lower depths, $z < -H_s$. Here, z is the vertical distance from the still water surface, and H_s is the characteristic wave height. In lower depths, the bubble plume is composed of very small bubbles $a \ll a_H$, where a is the bubble radius and a_H is the associated bubble Hinze scale, and the bubble number density, $N(a, z)$, has exponential dependence with respect to depth with an approximately constant size spectrum slope, α_1 . In the near surface zone, however, bubble void fraction has much stronger temporal and spatial variations, exponential dependence may not exist, and the size spectrum has two distinct depth- and time-dependent slopes of α_1 and α_2 for the bubbles smaller and larger than a_H respectively. The theoretical work by ([Garrett et al. 2000](#)), experimental work by ([Deane & Stokes 2002](#)), and numerical work by [Ma et al. \(2011\)](#) support the conclusion that $\alpha_2 \simeq -10/3$ at the early stages of active breaking.

Using a conductivity probe, [Lamarre & Melville \(1991, 1994\)](#) produced time-varying void fraction distribution in controlled 2D and 3D focused breaking wave packets. The results showed that the degassing rate was rapid, and less than 5% of the initial entrained bubbles remained in the water column one period after breaking, where the maximum ensemble-averaged bubble void fraction decreases from $\approx 50\%$ during the initial stages of active breaking down to $\approx 1\%$ at one wave period after breaking. They calculated the area, volume, mean void fraction and centroids of the bubble plume. It was shown that these integral properties evolved as a simple function of time and scaled fairly well from their small 2D to larger 3D packets. [Blenkinsopp & Chaplin \(2007\)](#) used two optical fibers to measure the time-dependent void fraction under breaking waves generated by propagating regular waves over a submerged sloping reef structure. They also found that the integral properties of the bubble plume evolved as a simple function of time. They showed that the bubble plume volume grew linearly to a maximum and then decayed exponentially in time. As concluded by [Lamarre & Melville \(1991\)](#), the contributions of bubbles to air-sea processes may be seriously underestimated if the existence of these transient bubble plumes of large bubbles is not taken into account. We note that the entire surf zone may be considered as the near surface zone in which transient bubble plumes with large spatio-temporal bubble void fraction variations evolve from the free surface down to the bed.

Few quantitative measurements of the bubble void fraction in controlled surf zone breaking waves exist ([Cox & Shin 2003](#), [Hoque & Aoki 2005](#), [Mori et al. 2007](#)), observing the maximum ensemble-averaged bubble void fraction in the range $15\% \sim 30\%$. [Cox & Shin \(2003\)](#) showed that the temporal variation of the ensemble-averaged void fraction above the still water level normalized by the wave period and time-averaged void fraction was self-similar, and that it could be modeled by linear growth followed by exponential decay. [Cox & Shin \(2003\)](#) and [Mori et al. \(2007\)](#) showed that the time-averaged bubble void fraction had a linear relationship with the time-averaged turbulent horizontal intensity and time-averaged turbulent kinetic energy

respectively. These observations have been made at a number of locations in the cross-section through the middle of an experimental tank, mostly in the transition region.

Several 3D numerical studies have been conducted to investigate the structure of turbulence and LBTCS ([Christensen & Deigaard 2001](#), [Christensen 2006](#), [Watanabe et al. 2005](#), [Lakehal & Liovic 2011](#), [Farahani & Dalrymple 2014](#), [Zhou et al. 2014](#)) in depth-limited breaking waves. In all of these numerical studies, however, most portions of the typical bubble size spectrum are unresolved because of a relatively coarse resolution or the neglect of the air dynamics in the numerical simulation. To account for bubble size distribution in surf zone breaking waves, we need to have a very fine grid resolution, about two orders of magnitude smaller than typical large-eddy simulation (LES) resolution. An example of such a LES simulation with a fine grid resolution has been done by [Lubin & Glockner \(2015\)](#) for deep water plunging breaking waves generated due to the evolution of a periodic unstable wave train with relatively short wave lengths $< 0.2\text{m}$. They solved the Navier-Stokes equations in both air and water with a grid resolution of $\sim 0.1\text{ mm}$, and showed the model captured the generation and evolution of small-scale aerated vortex filaments during the splash process. Such a high resolution two-phase LES simulation of laboratory-scale surf zone breaking waves is still impractical. Instead of resolving individual bubbles, [Derakhti & Kirby \(2014b\)](#) extended the Eulerian-Eulerian polydisperse two-fluid model of [Ma et al. \(2011\)](#) to an LES framework to study bubble entrainment and liquid-bubble interaction in turbulent bubbly flow in laboratory-scale, isolated, deep water focused breaking wave packets. Bubbles were entrained at the free surface using a bubble entrainment model, initially distributed based on the size spectrum observed by [Deane & Stokes \(2002\)](#). The SGS bubble-induced turbulence and the momentum transfer between the two phases were considered using statistical closure models. By comparing snapshots of the bubble void fraction distributions, bubble void fraction time series as well as integral properties of the bubble plumes with the corresponding experiments, the model was shown to capture the spatial and temporal evolution of entrained bubbles fairly accurately.

The process of air entrainment is highly 3D even in a long-crested plunger, as

shown by [Kiger & Duncan \(2012, Figure 11\)](#) and [Derakhti & Kirby \(2014b, Figure 3\)](#). The 3D distribution of entrained bubbles also can be seen in [Nadaoka et al. \(1989, Figure 3\)](#). It is known that the effects of LBTCS, such as the radial pressure gradient within a vortex core, result in the 3D intermittent distribution of bubble plumes in surf zone breaking waves. Quantitative examination of the relative importance of LBTCS on the intermittent transport of dispersed bubbles, however, has not yet been investigated. In this paper, we use the model of [Derakhti & Kirby \(2014b\)](#) to examine the role of LBTCS on the 3D intermittent transport of dispersed bubbles in the surf zone.

In §3.3, the model set-up and choice of experimental conditions are explained. The comparison of the predicted free surface evolution and time-averaged velocity and turbulence fields with the available measurements are presented in §3.4. The results are given in §3.5. Conclusions are given in §3.6.

3.3 Model Set-up and Averaging Procedures

3.3.1 Model Set-up and Choice of Experimental Conditions

A detailed description of the polydisperse two-fluid model used here as well as boundary conditions may be found in Appendix A. Here, the incident wave boundary condition and model set-up are discussed briefly.

Both weakly plunging/spilling (hereafter referred to as S1) and strong plunging (hereafter referred to as P1) periodic breaking waves over a plane slope are considered following the experimental set-up of [Ting & Nelson \(2011\)](#) and [Ting & Reimnitz \(2015\)](#), respectively. All model simulations are performed with the model initialized with quiescent conditions. At the inflow boundary, the free surface location and velocities are calculated using the theoretical relations for cnoidal waves as given in [Wiegel \(1960\)](#). The right end of the numerical domain is extended beyond the maximum run-up. [Figure 3.1](#) sketches the experimental layout. The input wave parameters are summarized in [Table 3.1](#). Besides the corresponding experiments in [Table 3.1](#), we also consider the void fraction measurements by [Cox & Shin \(2003\)](#) and the turbulence and velocity

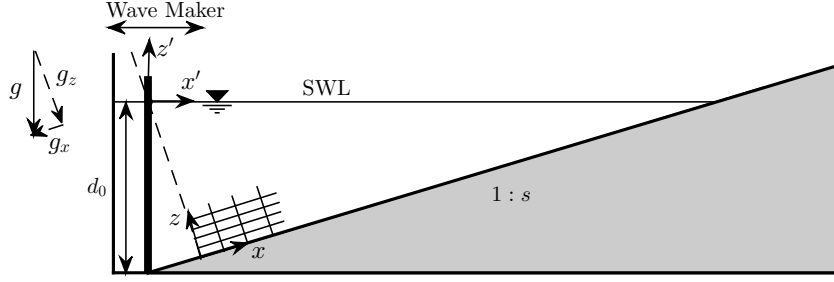


Figure 3.1: Side view of the experimental layout of the simulated cases and coordinate systems. The rectangular mesh is shown some part of the numerical grid.

Table 3.1: Input parameters for the simulated cases. Here, d_0 is the still water depth in the constant-depth region, H and T are the wave height and period of the cnoidal wave generated by the wavemaker, $(kH)_0 = 2\pi H_0/L_0$ is the corresponding deep water wave steepness of the generated wave, $\xi_0 = s/\sqrt{H_0/L_0}$ is the self similarity parameter, and s is the plane slope.

Cases	d_0 (m)	s	H (m)	T (s)	$(kH)_0$	ξ_0	H_b (m)	Breaking type	Exp.
P1	0.30	0.025	0.12	4.0	0.022	0.42	0.167	p	Ting & Reimnitz (2014)
S1	0.36	0.03	0.122	2.0	0.119	0.22	0.170	s/wp	Ting & Nelson (2014)

measurements by Ting & Kirby (1994) for model validation. The experimental set-ups in these two works are similar to S1, as summarized in Table 3.2. Mesh resolutions and domain sizes are summarized in Table 3.3. The model parameters for a polydisperse bubble phase are chosen as summarized in Derakhti & Kirby (2014b, Table 4).

3.3.2 Averaging Procedures and Scale Decomposition

As discussed in Derakhti & Kirby (2014b, §2.8), ensemble averaging, $\langle \cdot \rangle$, is approximated by spanwise averaging as

$$\langle \phi \rangle(i, k, t) \approx \sum_{j=21}^{N_y-20} \frac{1}{N_y - 40} \phi(i, j, k, t), \quad (3.1)$$

Table 3.2: Input parameters for the experiments which are similar with the simulated cases.

Similar Cases	d_0 (m)	s	T (s)	$(kH)_0$	ξ_0	H_b	Breaking type	Exp.
\sim S1	0.4	0.029	2.0	0.126	0.20	0.166	s	Ting & Kirby (1994)
\sim S1	0.51	0.029	2.0	0.111	0.215	0.155	s/wp	Cox & Shin (2003)

Table 3.3: Numerical set-up for the 3D LES cases. * These are the number of the available wave cycles after the simulation reaches a quasi-steady state conditions, which is approximately 15 wave periods after the start of the simulation. Here, superscripts b and nb refer to a simulation with and without the consideration of dispersed bubbles respectively.

Cases	Domain sizes (m)	Mesh sizes	Mesh resolutions (mm)	Num. of wave cycles*
	(L_x, L_z, L_y)	$N_x \times N_z \times N_y$	$(\Delta x, \Delta z, \Delta y)$	(NW^b, NW^{nb})
P1	(16.25, 0.49, 0.84)	$650 \times 70 \times 120$	(25, 7.0, 7.0)	(2,25)
S1	(16.25, 0.602, 0.896)	$650 \times 86 \times 128$	(25, 7.0, 7.0)	(15,41)

where ϕ is a field variable and N_y is the number of grid points in the spanwise direction (see Table 3.3). Here, we ignore 20 grid points near each wall, and then averaging is performed on the remaining grid points. The resolved turbulent fluctuation about this average is then given by $\phi'(i, j, k, t) = \phi(i, j, k, t) - \langle \phi \rangle(i, k, t)$.

Phase averaging is given by

$$\widehat{\phi}(i, j, k, n) = \sum_{m=1}^{NW} \frac{1}{NW} \phi(i, j, k, n + (m-1) * T/dt), \quad (3.2)$$

where $n = 1, \dots, T/dt$, T is the wave period, dt is the sampling interval, and thus T/dt is the number of available outputs per wave cycle which is 200 for both S1 and P1. NW is the number of the available wave cycles after the simulation reaches a quasi-steady state conditions, which is approximately 15 wave periods after the start of the simulation. Note that irregularities in the breaking process, e.g. , the change in the initial breaking location, result in the deviation of (3.2) from the corresponding ensemble-averaged value.

Time averaging is given by

$$\overline{\phi}(i, j, k) = \frac{1}{NW \times T} \int_{t_0}^{t_0 + NW \times T} \phi(i, j, k, t) \mathcal{H}(\psi(i, j, k, t) - 0.5) dt, \quad (3.3)$$

where \mathcal{H} is the Heaviside step function, and ψ is the volume fraction of the water within a computational cell. The points located between the troughs and the crests are located in the water and air alternatively depending on the local wave phase. To remove these unphysical zero values during time averaging, hereafter referred to as the conditional time averaging, (3.3) should be divided by the probability of being inside the water column, $P_w(i, j, k)$, given by

$$P_w(i, j, k) = \overline{\mathcal{H}(\psi(i, j, k, t) - 0.5)}. \quad (3.4)$$

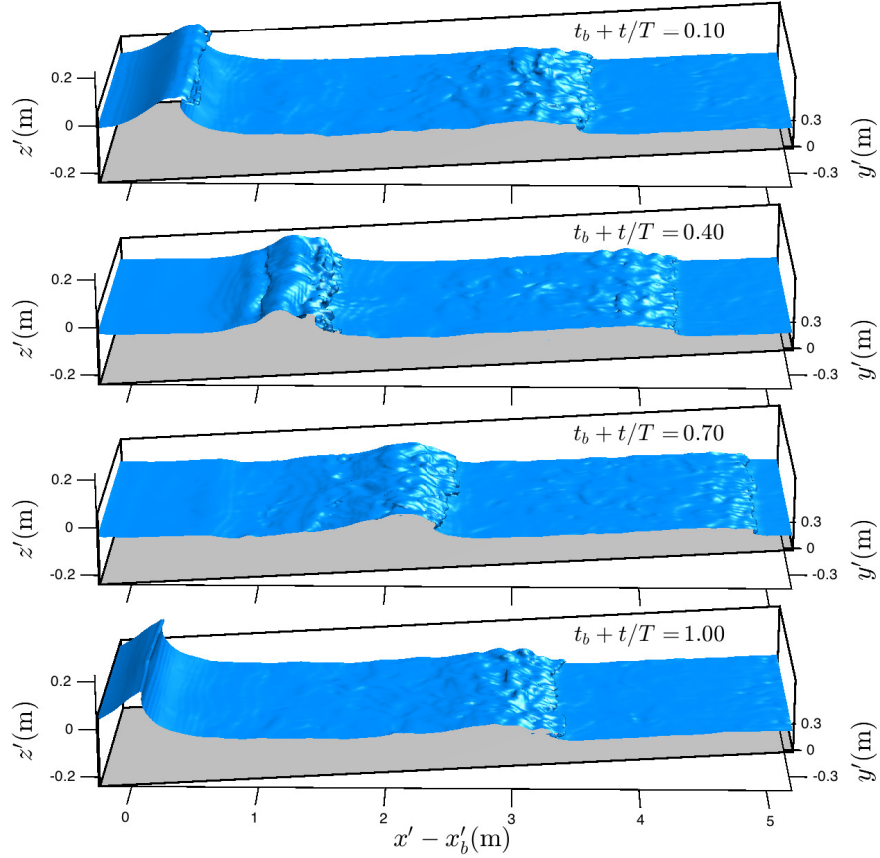


Figure 3.2: Snapshots of the free-surface (isosurface of $\psi = 0.5$) evolution the weakly-plunging/spilling case S1 after 23 wave periods after the start of the simulation ($t_b = 46.91\text{s}$). Here, x_b is approximately the point of incipient wave breaking, and is defined as the cross-shore location at which a vertical tangent appears near the wave crest.

3.4 Model Validation

Extensive model validations including detailed comparisons of free surface evolution, bubble void fraction, integral properties of the bubble plume, and mean and turbulent velocity fields with the corresponding measurements have been performed by [Derakhti & Kirby \(2014a,b\)](#) in unsteady steepness-limited breaking wave packets. Here, we show that the model captures the evolution of free surface, velocity and turbulence fields in the surf zone fairly accurately.

3.4.1 Free Surface Evolution

Figure 3.2 shows snapshots of the free-surface evolution for the weakly-plunging/spilling case S1. It is seen that the model captures the large scales of the splash process and formation of a bore-like region, with apparent irregularities at the surface behind the propagating bore due to subsurface vortex-induced pressure fluctuations (Watanabe et al. 2005, §3.4). Figure 3.3 shows that the model reasonably captures the evolution of phase-averaged free surface elevations compared with the corresponding measurements of Ting & Nelson (2011) in the shoaling, transition and inner surf zones. The comparison of the predicted wave height, $H = \widehat{\langle \eta \rangle}_{max} - \widehat{\langle \eta \rangle}_{min}$, evolution with the measurements of Ting & Nelson (2011) and that of the spilling case of Ting & Kirby (1994) (see Table 3.2) from the outside of the surf zone up to the shore line is shown in Figure 3.4. The incident wave conditions and flume geometry of Ting & Nelson (2011) are very close to those of the spilling case of Ting & Kirby (1994). This Figure shows that the spatial evolution of H relative to the initial break point at $x' = x_b$ is also comparable for these two breaking wave cases.

3.4.2 Spanwise-time-averaged Organized and Turbulent Fields

It is well-established that the ensemble-time-averaged velocity, called undertow, and turbulent kinetic energy in the surf zone scale with the local linear wave phase speed \sqrt{gh} , where $h = d + \bar{\eta}$ is the local mean sea level. Figure 3.5 shows the spatial distribution of the normalized conditional spanwise-time-averaged, $(P_w^{-1}\overline{\langle k \rangle})^{1/2}/\sqrt{gh}$, and the spanwise-time-averaged, $\overline{\langle k \rangle}^{1/2}/\sqrt{gh}$, turbulent kinetic energy for S1. It is seen that the conditional time averaging gives a consistent trend of characteristic time-averaged k above the troughs in which the corresponding values of $(P_w^{-1}\overline{\langle k \rangle})^{1/2}/\sqrt{gh}$ systematically decreases from the transition region toward the shoreline. Figure 3.6 shows that both the magnitude and spatial variation of the predicted $\overline{\langle k \rangle}^{1/2}/\sqrt{gh}$ and $\overline{\langle u \rangle}/\sqrt{gh}$ are consistent with the corresponding measured values of Ting & Kirby (1994) in the transition and inner surf zones.

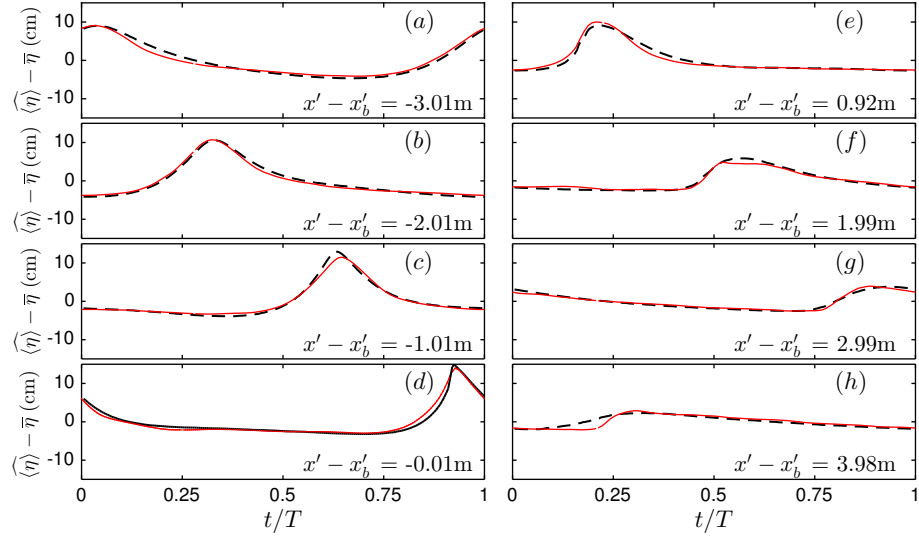


Figure 3.3: Spanwise-phase-averaged free surface elevations at different cross-shore locations for the weakly-plunging/spilling case S1. Comparison between --- the simulation and — the corresponding measurements by Ting & Nelson (2011). Here, $\hat{\cdot}$ indicates phase averaging over N successive waves after the wave field reaches to a steady state condition, where N is 15 in the simulation, and is 10 the measurements. x_b is approximately the point of incipient wave breaking, and is the cross-shore location at which a vertical tangent appears near the wave crest. No spanwise averaging was involved in the measurement.

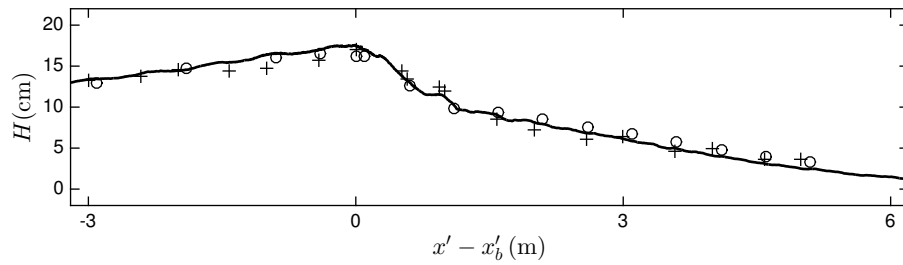


Figure 3.4: Cross-shore variation of the wave height $H = \langle \hat{\eta} \rangle_{max} - \langle \hat{\eta} \rangle_{min}$ for the weakly-plunging/ spilling case S1. Comparison between — the simulation and +++ the corresponding measurements by Ting & Nelson (2011). ooo show the results for the spilling case of Ting & Kirby (1994).

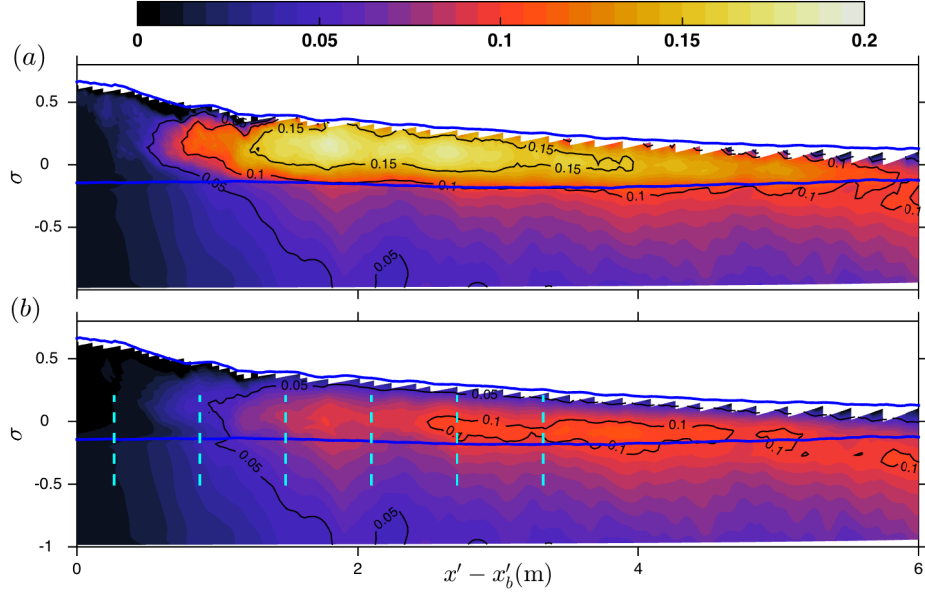


Figure 3.5: Spatial distribution of (a) the normalized conditional spanwise-time-averaged, $(P_w^{-1}\langle k \rangle)^{1/2}/\sqrt{gh}$, and (b) the spanwise-time-averaged, $\langle k \rangle^{1/2}/\sqrt{gh}$, turbulent kinetic energy for S1. Thick solid lines show the troughs and the crests levels. Vertical dashed lines show the cross-shore locations of the data-model comparisons shown in Figure 3.6. Here, $\sigma = (z - \bar{\eta})/h$.

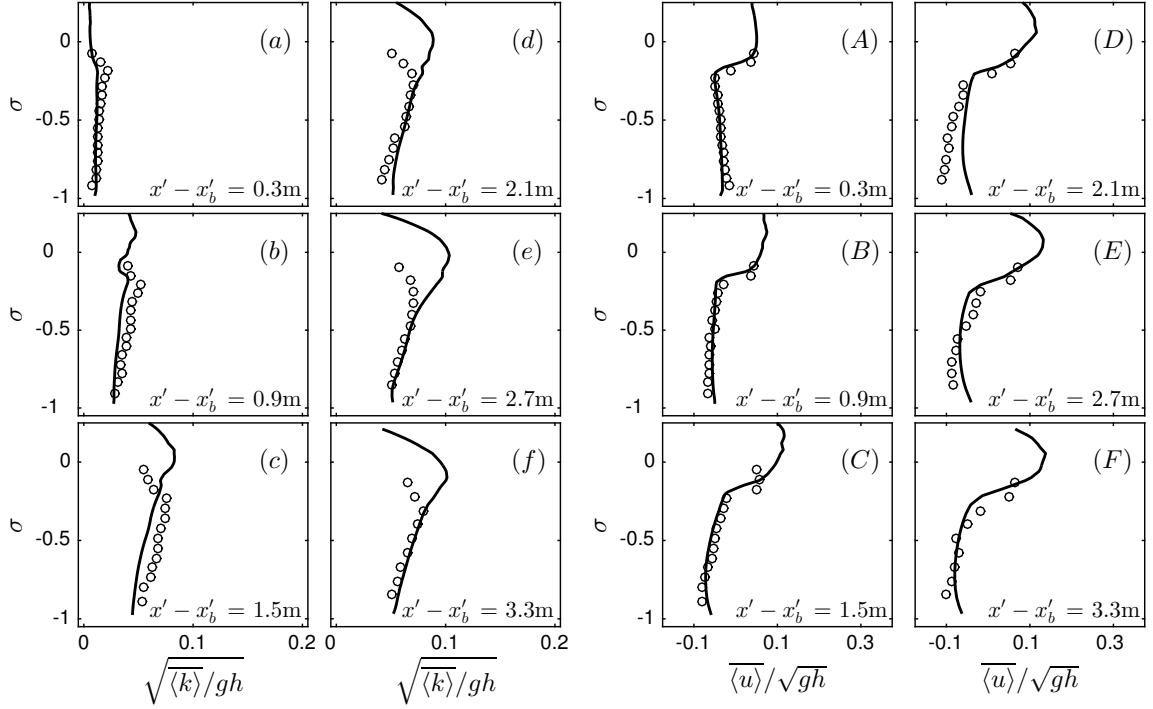


Figure 3.6: Spanwise-time-averaged normalized (a – f) turbulent kinetic energy, $\overline{\langle k \rangle}^{1/2} / \sqrt{gh}$, profiles and (A–F) normalized horizontal velocity, $\overline{\langle u \rangle} / \sqrt{gh}$, (undertow) profiles for the weakly-plunging/spilling case S1 at different cross-shore locations after the initial break point. $\circ \circ \circ$ show measurements of Ting & Kirby (1994). Here, $\sigma = (z - \bar{\eta}) / h$

3.5 The Role of the LBTCS in Bubble Transport in the Surf Zone

3.5.1 Coherent Structure Definition and Identification

A number of various definitions for coherent structures are available in the literature. [Robinson \(1991\)](#) defined a coherent structure as a 3D region of the flow over which at least one fundamental flow variable (velocity component, density, temperature, etc.) exhibits significant correlation with itself or with another variable over a range of scales and/or time that is significantly larger than the smallest local scales of the flow. Here, we are interested in LBTCS with length scales on the order of the local wave height. A turbulent breaking-induced coherent structure may be a vortical structure (VS), a compact region of vorticity surrounded by irrotational fluid, or a bursting region with large Reynolds stresses associated with the production of turbulence in the splash/bore-like region via downward ejections of fluid into lower depths. In this paper, the latter is referred to as a downburst structure (DBS).

There are several methods that are usually used for the identification of VS ([Jeong & Hussain 1995](#), [Chakraborty et al. 2005](#)). Local or point-wise methods of vortex identification define a function which can be evaluated at every point in the domain, and then classify each point as being inside or outside a vortex by setting a threshold value. In this section, we briefly present the selected criteria for the identification of VS and DBS.

Here, we use the Q -criterion ([Hunt et al. 1988](#)) to identify the VS, with the threshold values Q_{th} of 25 and 50 for the weakly plunging/spilling case S1 and the plunging case P1 respectively. The Q criterion defines vortices as flow regions with positive second invariant of $\nabla\mathbf{u}$, i.e. $Q > 0$. In addition, the pressure in the eddy must be lower than the ambient pressure. For an incompressible flow, the second invariant can be written as

$$Q = \frac{1}{2}(\|\mathbf{\Omega}\|^2 - \|\mathbf{S}\|^2), \quad (3.5)$$

where $\|\mathbf{\Omega}\| = tr[\mathbf{\Omega}\mathbf{\Omega}^t]^{1/2}$ and $\|\mathbf{S}\| = tr[\mathbf{S}\mathbf{S}^t]^{1/2}$. $S = \frac{1}{2}(\partial u_i/\partial x_j + \partial u_j/\partial x_i)$ and $\mathbf{\Omega} = \frac{1}{2}(\partial u_i/\partial x_j - \partial u_j/\partial x_i)$ are the symmetric and antisymmetric components of $\nabla\mathbf{u}$. Here

we use the Q criterion without the additional pressure condition as in [Chakraborty et al. \(2005\)](#). Both Q and λ_2 ([Jeong & Hussain 1995](#)) criteria result in similar looking vortical structures in the cases considered.

Although several experimental studies ([Ting 2008](#), [Ting & Nelson 2011](#), [Ting & Reimnitz 2015](#)) have discussed the existence of the DBS and their dynamical effects on the near-bed velocity field in depth-limited breaking waves, no quantitative criteria have been proposed for the identification of these structures. We consider a point $\mathbf{x} = (x, y, z, t)$ as being inside a DBS if

$$|\tau(\mathbf{x})| > \beta u'_{rms}(x, z, t) w'_{rms}(x, z, t) + \gamma \quad (3.6)$$

$$w'(\mathbf{x}) < 0 \quad (3.7)$$

$$Q(\mathbf{x}) < Q_{th}, \quad (3.8)$$

where $()'$ refers to the turbulent fluctuations about the corresponding spanwise-averaged value defined by [\(5.2\)](#), $\beta = 1.5$ and $\gamma = 0.006(\text{m}^2\text{s}^{-2})$.

3.5.2 Intermittent 3D Bubble Distribution

Figure [3.7](#) shows the evolution of the bubble plume (isosurface of $\alpha_b = 0.5\%$) in P1 and S1. The shape and structure of the bubble plume for P1 are also comparable with photographs taken by [Ting & Reimnitz \(2015, Figure 6\)](#), where the time interval between successive panels in [Figure 3.7](#) are approximately twice larger than that in [Ting & Reimnitz \(2015, Figure 6\)](#). In addition, the oblique extension of the bubble plume behind the splash-up regions and the propagating bores is consistent with the previous observations of bubble plume structure such as [Nadaoka et al. \(1989, Figure 8\)](#) and [Watanabe et al. \(2005, Figure 17\)](#).

It is seen that during each splash-up cycle the bubble plume is extended obliquely towards the bottom. [Figures 3.8 and 3.9](#) show snapshots of the evolution of both the LBTCS and bubble plume underneath the first and second splash-up regions. The VS generated during the first splash-up cycle ([Figure 3.8](#)) is approximately twice larger

than those generated during the second splash-up cycle (Figure 3.9). After the obliquely descending VS reaches the bottom, the vortex loop interacts with the bottom and breaks into the two broken legs. The broken legs tend to be attached to the bottom and move away from each other, sweeping a large area near the bed. The life time of the broken VS decreases as the local depth decreases.

The size of the predicted VS shown in Figure 3.9 are fairly reasonably comparable with the corresponding measurement shown in Ting et al. (2013, Figure 8) and Ting & Reimnitz (2015, Figure 7), indicating the model accurately captures the kinematics of the VS in the considered cases. Qualitatively, the 3D distribution of the bubble plume is highly correlated with that of the LBTCS, with high bubble void fraction regions located inside the VS. High bubble void fractions seem to transport down to the bed and stay in the core of the VS for a long time. As shown in Figures 3.10 and 3.11, the near-bed bubble void fractions could be greater than 5%. The results show that the distribution of bubble void fraction in the surf zone is highly 3D and intermittent both in time and space. These 3D distribution of entrained bubbles are consistent with the observation of Nadaoka et al. (1989, Figure 3). Figures 3.12, 3.13 and 3.14 show generally similar results for weakly plunging/spilling case S1 as in the plunging case P1. Due to the weaker first jet impact and splash-up, however, the resultant obliquely descending VS are smaller than those in P1, containing less spatially distributed bubble plume with smaller bubble void fractions.

3.5.3 Preferential Accumulation of Bubbles into the LBTCS

Preferential accumulation is one of the main characteristics of dispersed multi-phase flows. It is well-known that heavier-than-fluid particles (e.g. , sediment) tend to accumulate in regions of high strain rate and avoid regions of intense vorticity. In contrast, lighter-than-fluid particles (e.g. , bubbles) tend to congregate in vortical regions. This is mainly due to the local low-pressure region in a vortex core, as shown in Figure 3.15. Figures 3.16 and 3.17 show the resultant dynamic pressure gradient in the vertical and spanwise directions for P1 and S1 respectively. Comparing Figures

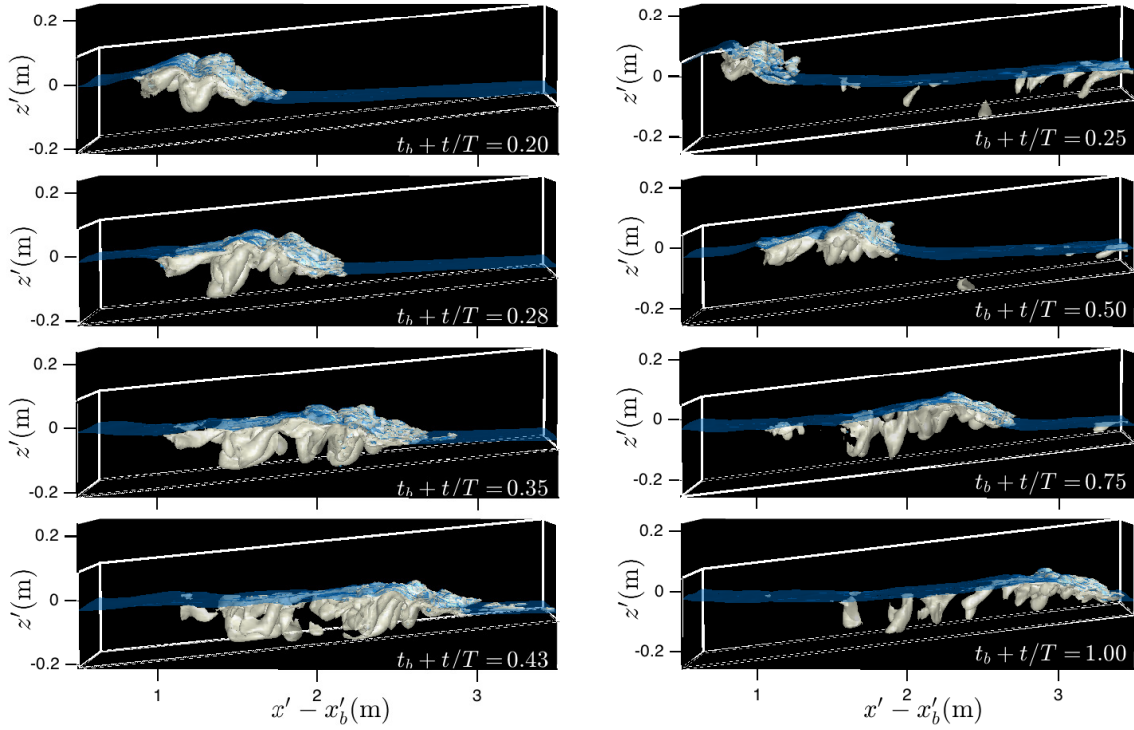


Figure 3.7: Snapshots of the bubble plume (isosurface of $\alpha_b = 0.5\%$) evolution for (right) plunging case P1, and (left) the weakly-plunging/spilling case S1. Here, $t_b = 90.78$ s and $t_b = 46.91$ s for P1 and S1 respectively.

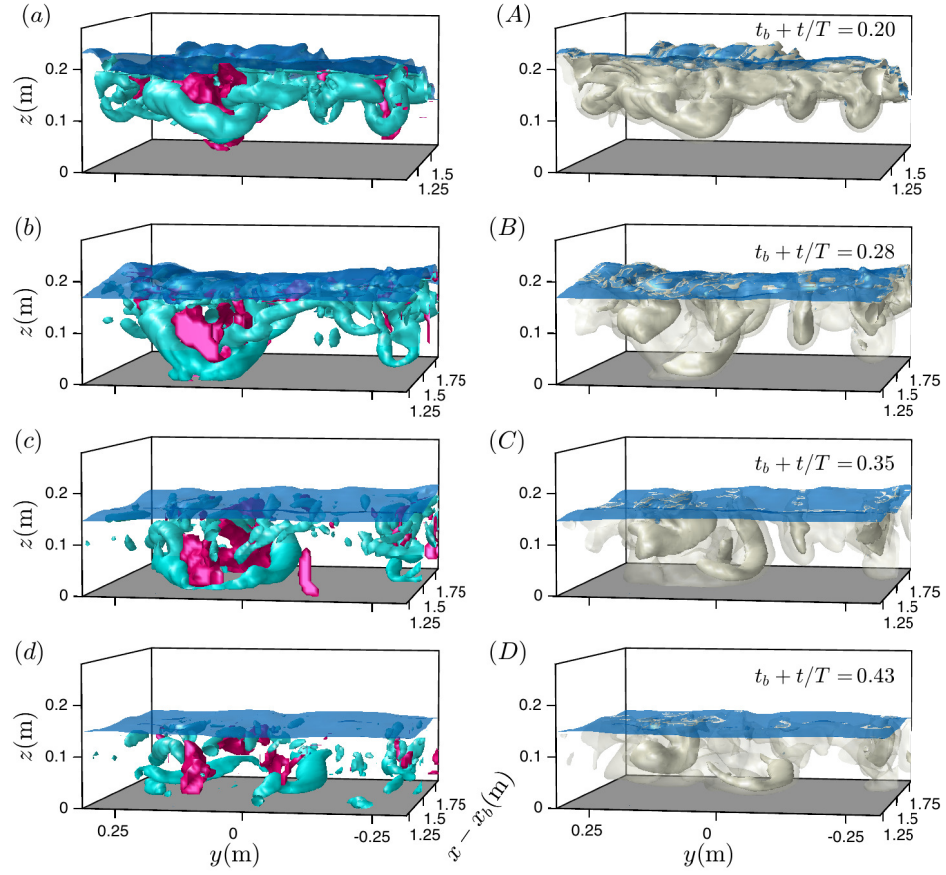


Figure 3.8: Snapshots of the evolution of (a–d) LBTCS, blue and red volumes are VS and DBS respectively, and (A–D) bubble plume, opaque and transparent volumes are the isosurfaces of $\alpha_b = 1\%$ and $\alpha_b = 0.2\%$ respectively, for the plunging case P1 underneath the first splash-up. Waves are propagating in the positive x direction, into the paper.

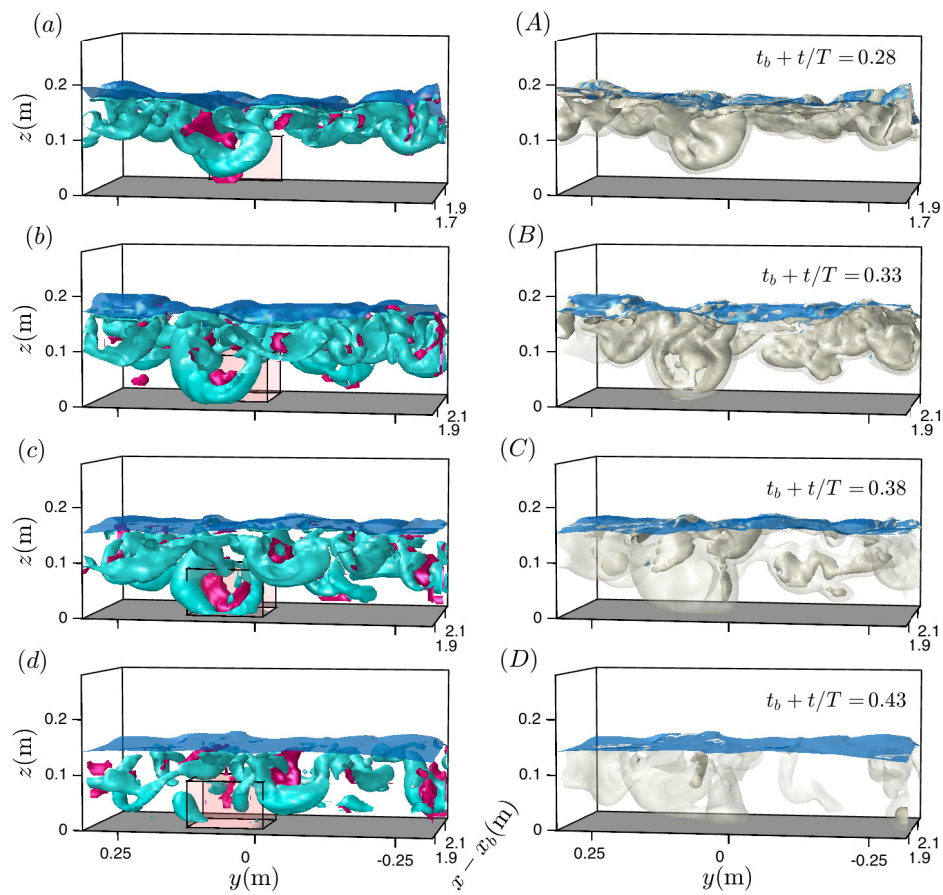


Figure 3.9: As in Figure 3.8 except underneath the second splash-up. The box volume shows approximately the location of 3D velocity measurements by [Ting & Reimnitz \(2015\)](#).

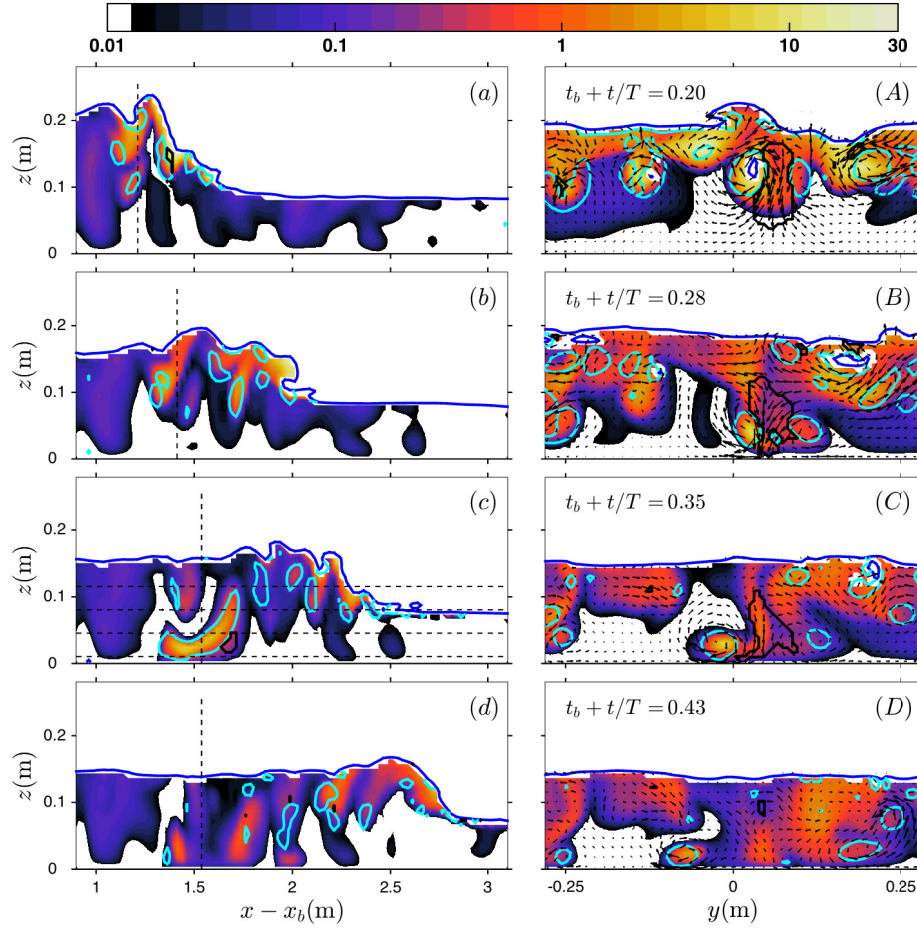


Figure 3.10: Snapshots of the bubble void fraction (%) distribution at ($a - d$) the mid cross-shore section and ($A - D$) different along-shore sections for the plunging case P1. Black and blue contours indicate the locations of DBS and VS respectively. Arrows in the right panels show the turbulent velocity vectors at the along-shore sections. For clarity only one-half of the arrows are shown. Arrows at each panel scale accordingly to give a better visibility. The vertical dashed line in each left panel shows the cross-shore location of the corresponding along-shore section shown in the right panel of that row. Horizontal dashed lines in panel c are the vertical elevations of the horizontal sections shown in Figure 3.11.

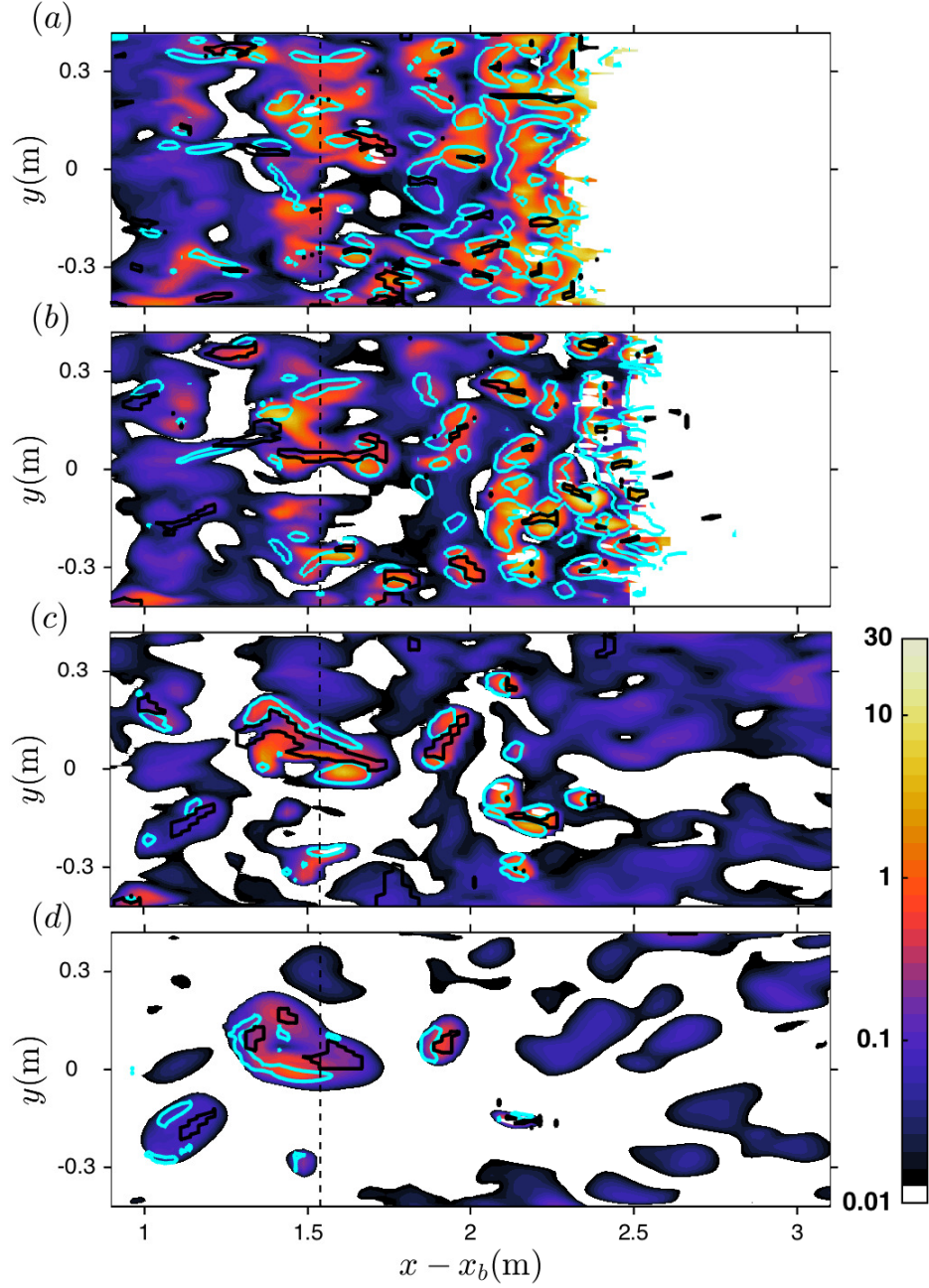


Figure 3.11: Horizontal distribution of the bubble void fraction (%) at $t_b + t/T = 0.35$ for the plunging case P1 at different vertical elevations shown in Figure 3.10. (a) $z = 115.5$ mm, (b) $z = 80.5$ mm, (c) $z = 45.5$ mm, and (d) $z = 10.5$ mm. Black and blue contours indicate the locations of DBS and VS respectively. The dashed lines show the cross-shore location of the along-shore sections shown in the right column of Figure 3.10.

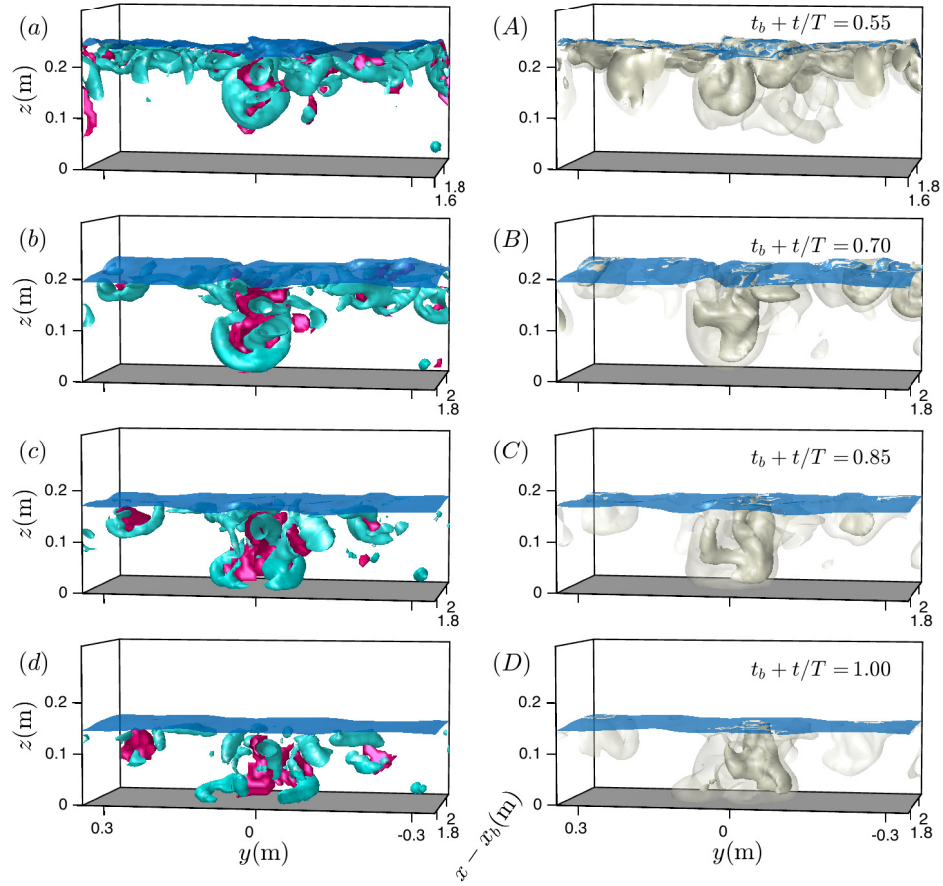


Figure 3.12: Snapshots of the evolution of (a – d) LBTCS, blue and red volumes are VS and DBS respectively, and (A – D) bubble plume, opaque and transparent volumes are the isosurfaces of $\alpha_b = 05\%$ and $\alpha_b = 0.1\%$ respectively, for the weakly-plunging/spilling case S1 underneath the first splash-up. Waves are propagating in the positive x direction.

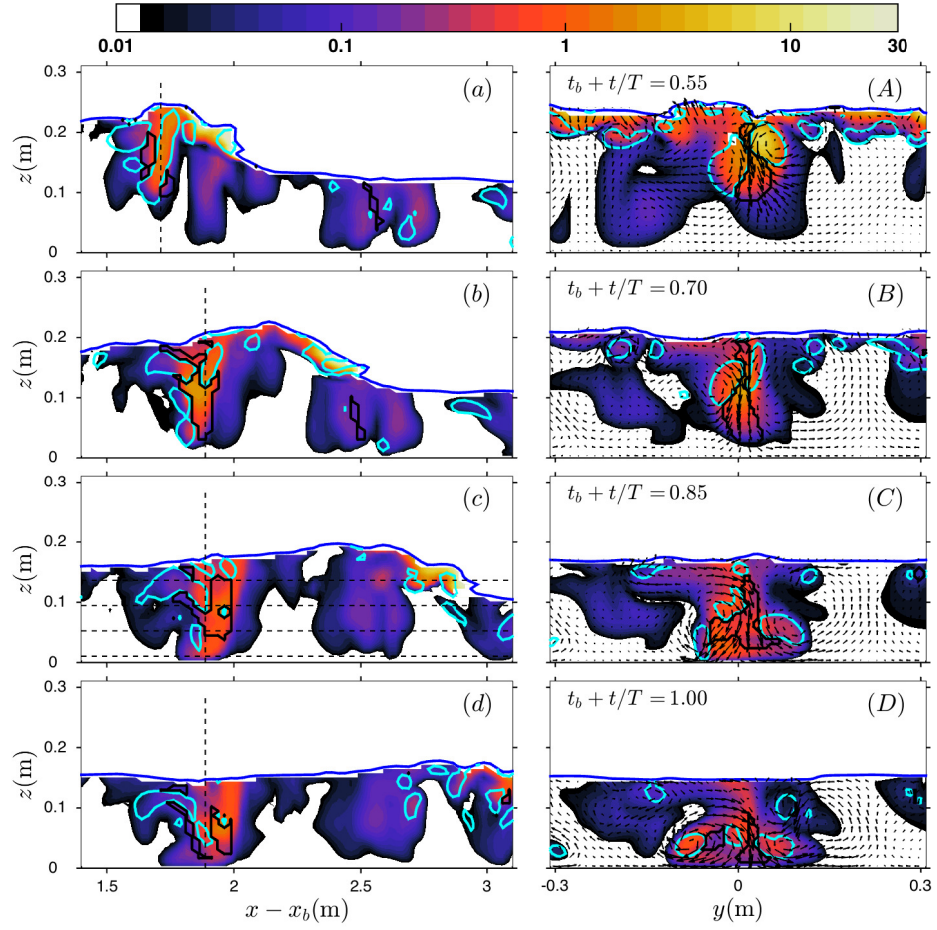


Figure 3.13: As in Figure 3.10 except for the weakly-plunging/spilling case S1.

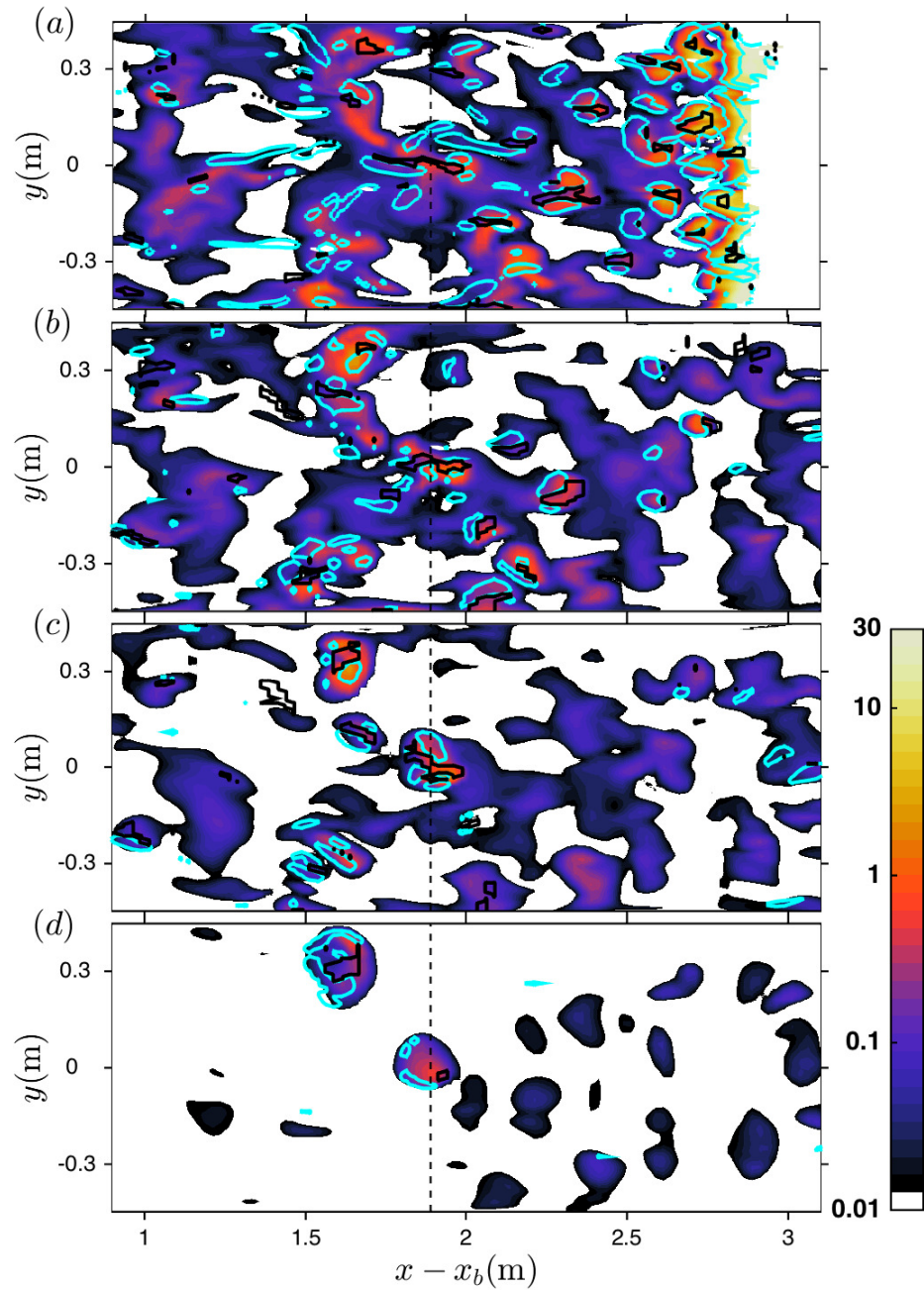


Figure 3.14: Horizontal distribution of the bubble void fraction (%) at $t_b + t/T = 0.85$ for the weakly plunging/spilling case S1 at different vertical elevations shown in Figure 3.13. (a) $z = 136.5$ mm, (b) $z = 94.5$ mm, (c) $z = 52.5$ mm, and (d) $z = 10.5$ mm. Black and blue contours indicate the locations of DBS and VS respectively. The dashed lines show the cross-shore location of the along-shore sections shown in the right column of Figure 3.13.

3.16 and 3.17 with Figures 3.10 and 3.13, it is seen that greater accumulation occurs at the VS parts with larger dynamic pressure gradient.

Figures 3.18 and 3.19 show the corresponding drag, lift and virtual mass forces on dispersed bubbles in the vertical and spanwise directions in S1 respectively. In the vertical direction the magnitude of the drag force is at least an order of magnitude larger than the other two forces. In the spanwise direction the drag force is still larger than the other two forces, but its magnitude is comparable with them. The lift force is mainly in the spanwise direction and towards the part of the VS with negative turbulent vertical velocity. The total interfacial forces on the bubbles in the vertical and spanwise directions are presented in Figure 3.20. The total interfacial force in the spanwise direction changes its sign across the VS consistent with the dynamic pressure gradient distribution shown in Figure 3.17. The total interfacial force in the vertical direction are larger near the part of the VS with negative turbulent vertical velocity.

We showed that the dispersed bubbles at lower depths are mainly associated with the LBTCS. However, higher bubble void fractions are not exactly located at the center of the vortex cores. As shown in Figure 3.8B, the trapped bubbles in the large VS are not uniformly distributed within the vortex loop. However, the entrapped bubbles in the VS shown in Figure 3.9B are nearly uniformly distributed through the vortex loop. Non-uniform void fraction distribution is also seen in Figure 3.13A. In addition, at some instances high void fraction regions are located inside the DBS rather than the vortex cores as shown in Figure 3.13B,C. These complicated 3D bubble distributions in the VS and DBS are due to the 3D distribution of the total interfacial forces, mainly the drag force, and that of the dynamic pressure gradient.

Figure 3.21 shows the spatial distribution of the conditional time-averaged bubble void fraction inside the VS, DBS and outside of the LBTCS as well as the time-averaged results from the 2D simulation for the weakly plunging/spilling case S1. The results are obtained by averaging over 15 wave cycles after the wave field reaches a quasi-steady state. It is seen that the time-averaged bubble void fraction inside the VS and DBS are an order of magnitude larger than that outside the LBTCS. In the

2D simulation, DBS and 3D VS do not exist and thus the vertical transport of the bubbles below the tough level is significantly underestimated compared with that in the 3D simulation.

3.6 Conclusions

In this paper, we use the model of [Derakhti & Kirby \(2014b\)](#) to examine the role of large-scale breaking-induced turbulent coherent structures (LBTCS) on the 3D intermittent transport of dispersed bubbles in the surf zone. The relative importance of preferential accumulation of dispersed bubbles in coherent vortex cores was investigated.

It was shown that the 3D distribution of the bubble plume is highly correlated with that of the LBTCS, with high bubble void fraction regions are located closer to the part of the VS with negative turbulent vertical velocity. These complicated 3D bubble distribution into the VS and DBS are due to the 3D distribution of the total interfacial forcing, mainly the drag force, and that of the dynamic pressure. High bubble void fractions seem to transport down to the bed and stay in the core of the VS for a long time. Near-bed bubble void fractions greater than 5% have been observed in the considered plunging case. It was shown that the time-averaged bubble void fraction inside the VS and DBS are an order of magnitude larger than that outside the LBTCS. In the 2D simulation, the vertical transport of the bubbles below the tough level is significantly underestimated compared with that in the 3D simulation, due to the absence of the DBS and 3D VS.

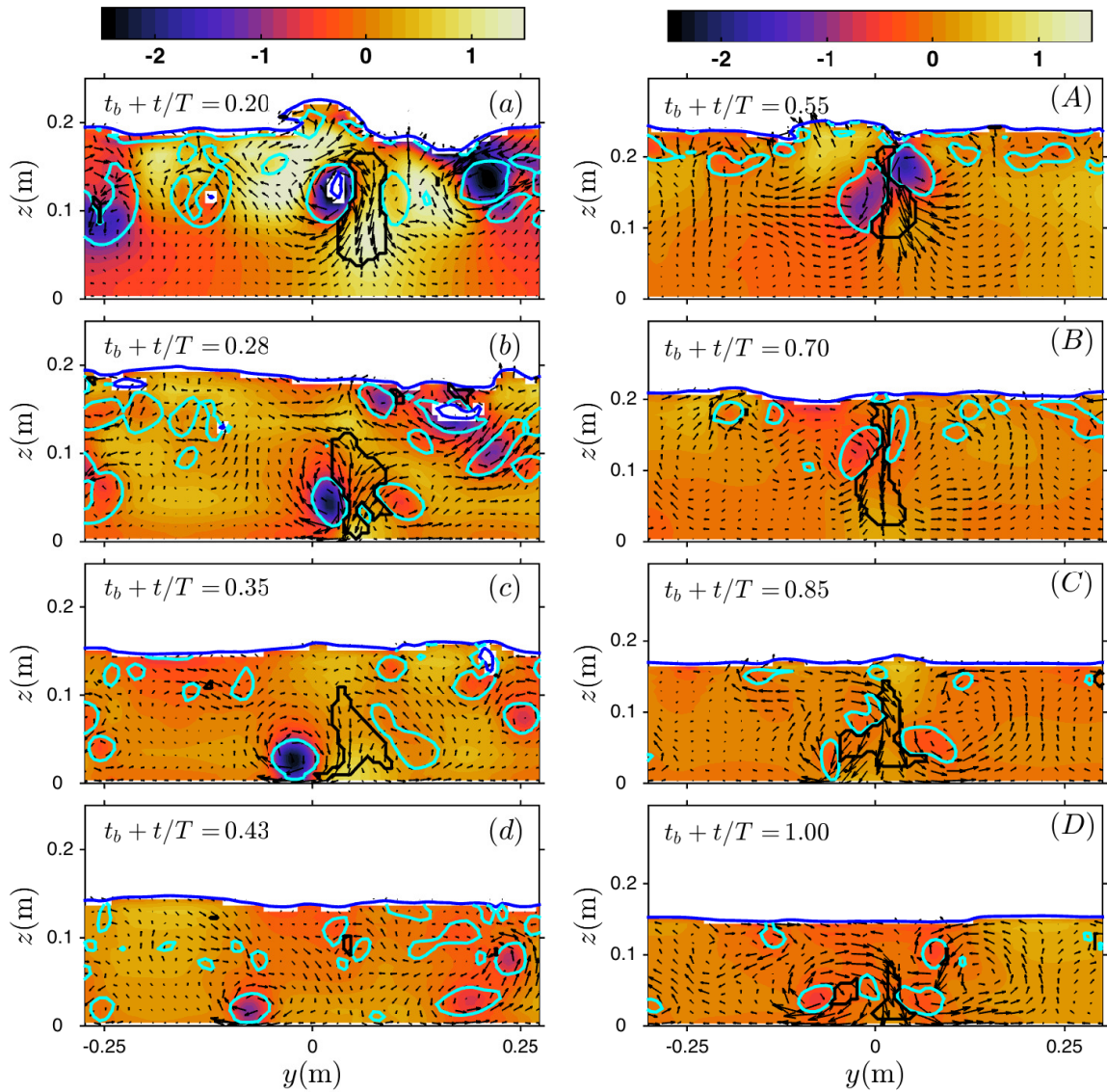


Figure 3.15: Snapshots of the spatial distribution of the dynamic pressure in (a – d) the plunging case P1 and (A – D) the weakly plunging/spilling case S1. Black and blue contours indicate the locations of DBS and VS respectively. Arrows in the right panels show the turbulent velocity vectors at the along-shore sections. For clarity only one-half of the arrows are shown. Arrows at each panel scale accordingly to give a better visibility. The reference value is $0.01\rho g$.

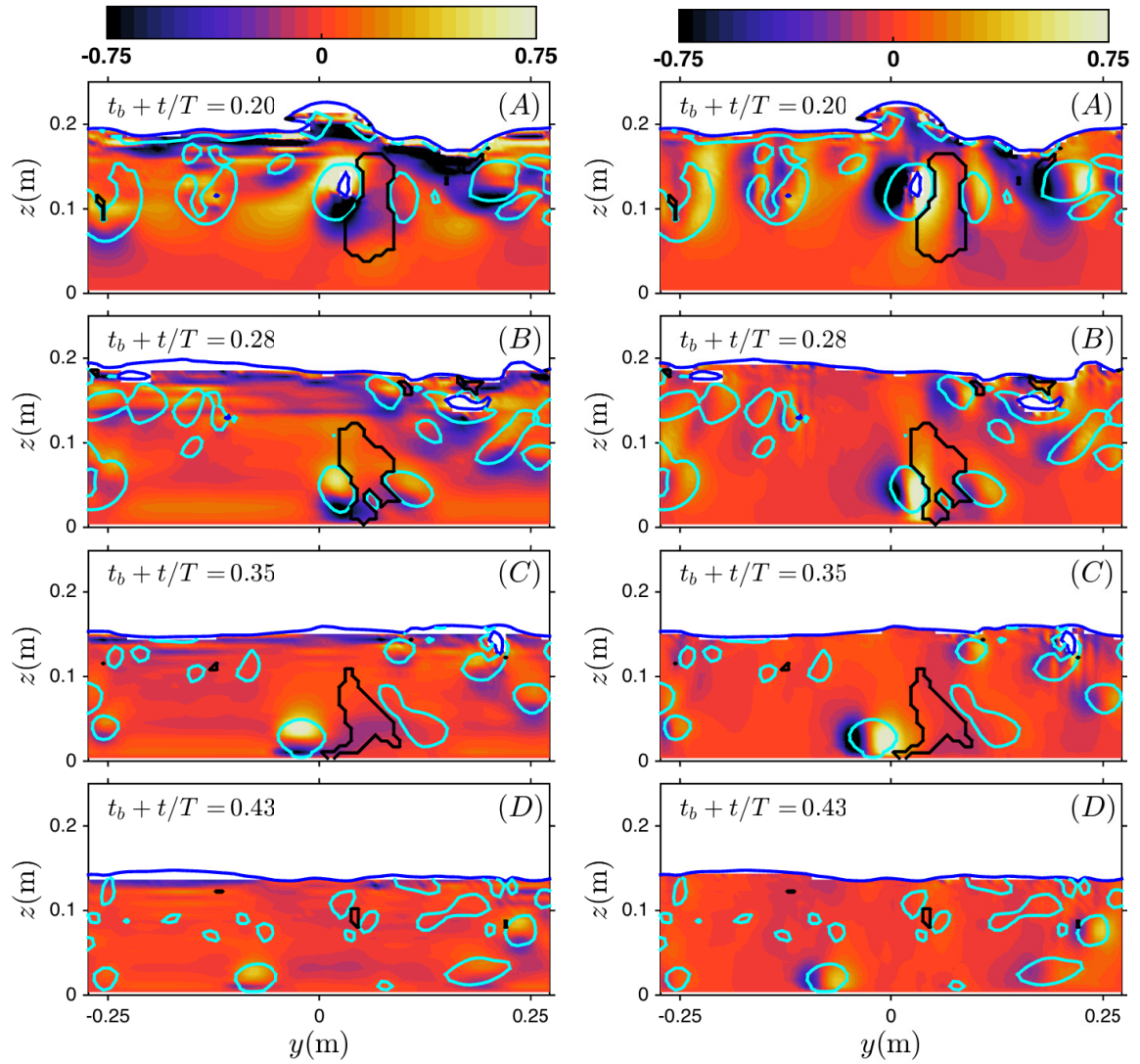


Figure 3.16: Snapshots of the spatial distribution of the dynamic pressure gradient in the (*a – d*)vertical and (*A – D*) spanwise directions in the plunging case P1. Black and blue contours indicate the locations of DBS and VS respectively. The reference value is ρg .

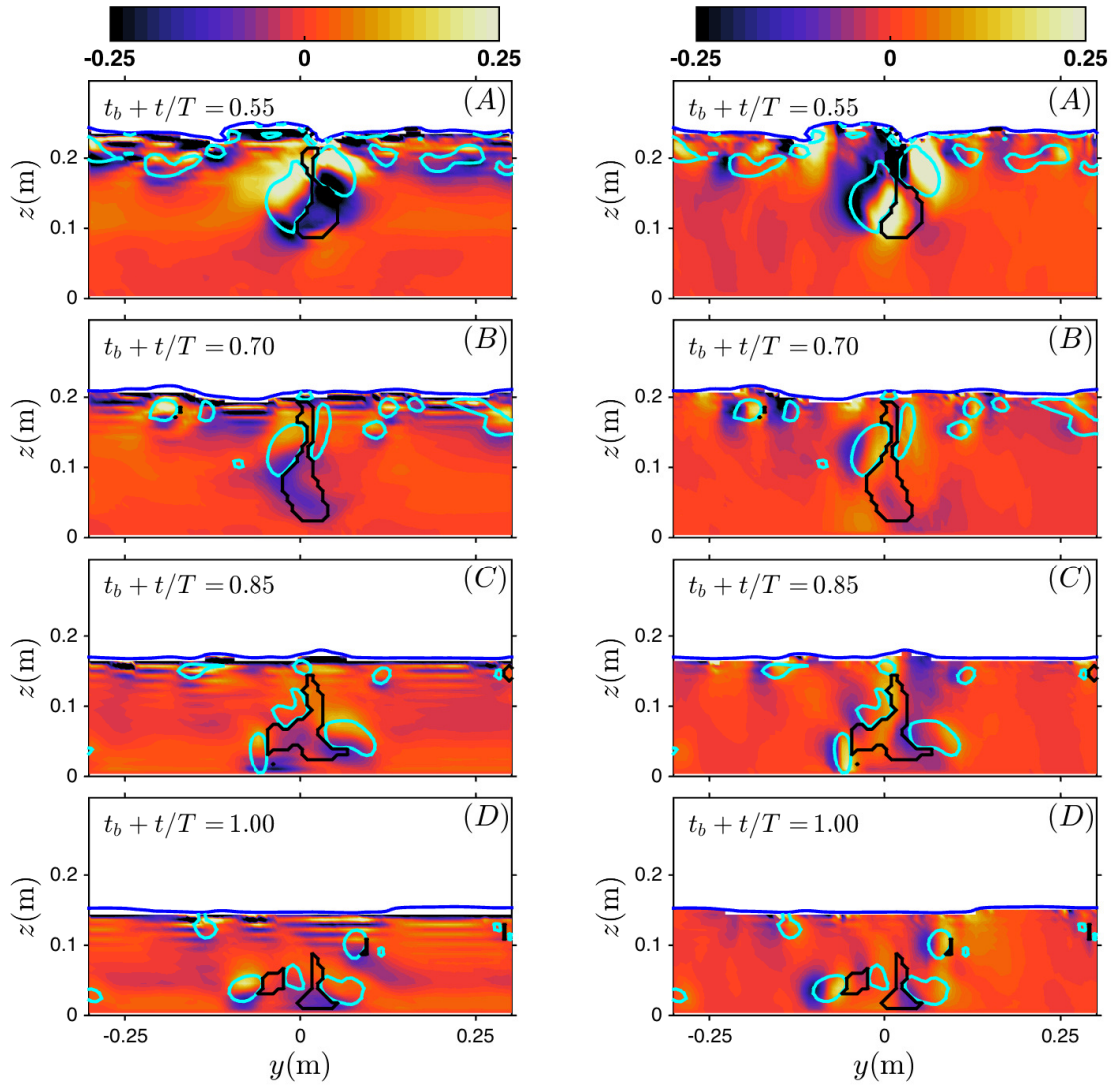


Figure 3.17: Snapshots of the spatial distribution of the dynamic pressure gradient in the $(a-d)$ vertical and $(A-D)$ spanwise directions in the weakly plunging/spilling case S1. Black and blue contours indicate the locations of DBS and VS respectively. The reference value is ρg .

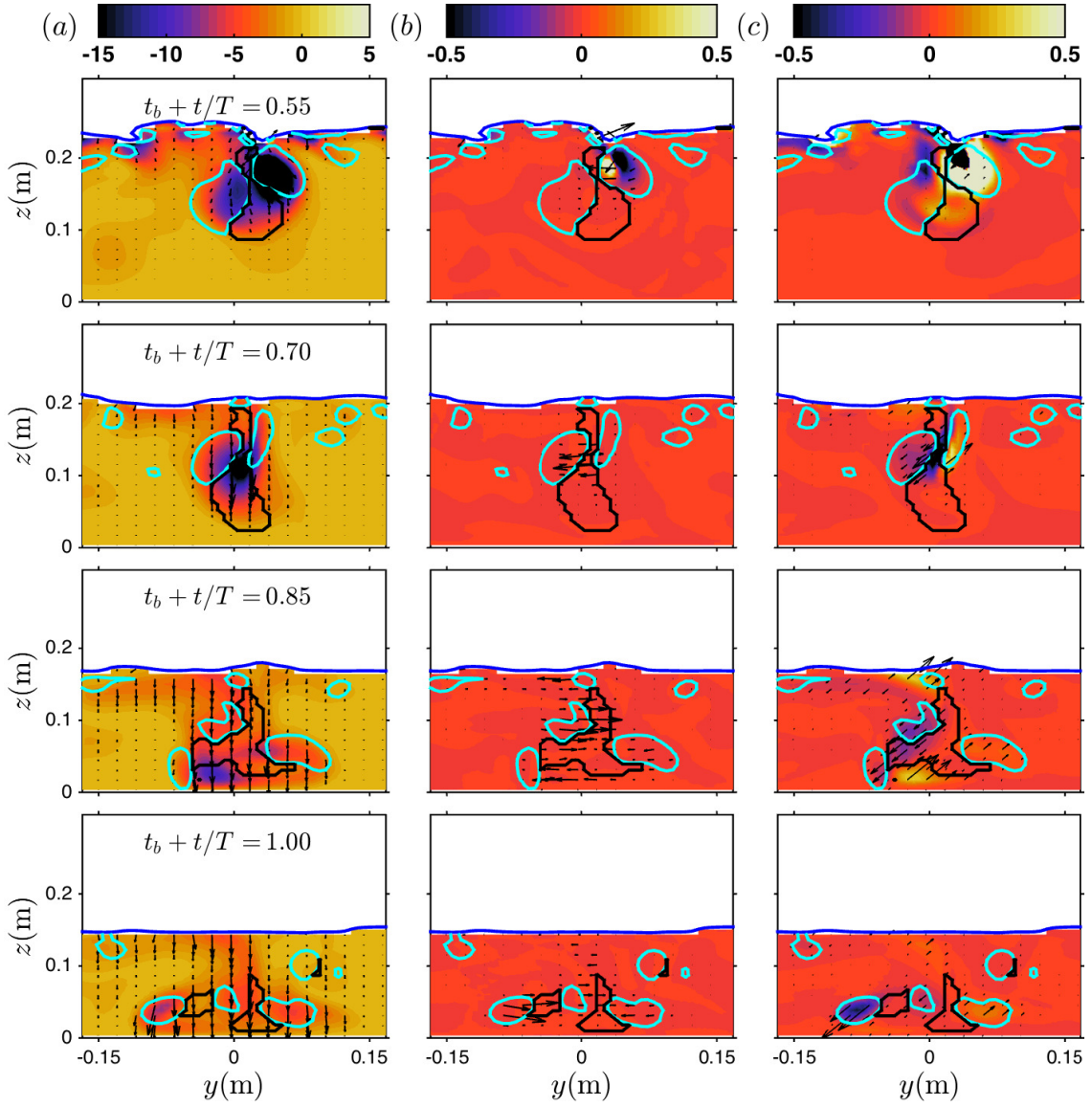


Figure 3.18: Snapshots of the spatial distribution of (a) drag, (b) lift and (c) virtual mass forces in the vertical direction per unit volume of the liquid in the weakly plunging/spilling case S1. Black and blue contours indicate the locations of DBS and VS respectively. Arrows show the corresponding vector force at the along-shore sections. Arrows at each panel scale accordingly to give a better visibility. The reference value is $0.01\rho g$.

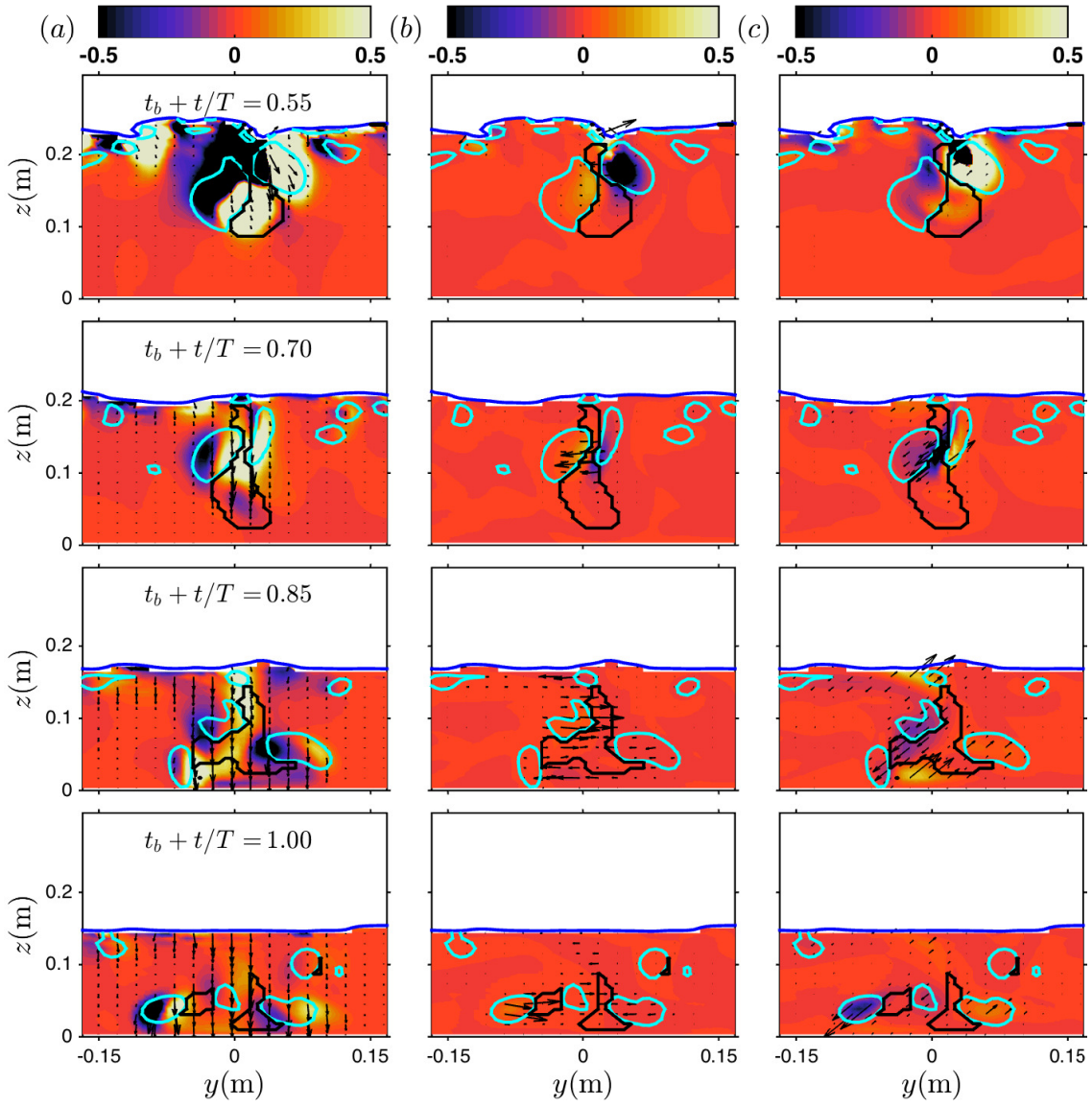


Figure 3.19: Snapshots of the spatial distribution of (a) drag, (b) lift and (c) virtual mass forces in the spanwise direction per unit volume of the liquid in the weakly plunging/spilling case S1. Black and blue contours indicate the locations of DBS and VS respectively. Arrows show the corresponding vector force at the along-shore sections. Arrows at each panel scale accordingly to give a better visibility. The reference value is $0.01\rho g$.

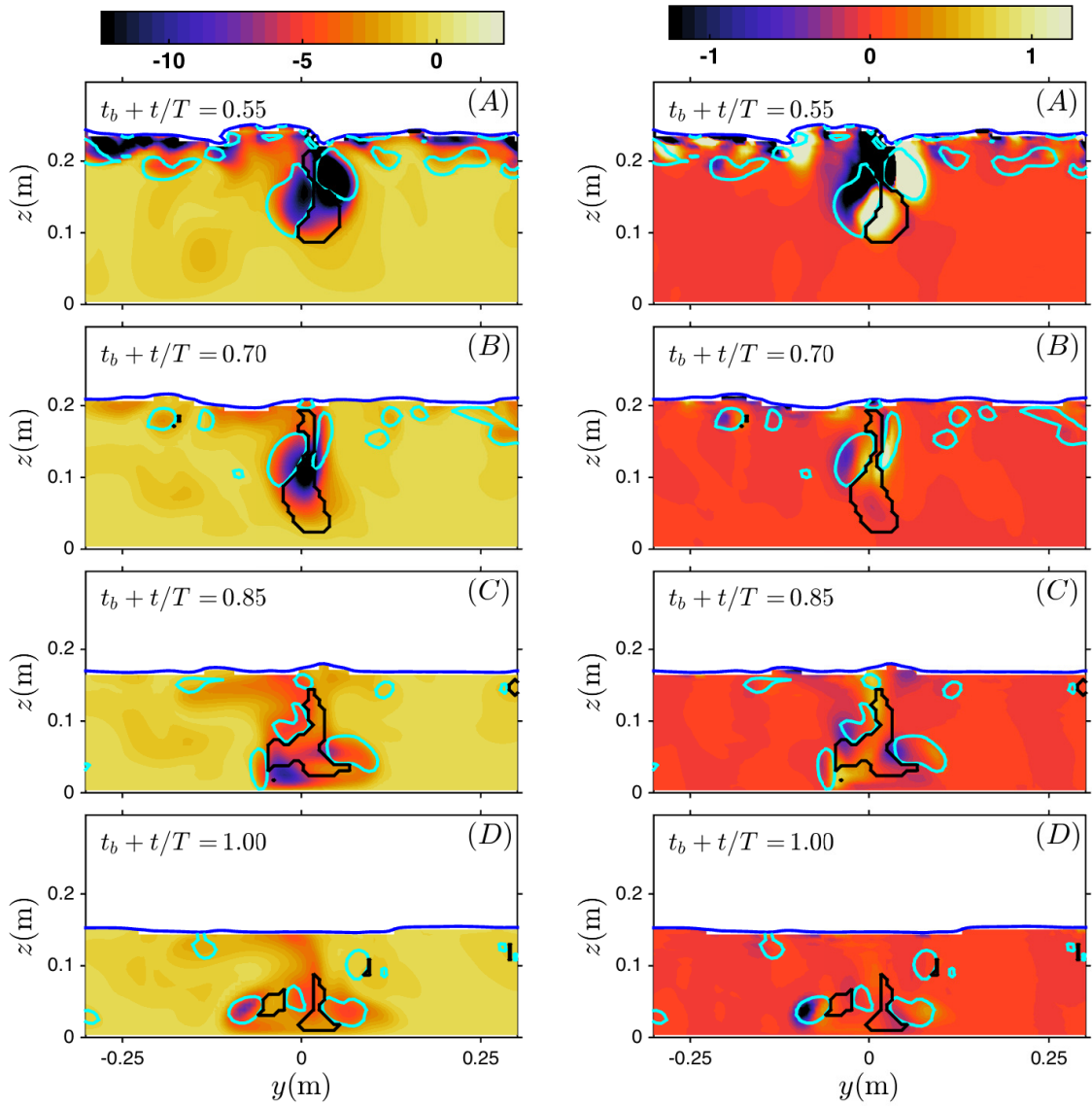


Figure 3.20: Snapshots of the spatial distribution of the total interfacial forces per unit volume of the liquid in the $(a - d)$ vertical and $(A - D)$ spanwise directions in the weakly plunging/spilling case S1. Black and blue contours indicate the locations of DBS and VS respectively. The reference value is $0.01\rho g$.

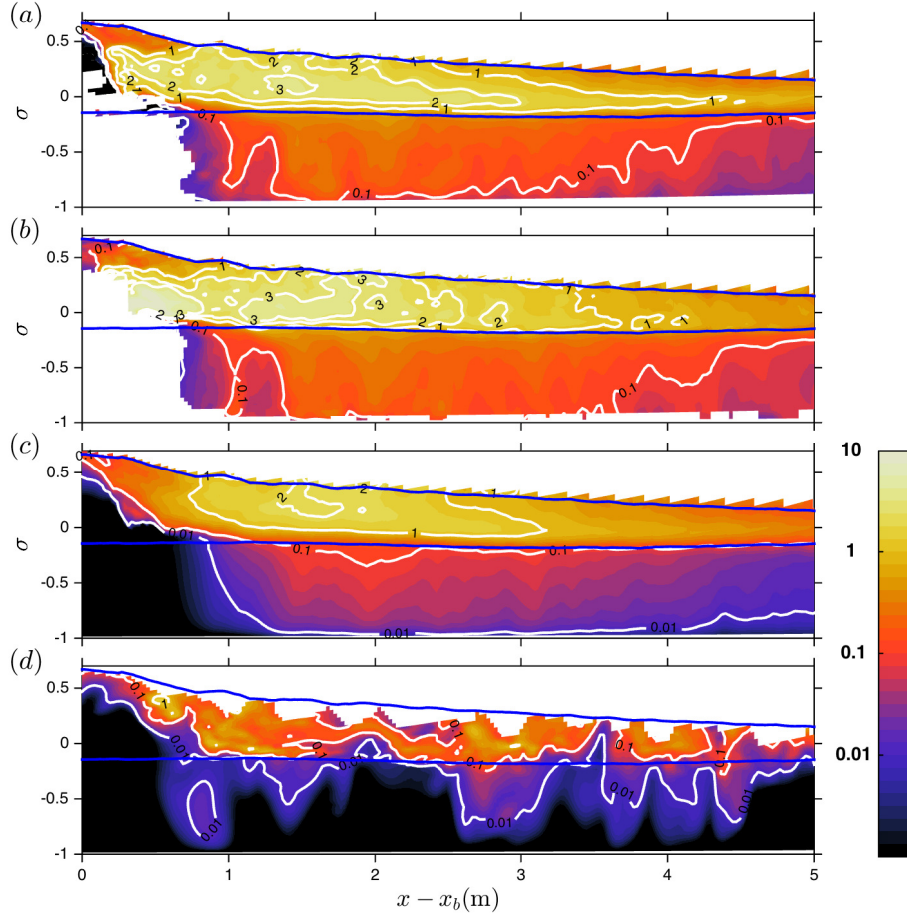


Figure 3.21: Spatial distribution of the conditional time-averaged bubble void fraction (%) for the weakly plunging/spilling case S1, (a) inside the VS $\langle \alpha_b \rangle_{VS}$, (b) inside the DBS $\langle \alpha_b \rangle_{DBS}$, (c) $P_w^{-1} \langle \alpha_b \rangle$ in the 3D simulation. Panel (d) gives the corresponding conditional time-averaged bubble void fraction $P_w^{-1} \langle \alpha_b \rangle$ for the corresponding 2D simulation. Blue solid lines show trough and crest elevations. Here, $\sigma = (z - \bar{\eta})/h$.

Chapter 4

NHWAVE: GOVERNING EQUATIONS, EXACT BOUNDARY CONDITIONS AND TURBULENCE MODELING

4.1 Abstract

We derive a new set of equations, in conservative form, describing the kinematics and dynamics of continuous and dispersed phases in a multiphase mixture in a surface- and terrain-following σ -coordinate system, together with exact surface and bottom boundary conditions for the velocity and dynamic pressure fields as well as a Neumann-type boundary condition for scalar fluxes. It is shown that the new boundary conditions significantly improve the predicted velocity and turbulence fields under regular surf zone breaking waves, compared with commonly used, simplified stress boundary conditions developed by ignoring the effects of surface and bottom slopes in the transformation of stress terms. Also, by comparing the predicted velocity field under a deep water standing wave in a closed basin, we show that the new model does not generate unphysical vorticity at the free surface, in contrast to the simplified case. A new numerical scheme is used for terms including vertical gradients, preserving second-order accuracy for a general non-uniform vertical grid.

4.2 Introduction

Surface wave breaking plays an important role in numerous environmental and technical processes such as air-sea interaction, acoustic underwater communications, optical properties of the water columns, nearshore mixing and coastal morphodynamics. Wave breaking is a highly dissipative process, limiting the maximum height of surface waves. It is also a source of turbulence, enhancing transport and mixing in the ocean surface layer. It entrains large volumes of air that rapidly evolve into a distribution

of bubble sizes, which in turn interact with liquid turbulence and organized motions. In shallow water, this process becomes more complicated when both bottom effects and sediment alter a flow field (Banner & Peregrine 1993, Melville 1996, Duncan 2001, Kiger & Duncan 2012, Perlin et al. 2013, Derakhti & Kirby 2014b).

Although large-eddy simulations (LES) combined with the well-known volume-of-fluid (VOF) method for free-surface tracking (Watanabe et al. 2005, Lakehal & Liovic 2011, Derakhti & Kirby 2014b) can resolve turbulence and mean flow dynamics under breaking waves quite well, they are computationally expensive even for laboratory-scale events. A lower-resolution framework is needed to study long-term, $\mathcal{O}(\text{days})$, and large-scale, $\mathcal{O}(100\text{m} \sim 10\text{km})$, breaking-driven circulations as well as transport of sediment, bubbles, and other suspended materials. Computationally efficient Boussinesq-type models (e.g., Wei et al. 1995, Shi et al. 2012) can often yield acceptable predictions of surface elevations and depth-averaged currents in the nearshore region. Such single layer models, however, cannot provide any vertical structure of mean flow, and thus recourse must be made to models which either provide estimates of vertical structures through closure hypotheses (Kim et al. 2009) or which utilize a three-dimensional (3D) framework from the outset.

During the past decade, several 3D wave-resolving non-hydrostatic models based on Reynolds-averaged Navier-Stokes (RANS) equations, such as NHWAVE (Ma et al. 2012), SWASH (Zijlema et al. 2011), and Bradford (2011), have been developed for coastal applications using surface- and terrain-following curvilinear (x, y, σ) coordinates, hereafter is referred as the σ -coordinate system. A direct simplification of this new framework, in comparison with VOF-based models, is achieved by assuming the free surface to be a single-valued function of horizontal location. By using a σ -coordinate system, the free surface is always located at an upper computational boundary, determined by applying free-surface boundary conditions. A pressure boundary condition at the free surface can thus be accurately prescribed, and dispersion characteristics of short waves are typically captured by using a few vertical levels. However, the effects of surface and bottom slopes in the dynamic boundary conditions at the

top and bottom interfaces, e.g., the continuity of the tangential surface stress, have been ignored in most of the previous studies using the σ -coordinate system, following previous practice in large-scale ocean circulation models. Although this assumption is fairly reasonable for wave-averaged models, it is not accurate for highly nonlinear and breaking waves in wave-resolving computations, or in the presence of rapid bottom changes. Ignoring surface slopes effects in the surface boundary condition for stresses also leads to the generation of an unphysical vorticity, as discussed in §5.1.

A previous version of the non-hydrostatic model NHWAVE has been described in [Ma et al. \(2012\)](#), [Ma, Kirby & Shi \(2013\)](#) (hereafter referred to as the old model). NHWAVE solves the RANS equations in well-balanced conservative form, formulated in the σ -coordinate system. The governing equations are discretized by a combined finite-volume/finite-difference approach with a Godunov-type shock-capturing scheme. The model is wave-resolving, and can provide instantaneous descriptions of surface displacements and wave orbital velocities. The model has been applied to study tsunami wave generation by submarine landslides ([Ma, Kirby & Shi 2013](#), [Tappin et al. 2014](#)), wave damping in vegetated environments ([Ma, Kirby, Su, Figlus & Shi 2013](#)), nearshore suspended sediment transport ([Ma, Chou & Shi 2014](#)), and wave interactions with porous structures ([Ma, Shi, Hsiao & Wu 2014](#)). In these studies, the effects of surface and bottom slopes in the surface and bottom dynamic boundary conditions as well as in the horizontal diffusion terms were ignored, as done, to the best of our knowledge, in all of the existing non-hydrostatic models using the σ -coordinate system.

In this paper, we first derive a new set of governing equations, in a conservative form, based on the mixture theory in the σ -coordinate system, describing the kinematics and dynamics of the continuous and dispersed phases in a multi-phase mixture. Here, we assume a dilute suspension regime and particles with small Stokes number. The effects of baroclinic pressure and turbulence modulation due to density variations are considered. The exact surface and bottom dynamic boundary conditions for the velocity and dynamic pressure fields are derived, using the continuity of the normal

and tangential stresses at the top and bottom interfaces. A Neumann-type boundary condition for scalar fluxes is also derived. It is shown that the new boundary conditions significantly improve the velocity and turbulence fields predictions under surf zone breaking waves compared with the commonly used simplified stress boundary conditions in non-hydrostatic studies using the σ -coordinate system. In addition, a new numerical scheme is implemented for terms with vertical gradients, preserving second-order accuracy for a general non-uniform vertical grid. The model’s capability for reproducing the evolution of the free surface, velocity, vorticity, and turbulence fields under different breaking waves from the surf zone to deep water is examined in detail in a companion paper ([Derakhti et al. 2016b](#)).

The paper is organized as follows. In §4.3, new conservative forms of the continuity and momentum equations for a multiphase mixture in the σ -coordinate system are derived, and the main assumptions are discussed. In §4.4, exact surface and bottom kinematic and dynamic boundary conditions as well as a Neumann-type boundary condition for a scalar quantity are derived. In §4.5, the details of the numerical scheme to obtain a hydrostatic velocity field as well as the non-hydrostatic velocity correction scheme are presented. In §4.6, the new model results for the velocity field under a deep water standing wave in a closed basin are compared with that predicted by the old model. Turbulence predictions under spilling periodic surf zone breaking waves using the new dynamic boundary conditions are compared with those from the old model as well as the corresponding measurements of [Ting & Kirby \(1994\)](#). In addition, to examine the two-dimensional isotropy of the new model, the evolution of an initial two-dimensional Gaussian hump in a closed box is presented. Conclusions are given in §4.7.

4.3 Governing Equations in Conservative Form

We first derive the continuity and momentum equations for a multiphase mixture in the σ -coordinate system assuming a dilute suspension regime with particles with small Stokes numbers. Using the Boussinesq approximation, the mixture density

variations are ignored except in the gravity term. The scalar transport equation is also derived using the same way as used to derive the momentum equation. Finally, different turbulence models including the standard $k - \epsilon$ and that by [Yakhot et al. \(1992\)](#) which is based on the renormalization group (RNG) approach, are presented. The exact surface and bottom boundary conditions are derived in the next section.

4.3.1 Continuity and Momentum Equations

In the absence of heat and mass transfers, the continuity and momentum equations in Cartesian coordinates (x_1^*, x_2^*, x_3^*) , where $x_1^* = x^*$, $x_2^* = y^*$ and $x_3^* = z^*$ for each phase in the mixture can be written as

$$\frac{\partial \chi^k \rho^k}{\partial t^*} + \frac{\partial}{\partial x_j^*} (\chi^k \rho^k u_j^k) = 0, \quad (4.1)$$

$$\frac{\partial \chi^k \rho^k u_i^k}{\partial t^*} + \frac{\partial}{\partial x_j^*} (\chi^k \rho^k u_i^k u_j^k) = \chi^k \frac{\partial \Pi_{ij}^k}{\partial x_j^*} + \chi^k \rho^k g_i \delta_{i3}, \quad (4.2)$$

where δ is the Kronecker delta function, $(i, j) = 1, 2, 3$, and $\chi(\mathbf{x}, t)$ is a phase-indicator function at time t and point \mathbf{x} , defined by

$$\chi^k(\mathbf{x}, t) = \begin{cases} 1 & \text{if } \mathbf{x} \text{ lies in phase } k \text{ at time } t \\ 0 & \text{otherwise} \end{cases} \quad (4.3)$$

to determine the volumes occupied by each phase. Here, k refers either to the dispersed bubble phase, suspended sediment or to the liquid phase. In addition, ρ^k is the phase density, u^k is the phase velocity, and $\mathbf{g} = (0, 0, -g)$ is the gravitational acceleration. For an incompressible fluid, the net fluid stress, composed of the pressure contribution p^k plus the viscous stress σ_{ij}^k , is defined by $\Pi_{ij}^k = -p^k \delta_{ij} + \sigma_{ij}^k$. In a Newtonian fluid, we may assume that $\sigma_{ij}^k = 2\mu^k e_{ij}^k$, where $e_{ij}^k = 1/2(\partial u_i^k / \partial x_j^* + \partial u_j^k / \partial x_i^*)$ is the strain rate tensor and μ^k is the phase dynamic viscosity.

As we aim to capture ensemble-averaged large-scales of the process, as opposed to the details of the interaction between different phases in the mixture, we may simplify

the problem by summing up the continuity and momentum equations for all phases in the mixture and defining the ensemble-averaged bulk density, velocity, net stress gradient, and Reynolds stress of the mixture, $()^m$, as (Drew & Passman 1999)

$$\begin{aligned}
\rho^m &= \langle \Sigma \chi^k \rho^k \rangle = \alpha^l \rho^l + \alpha^b \rho^b + \alpha^c \rho^c \\
u_i^m &= \frac{\langle \Sigma \chi^k \rho^k u_i^k \rangle}{\rho^m} \\
\frac{\partial \Pi_{ij}^m}{\partial x_j^*} &= \langle \Sigma \chi^k \frac{\partial \Pi_{ij}^k}{\partial x_j^*} \rangle = \frac{\partial}{\partial x_j^*} \left(-p^m \delta_{ij} + 2\mu^m e_{ij}^m \right) \\
\tau_{ij}^m &= \langle \Sigma \chi^k \rho^k u_i^k u_j^k \rangle - \rho^m u_i^m u_j^m,
\end{aligned} \tag{4.4}$$

where $\langle . \rangle$ indicates ensemble averaging, and $\alpha^k = \langle \chi^k \rangle$ is the ensemble-averaged volume fraction of phase k in the mixture. By doing this, all small-scale processes, e.g. the shear-induced dissipation, become subgrid-scale and need to be modeled. Although there is no universal model for τ_{ij}^m , even in the case of a single phase flow, we use the common eddy viscosity approach to relate the anisotropic part of the mixture Reynolds stress, $\tau_{ij}^{m,dev}$, to the mixture rate of strain, e_{ij}^m as

$$\tau_{ij}^{m,dev} \equiv \tau_{ij}^m - \frac{\delta_{ij}}{3} \tau_{kk}^m = -2\rho^m (\nu_t^m)_j e_{ij}^m, \tag{4.5}$$

where $(\nu_t^m)_j$ is the mixture turbulent eddy viscosity in the j direction (j is not a free index here), obtained from an appropriate turbulence model, and may include both shear-induced and bubble-induced eddy viscosity (see Derakhti & Kirby 2014b, for more details). If a grid resolution in the horizontal directions is considerably different from that in the vertical direction, the horizontal turbulent eddy viscosity $(\nu_t^m)_1 = (\nu_t^m)_2$ may be different from that in the vertical direction $(\nu_t^m)_3$. We further assume a static constant reference density for the liquid phase as ρ_0 , corresponding to a reference temperature and salinity of the liquid phase, and employ the Boussinesq approximation to neglect the density variations in the momentum equation except in the gravity term. This is a common assumption in geophysical flows, as density variations due to the

temperature and salinity changes are small, say $|\rho^m - \rho_0| < 0.05\rho_0$. In the case of a multiphase flow, we need to have a small void fraction for dispersed phases, referred as a dilute regime, in order for the Boussinesq approximation to be applicable. Although the dilute regime is usually the case for suspended sediment studies, we may have relatively large bubble void fractions near the bore-front region of a breaking wave. However, comparing with the simplification associated with assuming a single-valued free-surface, and, thus, losing the details of vorticity and turbulence generation at the turbulent bore-front, the Boussinesq approximation may have a secondary effect. Applying the above mentioned assumptions, the ensemble-averaged form of (4.1) and (4.2) reads as

$$\frac{\partial u_j^m}{\partial x_j^*} = 0 \quad (4.6)$$

$$\frac{\partial u_i^m}{\partial t^*} + \frac{\partial u_i^m u_j^m}{\partial x_j^*} = \frac{1}{\rho_0} \frac{\partial \mathcal{S}_{ij}^m}{\partial x_j^*} + \frac{\rho^m}{\rho_0} g_i \delta_{i3}, \quad (4.7)$$

where $\mathcal{S}_{ij}^m = \Pi_{ij}^m - \tau_{ij}^m$ is the total ensemble-averaged mixture stress tensor.

The governing equations (4.6) and (4.7) are next transformed into the σ -coordinate system, which is given by

$$t = t^* \quad x = x^* \quad y = y^* \quad \sigma = \frac{z^* + d}{D} \quad (4.8)$$

where $D = d + \langle \eta \rangle$ is the total water depth, d is the still water depth, and $\langle \eta \rangle$ is the ensemble-averaged free surface elevation. In the case of a multi-valued surface, however, the definition of the ensemble-averaged free surface elevation is arbitrary, and, we assume $\langle \eta \rangle$ is sufficiently smooth to be considered as a single-valued mean air-water interface as defined in [Brocchini & Peregrine \(2001, figure 1\)](#). Using chain differentiation rule gives

$$\frac{\partial \psi}{\partial t^*} = \frac{\partial \psi}{\partial t} + \frac{\partial \psi}{\partial \sigma} \sigma_{t^*}, \quad \frac{\partial \psi}{\partial x_j^*} = \frac{\partial \psi}{\partial x_j} \lambda_j + \frac{\partial \psi}{\partial \sigma} \sigma_{x_j^*}, \quad (4.9)$$

where $\lambda_j = 1 - \delta_{3j}$, $\partial()/\partial t^* = ()_{t^*}$, $\partial()/\partial x_j^* = ()_{x_j^*}$, and

$$\begin{aligned}\sigma_{t^*} &= \frac{1}{D} (d_t - \sigma D_t), & \sigma_{x_j^*} &= \frac{1}{D} \left\{ (d_{x_j} - \sigma D_{x_j}) \lambda_j + \delta_{3j} \right\} \\ \frac{\partial \sigma_{t^*}}{\partial \sigma} &= -\frac{D_t}{D}, & \frac{\partial \sigma_{x_j^*}}{\partial \sigma} &= -\frac{D_{x_j}}{D} \lambda_j.\end{aligned}\quad (4.10)$$

where hereafter summation inside expressions involving λ_j is not implied. Each term of (4.6) and (4.7) is transformed into the σ -coordinate system by multiplying by D and using (4.9) and (4.10) as

$$\begin{aligned}D \frac{\partial \psi}{\partial x_j^*} &= D \frac{\partial \psi}{\partial x_j} \lambda_j + D \frac{\partial \psi}{\partial \sigma} \sigma_{x_j^*} \\ &= \frac{\partial D \psi}{\partial x_j} \lambda_j + \left(-\frac{D_{x_j}}{D} \lambda_j \right) D \psi + \left(\sigma_{x_j^*} \right) \frac{\partial D \psi}{\partial \sigma} \\ &= \frac{\partial D \psi}{\partial x_j} \lambda_j + \frac{\partial \sigma_{x_j^*} D \psi}{\partial \sigma}.\end{aligned}\quad (4.11)$$

Multiplying (4.7) by D and using (4.11), the momentum equation in conservative form can be written as

$$\begin{aligned}\frac{\partial D u_i^m}{\partial t} + \frac{\partial D u_i^m u_j^m}{\partial x_j} \lambda_j + \frac{\partial}{\partial \sigma} \left(D [\sigma_{t^*} + \sigma_{x_j^*} u_j^m] u_i^m \right) &= \\ \frac{1}{\rho_0} \frac{\partial D [\mathcal{S}_{ij}^s + \mathcal{S}_{ij}^d]}{\partial x_j} \lambda_j + \frac{1}{\rho_0} \frac{\partial}{\partial \sigma} \left(D \sigma_{x_j^*} [\mathcal{S}_{ij}^s + \mathcal{S}_{ij}^d] \right) + D \frac{\rho^m}{\rho_0} g_i \delta_{i3},\end{aligned}\quad (4.12)$$

where the total ensemble-averaged mixture stress tensor, $\mathcal{S}_{ij}^m = \mathcal{S}_{ij}^d + \mathcal{S}_{ij}^s$, is written as a combination of the static stress due to the hydrostatic pressure \mathcal{S}_{ij}^s , and the dynamic stress due to the fluid motion \mathcal{S}_{ij}^d , given by

$$\begin{aligned}\mathcal{S}_{ij}^s &= -p^s \delta_{ij} \\ \mathcal{S}_{ij}^d &= \mathcal{S}_{ij}^m - \mathcal{S}_{ij}^s = -\left(p^d + \frac{1}{3} T_{kk}^m \right) \delta_{ij} + 2\rho_0 (\nu_{eff})_j e_{ij}^m,\end{aligned}\quad (4.13)$$

where $(\nu_{eff})_n = \nu^m + (\nu_t^m)_n$, $n = 1, 2, 3$. Here, the total mixture pressure is divided

into the dynamic pressure $p^d = p^m - p^h$, and the hydrostatic pressure given by

$$\frac{\partial p^h}{\partial \sigma} = -D\rho^m g, \quad (4.14)$$

where $g_3 = -g$ and, thus,

$$\begin{aligned} p^h &= gD \int_{\sigma}^1 [\rho_0 + (\rho^m - \rho_0) d\sigma] + p^h \Big|_{\sigma=1} \\ &= \rho_0 g D (1 - \sigma) + p_{bar}^h + p^h \Big|_{\sigma=1}, \end{aligned} \quad (4.15)$$

where $p_{bar}^h = gD \int_{\sigma}^1 (\rho^m - \rho_0) d\sigma$ is the hydrostatic baroclinic pressure due to the non-constant density field, and $p^h \Big|_{\sigma=1}$ is the hydrostatic pressure at the free surface.

We want to make sure that, in a case of no fluid motion, the source terms due to \mathcal{S}_{ij}^s in the horizontal directions are zero, producing no artificial motions. To obtain an appropriate form of (4.12) to satisfy this property, typically referred as the ‘‘well-balanced’’ form of the momentum equation (Rogers et al. 2003), the right hand-side terms due to \mathcal{S}_{ij}^s can be rewritten as

$$\begin{aligned} \frac{1}{\rho_0} \frac{\partial D \mathcal{S}_{ij}^s}{\partial x_j} \lambda_j &= \left\{ -\frac{1}{\rho_0} \frac{\partial D p_{bar}^h}{\partial x_j} - \frac{D}{\rho_0} \left(\frac{\partial p^h}{\partial x_j} \Big|_{\sigma=1} + \rho_0 g (1 - \sigma) D_{x_j} \right) \right. \\ &\quad \left. - \frac{D_{x_j}}{\rho_0} \left(p^h \Big|_{\sigma=1} + \rho_0 g D (1 - \sigma) \right) \right\} \lambda_j \delta_{ij} \\ \frac{1}{\rho_0} \frac{\partial}{\partial \sigma} \left(D \sigma_{x_j}^* \mathcal{S}_{ij}^s \right) &= -D \frac{\rho^m}{\rho_0} g_i \delta_{i3} - \frac{1}{\rho_0} \frac{\partial D p_{bar}^h \sigma_{x_j}^*}{\partial \sigma} \lambda_j \delta_{ij} \\ &\quad + \left\{ \frac{D_{x_j}}{\rho_0} \left(p^h \Big|_{\sigma=1} + \rho_0 g D (1 - \sigma) \right) \right. \\ &\quad \left. + \frac{d_{x_j} - \sigma D_{x_j}}{\rho_0} \rho_0 g D \right\} \lambda_j \delta_{ij}. \end{aligned} \quad (4.16)$$

Thus the summation of the hydrostatic terms and the body force becomes

$$\begin{aligned} \frac{1}{\rho_0} \left\{ \frac{\partial D \mathcal{S}_{ij}^s}{\partial x_j} \lambda_j + \frac{\partial D \sigma_{x_j^*} \mathcal{S}_{ij}^s}{\partial \sigma} \right\} + D \frac{\rho^m}{\rho_0} g_i \delta_{i3} = -\frac{1}{\rho_0} \left\{ \frac{\partial D p_{bar}^h}{\partial x_i} + \frac{\partial D p_{bar}^h \sigma_{x_i^*}}{\partial \sigma} \right\} \lambda_i \\ \left\{ -\frac{D}{\rho_0} \frac{\partial p^h}{\partial x_i} \Big|_{\sigma=1} + g \langle \eta \rangle d_{x_i} \right\} \lambda_i - \frac{\partial}{\partial x_j} \left(g d \langle \eta \rangle + g \langle \eta^2 \rangle / 2 \right) \lambda_j \delta_{ij}. \end{aligned} \quad (4.17)$$

Keeping the first two terms as source terms, the conservative well-balanced form of the momentum equation in the σ -coordinate system reads as

$$\begin{aligned} \frac{\partial U_i}{\partial t} + \frac{\partial}{\partial x_j} \left(U_i U_j / D + [g d \langle \eta \rangle + g \langle \eta \rangle^2 / 2] \delta_{ij} \right) \lambda_j + \frac{\partial U_i \Omega / D}{\partial \sigma} = \\ -\frac{1}{\rho_0} \left\{ D \frac{\partial p^h}{\partial x_i} \Big|_{\sigma=1} - \rho_0 g \langle \eta \rangle d_{x_i} \right\} \lambda_i \quad (\text{barotropic pressure terms}) \\ -\frac{1}{\rho_0} \left\{ \frac{\partial \mathcal{P}_{bar}}{\partial x_i} + \frac{\partial \sigma_{x_i^*} \mathcal{P}_{bar}}{\partial \sigma} \right\} \lambda_j \quad (\text{baroclinic pressure terms}) \\ -\frac{1}{\rho_0} \left\{ \frac{\partial \mathcal{P}}{\partial x_i} \lambda_i + \frac{\partial \sigma_{x_i^*} \mathcal{P}}{\partial \sigma} \right\} \quad (\text{dynamic pressure terms}) \\ + \frac{\partial 2(\nu_{eff})_j \mathcal{E}_{ij}}{\partial x_j} \lambda_j + \frac{\partial 2\sigma_{x_j^*} (\nu_{eff})_j \mathcal{E}_{ij}}{\partial \sigma} \quad (\text{diffusion terms}), \end{aligned} \quad (4.18)$$

where

$$\begin{aligned} U_i &= D u_i^m \\ \Omega &= D \left(\sigma_{t^*} + \sigma_{x_j^*} u_j^m \right) = D \sigma_{t^*} + \sigma_{x_j^*} U_j \\ \mathcal{P}_{bar} &= D p_{bar}^h \\ \mathcal{P} &= D \left(p^d + \frac{1}{3} \tau_{kk}^m \right) = D \left(p^d + \frac{2}{3} \rho_0 k \right) \\ \mathcal{E}_{ij} &= D e_{ij}^m = \frac{1}{2} \left\{ \frac{\partial U_i}{\partial x_j} \lambda_j + \frac{\partial U_j}{\partial x_i} \lambda_i + \frac{\partial}{\partial \sigma} \left(\sigma_{x_j^*} U_i + \sigma_{x_i^*} U_j \right) \right\}. \end{aligned} \quad (4.19)$$

and k is the ensemble-averaged turbulent kinetic energy.

Multiplying (4.6) by D and using (4.11), we have

$$D \frac{\partial u_j^m}{\partial x_j^*} = \frac{\partial U_j}{\partial x_j} \lambda_j + \frac{\partial \sigma_{x_j^*} U_j}{\partial \sigma} = \frac{\partial U_j}{\partial x_j} \lambda_j + \frac{\partial (\Omega - D \sigma_{t^*})}{\partial \sigma} \quad (4.20)$$

Using (4.10), the continuity equation in the σ coordinates can be written as

$$\frac{\partial D}{\partial t} + \frac{\partial U}{\partial x} + \frac{\partial V}{\partial y} + \frac{\partial \Omega}{\partial \sigma} = 0 \quad (4.21)$$

Assuming a dilute suspension regime (void fractions less than 0.1) and particles with a small Stokes number (less than 0.2), the velocity of the dispersed phases, then, are obtained by simply adding their settling/rising velocity to the liquid phase velocity (see Balachandar & Eaton 2010, for more details). The dispersed phase void fractions are obtained from the scalar transport equation as given in the following.

4.3.2 Scalar Transport Equation

The scalar transport equation for a ensemble-averaged passive scalar, $\langle c \rangle$, in Cartesian coordinates reads as

$$\frac{\partial \langle c \rangle}{\partial t^*} + \frac{\partial}{\partial x_j^*} \left([u_j^m + w_c \delta_{3j}] \langle c \rangle \right) = \frac{\partial}{\partial x_j^*} \left(\nu_j \frac{\partial \langle c \rangle}{\partial x_j^*} \right) + \Gamma_{\langle c \rangle}, \quad (4.22)$$

where $\nu_n = \nu^m + (\nu_t^m / \sigma_{\langle c \rangle})_n$, and $\sigma_{\langle c \rangle}$ is the corresponding Schmidt number. Here, $\Gamma_{\langle c \rangle}$ represents the associated source/sink terms for $\langle c \rangle$, and w_c is a settling or rising velocity of $\langle c \rangle$, equal to zero for a neutrally buoyant quantity. Doing the same procedure as we did for the transformation of the momentum equation, i.e., multiplying (4.22) by D and using (4.11), the conservative form of the scalar transport equation in the σ -coordinate system can be written as

$$\begin{aligned} \frac{\partial \mathcal{C}}{\partial t} + \frac{\partial \mathcal{C} U_j / D}{\partial x_j} \lambda_j + \frac{\partial}{\partial \sigma} \left(\mathcal{C} [\Omega / D + \sigma_{x_j^*} w_c \delta_{3j}] \right) = \\ + \frac{\partial \nu_j \mathcal{D}_j}{\partial x_j} \lambda_j + \frac{\partial \sigma_{x_j^*} \nu_j \mathcal{D}_j}{\partial \sigma} + D \Gamma_{\langle c \rangle}. \end{aligned} \quad (4.23)$$

where

$$\begin{aligned}\mathcal{C} &= D\langle c \rangle \\ \mathcal{D}_j &= \frac{\partial \mathcal{C}}{\partial x_j} \lambda_j + \frac{\partial \sigma_{x_j^*} \mathcal{C}}{\partial \sigma}.\end{aligned}\tag{4.24}$$

In the case of negligibly small surface and bottom slopes ($\nabla_h d$ and $\nabla_h \langle \eta \rangle \approx 0$), equation (4.23) simplifies to those given in [Ma, Kirby & Shi \(2013\)](#), [Ma, Chou & Shi \(2014\)](#).

4.3.3 Turbulence Model

An appropriate turbulence model is needed to estimate ν_t^m as well as to provide the bulk turbulence statistics such as the ensemble-averaged turbulent kinetic energy and dissipation rate. In many numerical approaches, depending on the grid size in the vertical and horizontal directions, the corresponding eddy viscosity for the vertical, $\nu_t^v = (\nu_t^m)_3$, and horizontal, $\nu_t^h = (\nu_t^m)_{1,2}$, directions may not be of the same order. Here, we assume the more physically reasonable formulation $\nu_t^m = \nu_t^v = \nu_t^h$.

The Smagorinsky subgrid and $k - \epsilon$ models are commonly used turbulence models, depending on the grid resolution. The constant Smagorinsky model reads as

$$\nu_t^m = \frac{(c_s \Delta)^2}{D} \sqrt{2 \mathcal{E}_{ij} \mathcal{E}_{ij}},\tag{4.25}$$

where Δ is the length scale on the order of the grid size, and $c_s \sim 0.1 - 0.2$ is the only input parameter. Having relatively larger grid sizes, which is usually the case in non-hydrostatic modeling using a few vertical levels, a $k - \epsilon$ turbulence model is more appropriate to estimating ν_t^m as below

$$\nu_t^m = c_\mu \frac{k^2}{\epsilon} = c_\mu \frac{\mathcal{K}^2}{D \mathcal{E}},\tag{4.26}$$

where c_μ is an empirical coefficient, k is the ensemble-averaged turbulent kinetic energy, and ϵ is the ensemble-averaged turbulent dissipation rate. To obtain $\mathcal{K} = Dk$ and

$\mathcal{E} = D\epsilon$, their transport equations need to be solved. Using (4.23) and replacing \mathcal{C} by \mathcal{K} and \mathcal{E} , we can write

$$\begin{aligned} \frac{\partial \mathcal{K}}{\partial t} + \frac{\partial \mathcal{K}U_j/D}{\partial x_j} \lambda_j + \frac{\partial \mathcal{K}\Omega/D}{\partial \sigma} &= \frac{\partial}{\partial x_j} \left(\nu^{\mathcal{K}} \left[\frac{\partial \mathcal{K}}{\partial x_j} \lambda_j + \frac{\partial \sigma_{x_j^*} \mathcal{K}}{\partial \sigma} \right] \right) \lambda_j \\ &+ \frac{\partial}{\partial \sigma} \left(\nu^{\mathcal{K}} \sigma_{x_j^*} \left[\frac{\partial \mathcal{K}}{\partial x_j} \lambda_j + \frac{\partial \sigma_{x_j^*} \mathcal{K}}{\partial \sigma} \right] \right) + \mathcal{P}_s + \mathcal{P}_\rho - \mathcal{E}, \end{aligned} \quad (4.27)$$

and

$$\begin{aligned} \frac{\partial \mathcal{E}}{\partial t} + \frac{\partial \mathcal{E}U_j/D}{\partial x_j} \lambda_j + \frac{\partial \mathcal{E}\Omega/D}{\partial \sigma} &= \frac{\partial}{\partial x_j} \left(\nu^{\mathcal{E}} \left[\frac{\partial \mathcal{E}}{\partial x_j} \lambda_j + \frac{\partial \sigma_{x_j^*} \mathcal{E}}{\partial \sigma} \right] \right) \lambda_j \\ &+ \frac{\partial}{\partial \sigma} \left(\nu^{\mathcal{E}} \sigma_{x_j^*} \left[\frac{\partial \mathcal{E}}{\partial x_j} \lambda_j + \frac{\partial \sigma_{x_j^*} \mathcal{E}}{\partial \sigma} \right] \right) + \frac{\mathcal{E}}{\mathcal{K}} [c_{1\mathcal{E}}(\mathcal{P}_s + c_{3\mathcal{E}}\mathcal{P}_\rho) - c_{2\mathcal{E}}\mathcal{E}], \end{aligned} \quad (4.28)$$

where $\nu^{\mathcal{K}} = \nu + \nu_t/\sigma_{\mathcal{K}}$, $\nu^{\mathcal{E}} = \nu + \nu_t/\sigma_{\mathcal{E}}$, and $c_{3\mathcal{E}} = 0$ as in [Ma, Kirby & Shi \(2013\)](#). In the standard $k - \epsilon$ model ([Rodi 1980](#)) we have,

$$c_\mu = 0.09, \quad c_{1\mathcal{E}} = 1.44, \quad c_{2\mathcal{E}} = 1.92, \quad \sigma_{\mathcal{K}} = 1.0, \quad \sigma_{\mathcal{E}} = 1.3. \quad (4.29)$$

Using the RNG approach with scale expansions for the Reynolds stress and production of dissipation terms, [Yakhot et al. \(1992\)](#) derived a dynamic procedure to determine $c_{2\mathcal{E}}$ as

$$c_{2\mathcal{E}} = 1.68 + \frac{c_\mu \zeta^3 (1 - \zeta/4.38)}{1 + 0.012\zeta^3}, \quad (4.30)$$

where $\zeta = \frac{\mathcal{K}}{D\mathcal{E}} \sqrt{2\mathcal{E}_{ij}\mathcal{E}_{ij}}$ is the ratio of the turbulent and mean strain time scales. The rest of the closure coefficients are given by

$$c_\mu = 0.085, \quad c_{1\mathcal{E}} = 1.42, \quad \sigma_{\mathcal{K}} = 0.72, \quad \sigma_{\mathcal{E}} = 0.72. \quad (4.31)$$

Finally, the rate of shear, \mathcal{P}_s , and buoyancy, \mathcal{P}_ρ , production rates are given by

$$\mathcal{P}_s = -\tau_{ij}^m \left[\frac{\partial U_i}{\partial x_j} \lambda_j + \frac{\partial \sigma_{x_j^*} U_i}{\partial \sigma} \right], \quad \mathcal{P}_\rho = c_\mu \frac{\mathcal{K}^2}{D\mathcal{E}} \frac{g}{\rho_0} \frac{\partial \rho_m}{\partial \sigma} \quad (4.32)$$

where the Reynolds stress τ_{ij}^m may be estimated using a linear model given by (4.5) or a nonlinear model, (Lin & Liu 1998, Ma, Kirby & Shi 2013), given by

$$\begin{aligned} \frac{\tau_{ij}^m}{\rho^m} = & -2C_d \frac{\mathcal{K}^2}{D^2 \mathcal{E}} \mathcal{E}_{ij} + \frac{2\mathcal{K}}{3D} \delta_{ij} \\ & - C_1 \frac{\mathcal{K}^3}{D\mathcal{E}^2} \left(\frac{\partial u_i^m}{\partial x_l^*} \frac{\partial u_l^m}{\partial x_j^*} + \frac{\partial u_j^m}{\partial x_l^*} \frac{\partial u_l^m}{\partial x_i^*} - \frac{2}{3} \frac{\partial u_l^m}{\partial x_k^*} \frac{\partial u_k^m}{\partial x_l^*} \delta_{ij} \right) \\ & - C_2 \frac{\mathcal{K}^3}{D\mathcal{E}^2} \left(\frac{\partial u_i^m}{\partial x_k^*} \frac{\partial u_j^m}{\partial x_k^*} - \frac{1}{3} \frac{\partial u_l^m}{\partial x_k^*} \frac{\partial u_l^m}{\partial x_k^*} \delta_{ij} \right) \\ & - C_3 \frac{\mathcal{K}^3}{D\mathcal{E}^2} \left(\frac{\partial u_k^m}{\partial x_i^*} \frac{\partial u_k^m}{\partial x_j^*} - \frac{1}{3} \frac{\partial u_l^m}{\partial x_k^*} \frac{\partial u_l^m}{\partial x_k^*} \delta_{ij} \right) \end{aligned} \quad (4.33)$$

C_d , C_1 , C_2 and C_3 are empirical coefficients as given by Lin & Liu (1998)

$$\begin{aligned} C_d = \frac{2}{3} \left(\frac{1}{7.4 + 2S_{max}} \right), \quad C_1 = \frac{1}{185.2 + 3D_{max}^2} \\ C_2 = -\frac{1}{58.5 + 2D_{max}^2}, \quad C_3 = \frac{1}{370.4 + 3D_{max}^2} \end{aligned} \quad (4.34)$$

where

$$\begin{aligned} S_{max} = \frac{\mathcal{K}}{\mathcal{E}} \max \left\{ \left| \frac{\partial u_i^m}{\partial x_i^*} \right| \right\} \text{ (indices not summed)} \\ D_{max} = \frac{\mathcal{K}}{\mathcal{E}} \max \left\{ \left| \frac{\partial u_i^m}{\partial x_j^*} \right| \right\} \end{aligned} \quad (4.35)$$

The above coefficients ensure the non-negativity of turbulent kinetic energy and bounded Reynolds stress.

Additional source terms for both of \mathcal{K} and \mathcal{E} equations may be considered to account for bubble-induced turbulent and/or dissipation, as discussed in Ma et al. (2011).

4.4 Surface and Bottom Boundary Conditions

The free surface and the bottom may be expressed as $F = z^* - \xi = 0$ where $\xi = \langle \eta \rangle$ at the free surface ($\sigma = 1$), and $\xi = -d$ at the bottom ($\sigma = 0$). We define the local coordinate system $(\mathbf{x}'_1, \mathbf{x}'_2, \mathbf{x}'_3)$, such that \mathbf{x}'_3 is the normal to $F = 0$ pointing outward, given by

$$\mathbf{x}'_3 = \frac{\nabla F}{|F|} = \frac{1}{A}(-\xi_{x_1^*}, -\xi_{x_2^*}, 1) = \frac{1}{A}(-\xi_x, -\xi_y, 1), \quad (4.36)$$

where $A = |F| = \sqrt{1 + \xi_x^2 + \xi_y^2}$. The other two unit vectors can be any orthogonal pair of vectors ($\mathbf{x}'_1 \cdot \mathbf{x}'_2 = 0$) in the plane tangent to the $F = 0$ surface. Here, we choose

$$\begin{aligned} \mathbf{x}'_1 &= \frac{1}{B}(1, 0, \xi_x), & B &= \sqrt{1 + \xi_x^2} \\ \mathbf{x}'_2 &= \mathbf{x}'_3 \times \mathbf{x}'_1 = \frac{1}{AB}(-\xi_x \xi_y, 1 + \xi_x^2, \xi_y) \end{aligned} \quad (4.37)$$

The transformation of any vector, $\boldsymbol{\varphi}$, in the Cartesian coordinates into the local coordinates, $\boldsymbol{\varphi}'$, on $F = 0$ is given by

$$\varphi'_j = \mathbf{C}_{ij} \varphi_i, \quad \mathbf{C} = \begin{bmatrix} \frac{1}{B} & \frac{-\xi_x \xi_y}{AB} & \frac{-\xi_x}{A} \\ 0 & \frac{1 + \xi_x^2}{AB} & \frac{-\xi_y}{A} \\ \frac{\xi_x}{B} & \frac{\xi_y}{AB} & \frac{1}{A} \end{bmatrix}, \quad (4.38)$$

where \mathbf{C}_{ij} is the cosine of the angle between the \mathbf{x}^*_i and \mathbf{x}'_j axes. In addition, the transformation of any tensor in Cartesian coordinates into the local coordinates on $F = 0$ is given by

$$\varphi'_{mn} = \mathbf{C}_{im} \mathbf{C}_{jn} \varphi_{ij}. \quad (4.39)$$

4.4.1 Kinematic Boundary Conditions

Assuming no mass flux at the interface, a particle initially on the interface will remain on the interface in which we can write $DF/Dt^* = \partial F/\partial t^* + \langle u_j^m \rangle \partial F/\partial x_j^* = 0$.

Thus, the kinematic surface and bottom boundary conditions in the σ coordinates are simply written as

$$W\Big|_{\sigma=0,1} = D\xi_t + \xi_x U\Big|_{\sigma=0,1} + \xi_y V\Big|_{\sigma=0,1} \quad (4.40)$$

where $\xi = \langle \eta \rangle$ at the free surface ($\sigma = 1$), and $\xi = -d$ at the bottom ($\sigma = 0$). Because $\sigma_{t^*}\Big|_{\sigma=0,1} = -\xi_t/D$, $\sigma_{x_1^*}\Big|_{\sigma=0,1} = -\xi_x/D$, and $\sigma_{x_2^*}\Big|_{\sigma=0,1} = -\xi_y/D$, we have

$$\begin{aligned} \Omega\Big|_{\sigma=0,1} &= D\sigma_{t^*}\Big|_{\sigma=0,1} + \sigma_{x_j^*}\Big|_{\sigma=0,1} U_j\Big|_{\sigma=0,1} \\ &= -\xi_t - \frac{\xi_x}{D} U\Big|_{\sigma=0,1} - \frac{\xi_y}{D} V\Big|_{\sigma=0,1} + \frac{1}{D} W\Big|_{\sigma=0,1} \\ &= 0 \\ \frac{\partial \Omega}{\partial \sigma}\Big|_{\sigma=0,1} &= -\frac{\xi_x}{D} \frac{\partial U}{\partial \sigma}\Big|_{\sigma=0,1} - \frac{\xi_y}{D} \frac{\partial V}{\partial \sigma}\Big|_{\sigma=0,1} + \frac{1}{D} \frac{\partial W}{\partial \sigma}\Big|_{\sigma=0,1} \\ &= 0. \end{aligned} \quad (4.41)$$

meaning that in the σ coordinates, the surface and bottom vertical velocity as well as vertical acceleration are always zero.

4.4.2 Tangential Stress Boundary Conditions

Using (4.39), the transformed total stress on $F = 0$ is given by

$$\mathcal{S}'_{3i}\Big|_{\sigma=0,1} = \mathbf{C}_{ji} \left(-\frac{\xi_x}{A} \mathcal{S}_{1j} - \frac{\xi_y}{A} \mathcal{S}_{2j} + \frac{1}{A} \mathcal{S}_{3j} \right)\Big|_{\sigma=0,1}, \quad (4.42)$$

where $\mathcal{S}_{ij} = \mathcal{S}^p \delta_{ij} + \mathcal{S}_{ij}^v$ is the total mixture stress including the pressure, $\mathcal{S}^p = -(p^h + \mathcal{P}/D)$, and viscous stress $\mathcal{S}_{ij}^v = 2\rho_0(\nu_{eff})_j(\mathcal{E}_{ij}/D)$ contributions. Thus, the

components of the total stress tensor $(\mathcal{S}'_{31}, \mathcal{S}'_{32}, \mathcal{S}'_{33})$ on $F = 0$ are given by

$$\begin{aligned}
\mathcal{S}'_{31}\Big|_{\sigma=0,1} &= \frac{1}{AB} \left\{ -\xi_x [\mathcal{S}_{11} - \mathcal{S}_{33}] + [1 - \xi_x^2] \mathcal{S}_{13} - \xi_y [\mathcal{S}_{12} + \xi_x \mathcal{S}_{23}] \right\}_{\sigma=0,1} \\
\mathcal{S}'_{32}\Big|_{\sigma=0,1} &= \frac{1}{A^2 B} \left\{ \xi_y [\xi_x^2 \mathcal{S}_{11} - (1 + \xi_x^2) \mathcal{S}_{22} + \mathcal{S}_{33}] + [1 + \xi_x^2 - \xi_y^2] \mathcal{S}_{23} \right. \\
&\quad \left. - \xi_x [(1 + \xi_x^2 - \xi_y^2) \mathcal{S}_{12} + 2\xi_y \mathcal{S}_{13}] \right\}_{\sigma=0,1} \\
&= -\frac{\xi_x \xi_y}{A} \mathcal{S}'_{31}\Big|_{\sigma=0,1} + \frac{B}{A^2} \left\{ -\xi_y [\mathcal{S}_{22} - \mathcal{S}_{33}] + [1 - \xi_y^2] \mathcal{S}_{23} \right. \\
&\quad \left. - \xi_x [\mathcal{S}_{12} + \xi_y \mathcal{S}_{13}] \right\}_{\sigma=0,1} \\
\mathcal{S}'_{33}\Big|_{\sigma=0,1} &= \frac{1}{A^2} \left\{ \xi_x^2 \mathcal{S}_{11} + \xi_y^2 \mathcal{S}_{22} + \mathcal{S}_{33} + 2\xi_x \xi_y \mathcal{S}_{12} - 2\xi_x \mathcal{S}_{13} - 2\xi_y \mathcal{S}_{23} \right\}_{\sigma=0,1}.
\end{aligned} \tag{4.43}$$

The coefficients of the normal stress components sum to zero in $\mathcal{S}'_{31}\Big|_{\sigma=0,1}$ and $\mathcal{S}'_{32}\Big|_{\sigma=0,1}$ and, thus, there are no pressure contribution in the tangential stresses on $F = 0$. We remark that, the apparent lack of symmetry in $\mathcal{S}'_{31}\Big|_{\sigma=0,1}$ and $\mathcal{S}'_{32}\Big|_{\sigma=0,1}$ is because of our arbitrary choice of $\mathbf{x}'_1, \mathbf{x}'_2$ in the local coordinate system. However, the corresponding equations for the continuity of the tangential stress in the global Cartesian coordinate, e.g., (4.45) and (4.49) for $\sigma = 1$, are completely symmetric.

If the state of stress in the external media is available, the continuity of the tangential stress on $F = 0$ reads as

$$\mathcal{S}'_{31}\Big|_{\sigma=0,1} = \mathcal{S}'_{31}{}^{ext}\Big|_{\sigma=0,1}, \quad \mathcal{S}'_{32}\Big|_{\sigma=0,1} = \mathcal{S}'_{32}{}^{ext}\Big|_{\sigma=0,1}, \tag{4.44}$$

where $\mathcal{S}'_{3i}{}^{ext}\Big|_{\sigma=0,1}$ is the external stress on $F = 0$ in the i direction, e.g., the wind stress parallel to the free surface or the bottom shear stress, where $(\)'$ represent the local coordinate system given by (4.36). However, if the external media is assumed to be rigid, $\mathcal{S}'_{3i}{}^{ext}\Big|_{\sigma=0,1}$ is replaced by the estimated shear stress near the rigid boundary.

Multiplying (4.44) by D and using (4.43), and assuming the same turbulent

eddy viscosity in all directions, $(\nu_{eff})_n = \nu_{eff}$, $(n = 1, 2, 3)$ on $F = 0$, we obtain

$$\begin{aligned} -\xi_x [\mathcal{E}_{11} - \mathcal{E}_{33}] + [1 - \xi_x^2] \mathcal{E}_{13} - \xi_y [\mathcal{E}_{12} + \xi_x \mathcal{E}_{23}] &= \frac{AD}{2\rho_0 \nu_{eff}} \mathcal{F}_1^{ext} \Big|_{\sigma=0,1} \\ -\xi_y [\mathcal{E}_{22} - \mathcal{E}_{33}] + [1 - \xi_y^2] \mathcal{E}_{23} - \xi_x [\mathcal{E}_{12} + \xi_y \mathcal{E}_{13}] &= \frac{AD}{2\rho_0 \nu_{eff}} \mathcal{F}_2^{ext} \Big|_{\sigma=0,1}, \end{aligned} \quad (4.45)$$

where

$$\begin{aligned} \mathcal{F}_1^{ext} &= B \mathcal{J}'_{31}{}^{ext} \\ \mathcal{F}_2^{ext} &= \frac{\xi_x \xi_y}{B} \mathcal{J}'_{31}{}^{ext} + \frac{A}{B} \mathcal{J}'_{32}{}^{ext}. \end{aligned} \quad (4.46)$$

Rearranging (4.45), the condition of continuity of the tangential stress on $F = 0$ finally gives

$$\begin{aligned} \frac{\partial U}{\partial \sigma} \Big|_{\sigma=0,1} &= \frac{D^2}{A\rho_0 \nu_{eff}} \mathcal{F}_1^{ext} \Big|_{\sigma=0,1} - \xi_x \frac{\partial W}{\partial \sigma} \Big|_{\sigma=0,1} \\ &+ \frac{D}{A^2} \left\{ 2\xi_x (U)_x - [1 - \xi_x^2] (W)_x + \xi_y [(U)_y + (V)_x + \xi_x (W)_y] \right\}_{\sigma=0,1} \\ \frac{\partial V}{\partial \sigma} \Big|_{\sigma=0,1} &= \frac{D^2}{A\rho_0 \nu_{eff}} \mathcal{F}_2^{ext} \Big|_{\sigma=0,1} - \xi_y \frac{\partial W}{\partial \sigma} \Big|_{\sigma=0,1} \\ &+ \frac{D}{A^2} \left\{ 2\xi_y (V)_y - [1 - \xi_y^2] (W)_y + \xi_x [(V)_x + (U)_y + \xi_y (W)_x] \right\}_{\sigma=0,1}, \end{aligned} \quad (4.47)$$

where

$$\begin{aligned} (U_i)_x &= \partial U_i / \partial x - U_i D_x / D = D \frac{\partial u_i^m}{\partial x} \\ (U_i)_y &= \partial U_i / \partial y - U_i D_y / D = D \frac{\partial u_i^m}{\partial y}. \end{aligned} \quad (4.48)$$

The tangential stress at $\sigma = 1$, which represents the ensemble-averaged free-surface location, is a combination of the wind-induced shear stress and the Reynolds-type stress in the case of the existence of high turbulence near the free surface such as in the bore-front region (see, for more details, [Brocchini & Peregrine 2001](#), §5). If we

only consider the wind stress and ignore the latter, using (4.43) we have

$$\begin{aligned}\mathcal{F}_1^{ext}\Big|_{\sigma=1} &= \frac{1}{A} \left\{ (1 - \xi_x^2) \tau_{wx} - \xi_x \xi_y \tau_{wy} \right\} \\ \mathcal{F}_2^{ext}\Big|_{\sigma=1} &= \frac{1}{A} \left\{ (1 - \xi_y^2) \tau_{wy} - \xi_x \xi_y \tau_{wx} \right\},\end{aligned}\tag{4.49}$$

where τ_{wx} and τ_{wy} are the wind stresses at the x and y directions, respectively. In the case of negligibly small wind speeds, $\mathcal{F}_1^{ext}\Big|_{\sigma=1} = \mathcal{F}_2^{ext}\Big|_{\sigma=1} = 0$.

At the bottom, the external shear stress parallel to the bottom, or bottom stress, can be estimated from the law of the wall as

$$\mathcal{S}'_{31}{}^{ext}\Big|_{\sigma=0} \approx \rho_0 u_*^2 \frac{U'}{U'_b}, \quad \mathcal{S}'_{32}{}^{ext}\Big|_{\sigma=0} \approx \rho_0 u_*^2 \frac{V'}{U'_b}\tag{4.50}$$

where $U'_b = \sqrt{U'^2 + V'^2}\Big|_{\sigma=\Delta\sigma_1/2}$ is the magnitude of velocity parallel to the bed at the first grid cell above the bed. Using (4.38), U' and V' , the horizontal velocities (velocity times D) parallel to the bed, are given by

$$\begin{aligned}U' &= \mathbf{C}_{j1} U_j = \frac{1}{B} \left(U - d_x W \right) \Big|_{\sigma=\Delta\sigma_1/2} \\ V' &= \mathbf{C}_{j2} U_j = \frac{1}{AB} \left(-d_x d_y U + [1 + d_x^2] V - d_y W \right) \Big|_{\sigma=\Delta\sigma_1/2},\end{aligned}\tag{4.51}$$

and u_* is the friction velocity given by

$$u_* = \frac{\kappa \beta U'_b}{D \ln(z_b/z_0)}\tag{4.52}$$

where $\kappa = 0.41$ is the Van Karman constant, $\beta \leq 1$ represents the stratification effects in the bottom boundary layer. Here, z_b and z_0 are the distances from the bed at which the ensemble-averaged velocities parallel to the bed are assumed to be U'_b/D and zero respectively, depending on the boundary layer characteristics as well as the roughness length-scale, k_s . For a fully rough turbulent boundary layer, it is typically assumed that $z_0 = k_s/30$.

4.4.3 Normal Stress Boundary Condition

If the state of stress in the external media is available, the continuity of the normal stress reads as

$$D\mathcal{S}'_{33}\Big|_{\sigma=0,1} = \left\{ - \left(Dp^h + \mathcal{P} \right) + \frac{2\rho_0\nu_{eff}}{A^2} \left(\xi_x^2 \mathcal{E}_{11} + \xi_y^2 \mathcal{E}_{22} + \mathcal{E}_{33} + 2\xi_x \xi_y \mathcal{E}_{12} - 2\xi_x \mathcal{E}_{13} - 2\xi_y \mathcal{E}_{23} \right) \right\}_{\sigma=0,1} = D\mathcal{S}'_{33}\Big|_{\sigma=0,1}^{ext}. \quad (4.53)$$

where the normal stress in the local coordinate, $\mathcal{S}'_{33}\Big|_{\sigma=0,1}$, is obtained using (4.42). Rearranging (4.53), we have

$$\mathcal{P}\Big|_{\sigma=0,1} = -D \left(p^h\Big|_{\sigma=0,1} + \mathcal{S}'_{33}\Big|_{\sigma=0,1}^{ext} \right) - \frac{\rho_0\nu_{eff}}{A^2} \left\{ 2\xi_x [(W)_x - \xi_x(U)_x] + 2\xi_y [(W)_y - \xi_y(V)_y] - 2\xi_x \xi_y [(U)_y + (V)_x] \right\}_{\sigma=0,1} \quad (4.54)$$

Neglecting viscous stresses in the air side, we have $\mathcal{S}'_{33}\Big|_{\sigma=1}^{ext} = -p_{atm}$ on the free surface. The atmospheric pressure, p_{atm} , can be absorbed in the hydrostatic pressure term as $p^h\Big|_{\sigma=1} = p_{atm}$. Thus, the Dirichlet-type boundary condition for the modified dynamic pressure reads as

$$\mathcal{P}\Big|_{\sigma=1} = -\frac{\rho_0\nu_{eff}\Big|_{\sigma=1}}{A^2} \left\{ 2\xi_x [(W)_x - \xi_x(U)_x] + 2\xi_y [(W)_y - \xi_y(V)_y] - 2\xi_x \xi_y [(U)_y + (V)_x] \right\}_{\sigma=1}. \quad (4.55)$$

At the bottom, however, such a relation can not be applied unless the bottom is a dynamically coupled layer. In the case of a rigid bottom, using the vertical momentum equation we can write

$$\frac{\partial \mathcal{P}}{\partial \sigma}\Big|_{\sigma=0} = -D\rho_0 \left\{ \frac{\partial W}{\partial t} + \frac{\partial WU/D}{\partial x} + \frac{\partial WV/D}{\partial y} + \frac{\partial W\Omega/D}{\partial \sigma} \right\}_{\sigma=0} + D\rho_0 \left\{ \frac{\partial 2(\nu_{eff})_j \mathcal{E}_{3j}}{\partial x_j} \lambda_j + \frac{\partial 2\sigma_{x_j}^* (\nu_{eff})_j \mathcal{E}_{3j}}{\partial \sigma} \right\}_{\sigma=0}. \quad (4.56)$$

Neglecting the Reynolds stress gradients at the bottom and using (4.41), a Neumann-type boundary condition for the modified dynamic pressure at the bottom reads as

$$\frac{\partial \mathcal{P}}{\partial \sigma} \Big|_{\sigma=0} = -D\rho_0 \left\{ \frac{\partial W}{\partial t} + \frac{\partial WU/D}{\partial x} + \frac{\partial WV/D}{\partial y} \right\} \Big|_{\sigma=0}. \quad (4.57)$$

4.4.4 Neumann-type Boundary Condition for a Scalar Quantity

The Neumann boundary condition for a scalar quantity, $\langle c \rangle$, normal to the interface, $F = 0$, may be expressed as

$$\frac{\partial \langle c \rangle}{\partial x'_3} \Big|_{\sigma=0,1} = \langle f \rangle \Big|_{\sigma=0,1}, \quad (4.58)$$

where $\langle f \rangle \Big|_{\sigma=0,1}$ represent the corresponding ensemble-averaged flux of $\langle c \rangle$ across the interface. In the case of $\langle f \rangle \Big|_{\sigma=0,1} = 0$, (4.58) is called a zero-gradient boundary condition for $\langle c \rangle$ on the interface, commonly used for passive scalars such as salinity, the turbulent kinetic energy, and dissipation rate. Multiplying (4.58) by D and using (4.36), we have

$$D \frac{\partial \langle c \rangle}{\partial x'_3} \Big|_{\sigma=0,1} = D(\nabla \langle c \rangle) \Big|_{\sigma=0,1} \cdot \mathbf{x}'_3 = D \frac{\partial \langle c \rangle}{\partial x'_j} \Big|_{\sigma=0,1} x'_{3j} = \mathcal{F} \Big|_{\sigma=0,1}. \quad (4.59)$$

where $\mathcal{F} \Big|_{\sigma=0,1} = D \langle f \rangle \Big|_{\sigma=0,1}$. Using (4.11), the Neumann-type boundary condition for $\mathcal{C} = D \langle c \rangle$ normal to the interface on $F = 0$ can be written as

$$\frac{\partial \mathcal{C}}{\partial \sigma} \Big|_{\sigma=0,1} = \left\{ \frac{D}{A} \mathcal{F} + \frac{D^2}{A^2} \left(\xi_x \frac{\partial \mathcal{C}/D}{\partial x} + \xi_y \frac{\partial \mathcal{C}/D}{\partial y} \right) \right\} \Big|_{\sigma=0,1}, \quad (4.60)$$

As mentioned, $A = \sqrt{1 + \xi_x^2 + \xi_y^2}$, and $\xi = \langle \eta \rangle$ at the free surface ($\sigma = 1$), and $\xi = -d$ at the bottom ($\sigma = 0$).

4.4.5 Boundary Conditions for \mathcal{K} and \mathcal{E}

Here, $\sigma = 1$ represents the ensemble-averaged free-surface location, suggesting that a zero-tangential stress and zero-gradient flux for the turbulent kinetic energy may not be accurate in the bore-front region, due to highly turbulent two-phase air-water mixture (Brocchini & Peregrine 2001, §5). In the present study, however, a zero-gradient boundary condition, $\mathcal{F} = 0$, is imposed for both \mathcal{K} and \mathcal{E} using (4.60).

The Dirichlet-type boundary conditions for both \mathcal{K} and \mathcal{E} is used near the bottom, given by

$$\mathcal{K}_b = D \frac{u_*^2}{\sqrt{c_\mu}}, \quad \mathcal{E}_b = D \frac{u_*^3}{\kappa z_b} \quad (4.61)$$

where κ is the Von Karman constant, z_b is the distance from the bed, and u_* is a friction velocity given by (4.52). Strictly speaking, this is based on the mixing length assumption and the simplified k -equation (turbulence production equals to dissipation) for a steady boundary layer.

4.5 Numerical Method

To solve the momentum equation (4.18), an intermediate velocity field \mathbf{U}^* is first obtained by neglecting the dynamic pressure effects as

$$\frac{\mathbf{U}^* - \mathbf{U}^n}{\Delta t} - \mathbf{S}_{\tau 2}^* = - \left\{ \frac{\partial \mathbf{F}}{\partial x} + \frac{\partial \mathbf{G}}{\partial y} + \frac{\partial \mathbf{H}}{\partial \sigma} \right\}^n + \left\{ \mathbf{S}_{p^h} + \mathbf{S}_{\mathcal{P}_{bar}} + \mathbf{S}_{\tau 1} \right\}^n \quad (4.62)$$

and, then, the dynamic pressure effects are considered as

$$\frac{\mathbf{U}^{n'} - \mathbf{U}^*}{\Delta t} = \mathbf{S}_{\mathcal{P}}^{n'}, \quad (4.63)$$

As in Ma et al. (2012), the two-stage second-order Runge-Kutta scheme is used, in which (4.62) and (4.63) are solved two times at each time step. The final velocity field at the new time level, $n + 1$, is given by

$$\mathbf{U}^{n+1} = \frac{1}{2} \mathbf{U}^n + \frac{1}{2} \mathbf{U}^{n'}, \quad (4.64)$$

where n' and n'' indicate the first and second Runge-Kutta stage. The fluxes, source terms and pressure terms in (4.62) and (4.63) are given by

$$\begin{aligned}
\mathbf{F} &= \begin{pmatrix} \frac{UU}{D} + \frac{1}{2}g\langle\eta\rangle^2 + gd\langle\eta\rangle \\ \frac{UV}{D} \\ \frac{UW}{D} \end{pmatrix} \quad \mathbf{G} = \begin{pmatrix} \frac{UV}{D} \\ \frac{VV}{D} + \frac{1}{2}g\langle\eta\rangle^2 + gd\langle\eta\rangle \\ \frac{VW}{D} \end{pmatrix} \\
\mathbf{H} &= \begin{pmatrix} \frac{U\Omega}{D} \\ \frac{V\Omega}{D} \\ \frac{W\Omega}{D} \end{pmatrix} \quad \mathbf{S}_{ph} = \begin{pmatrix} \frac{-D}{\rho_0} \frac{\partial p_{\sigma=1}^h}{\partial x} + g\langle\eta\rangle \frac{\partial d}{\partial x} \\ \frac{-D}{\rho_0} \frac{\partial p_{\sigma=1}^h}{\partial y} + g\langle\eta\rangle \frac{\partial d}{\partial y} \\ 0 \end{pmatrix} \quad \mathbf{S}_{\tau 1} = \begin{pmatrix} \mathbf{S}_{\tau 1x} \\ \mathbf{S}_{\tau 1y} \\ \mathbf{S}_{\tau 1\sigma} \end{pmatrix} \\
\mathbf{S}_{\tau 2} &= \begin{pmatrix} \frac{\partial}{\partial \sigma} \left(\nu_{eff}^h \left[2\sigma_{x^*} \frac{\partial \sigma_{x^*} U}{\partial \sigma} + \sigma_{y^*} \frac{\partial \sigma_{y^*} U}{\partial \sigma} \right] + \nu_{eff}^v \left[\frac{1}{D^2} \frac{\partial U}{\partial \sigma} \right] \right) \\ \frac{\partial}{\partial \sigma} \left(\nu_{eff}^h \left[\sigma_{x^*} \frac{\partial \sigma_{x^*} V}{\partial \sigma} + 2\sigma_{y^*} \frac{\partial \sigma_{y^*} V}{\partial \sigma} \right] + \nu_{eff}^v \left[\frac{1}{D^2} \frac{\partial V}{\partial \sigma} \right] \right) \\ \frac{\partial}{\partial \sigma} \left(\nu_{eff}^h \left[\sigma_{x^*} \frac{\partial \sigma_{x^*} W}{\partial \sigma} + \sigma_{y^*} \frac{\partial \sigma_{y^*} W}{\partial \sigma} \right] + \nu_{eff}^v \left[\frac{2}{D^2} \frac{\partial W}{\partial \sigma} \right] \right) \end{pmatrix} \\
\mathbf{S}_{\mathcal{P}_{bar}} &= \begin{pmatrix} \frac{-1}{\rho_0} \left(\frac{\partial \mathcal{P}_{bar}}{\partial x} + \frac{\partial \sigma_{x^*} \mathcal{P}_{bar}}{\partial \sigma} \right) \\ \frac{-1}{\rho_0} \left(\frac{\partial \mathcal{P}_{bar}}{\partial y} + \frac{\partial \sigma_{y^*} \mathcal{P}_{bar}}{\partial \sigma} \right) \\ 0 \end{pmatrix} \quad \mathbf{S}_{\mathcal{P}} = \begin{pmatrix} \frac{-1}{\rho_0} \left(\frac{\partial \mathcal{P}}{\partial x} + \frac{\partial \sigma_{x^*} \mathcal{P}}{\partial \sigma} \right) \\ \frac{-1}{\rho_0} \left(\frac{\partial \mathcal{P}}{\partial y} + \frac{\partial \sigma_{y^*} \mathcal{P}}{\partial \sigma} \right) \\ \frac{-1}{\rho_0 D} \frac{\partial \mathcal{P}}{\partial \sigma} \end{pmatrix}
\end{aligned} \tag{4.65}$$

and

$$\begin{aligned}
\mathbf{S}_{\tau 1x} &= \frac{\partial}{\partial x} \left(\nu_{eff}^h \left[2 \frac{\partial U}{\partial x} + 2 \frac{\partial \sigma_{x^*} U}{\partial \sigma} \right] \right) + \frac{\partial}{\partial y} \left(\nu_{eff}^h \left[\frac{\partial U}{\partial y} + \frac{\partial V}{\partial x} + \frac{\partial \sigma_{y^*} U + \sigma_{x^*} V}{\partial \sigma} \right] \right) \\
&\quad + \frac{\partial}{\partial \sigma} \left(\nu_{eff}^h \left[2\sigma_{x^*} \frac{\partial U}{\partial x} + \sigma_{y^*} \left(\frac{\partial U}{\partial y} + \frac{\partial V}{\partial x} + \frac{\partial \sigma_{x^*} V}{\partial \sigma} \right) \right] + \frac{\nu_{eff}^v}{D} \left[\frac{\partial W}{\partial x} + \frac{\partial \sigma_{x^*} W}{\partial \sigma} \right] \right) \\
\mathbf{S}_{\tau 1y} &= \frac{\partial}{\partial y} \left(\nu_{eff}^h \left[2 \frac{\partial V}{\partial y} + 2 \frac{\partial \sigma_{y^*} V}{\partial \sigma} \right] \right) + \frac{\partial}{\partial x} \left(\nu_{eff}^h \left[\frac{\partial V}{\partial x} + \frac{\partial U}{\partial y} + \frac{\partial \sigma_{x^*} V + \sigma_{y^*} U}{\partial \sigma} \right] \right) \\
&\quad + \frac{\partial}{\partial \sigma} \left(\nu_{eff}^h \left[2\sigma_{y^*} \frac{\partial V}{\partial y} + \sigma_{x^*} \left(\frac{\partial V}{\partial x} + \frac{\partial U}{\partial y} + \frac{\partial \sigma_{y^*} U}{\partial \sigma} \right) \right] + \frac{\nu_{eff}^v}{D} \left[\frac{\partial W}{\partial y} + \frac{\partial \sigma_{y^*} W}{\partial \sigma} \right] \right) \\
\mathbf{S}_{\tau 1\sigma} &= \frac{\partial}{\partial x} \left(\nu_{eff}^h \left[\frac{\partial W}{\partial x} + \frac{\partial \sigma_{x^*} W + U/D}{\partial \sigma} \right] \right) + \frac{\partial}{\partial y} \left(\nu_{eff}^h \left[\frac{\partial W}{\partial y} + \frac{\partial \sigma_{y^*} W + V/D}{\partial \sigma} \right] \right) \\
&\quad + \frac{\partial}{\partial \sigma} \left(\nu_{eff}^h \left[\sigma_{x^*} \left[\frac{\partial W}{\partial x} + \frac{1}{D} \frac{\partial U}{\partial \sigma} \right] + \sigma_{y^*} \left(\frac{\partial W}{\partial y} + \frac{1}{D} \frac{\partial V}{\partial \sigma} \right) \right] \right).
\end{aligned} \tag{4.66}$$

In addition, D^* is obtained using the integrated form of (4.21) as,

$$D^* = D - \Delta t \left(\frac{\partial \int_0^1 U d\sigma}{\partial x} + \frac{\partial \int_0^1 V d\sigma}{\partial y} \right). \quad (4.67)$$

The fluxes, \mathbf{F} , \mathbf{G} , \mathbf{H} , in (4.62) are obtained using the second-order shock-capturing Godunov-type Finite-volume scheme using HLLC Reiman solver as described in Ma, Kirby & Shi (2013). The source terms are calculated using centered second-order finite-difference schemes. The 3-point finite-difference approximation for a non-uniform grid (see F for the details) is used for terms with a gradient in the σ direction. Both the fluxes and source terms are obtained using the values at the previous time stage. In §4.1, we present the details of the scheme for calculating hydrostatic velocity field at the intermediate time stage $(\)^*$, following by the implicit non-hydrostatic velocity correction to satisfy divergence free condition for the velocity field in §4.2. In §4.3 the truncation error of different terms are presented.

4.5.1 Hydrostatic Velocity Calculation

There is no horizontal gradient involved in $\mathbf{S}_{\tau 2}^*$, and, thus, by applying (F.11) it can be discretized using $\mathbf{U}_{i,j,k-1}^*$, $\mathbf{U}_{i,j,k}^*$ and $\mathbf{U}_{i,j,k+1}^*$, where $k = 2, \dots, K - 1$, where K is the number of the vertical levels, as

$$\mathbf{A}_k \mathbf{U}_{i,j,k-1}^* + \mathbf{B}_k \mathbf{U}_{i,j,k}^* + \mathbf{C}_k \mathbf{U}_{i,j,k+1}^* = \mathbf{U}_{i,j,k}^n + \Delta t \mathbf{R}_{U^*} \Big|_{i,j,k}^n, \quad (4.68)$$

where

$$\begin{aligned}
\mathbf{A}_k &= -\Delta t \left\{ \frac{\alpha^c}{\Delta\sigma_k} \left(\Gamma_{k+\frac{1}{2}}^{k-1} - \Gamma_{k-\frac{1}{2}}^{k-1} \right) + \frac{\Gamma_{k+\frac{1}{2}}^{k-1} + \Gamma_{k-\frac{1}{2}}^{k-1}}{\Delta\sigma_{k-1}^c (\Delta\sigma_{k-1}^c + \Delta\sigma_k^c)} \right\} \\
\mathbf{B}_k &= 1 - \Delta t \left\{ \frac{\beta^c}{\Delta\sigma_k} \left(\Gamma_{k+\frac{1}{2}}^k - \Gamma_{k-\frac{1}{2}}^k \right) - \frac{\Gamma_{k+\frac{1}{2}}^k + \Gamma_{k-\frac{1}{2}}^k}{\Delta\sigma_{k-1}^c \Delta\sigma_k^c} \right\} \\
\mathbf{C}_k &= -\Delta t \left\{ \frac{\gamma^c}{\Delta\sigma_k} \left(\Gamma_{k+\frac{1}{2}}^{k+1} - \Gamma_{k-\frac{1}{2}}^{k+1} \right) + \frac{\Gamma_{k+\frac{1}{2}}^{k+1} + \Gamma_{k-\frac{1}{2}}^{k+1}}{\Delta\sigma_k^c (\Delta\sigma_{k-1}^c + \Delta\sigma_k^c)} \right\} \\
\mathbf{R}_{\mathbf{U}^*} \Big|_{i,j,k}^n &= - \left\{ \frac{\partial \mathbf{F}}{\partial x} + \frac{\partial \mathbf{G}}{\partial y} + \frac{\partial \mathbf{H}}{\partial \sigma} \right\}_{i,j,k}^n + \left\{ \mathbf{S}_{p^h} + \mathbf{S}_{\mathcal{P}_{bar}} + \mathbf{S}_{\tau 1} \right\}_{i,j,k}^n \\
\Gamma_{\theta}^{\Theta} &= \begin{pmatrix} \nu_{\theta}^h \left\{ 2(\sigma_{x^*})_{\theta}(\sigma_{x^*})_{\Theta} + (\sigma_{y^*})_{\theta}(\sigma_{y^*})_{\Theta} \right\} + \nu_{\theta}^v \frac{1}{D^2} \\ \nu_{\theta}^h \left\{ (\sigma_{x^*})_{\theta}(\sigma_{x^*})_{\Theta} + 2(\sigma_{y^*})_{\theta}(\sigma_{y^*})_{\Theta} \right\} + \nu_{\theta}^v \frac{1}{D^2} \\ \nu_{\theta}^h \left\{ (\sigma_{x^*})_{\theta}(\sigma_{x^*})_{\Theta} + (\sigma_{y^*})_{\theta}(\sigma_{y^*})_{\Theta} \right\} + \nu_{\theta}^v \frac{2}{D^2} \end{pmatrix},
\end{aligned} \tag{4.69}$$

where the horizontal indices of all terms are i, j , and, $\Delta\sigma_{k-1}^c = (\Delta\sigma_k + \Delta\sigma_{k-1})/2$, $\Delta\sigma_k^c = (\Delta\sigma_{k+1} + \Delta\sigma_k)/2$, $\Delta\sigma_{k-1} = \sigma_k - \sigma_{k-1}$, $\Delta\sigma_k = \sigma_{k+1} - \sigma_k$, and

$$\begin{aligned}
\alpha^c &= \frac{-\Delta\sigma_k^c}{\Delta\sigma_{k-1}^c (\Delta\sigma_{k-1}^c + \Delta\sigma_k^c)} \\
\beta^c &= \frac{\Delta\sigma_k^c - \Delta\sigma_{k-1}^c}{\Delta\sigma_{k-1}^c \Delta\sigma_k^c} \\
\gamma^c &= \frac{\Delta\sigma_{k-1}^c}{\Delta\sigma_k^c (\Delta\sigma_{k-1}^c + \Delta\sigma_k^c)}.
\end{aligned} \tag{4.70}$$

For the top layer, $k = K$, we use $\mathbf{U}_{i,j,K-1}^*$, $\mathbf{U}_{i,j,K}^*$ and $\mathbf{U}_{i,j,top}^*$, where the coefficients and right-hand side of (4.57) are given by

$$\begin{aligned}
\mathbf{A}_K &= -\Delta t \left\{ \frac{\frac{3}{2}\mathbf{\Gamma}_{K-\frac{1}{2}}^{k-1}}{\Delta\sigma_{K-1}^c(\Delta\sigma_{K-1}^c + \frac{\Delta\sigma_K}{2})} \right\} \\
\mathbf{B}_K &= 1 - \Delta t \left\{ -\frac{(\frac{3}{2} - \Delta\sigma_{K-1}^c/\Delta\sigma_K)\mathbf{\Gamma}_{K-\frac{1}{2}}^k}{\Delta\sigma_{K-1}^c \frac{\Delta\sigma_K}{2}} \right\} \\
\mathbf{C}_K &= 0 \\
\mathbf{R}_{U^*} \Big|_{i,j,K}^n &= -\left\{ \frac{\partial \mathbf{F}}{\partial x} + \frac{\partial \mathbf{G}}{\partial y} + \frac{\partial \mathbf{H}}{\partial \sigma} \right\}_{i,j,K}^n + \left\{ \mathbf{S}_{p^h} + \mathbf{S}_{\mathcal{P}_{bar}} + \mathbf{S}_{\tau 1} \right\}_{i,j,k}^n + \mathbf{R}_{U^*} \Big|_{i,j,\sigma=1}^n \\
\mathbf{R}_{U^*} \Big|_{i,j,\sigma=1}^n &= \frac{1}{\Delta\sigma_K} \left(\begin{array}{l} \left\{ \nu^h [2\sigma_{x^*}\sigma_{x^*} + \sigma_{y^*}\sigma_{y^*}] + \nu^v \frac{1}{D^2} \right\} \frac{\partial U}{\partial \sigma} - \nu^h \left\{ 2\sigma_{x^*}D_x + \sigma_{y^*}D_y \right\} \frac{U}{D} \\ \left\{ \nu^h [\sigma_{x^*}\sigma_{x^*} + 2\sigma_{y^*}\sigma_{y^*}] + \nu^v \frac{1}{D^2} \right\} \frac{\partial V}{\partial \sigma} - \nu^h \left\{ \sigma_{x^*}D_x + 2\sigma_{y^*}D_y \right\} \frac{V}{D} \\ \left\{ \nu^h [\sigma_{x^*}\sigma_{x^*} + \sigma_{y^*}\sigma_{y^*}] + \nu^v \frac{2}{D^2} \right\} \frac{\partial W}{\partial \sigma} - \nu^h \left\{ \sigma_{x^*}D_x + \sigma_{y^*}D_y \right\} \frac{W}{D} \end{array} \right)_{i,j,\sigma=0}^n \\
&\quad + \left\{ \frac{(\Delta\sigma_K - \Delta\sigma_{K-1}^c)\mathbf{\Gamma}_{K-\frac{1}{2}}^{top}}{\frac{[\Delta\sigma_K]^2}{2}(\Delta\sigma_{K-1}^c + \frac{\Delta\sigma_K}{2})} \right\} \mathbf{U}_{\sigma=1}
\end{aligned} \tag{4.71}$$

and for the bottom layer, $k = 1$, we use $\mathbf{U}_{i,j,bot}^*$, $\mathbf{U}_{i,j,1}^*$ and $\mathbf{U}_{i,j,2}^*$, where the coefficients and right-hand side of (4.57) are given by

$$\begin{aligned}
\mathbf{A}_1 &= 0 \\
\mathbf{B}_1 &= 1 - \Delta t \left\{ -\frac{(\frac{3}{2} - \Delta\sigma_1^c/\Delta\sigma_1)\mathbf{\Gamma}_{1+\frac{1}{2}}^1}{\Delta\sigma_1^c \frac{\Delta\sigma_1}{2}} \right\} \\
\mathbf{C}_1 &= -\Delta t \left\{ \frac{\frac{3}{2}\mathbf{\Gamma}_{1+\frac{1}{2}}^2}{\Delta\sigma_1^c(\Delta\sigma_1^c + \frac{\Delta\sigma_1}{2})} \right\} \\
\mathbf{R}_{U^*} \Big|_{i,j,1}^n &= -\left\{ \frac{\partial \mathbf{F}}{\partial x} + \frac{\partial \mathbf{G}}{\partial y} + \frac{\partial \mathbf{H}}{\partial \sigma} \right\}_{i,j,1}^n + \left\{ \mathbf{S}_{p^h} + \mathbf{S}_{\mathcal{P}_{bar}} + \mathbf{S}_{\tau 1} \right\}_{i,j,k}^n + \mathbf{R}_{U^*} \Big|_{i,j,\sigma=0}^n \\
\mathbf{R}_{U^*} \Big|_{i,j,\sigma=0}^n &= \frac{-1}{\Delta\sigma_1} \left(\begin{array}{l} \left\{ \nu^h [2\sigma_{x^*}\sigma_{x^*} + \sigma_{y^*}\sigma_{y^*}] + \nu^v \frac{1}{D^2} \right\} \frac{\partial U}{\partial \sigma} - \nu^h \left\{ 2\sigma_{x^*}D_x + \sigma_{y^*}D_y \right\} \frac{U}{D} \\ \left\{ \nu^h [\sigma_{x^*}\sigma_{x^*} + 2\sigma_{y^*}\sigma_{y^*}] + \nu^v \frac{1}{D^2} \right\} \frac{\partial V}{\partial \sigma} - \nu^h \left\{ \sigma_{x^*}D_x + 2\sigma_{y^*}D_y \right\} \frac{V}{D} \\ \left\{ \nu^h [\sigma_{x^*}\sigma_{x^*} + \sigma_{y^*}\sigma_{y^*}] + \nu^v \frac{2}{D^2} \right\} \frac{\partial W}{\partial \sigma} - \nu^h \left\{ \sigma_{x^*}D_x + \sigma_{y^*}D_y \right\} \frac{W}{D} \end{array} \right)_{i,j,\sigma=1}^n \\
&\quad + \left\{ \frac{(\Delta\sigma_1 - \Delta\sigma_1^c)\mathbf{\Gamma}_{1+\frac{1}{2}}^{bot}}{\frac{[\Delta\sigma_1]^2}{2}(\Delta\sigma_1^c + \frac{\Delta\sigma_1}{2})} \right\} \mathbf{U}_{\sigma=0}
\end{aligned} \tag{4.72}$$

and then, $\mathbf{U}_{i,j,k}^*$ is obtained (for $k = 1, \dots, K$) using the Thomas algorithm. Finally, the exact boundary conditions described in §3 are used to obtain the velocities at the

ghost cells.

4.5.2 Implicit Non-hydrostatic Velocity Correction

The final velocity field at the first Runge-Kutta stage, $\mathbf{U}^{n'} = \mathbf{U}^* + \Delta t \mathbf{S}_{\mathcal{P}}$, is obtained from the intermediate velocity field, \mathbf{U}^* , using the following form of the continuity equation (4.20),

$$\frac{\partial U^{n'}}{\partial x} + \frac{\partial V^{n'}}{\partial y} + \frac{\partial}{\partial \sigma} \left[\sigma_{x^*} U^{n'} + \sigma_{y^*} V^{n'} + W^{n'} / D^{n'} \right] = 0 \quad (4.73)$$

and replacing $\mathbf{U}^{n'}$ by $\mathbf{S}_{\mathcal{P}}^{n'}$ using (4.63), we have

$$\begin{aligned} & \frac{\partial}{\partial x} \left(\frac{\partial \mathcal{P}^{n'}}{\partial x} + \frac{\partial \sigma_{x^*}^* \mathcal{P}^{n'}}{\partial \sigma} \right) + \frac{\partial}{\partial y} \left(\frac{\partial \mathcal{P}^{n'}}{\partial y} + \frac{\partial \sigma_{y^*}^* \mathcal{P}^{n'}}{\partial \sigma} \right) \\ & + \frac{\partial}{\partial \sigma} \left(\sigma_{x^*}^* \left[\frac{\partial \mathcal{P}^{n'}}{\partial x} + \frac{\partial \sigma_{x^*}^* \mathcal{P}^{n'}}{\partial \sigma} \right] + \sigma_{y^*}^* \left[\frac{\partial \mathcal{P}^{n'}}{\partial y} + \frac{\partial \sigma_{y^*}^* \mathcal{P}^{n'}}{\partial \sigma} \right] + \frac{1}{D^{*2}} \frac{\partial \mathcal{P}^{n'}}{\partial \sigma} \right) \quad (4.74) \\ & = \frac{\rho_0}{\Delta t} \left(\frac{\partial U^*}{\partial x} + \frac{\partial V^*}{\partial y} + \frac{\partial \sigma_{x^*}^* U^* + \sigma_{y^*}^* V^* + W^* / D^*}{\partial \sigma} \right) \end{aligned}$$

where the same process is repeated for the second Runge-Kutta stage, $()^{n''}$. The above equation is discretized using (F.1), (F.5) as well as the conventional centered difference scheme for the horizontal gradients. The resulting linear discretized equation, for $k = 1, \dots, K$, is given by

$$\begin{aligned} & a_1 \mathcal{P}_{i,j-1,k-1}^{n'} + a_2 \mathcal{P}_{i-1,j,k-1}^{n'} + a_3 \mathcal{P}_{i,j,k-1}^{n'} + a_4 \mathcal{P}_{i+1,j,k-1}^{n'} + a_5 \mathcal{P}_{i,j+1,k-1}^{n'} + a_6 \mathcal{P}_{i,j-1,k}^{n'} \\ & + a_7 \mathcal{P}_{i-1,j,k}^{n'} + a_8 \mathcal{P}_{i,j,k}^{n'} + a_9 \mathcal{P}_{i+1,j,k}^{n'} + a_{10} \mathcal{P}_{i,j+1,k}^{n'} + a_{11} \mathcal{P}_{i,j-1,k+1}^{n'} \quad (4.75) \\ & + a_{12} \mathcal{P}_{i-1,j,k+1}^{n'} + a_{13} \mathcal{P}_{i,j,k+1}^{n'} + a_{14} \mathcal{P}_{i+1,j,k+1}^{n'} + a_{15} \mathcal{P}_{i,j+1,k+1}^{n'} \\ & = (R_{\mathcal{P}}^*)_{i,j,k} \end{aligned}$$

where

$$\begin{aligned}
a_1 &= \frac{-\alpha}{2\Delta y} \left(\{\sigma_{y^*}\}_{i,j-1,k-1}^* + \{\sigma_{y^*}\}_{i,j,k-1}^* \right) \\
a_2 &= \frac{-\alpha}{2\Delta x} \left(\{\sigma_{x^*}\}_{i-1,j,k-1}^* + \{\sigma_{x^*}\}_{i,j,k-1}^* \right) \\
a_3 &= -2\alpha \{\sigma_{x^*}\}_{i,j,k-1}^* \left(\frac{\{\sigma_{x^*}\}_{i,j,k-\frac{1}{2}}^*}{\Delta\sigma_{k-1}} - \beta \{\sigma_{x^*}\}_{i,j,k}^* \right) \\
&\quad - 2\alpha \{\sigma_{y^*}\}_{i,j,k-1}^* \left(\frac{\{\sigma_{y^*}\}_{i,j,k-\frac{1}{2}}^*}{\Delta\sigma_{k-1}} - \beta \{\sigma_{y^*}\}_{i,j,k}^* \right) - \frac{2\alpha}{[D^*]^2 \Delta\sigma_k} \\
a_4 &= \frac{\alpha}{2\Delta x} \left(\{\sigma_{x^*}\}_{i+1,j,k-1}^* + \{\sigma_{x^*}\}_{i,j,k-1}^* \right) \\
a_5 &= \frac{\alpha}{2\Delta y} \left(\{\sigma_{y^*}\}_{i,j+1,k-1}^* + \{\sigma_{y^*}\}_{i,j,k-1}^* \right) \\
a_6 &= \frac{-\beta}{2\Delta y} \left(\{\sigma_{y^*}\}_{i,j-1,k}^* + \{\sigma_{y^*}\}_{i,j,k}^* \right) + \frac{1}{[\Delta y]^2} \\
a_7 &= \frac{-\beta}{2\Delta x} \left(\{\sigma_{x^*}\}_{i-1,j,k}^* + \{\sigma_{x^*}\}_{i,j,k}^* \right) + \frac{1}{[\Delta x]^2} \\
a_8 &= 2\{\sigma_{x^*}\}_{i,j,k}^* \left(\frac{\alpha \{\sigma_{x^*}\}_{i,j,k-\frac{1}{2}}^*}{\Delta\sigma_{k-1}} + \beta^2 \{\sigma_{x^*}\}_{i,j,k}^* - \frac{\gamma \{\sigma_{x^*}\}_{i,j,k+\frac{1}{2}}^*}{\Delta\sigma_k} \right) \\
&\quad + 2\{\sigma_{y^*}\}_{i,j,k}^* \left(\frac{\alpha \{\sigma_{y^*}\}_{i,j,k-\frac{1}{2}}^*}{\Delta\sigma_{k-1}} + \beta^2 \{\sigma_{y^*}\}_{i,j,k}^* - \frac{\gamma \{\sigma_{y^*}\}_{i,j,k+\frac{1}{2}}^*}{\Delta\sigma_k} \right) \\
&\quad - \frac{2}{[D^*]^2 \Delta\sigma_k \Delta\sigma_{k-1}} - \frac{2}{[\Delta x]^2} - \frac{2}{[\Delta y]^2} \\
a_9 &= \frac{\beta}{2\Delta x} \left(\{\sigma_{x^*}\}_{i+1,j,k}^* + \{\sigma_{x^*}\}_{i,j,k}^* \right) + \frac{1}{[\Delta x]^2} \\
a_{10} &= \frac{\beta}{2\Delta y} \left(\{\sigma_{y^*}\}_{i,j+1,k}^* + \{\sigma_{y^*}\}_{i,j,k}^* \right) + \frac{1}{[\Delta y]^2} \\
a_{11} &= \frac{-\gamma}{2\Delta y} \left(\{\sigma_{y^*}\}_{i,j-1,k+1}^* + \{\sigma_{y^*}\}_{i,j,k+1}^* \right) \\
a_{12} &= \frac{-\gamma}{2\Delta x} \left(\{\sigma_{x^*}\}_{i-1,j,k+1}^* + \{\sigma_{x^*}\}_{i,j,k+1}^* \right) \\
a_{13} &= 2\gamma \{\sigma_{x^*}\}_{i,j,k+1}^* \left(\frac{\{\sigma_{x^*}\}_{i,j,k+\frac{1}{2}}^*}{\Delta\sigma_k} + \beta \{\sigma_{x^*}\}_{i,j,k}^* \right) \\
&\quad + 2\gamma \{\sigma_{y^*}\}_{i,j,k+1}^* \left(\frac{\{\sigma_{y^*}\}_{i,j,k+\frac{1}{2}}^*}{\Delta\sigma_k} + \beta \{\sigma_{y^*}\}_{i,j,k}^* \right) + \frac{2\gamma}{[D^*]^2 \Delta\sigma_{k-1}} \\
a_{14} &= \frac{\gamma}{2\Delta x} \left(\{\sigma_{x^*}\}_{i+1,j,k+1}^* + \{\sigma_{x^*}\}_{i,j,k+1}^* \right) \\
a_{15} &= \frac{\gamma}{2\Delta y} \left(\{\sigma_{y^*}\}_{i,j+1,k+1}^* + \{\sigma_{y^*}\}_{i,j,k+1}^* \right), \\
R_{\mathcal{P}}^* &= \frac{\rho_0}{\Delta t} \left(\frac{\partial U^*}{\partial x} + \frac{\partial V^*}{\partial y} + \frac{\partial \sigma_{x^*}^* U^* + \sigma_{y^*}^* V^* + W^* / D^*}{\partial \sigma} \right)_{i,j,k}
\end{aligned} \tag{4.76}$$

where

$$\begin{aligned}
\alpha &= \frac{-\Delta\sigma_k}{\Delta\sigma_{k-1}(\Delta\sigma_{k-1} + \Delta\sigma_k)} \\
\beta &= \frac{\Delta\sigma_k - \Delta\sigma_{k-1}}{\Delta\sigma_{k-1}\Delta\sigma_k} \\
\gamma &= \frac{\Delta\sigma_{k-1}}{\Delta\sigma_k(\Delta\sigma_{k-1} + \Delta\sigma_k)}
\end{aligned} \tag{4.77}$$

To calculate the right hand-side term, $(R_{\mathcal{P}}^*)_{i,j,k}$, the velocities are interpolated at the σ_k level using (E.1). The pressure at the free-surface, \mathcal{P}_{K+1} , are obtained using the Dirichlet boundary condition given by (4.55), and, thus, at $k = K$, the terms including \mathcal{P}_{K+1} are moved to the right-hand side. At the bottom, $k = 1$, the discretized Neumann boundary condition (4.56) reads as

$$\left. \frac{\partial \mathcal{P}}{\partial \sigma} \right|_{i,j,1} = \alpha \mathcal{P}_{i,j,1-1} + \beta \mathcal{P}_{i,j,1} + \gamma \mathcal{P}_{i,j,1+1} = RHS_{(4.56)} \Big|_{i,j,1}. \tag{4.78}$$

Thus,

$$\mathcal{P}_{i,j,1-1} = +\frac{1}{\alpha} RHS_{(4.56)} \Big|_{i,j,1} - \frac{\beta}{\alpha} \mathcal{P}_{i,j,1} - \frac{\gamma}{\alpha} \mathcal{P}_{i,j,1+1}. \tag{4.79}$$

and the terms including \mathcal{P}_{1-1} are replaced by using the above equation.

4.5.3 Truncation Error Analysis

Because a uniform grid is used in the horizontal directions, the truncation error of the first and second horizontal derivatives is on the order of $(\Delta x)^2$ and $(\Delta y)^2$ using the conventional centered difference scheme. In the case of having a non-uniform grid in the vertical direction, however, the truncation error of the second derivatives with respect to σ is on the order of $\Delta\sigma_k\Delta\sigma_{k-1}$ and $\Delta\sigma_k - \Delta\sigma_{k-1}$; see F for details. Thus, the arrangement of the σ levels should be selected such that $\Delta\sigma_k\Delta\sigma_{k-1} \approx \Delta\sigma_k - \Delta\sigma_{k-1}$ or $|1 - R_k|/R_k \approx \Delta\sigma_{k-1}$ where $R_k = \Delta\sigma_k/\Delta\sigma_{k-1}$. For $R_k < 1$, we should have

$R_k \approx 1/(1 + \sigma_{k-1})$, and, thus, as σ_{k-1} decreases, R_k should be increased, to maintain second-order accuracy in the vertical direction at the finer vertical levels. The effects of the vertical grid design on the velocity and dynamic pressure fields will be examined in a separate paper. In the present study, we always use constant σ levels.

4.6 The Role of Surface Slopes in the Near-surface Velocity and Turbulence Fields

In this section, the new model results of the velocity field under a deep water standing wave in a closed basin as well as the turbulence field under the surf zone regular spilling breaking waves have been compared with those predicted by the old model, [Ma et al. \(2012\)](#). In addition, the evolution of an initial two dimensional Gaussian hump is presented, showing the new model preserves two-dimensional isotropy in the horizontal plane.

4.6.1 Standing Wave in a Closed Basin

Using the simplified velocity boundary condition, e.g., $\partial u/\partial\sigma = 0$, imposes an unphysical source of vorticity at the free surface in the case of a non-zero horizontal gradient of the vertical velocity, $\partial w/\partial x \neq 0$, generating an unphysical circulation pattern. A deep water standing wave in a closed basin, with length of $L = 20\text{m}$ and depth of $D = 10\text{m}$, is selected to examine this effect. The initial surface elevation is $\eta_0 = a \cos kx$, where $k = 2\pi/L$, $a = 0.1\text{m}$ is the amplitude of the standing wave and L is the wave length, equals to the basin's length. Since $kD = \pi$, the wave is highly dispersive. Based on the linear dispersion relation, the wave period is equal to $T = 5.79\text{s}$. A uniform grid spacing of 0.2m in the horizontal direction, and 10 constant σ levels are used. The simulation time is 36.0s , about 10 wave periods. To calculate long-time averaged velocity field, the results are first interpolated into an Eulerian grid of $\Delta z = 0.1\text{m}$ and $\Delta x = 0.2\text{m}$, and, then, time averaging is performed over 10 wave periods. [Figure 4.1](#) shows the existence of an unphysical circulation pattern in the model results using $\partial u/\partial\sigma = 0$ boundary conditions. Using the linear

theory, it can be shown that the magnitude of the instantaneous unphysical vorticity at the free surface is $\omega(ka)$. In the deep water regime, it then becomes $ag^{-1}T^{-3}$, and increases with increasing wave height or decreasing wave period. In addition, using the exact boundary conditions, the potential energy loss is decreased compared with the linearized analytical solution, especially at cases with few vertical levels as shown in figure 4.2.

4.6.2 Two-dimensional Isotropy Test

In this section, the evolution of an initial two dimensional Gaussian hump, $f(x, y, t = 0) = 0.1e^{-(x^2+y^2)/4}$, in a closed box with the length of 20m and 1m depth will be presented. Uniform grid of $\Delta x = \Delta y = 0.1\text{m}$ in the horizontal directions, and the vertical resolution of 2 vertical uniform levels are used. As shown in figures 4.3 and 4.4, the initial surface displacement generates completely circular waves propagating to the side walls. The reflected waves from the side walls generate a relatively complex pattern at later times. The results show the new model preserves two-dimensional isotropy in the horizontal plane very accurately. In other words, the new boundary conditions and numerical schemes are not biased in the either x and y directions.

4.6.3 Surf zone Regular Breaking Waves

The surf zone regular spilling breaking case of Ting & Kirby (1994) is selected here, to examine the role of surface slopes on the prediction of ensemble-averaged turbulent characteristics under surf zone breaking waves. This experiment has been widely used by other researchers to validate both non-hydrostatic and VOF-based multilevels coastal numerical models. The details of the model comparisons with the corresponding measurement are given in Derakhti et al. (2016b). Here, we only present the comparison between the predicted turbulent kinetic energy, k , field by the new and old model. Uniform grid of $\Delta x = 0.025\text{m}$ is used in the horizontal direction. The vertical resolution of 10 vertical uniform levels is used. At the left inflow boundary, the free surface location and velocities are calculated using the theoretical relations

for Cnoidal waves. The right end of the numerical domain is extended beyond the maximum run-up, and the wetting/drying cells are treated as described in [Ma et al. \(2012, §3.4\)](#) by setting $D_{min} = 0.001\text{m}$. Here, $\overline{(\)}$ refers to wave averaging over five subsequent waves after the results reach the quasi-steady state. The mean sea level is defined as $h = d + \overline{\eta}$, where d is the still water depth and $\overline{\eta}$ is the wave set-down/set-up. As in [Ting & Kirby \(1994\)](#), $x = 0$ is the cross-shore location in which $d = 0.38\text{m}$, and $x^* = x - x_b$ is the horizontal distance from the initial break point, x_b .

Figure 4.5 shows the turbulent kinetic energy, k , prediction by the new model is significantly improved compared with that predicted by the old model. The wrong location of high k regions predicted by the old model is mainly due to imposing $\partial u / \partial \sigma = 0$ boundary condition at the free surface, leading to a significantly change of the production term at the bore-front region. In addition, the k values predicted by the old model are much larger than those predicted by the new model. The new model results are more comparable with the corresponding measurements of [Ting & Kirby \(1994\)](#) as shown in figure 4.6. Figure 4.6 also shows that the RNG-based $k - \epsilon$ model gives a better estimation of k compared with the standard $k - \epsilon$ model, especially at the transition region. In addition, using the complete form of the diffusion terms in both the momentum and $k - \epsilon$ equations has an important role in the correct prediction of the k distribution inside the surf zone and prevents the unphysical continuous seaward propagation of the k patch as observed in the old model results.

4.7 Conclusions

In this paper, we derived a new set of governing equations based on the mixture theory in the σ -coordinate system, describing the kinematics and dynamics of the continuous and dispersed phases in a multi-phase mixture, assuming dilute suspension regime and particles with small Stokes number. The effects of baroclinic pressure and turbulence modulation due to density variations were considered. The exact surface and bottom dynamic boundary conditions for the velocity and dynamic pressure fields were derived, using the continuity of the normal and tangential stresses at the top

and bottom interfaces. A Neumann-type boundary condition for scalar fluxes was also derived. A new numerical scheme was implemented for terms with vertical gradients, preserving second-order accuracy for a general non-uniform vertical grid.

It was shown that the new boundary conditions significantly improved turbulent kinetic energy prediction under surf zone breaking waves compared with the simplified stress boundary conditions commonly used in non-hydrostatic studies using the σ -coordinate system. We found that the RNG-based $k - \epsilon$ model gave a better estimation of k compared with the standard $k - \epsilon$ model, especially in the transition region. Further, by comparing the predicted velocity field under a deep water standing wave in a closed basin, we showed that the new model did not generate unphysical vorticity at the free surface. The model capability and accuracy to reproduce the evolution of the free surface, velocity, vorticity, and turbulence fields under different breaking waves from the surf zone to deep water is examined in detail in a companion paper ([Derakhti et al. 2016b](#)).

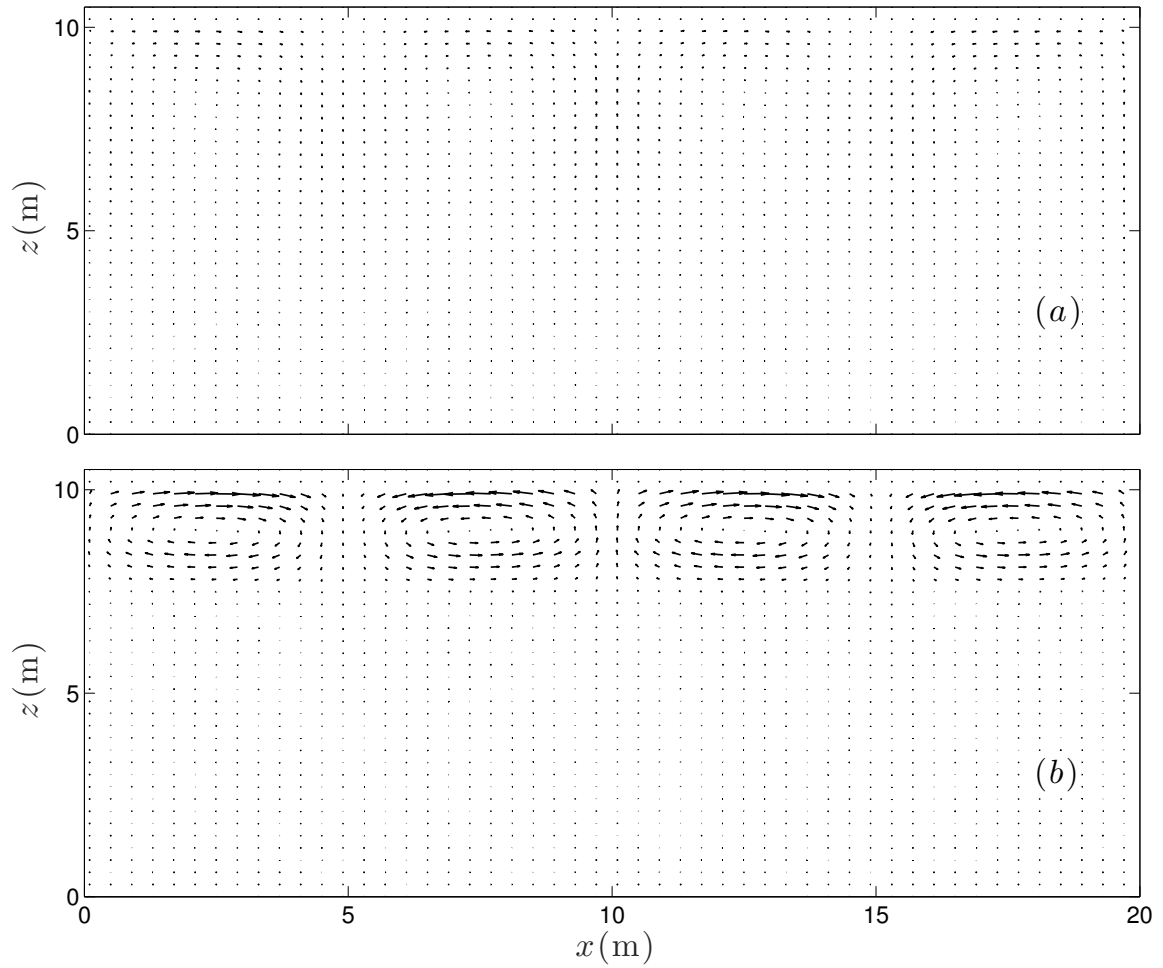


Figure 4.1: Spatial distribution of the long-time-averaged velocity field under a standing wave in a closed basin. Comparison between NHWAVE results with 10 vertical levels using the (a) exact and (b) old boundary conditions.

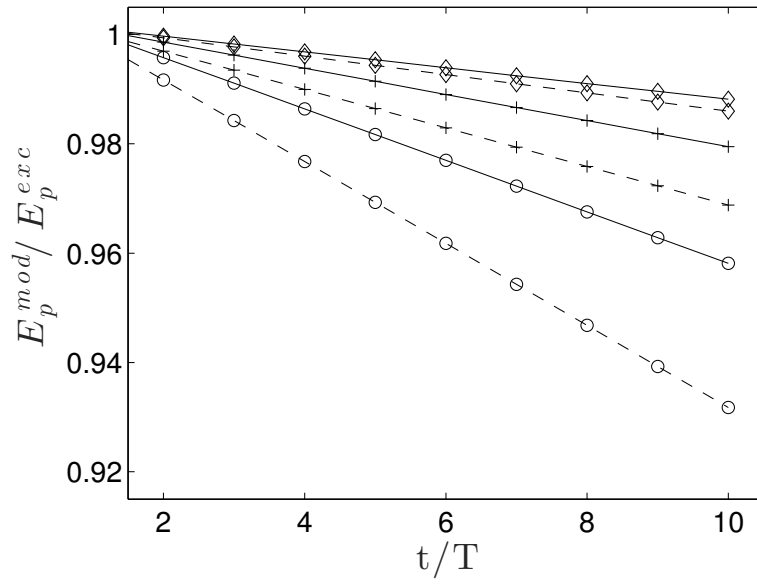


Figure 4.2: Time variation of the normalized wave-averaged potential energy of a standing wave in a closed basin. Comparison between NHWAVE results with (circle symbols) 3, (+ symbols) 5 and (diamonds symbols) 10 vertical levels using the (solid lines) exact and (dashed lines) old boundary conditions.

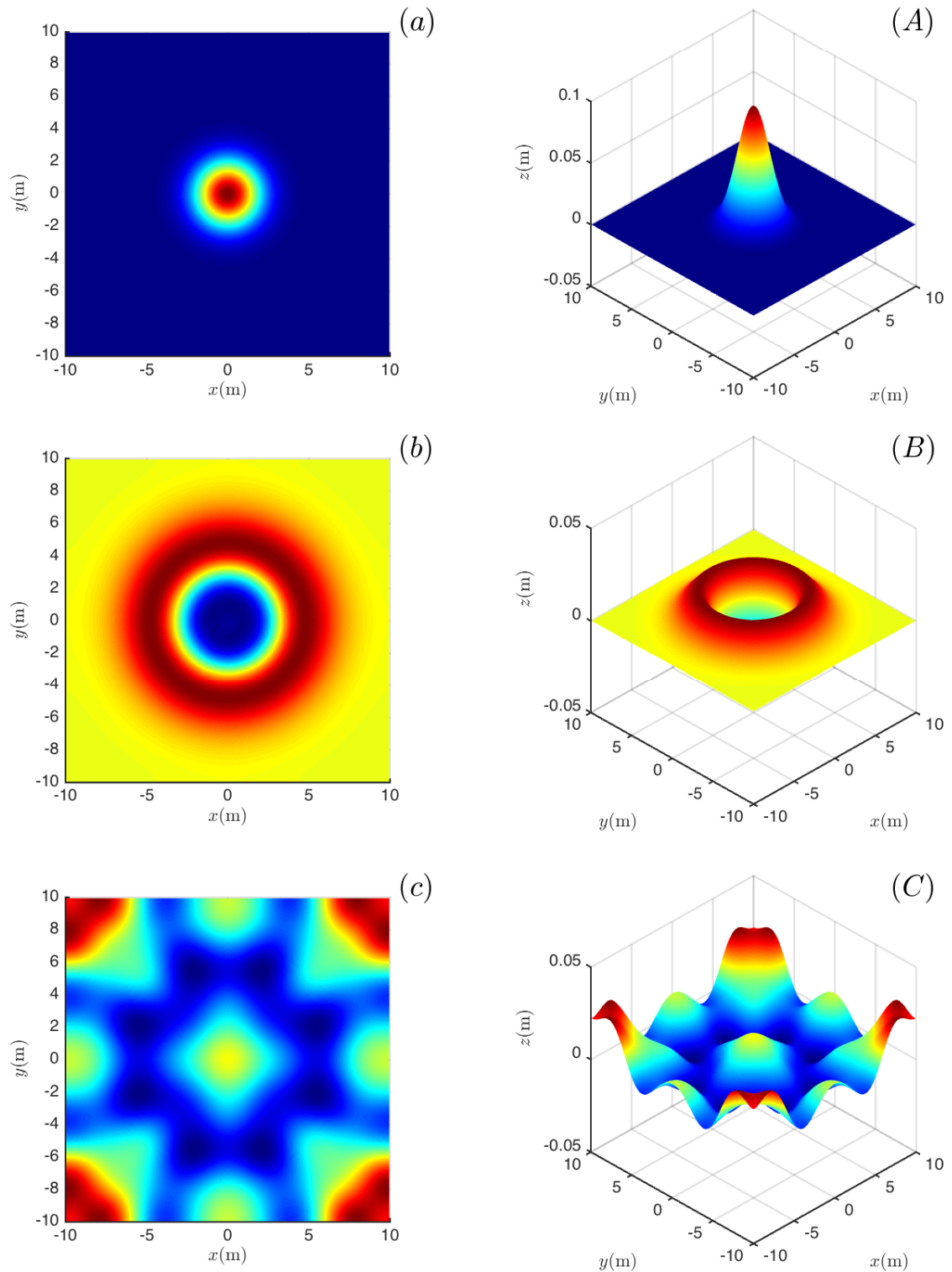


Figure 4.3: Snapshots of the two-dimensional free surface locations generated by the evolution of an initial two dimensional Gaussian hump at (a, A) $t - t_0 = 0.1\text{s}$, (b, B) $t - t_0 = 1.5\text{s}$, and (c, C) $t - t_0 = 9.9\text{s}$. (a, b, c) show the plan view, while (A, B, C) show the corresponding 3d view.

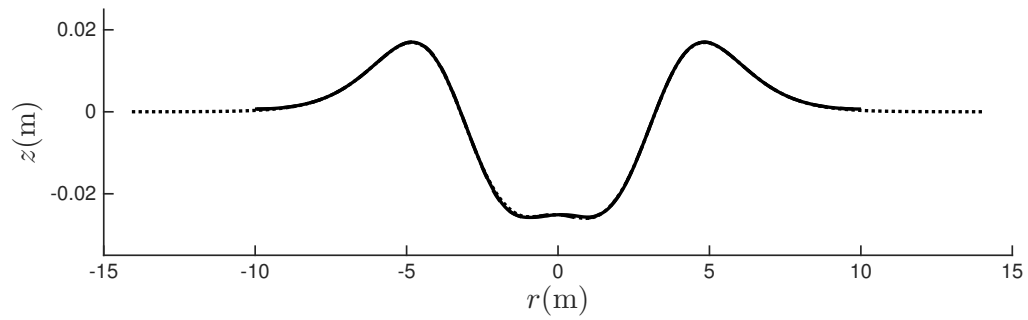


Figure 4.4: Cross sections of the two-dimensional free surface locations shown in figure 4.3(b, B), at (solid line) $x = 0$, (dashed line) $y = 0$ and (dotted line) $x = y$.

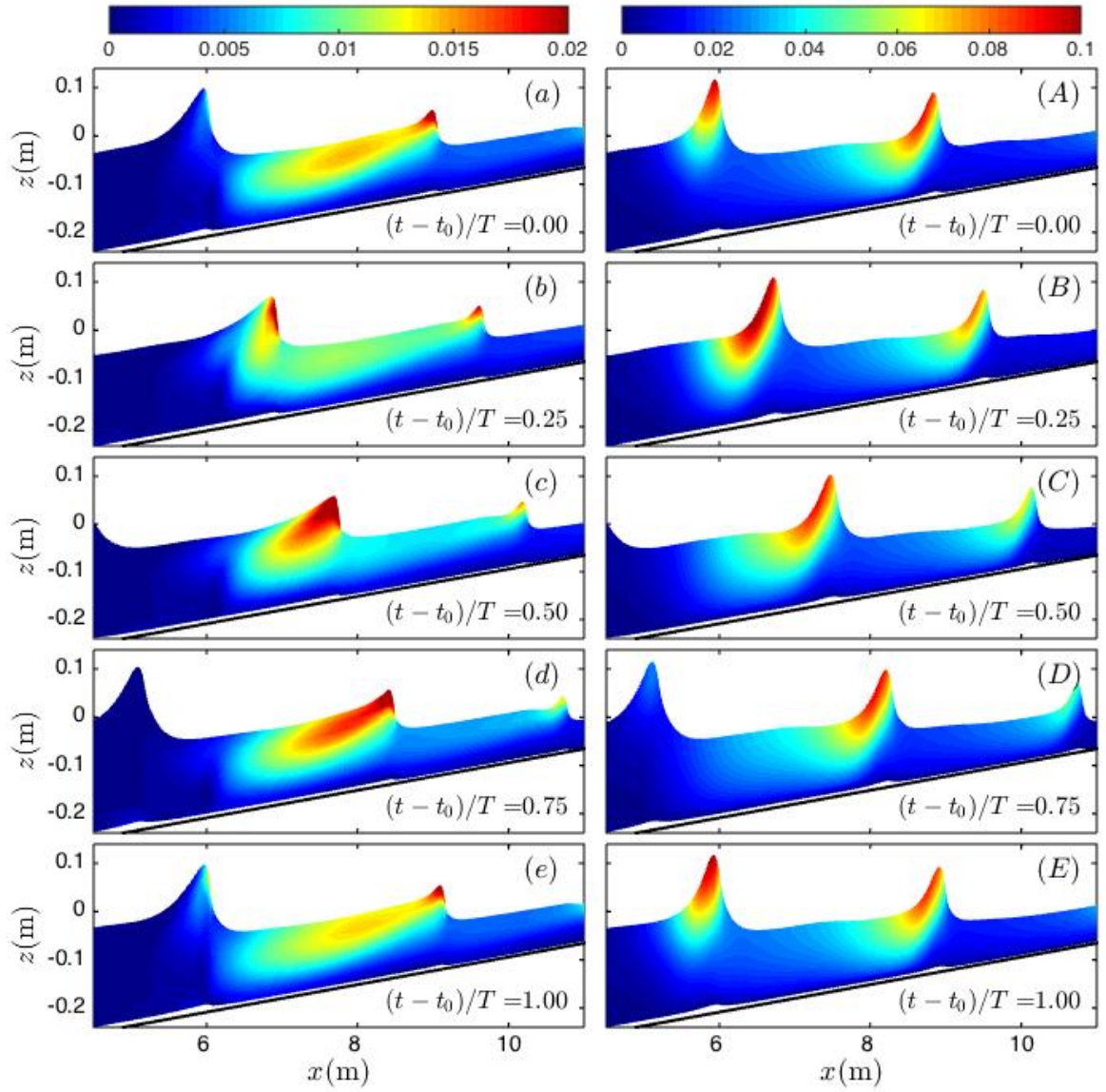


Figure 4.5: Snapshots of the turbulent kinetic energy, $k(\text{m}^2/\text{s}^2)$, distributions under the spilling periodic surf zone breaking waves. Comparison between NHWAVE results with 10 vertical levels using the (a–e) new and (A–E) old model. Here, $x = 0$ corresponds to the cross-shore location at which $d = 0.38$ as in [Ting & Kirby \(1994\)](#).

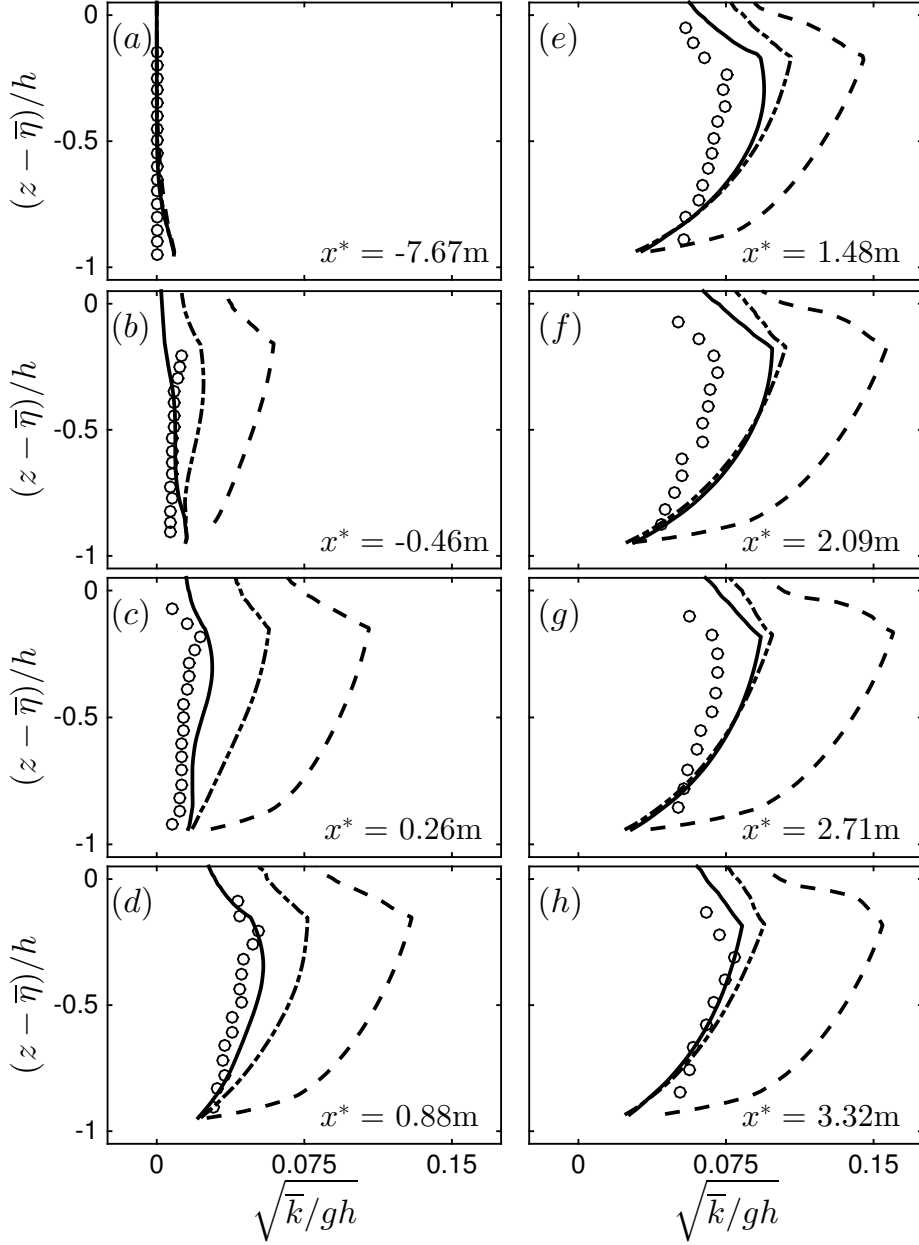


Figure 4.6: Time-averaged normalized turbulent kinetic energy, \sqrt{k}/gh , profiles at different cross-shore locations under the spilling periodic surf zone breaking waves. Comparison between NHWAVE results with 10 vertical levels using the new model with (solid lines) RNG-based, (dotted-dashed lines) standard $k - \epsilon$ and (dashed lines) the old model. Here, $x^* = x - x_b$, is the horizontal distance from the break point; and $h = d + \bar{\eta}$, where d is the still water depth and $\bar{\eta}$ is the wave set-up/set-down.

Chapter 5

WAVE BREAKING IN THE SURF ZONE AND DEEP WATER IN A NON-HYDROSTATIC MODEL

5.1 Abstract

We examine wave-breaking predictions ranging from shallow to deep water conditions using a non-hydrostatic model NHWAVE (Ma et al. 2012, Derakhti et al. 2016a), comparing results both with corresponding experiments and with the results of a volume-of-fluid (VOF)/Navier-Stokes solver (Ma et al. 2011, Derakhti & Kirby 2014b,a). Our study includes regular and irregular depth-limited breaking waves on planar and barred beaches as well as steepness-limited unsteady breaking waves in intermediate and deep water. Results show that the model accurately resolves breaking wave properties in terms of (1) time-dependent free-surface and velocity field evolution, (2) integral breaking-induced dissipation, (3) second- and third-order wave statistics, (4) time-averaged breaking-induced velocity field, and (5) turbulence statistics in depth-limited breaking waves both on planar and barred beaches. The breaking-induced dissipation is mainly captured by the $k - \epsilon$ turbulence model and involves no ad-hoc treatment, such as imposing hydrostatic conditions. In steepness-limited unsteady breaking waves, the turbulence model has not been triggered, and all the dissipation is imposed indirectly by the TVD shock-capturing scheme. Although the absence of turbulence in the steepness-limited unsteady breaking events which leads to the underestimation of the total breaking-induced dissipation, and, thus, the overprediction of the velocity and vorticity field in the breaking region, the model is capable of predicting (1) the dispersive and nonlinear properties of different wave packet components before and after the break point, (2) the overall wave height decay and spectral evolution, and (3) the structure of the mean velocity and vorticity fields including large

breaking-induced coherent vortices. The same equations and numerical methods are used for the various depth regimes, and vertical grid resolution in all simulated cases is at least an order of magnitude coarser than that of typical VOF-based simulations.

5.2 Introduction

One of the least understood and yet most important events in the ocean upper layer is the breaking of surface waves. Surface wave breaking, a complex, two-phase flow phenomenon, plays an important role in numerous environmental and technical processes such as air-sea interaction, acoustic underwater communications, optical properties of the water columns, nearshore mixing and coastal morphodynamics. Surface wave breaking is one of the most challenging process in coastal hydrodynamic modeling. Model results become even more dubious and problematic as model resolution decreases. During active breaking, perhaps the major simplification by any non-hydrostatic model is achieved by replacing a complex free surface by a single-valued function of horizontal location. Instead of having a jet/splash cycle in plunging breakers or formation of surface rollers and a turbulent bore in spilling breakers, this simplification leads to the formation of a relatively sharp wave-front, analogous to a jump discontinuity in a shock-front propagation, as a wave approaches breaking. The sharp wave-front propagates without any unphysical numerical oscillation when an appropriate shock-capturing scheme is used.

Although turbulence-resolving frameworks such as large-eddy simulations (LES) combined with the volume-of-fluid (VOF) method for free-surface tracking ([Watanabe et al. 2005](#), [Lakehal & Liovic 2011](#), [Derakhti & Kirby 2014b](#), [Zhou et al. 2014](#), [Lubin & Glockner 2015](#)) can resolve small scale processes such as breaking-induced turbulent coherent structures, they are still computationally expensive even for laboratory-scale events. A lower-resolution three-dimensional (3D) framework is needed to study long-term, $O(\text{hrs})$, and large-scale, $O(100m \approx 10km)$, breaking-driven circulation as well as transport of sediment, bubbles, and other suspended materials. During the past decade,

several 3D wave-resolving non-hydrostatic models based on Reynolds-averaged Navier-Stokes (RANS) equations have been developed for coastal applications (Ma et al. 2012, Young & Wu 2010, Zijlema et al. 2011, Bradford 2011, Shirkavand & Badiei 2014).

For surf zone breaking waves, when non-hydrostatic effects are retained, Smit et al. (2013) have emphasized that high resolution in the vertical direction (more than 15 levels) is needed for reasonable integral dissipation and corresponding wave-height decay resulting from discontinuity propagation. In place of common shock-capturing schemes (Toro 2009), they used a special treatment to maintain momentum conservation across flow discontinuity, observing that insufficient vertical resolution led to an underestimation of velocities, thereby delaying the initiation of breaking. They proposed a hydrostatic front approximation in which the non-hydrostatic part of pressure is switched off by analogy to the nonlinear shallow water equations. Using this technique, SWASH was shown to predict the evolution of wave-height statistics in a surf zone reasonably well compared with laboratory measurements of irregular waves on a plane slope, by using a few σ levels. In the present study, however, we will show that NHWAVE, as described in Derakhti et al. (2016a), accurately captures the wave-height decay in regular waves as well as wave-height statistics in irregular surf zone breaking waves using as few as 4 vertical σ levels, without recourse to disabling of non-hydrostatic effects.

Organized flow structures and their evolution have a critical role in long-term mixing and transport of fine sediment, bubbles, and other suspended materials in the ocean upper layer and surf zone. For example, large coherent vortices induced by individual whitecaps in deep and intermediate water (Rapp & Melville 1990, Pizzo & Melville 2013, Derakhti & Kirby 2014a) as well as undertow, longshore and rip currents (Longuet-Higgins 1970, Svendsen 1984) in the surf zone are fairly well-understood breaking-induced organized motions. Such organized motions need to be reasonably resolved in any RANS-based framework to truly estimate long-term transport and mixing processes at field scales. The effect of Langmuir circulation cells should also

be taken into account in deep water mixing. The available relevant literature on non-hydrostatic models mainly are related to surf zone breaking waves (or depth-limited breaking waves) and mostly focus on the capability of these models to predict free surface evolution and wave statistics, while less attention has been dedicated to velocity and turbulence fields. Although there are recent studies (Young & Wu 2010, Ai et al. 2014) examining the capability of non-hydrostatic models to resolve wave-wave nonlinear interaction and dispersion properties of non-breaking deep water waves, no study has examined non-hydrostatic model predictions of breaking-related processes in steepness-limited unsteady breaking waves.

Our goals here are (1) to carefully examine what level of detail of a velocity field and of turbulence statistics can be reproduced by the non-hydrostatic model NHWAVE as described by Derakhti et al. (2016a), across the inner shelf and nearshore regions, and (2) to establish whether this model is capable of providing accurate representations of breaking-wave properties in intermediate/deep water. Model results for regular and irregular depth-limited breaking waves over planar and barred beaches as well as steepness-limited unsteady breaking waves generated by the dispersive focusing technique will be presented in detail, focusing on wave-breaking-related large-scale processes categorized as (1) time dependent free-surface and mean velocity field evolution, (2) integral breaking-induced dissipation, (3) second- and third-order wave statistics, (4) wave-averaged breaking-induced organized velocity field, and (5) ensemble-averaged breaking-induced turbulence statistics.

The paper is organized as follows. A brief description of the model is presented in §5.3. Details of the numerical set-up, and comparisons of model results with measurements for depth-limited breaking waves on a planar beach and on a barred beach are given in §5.4 and §5.5 respectively. The numerical set-ups and comparisons of model results with measurements and with results of LES/VOF simulations of Derakhti & Kirby (2014b,a) for steepness-limited unsteady breaking waves are given in §5.6. Discussions and conclusions are presented in §5.7.

5.3 Mathematical Formulation and Numerical Methods

The non-hydrostatic model NHWAVE is originally described in [Ma et al. \(2012\)](#). NHWAVE solves the RANS equations in well-balanced conservative form, formulated in time-dependent, surface and terrain-following σ coordinates. The governing equations are discretized by a combined finite-volume/finite-difference approach with a Godunov-type shock-capturing scheme. The model is wave-resolving and can provide instantaneous descriptions of surface displacement and wave orbital velocities. The model has been applied to study tsunami wave generation by submarine landslides ([Ma, Kirby & Shi 2013](#), [Tappin et al. 2014](#)), wave damping in vegetated environments ([Ma, Kirby, Su, Figlus & Shi 2013](#)), nearshore suspended sediment transport ([Ma, Chou & Shi 2014](#)), and wave interaction with porous structures ([Ma, Shi, Hsiao & Wu 2014](#)). In these studies, the effects of surface and bottom slopes in the dynamic boundary conditions ([Ma et al. 2012](#), §3), as well as in the horizontal diffusion terms of the transport equation for suspended sediment concentration ([Ma, Kirby & Shi 2013](#), equation 10) and $k - \epsilon$ equations ([Ma, Kirby & Shi 2013](#), equations 13,14) were ignored. [Derakhti et al. \(2016a\)](#) have recently derived a new form of the governing equations together with the exact surface and bottom boundary conditions. They have shown that surface slope effects should be taken into account in order to accurately resolve turbulence statistics, such as turbulent kinetic energy (k) distribution, in surf zone breaking waves. Here, we use the [Derakhti et al. \(2016a\)](#) formulation together with the $k - \epsilon$ model based on the renormalization group theory ([Yakhot et al. 1992](#)). The reader is referred to [Derakhti et al. \(2016a\)](#) for the details of the governing equations, surface and bottom boundary conditions and numerical methods.

5.4 Depth-limited Breaking Waves on a Planar Beach

In this section, we consider model performance for the case of regular and irregular depth-limited wave breaking on a planar beach using the data sets of [Ting & Kirby \(1994\)](#) for regular waves and of [Bowen & Kirby \(1994\)](#) and [Mase & Kirby \(1992\)](#) for irregular waves. All experiments have been conducted in wave flumes approximately

40m long, 0.6m wide and 1.0m deep. Results for regular and irregular wave breaking cases are given in §3.1 and §3.2, respectively. In each section, the experimental and numerical set-ups for the corresponding cases will be described.

5.4.1 Regular Breaking Waves

Both spilling breaking (hereafter referred as TK1) and plunging breaking (hereafter referred as TK2) cases of Ting & Kirby (1994) are selected to examine the model capability and accuracy to reproduce the free surface and mean velocity field evolution, breaking-induced wave-averaged velocity field and k estimates. This experiment has been widely used by other researchers to validate both non-hydrostatic (Ma, Chou & Shi 2014, Bradford 2011, 2012, Smit et al. 2013, Shirkavand & Badiei 2014) and VOF-based (Ma et al. 2011, Lin & Liu 1998, Bradford 2000, Lakehal & Liovic 2011) numerical models. Figure 5.1 sketches the experimental layout and the cross-shore locations of the available velocity measurements. The velocity measurements were obtained using Laser Doppler velocimetry (LDV) along the centerline of the wave tank. Table 5.1 summarizes the input parameters for TK1 and TK2.

A uniform grid of $\Delta x = 0.025\text{m}$ is used in the horizontal direction. Grids with 4, 8, and 16 uniformly spaced σ levels are used to examine the effects of varying vertical resolution. At the inflow boundary, the free surface location and velocities are calculated using the theoretical relations for cnoidal waves as given in Wiegel (1960). The right end of the numerical domain is extended beyond the maximum run-up, and the wetting/drying cells are treated as described in Ma et al. (2012, §3.4) by setting $D_{min} = 0.001\text{m}$. In this section, $\langle \rangle$ and $\overline{(\)}$ refer to phase and time averaging over five subsequent waves after the results reach quasi-steady state, respectively. The corresponding measured averaged variables, were calculated by averaging over 102 successive waves starting at a minimum of 20 minutes after the initial wavemaker movement.

The mean depth is defined as $h = d + \bar{\eta}$, where d is the still water depth and $\bar{\eta}$ is the wave set-down/set-up. Here, $x = 0$ is the cross-shore location at which $d = 0.38\text{m}$ as in Ting & Kirby (1994), and $x^* = x - x_b$ is the horizontal distance

Table 5.1: Input parameters for the simulated surf zone regular breaking cases on a planar beach. Here, d_0 is the still water depth in the constant-depth region, H and T are the wave height and period of the cnoidal wave generated by the wavemaker, $(kH)_0$ is the corresponding deep water wave steepness of the generated wave, $\xi_0 = s/\sqrt{H_0/L_0}$ is the self similarity parameter, and s is the plane slope.

Case no.	d_0 (m)	H (m)	T (s)	$(kH)_0$	ξ_0	breaking type
<i>TK1</i>	0.4	0.125	2.0	0.126	0.20	spilling
<i>TK2</i>	0.4	0.128	5.0	0.015	0.59	plunging

from the initial break point, x_b . In [Ting & Kirby \(1994\)](#), the break point for spilling breakers was defined as the location where air bubbles begin to be entrained in the wave crest ($x_b = 6.40\text{m}$), whereas for plunging breakers it was defined as the point where the front face of the wave becomes nearly vertical ($x_b = 7.795\text{m}$). In the model the break point is taken to be the cross-shore location at which the wave height starts to decrease, approximately 0.7m seaward of the observed x_b for both TK1 and TK2.

5.4.1.1 Time-dependent Free Surface Evolution

Figure 5.2 shows the cross-shore distribution of crest, $\langle\eta\rangle_{max}$, and trough, $\langle\eta\rangle_{min}$, elevations as well as mean water level, $\bar{\eta}$ in the shoaling, transition and inner surf zone regions for the spilling case TK1 and plunging case TK2. Figures 5.3 and 5.4 show the phase-averaged water surface elevations at different cross-shore locations before and after the initial break point for TK1 and TK2, respectively. In the shoaling and inner surf zone regions, the model captures the water surface evolution reasonably well in both cases. The predicted cross-shore location of the initial break point, however, is slightly seaward of the measured location for both cases, regardless of the choice of vertical resolution (Figure 5.2 a,b), as in the two-dimensional (2D) VOF-based simulations ([Bradford 2000](#), Figures 1 and 7). In both cases, after shifting the results with respect to the cross-shore location of the break point, the model captured the free

surface evolution, wave height decay rate (Figure 5.2A,B), crest and trough elevations, as well as wave set-up reasonably well using as few as 4 σ levels.

5.4.1.2 Organized Flow Field

Figures 5.5 and 5.6 show the oscillatory part of the phase-averaged horizontal velocities $\langle u \rangle - \bar{u}$ normalized by the local phase speed \sqrt{gh} , at different cross-shore locations in the shoaling, transition and inner surf zone regions at about 5cm above the bed for TK1 and TK2, respectively. In general, the model captures the evolution of $\langle u \rangle - \bar{u}$ fairly reasonably both in time and space in both cases using as few as 4 σ levels, and the predicted $\langle u \rangle - \bar{u}$ of the simulations with different vertical resolutions are nearly the same. For the spilling case (Figure 5.5) there is an apparent landward increasing phase lead in the results of the simulation with 4 σ levels, indicating an overestimation of bore propagation speed at low vertical resolutions. This error is corrected at the higher resolutions of 8 and 16 σ levels.

Figure 5.7 shows the spatial distribution of the time-averaged velocity field using different vertical resolutions for TK1. To obtain the Eulerian mean velocities, the model results in the σ -coordinate system first were interpolated onto a fixed vertical mesh at each cross-shore location using linear interpolation, and then time averaging was performed. The predicted return current using 4 σ levels shown in 5.7(a) has not detached from the bed at $x^* \sim 0$ in contrast to the simulations with 8 and 16 σ levels. The results of the simulations with different vertical resolutions have approximately the same structure in the surf zone. A similar pattern of results was found for the plunging case TK2 and is not shown.

The amount of curvature in the predicted undertow profiles is greater than in the measured undertow profiles for both cases, as shown in Figures 5.8 and 5.9. This difference is more noticeable in the plunging case TK2, in which the measured profiles are approximately uniform with depth. Considering available undertow models using an eddy viscosity closure scheme (see Garcez Faria et al. 2000, among others), it is

known that the three factors determine the vertical profile of undertow currents; including (i) bottom boundary layer (BBL) processes, leading to a landward streaming velocity (Longuet-Higgins 1953, Phillips 1977) or a seaward streaming velocity due to a time-varying eddy viscosity within the wave turbulent BBL (Trowbridge & Madsen 1984), close to the bed; (ii) vertical variations of the eddy viscosity ν_t , affected mainly by breaking-generated turbulence; and (iii) wave forcing due to the cross-shore gradients of radiation stress, set-up, and convective acceleration of the depth-averaged undertow. As explained by Garcez Faria et al. (2000), the amount of curvature in the undertow profile is a function of both wave forcing and ν_t . Large values of wave forcing generates more vertical shear, resulting in a parabolic profile, whereas large values of ν_t reduce vertical shear, leading to a more uniform velocity profile with depth. As shown in the next section, we believe that the underprediction of turbulence, and, thus, the underprediction of ν_t results in greater vertical shear in the predicted undertow profiles, where the larger discrepancy in TK2 is due to the more noticeable underprediction of ν_t in TK2 compared with that in TK1. In addition, the difference between the predicted and measured return velocities close to the bed have relatively larger deviations in TK2 than in TK1. This may be due to the lack of second-order BBL effects, and, thus, the absence of the associated streaming velocity, in the present simulations.

Compared with measurements, the model predicts the time-averaged Eulerian horizontal velocity field fairly reasonably using as few as 4 σ levels for both cases.

5.4.1.3 Turbulence Statistics

Figure 5.10 shows snapshots of the predicted instantaneous k distribution using 4 and 8 σ levels for TK1. Increasing the vertical resolution decreases the predicted k levels in the transition region and increases k in the inner surf zone. Generally, the overall distribution of k is the same. The same trend is also observed for TK2 (not shown).

Figure 5.11 shows a comparison of modeled and measured $\langle k \rangle$ time series at about 4cm and 9cm above the bed at different cross-shore locations using 4, 8 and 16 σ

levels for TK1. Comparing different resolutions, a reasonable $\langle k \rangle$ level at different cross-shore locations is captured by the model using as few as 4 σ levels. $\langle k \rangle$ is overestimated higher in the water column during the entire wave period especially close to the break point. This overestimation has been also reported in previous VOF-based $k - \epsilon$ studies (Lin & Liu 1998, Ma et al. 2011). Lin & Liu (1998) argued that this is because the RANS simulation can not accurately predict the initiation of turbulence in a rapidly distorted shear flow such as breaking waves. Alternately, Ma et al. (2011) incorporated bubble effects into the conventional single phase $k - \epsilon$ model, and concluded that the exclusion of bubble-induced turbulence suppression is the main reason for the overestimation of turbulence intensity by single phase $k - \epsilon$. Comparing Figure 5.11 with the corresponding results from the VOF-based model Ma et al. (2011, Figure 7), we can conclude that predicted $\langle k \rangle$ values under spilling breaking waves by NHWAVE are at least as accurate as the VOF-based simulation without bubbles.

In the plunging case TK2, a different behavior is observed in the predicted $\langle k \rangle$ values shown in Figure 5.12 compared with the corresponding results for TK1, regardless of the various vertical resolutions. After the initial break point, $\langle k \rangle$ is underpredicted especially for lower elevations. Figure 5.12 shows $\langle k \rangle$ time series at 4cm and 9cm above the bed as well as the corresponding measurements of Ting & Kirby (1994) for TK2. The model could not resolve the sudden injection of k into the deeper depths at the initial stage of active breaking, and, thus, there is a considerable underprediction of $\langle k \rangle$ at the beginning of active breaking below trough level.

Figure 5.13 shows \bar{k} field using 4, 8 and 16 σ levels for TK1. The increase of the vertical resolution leads to a more concentrated patch of \bar{k} . A similar trend is also observed for TK2 (not shown). Figures 5.14 and 5.15 show the comparison of modeled and measured \bar{k} profiles at different cross-shore locations before and after the initial break point for TK1 and TK2 respectively. For TK2, the noticeable underprediction of $\langle k \rangle$ at the initial stage of active breaking shown in Figure 5.12 compensates relatively smaller overprediction of $\langle k \rangle$ at the other phases, resulting to apparent smaller \bar{k} values than those in the measurement in the shoreward end of the transition region and inner

surf zone, as shown in Figure 5.15(d-g).

It can be concluded that the vertical resolution of 4 σ levels is sufficient to capture the temporal and spatial evolutions of k for the spilling case TK1. For the plunging case TK2, the vertical advection of k into the deeper depths can not be captured by increasing the σ levels, and, thus, k is always underpredicted at those depths.

5.4.2 Irregular Breaking Waves

In this section, we use one of three cases of Bowen & Kirby (1994) (hereafter referred as BK) and both cases of Mase & Kirby (1992) (hereafter referred as MK1 and MK2) in order to compare the model predictions of power spectra evolution, integral breaking-induced dissipation and wave statistics of the surf zone breaking irregular waves on a planar beach. The three cases have different dispersive and nonlinear characteristics as summarized in Table 5.2. The data set of Mase & Kirby (1992) has been used in a number of previous studies of spectral wave modeling in the surf zone. In particular, MK2 has a high relative depth of $k_p d_0 \sim 2$ at the constant-depth region and a high relative steepness of $(k_p H_{rms})_0 \sim 0.16$, and thus, is a highly dispersive and nonlinear case. In these two experiments, irregular waves with single-peaked spectra were generated and allowed to propagate over a sloping planar bottom. Figures 5.16 and 5.17 sketch the corresponding experimental layouts and the cross-shore locations of the available free surface measurements. Bowen & Kirby (1994) used a TMA spectrum with a width parameter $\gamma = 3.3$ to generate the initial condition at the wavemaker. In Mase & Kirby (1992), random waves were simulated using the Pierson-Moskowitz spectrum.

Uniform grid of $\Delta x = 0.025\text{m}$, 0.015m and 0.01m is used in the horizontal direction for BK, MK1 and MK2 cases, respectively. Resolutions of 4 and 8 σ levels are used to examine the effects of different vertical resolution. The cross-shore location of the numerical wavemaker is set to be the first gage location. The measured free surface and velocities determined from linear theory are constructed at the wavemaker

Table 5.2: Input parameters for the simulated surf zone irregular breaking cases on a planar beach. Here, d_0 is the still water depth in the constant-depth region, $k_p d_0$ and $(k_p H_{rms})_0$ are the dispersion and nonlinearity measure of the incident irregular waves respectively, f_p is the peak frequency of the input signal, $\xi_0 = s/\sqrt{(H_{rms})_0/L_0}$ is the self similarity parameter, $L_0 = g(2\pi)^{-1} f_p^{-2}$, and s is the plane slope.

Case no.	d_0 (m)	$k_p d_0$	$(k_p H_{rms})_0$	f_p (Hz)	ξ_0	dominated breaking type
<i>BK</i>	0.44	0.30	0.016	0.225	0.56	plunging
<i>MK1</i>	0.47	0.93	0.058	0.6	0.52	plunging
<i>MK2</i>	0.47	1.97	0.161	1.0	0.31	spilling

using the first 5000 Fourier components of the measured free surface time series. The right end of the numerical domain is extended beyond the maximum run-up, and the wetting/drying cells are treated as described in [Ma et al. \(2012, §3.4\)](#) by setting $D_{min} = 0.001\text{m}$. In this section, $\overline{(\)}$ refers to long-time averaging over several minutes, more than 300 waves. The first 1000 data points were ignored both in the model result and the corresponding experiment for all cases. The mean sea level is defined as $h = d + \bar{\eta}$, where d is the still water depth and $\bar{\eta}$ is the wave set-down/set-up. Here, $x^* = x - x_b$ is the horizontal distance from the x_b , we define as the cross-shore location in which H_{rms} is maximum.

5.4.2.1 Power Spectra Evolution and Integral Breaking-induced Dissipation

The shape and energy content of wave spectra in nearshore regions are observed to have a considerable spatial variation over distances on the order of a few wavelengths due to continued wave breaking-induced dissipation as well as triad nonlinear interactions between different spectral components ([Elgar & Guza 1985](#), [Mase & Kirby 1992](#)). Here, we will examine the model prediction of the integral breaking-induced

dissipation compared with the corresponding measurements by looking at the evolution of the power spectral density, $S(f)$, from outside the surf zone up to the swash region.

Figure 5.18 shows the variation of the computed $S(f)$ using 4 and 8 σ levels for the random breaking cases, BK, MK1 and MK2, as well as the corresponding measured $S(f)$. The measured signals were split into 2048 data points segments. Each segment multiplied by a cosine-taper window with the taper ratio of 0.05 to reduce the end effects. The measured spectrum is obtained by ensemble averaging over the computed spectra of 11, 8, 7 segments for BK, MK1 and MK2 respectively and then band averaging over 5 neighboring bands. The resultant averaged spectra of BK, MK1 and MK2 have 110, 80 and 70 degrees of freedom, respectively. The sampling rate was 25 Hz ($f_{Nyq} = 12.5\text{Hz}$) for BK and MK1 and 20 Hz ($f_{Nyq} = 10\text{Hz}$) for MK2. The spectral resolution for BK, MK1 and MK2 are $\Delta f = 0.06\text{Hz}$, 0.06Hz and 0.05Hz , respectively. The spectrum for the computed wave field is obtained in a similar way, with the same spectral resolution and degrees of freedom. The first two rows of Figure 5.18 show $S(f)$ outside the surf zone, while the other panels cover the entire surf zone up to a shallowest depth of $d \sim 3\text{cm}$. Comparing with the measurements, the model captures the evolution of $S(f)$ in the shoaling region as well as in the surf zone fairly well. We used the measured surface elevation time series at $d = d_0$ as an input, and, thus, the infra-gravity waves are introduced in the domain as in the experiment. The more pronounced predicted energy at this frequency range ($f/f_p \approx 0.5$) compared with measurements at shoreward cross-shore locations is due to the absence of lateral side walls effects and the reflection from the upstream numerical boundary, which is located closer than the physical wavemaker used in the experiment to the plane slope, especially in MK1 and MK2. In addition the input low frequency climate is not exactly the same as in the measurement. The reason is that, we impose the input low frequency signal as a progressive wave at the numerical boundary while it was a standing wave in the measurement.

We can conclude that the integral breaking-induced dissipation is captured by the model, using as few as 4 σ levels. In addition, an asymptotic f^{-2} spectral shape of

the wave spectrum in the inner surf zone (Kaihatu et al. 2007), due to the sawtooth-like shape of surf zone waves, is fairly reasonably captured by the model in all cases.

5.4.2.2 Wave Statistics

Second-order wave statistics such as a significant wave height and a significant wave period, characterize the relative strength/forcing of irregular waves which need to be estimated for different coastal/inner-shelf related calculations and designs. These may be defined based on the wave spectrum, $S(f)$, as a significant wave height $H_{m_0} = 4m_0^{1/2}$ and the mean zero-crossing period $T_{m_{02}} = (m_0/m_2)^{1/2}$, where $m_n = \int f^n S(f) df$, is the n th order moment of $S(f)$, or based on the statistics of a fairly large number of waves (Figure 5.19, first row) extracted from the associated surface elevation time series by using the zero-up crossing method. The second and third rows of Figure 5.19 show the cross-shore variations of the model predictions of $\bar{\eta}$, H_{m_0} , $T_{m_{02}}$ together with $H_{1/10}$ and $T_{1/10}$ which represent the averaged wave height and period of the one-tenth highest waves, using 4 and 8 σ levels as well as the corresponding measured values for the random breaking cases, BK, MK1 and MK2. At the very shallow depths $d < 0.05\text{cm}$ the model predictions of $H_{1/10}$ and $T_{1/10}$ deviates considerably from the measurements. This deviation is mainly due to the relatively higher energy of infra-gravity waves in the model results compared with that in the measurements, as discussed in the previous section. To eliminate the infra-gravity and very high frequency wave effects, both the measured and computed ensemble-averaged $S(f)$ have been band-pass filtered with limits $0.25f_p < f < 8.0f_p$, and then H_{m_0} and $T_{m_{02}}$ are obtained based on the resultant band-pass filtered spectra. Such deviations at the shallow depths does not exist between the model results of H_{m_0} and $T_{m_{02}}$ and the measurements. Comparing with the measurements, the model fairly reasonably predicts these second-order bulk statistics both in plunging and spilling dominated random breaking cases.

As waves propagate from deep into shallower depths, crests and troughs become sharper and wider, respectively. Furthermore, waves pitch forward, and in the surf zone, the waveform becomes similar to a sawtoothed form. Normalized wave skewness=

$\overline{\eta^3}/(\overline{\eta^2})^{3/2}$, and asymmetry = $\overline{\mathcal{H}(\eta)^3}/(\overline{\eta^2})^{3/2}$ (where \mathcal{H} denotes the Hilbert transform of the signal), are the statistical third-order moments characterizing these nonlinear features of a wave shape (Elgar & Guza 1985, Mase & Kirby 1992). Skewness and Asymmetry are the statistical measures of asymmetry about horizontal and vertical planes, respectively. These third-order moments are potentially useful for sediment transport and morphology calculations. The bottom row of Figure 5.19 shows the cross-shore variation of the predicted third-order bulk statistics from outside the surf zone to the swash region. Comparing with the measurements, the model accurately captures the nonlinear effects, including the energy transfer due to triad nonlinear interaction, in the entire water depths, using as few as 4 σ levels.

5.4.2.3 Time-averaged Velocity and \bar{k}

Although the only available data from Bowen & Kirby (1994) and Mase & Kirby (1992) are the free surface time series at different cross-shore locations, the predicted time-averaged velocity and \bar{k} fields are presented and compared with those of regular breaking waves.

Figure 5.20 shows the spatial distribution of the time-averaged velocity field using 4 and 8 σ levels for MK2. The normalized undertow current for the irregular wave cases have smaller magnitude than that for regular wave cases TK1 and TK2 with the same vertical structures within the surf zone. This is consistent with the measurements of Ting (2001) which has the similar incident wave conditions and experimental set-up compared with the simulated irregular breaking waves on a planar beach in the present study. In addition, the results with 4 σ levels have a nearly constant curvature at lower depths as oppose to the results with 8 levels where the curvature of the return current decreases at lower depths.

Ting (2001) observed that the mean of the highest one-third wave-averaged k values in his irregular waves in the middle surf zone was about the same as \bar{k} in a regular wave case TK1, where deep-water wave height to wavelength ratio of those two cases was on the same order. Here, the normalized \bar{k} values are at the same order or

even larger than those in regular breaking cases in the middle and inner surf zone. In the outer surf zone, however, the normalized \bar{k} values are smaller than those under regular breaking cases. Although the \bar{k} values decrease near the bottom in the outer surf zone similar to regular breaking cases, they have small vertical and cross-shore variations in the inner surf zone.

5.5 Depth-limited Breaking Waves on a Barred Beach

In this section, we use the data set of [Scott et al. \(2004\)](#), including a regular breaking case (hereafter referred as S1) and irregular breaking case (hereafter referred as S2), in order to examine the model predictions of free surface evolution as well as breaking-induced velocity and turbulence fields in depth-limited breaking waves on a barred beach. The experiment was conducted in the large wave flume at Oregon State University, approximately 104m long, 3.7m wide, and 4.6m deep. The bathymetry was designed to approximate the bar geometry for the averaged profile observed on October 11, 1994, of the DUCK94 field experiment at a 1:3 scale. The velocity measurements were carried out at 7 cross-shore locations using Acoustic Doppler Velocimeters (ADVs) sampling at 50 Hz. [Figure 5.22](#) sketches the experimental layout and the cross-shore locations of the available free-surface and velocity measurements. The regular case S1 is used by [Jacobsen et al. \(2014\)](#) to validate their 2D VOF-based model using RANS equations with $k - \omega$ turbulence closure. Here, both regular and irregular cases are considered; the corresponding results are given in §4.1 and §4.2 respectively. For both cases, a uniform grid of $\Delta x = 0.15\text{m}$ is used in the horizontal direction. Vertical resolutions of 4 and 8 σ levels are used. The right end of the numerical domain is extended beyond the maximum run-up, and the wetting/drying cells are treated by setting $D_{min} = 0.001\text{m}$ for both S1 and S2.

5.5.1 Regular Breaking Waves

[Table 5.3](#) summarizes the incident wave conditions for S1. The cross-shore location of the numerical wavemaker is set to be as the initial position of the physical

Table 5.3: Input parameters for the simulated depth-limited regular breaking waves on a barred beach. Here, H_0 and L_0 are the deep water wave height and wave length calculated using linear theory, $(kH)_0$ is the corresponding deep water wave steepness of the generated wave, $\xi_0 = s/\sqrt{H_0/L_0}$ is the self similarity parameter, and s is the averaged slope before the bar, assumed as $s \sim 1/12$. For the irregular wave case S2, $H = H_{s0}$ is the deep-water characteristic wave height, $T = T_p$ and $k = k_p$, where p refers to the peak frequency of the incident waves.

Case no.	H_0 (m)	T (s)	$(kH)_0$	ξ_0	breaking type
S1	0.64	4.0	0.148	0.52	plunging
S2	0.59	4.0	0.136	0.54	plunging

wavemaker. The measured free surface and velocities determined from linear theory are constructed at the wavemaker using the first 10 Fourier components of the measured free surface time series in front of the wavemaker. In this section, $\langle \rangle$ and $\overline{(\)}$ refer to phase and time averaging over five subsequent waves after the results reach the quasi-steady state, respectively. The corresponding measured averaged variables were calculated by phase averaging over 150 successive waves and ensemble averaging over at least 8 realizations.

The mean sea level is defined as $h = d + \bar{\eta}$, where d is the still water depth and $\bar{\eta}$ is the wave set-down/set-up. Here, $x = 0$ is the cross-shore location of the wavemaker location. The regular waves were observed to plunge at $x = 53\text{m}$.

5.5.1.1 Time-dependent Free Surface Evolution

Figure 5.23 shows the cross-shore distribution of the wave height $H = \langle \eta \rangle_{max} - \langle \eta \rangle_{min}$ as well as mean water level, $\bar{\eta}$ in the primary shoaling region up to the top of the bar ($x < 52.8\text{m}$), the top of the bar ($52.8\text{m} < x < 56.5\text{m}$), the shoreward face of the bar ($56.5\text{m} < x < 60\text{m}$), and the secondary shoaling region after the bar ($x > 60\text{m}$) for the regular case S1. The underprediction of the wave height near the breaking point is

similar to that in TK1 as shown in Figure 5.2(a). Compared with measurements, wave height decay in the breaking region and shoreward face of the bar ($53\text{m} < x < 60\text{m}$) is captured reasonably well. In the secondary shoaling region after the bar ($x > 60\text{m}$), the overshoot of the wave height is not captured, as also seen in the VOF-based simulation of Jacobsen et al. (2014, Figure 4A). The mean water level is accurately resolved from deep water up to the swash zone, as opposed to the VOF-based simulation of Jacobsen et al. (2014, Figure 4B) which overpredicts wave set-up after the bar.

Figure 5.24 shows the phase-averaged water surface elevations at different cross-shore locations before and after the bar for S1. Although the time evolution of the free surface elevations are comparable with the measurements at all cross-shore locations, the crest is underpredicted near the break-point as shown in panel (c) and after the bar as shown in panels (f) and (g). The secondary peak in the measured phase-averaged free surface elevations at $x = 69.3\text{m}$ is also visible in the predicted results, while its crest elevation is underpredicted by the model. This secondary peak is due to the generation of the higher harmonics on top of the bar propagating with different phase speed than the primary wave. The predicted cross-shore location of the initial break point is slightly seaward compared with the measurements as in TK1, regardless of the different vertical resolutions. In both cases, the model captured the free surface evolution, wave height decay rate, crest and trough elevations, as well as wave set-up reasonably well using as few as 4 σ levels.

5.5.1.2 Time-averaged Velocity and \bar{k}

Figure 5.25 shows the spatial distribution of the time-averaged velocity field using different vertical resolutions for S1. To obtain the Eulerian mean velocities, the model results in the σ -coordinate system first were interpolated onto a fixed vertical mesh at each cross-shore location using linear interpolation, and then time averaging was performed. As in TK1, the predicted return current using 4 σ levels shown in 5.25(a) has not detached from the bed shoreward of the breaking point, as opposed to the simulation with 8 σ levels. The results of the simulations with different vertical

resolutions have approximately the same structure after the breaking point, where the predicted undertow current using 8 σ levels has larger magnitude in the entire surf zone. The curvature of the undertow profile has strong spatial variations near the break points as shown in Figure 5.26(c), where the amount of curvature of the undertow profile at $x = 48.0\text{m}$ (red lines) considerably decreases compared with that at $x = 51.0\text{m}$ (black lines). This is due to the detachment of the undertow current from the bed, forming negative slopes at seaward of the break point. Figure 5.26(c) also shows that the model predicts breaking seaward of the measured break point. Finally, the measured undertow profiles at two different longshore locations (shown by open and solid circles) reveal that the time-averaged velocity field has strong variation in the spanwise direction close to the break point; the 3D effects are absent in our 2D simulation. Compared with the measured undertow profiles (Figure 5.26), the undertow current is resolved on top of and after the bar using as few as 4 σ levels.

Figure 5.27 shows the spatial distribution of \bar{k} using different vertical resolutions for S1. The values of the normalized time-averaged k , $\sqrt{\bar{k}/gh}$, are similar to those in TK1 and TK2 in the outer surf zone. Figure 5.28 shows the predicted \bar{k} profiles at the different cross-shore locations before, on the top of, and after the bar together with the corresponding measurements. Compared with the measurements, it is seen that the model predicts fairly reasonably the cross-shore variation of the breaking-induced turbulence using 4 σ levels, with the large k levels across the breaker bar, where the waves are breaking, and the subsequent decay of k level on the seaward face as well as after the bar.

5.5.2 Irregular Breaking Waves

The random waves of S2 were generated based on a TMA spectrum with a width parameter $\gamma = 20$ to generate the initial condition at the wavemaker. Table 5.3 summarizes the incident wave conditions for S2. The cross-shore location of the numerical wavemaker is set to be as the initial position of the physical wavemaker. The measured free surface and velocities determined from linear theory are constructed at

the wavemaker using the first 2000 Fourier components of the measured free surface time series in front of the wavemaker. In this section, $\overline{(\quad)}$ refers to long-time averaging over several minutes, more than 250 waves. The first 2500 data points were ignored both in the model and results and the corresponding experiment.

The mean sea level is defined as $h = d + \bar{\eta}$, where d is the still water depth and $\bar{\eta}$ is the wave set-down/set-up. Here, $x = 0$ is the cross-shore location of the wavemaker location. The random waves were observed to be both plunging and spilling as far offshore as $x = 42\text{m}$.

5.5.2.1 Power spectra evolution and integral breaking-induced dissipation

Here, we examine the model prediction of the integral breaking-induced dissipation compared with the corresponding measurements by looking at the evolution of the power spectral density, $S(f)$, across a fixed bar.

Figure 5.29 shows the variation of computed $S(f)$ using 4 and 8 σ levels for the random breaking case S2 as well as the corresponding measured $S(f)$. The measured signals were split into 8196 data points segments. Each segment multiplied by a cosine-taper window with the taper ratio of 0.05 to reduce the end effects. The measured spectrum is obtained by ensemble averaging over the computed spectra of 7 segments and then band averaging over the 5 neighboring bands. Thus the resultant averaged spectra have 70 degrees of freedom. The sampling rate was 50 Hz ($f_{Nyq} = 25\text{Hz}$). The spectrum resolution is $\Delta f = 0.03\text{Hz}$. The computed spectrum is obtained in a similar way, with the same spectral resolution and degrees of freedom. Panels (a),(b), and (c) show the $S(f)$ in the shoaling zone before the break point $x = 53\text{m}$. The decrease of energy at the dominant peak frequency and increase of energy at higher and lower harmonics before the breaking region due to the nonlinear interaction, shown at panel (c), as well as the decrease of energy at the dominant peak frequency and higher frequency range across the bar, shown in panel (d), are captured by the model using 4 σ levels. However, the energy at low-frequency range is overpredicted while the energy at the second harmonic is underpredicted across and after the bar. No wave absorption

at the wavemaker exists both in the simulation and the experiment, and thus the reflected long waves from the bar and the beach face are reflected back in the domain as in the experiment. The more pronounced predicted energy at this frequency range ($f/f_p \approx 0.5$) comparing with the measurements may be due to the inherent difference between the numerical wavemaker and that in the experiment and the absence of lateral side walls effects in the present 2D simulation. The underprediction of the second harmonics across the bar is unresolved.

5.5.2.2 Wave Statistics

Figure 5.30(a) shows the cross-shore variations of the model predictions of $\bar{\eta}$, H_{m_0} , $T_{m_{02}}$, normalized wave skewness, and normalized wave asymmetry using 4 and 8 σ levels as well as the corresponding measured values for the random breaking case S2. These bulk statistics are calculated as explained in §3.2.1. Comparing with the measurements, the model fairly reasonably predicts the wave set-down/set-up as well as the second- and third-order bulk statistics for S2 using 4 σ levels. As in the regular case S1 (Figure 5.23a), the wave height after the bar, $x > 60\text{m}$, is underpredicted.

5.5.2.3 Time-averaged Velocity and k field

Figure 5.31 shows the spatial distribution of the time-averaged velocity field using different vertical resolutions of 4 and 8 levels for S2. The Eulerian mean velocities were obtained as described before. The predicted undertow current using 4 and 8 σ levels have approximately the same structure and magnitude in the surf zone, and have the smaller magnitude compared with those under the regular case S1. Comparing the results with the measured undertow profiles shown in Figure 5.32, the undertow current is reasonably well captured across the bar and trough using as few as 4 σ levels, with smaller amount of curvature at lower depths which is partially because of the underprediction of the k and as a result the underprediction of the turbulent eddy viscosity at those depths, as explained in §3.1.2.

Figure 5.33 shows the spatial distribution of the time-averaged k field using different vertical resolutions for S2. The values of the normalized time-averaged k , \sqrt{k}/gh , are smaller than those in the regular case S1 in the entire surf zone, having the same structure near the bar and the steep beach. Figure 5.34 shows the predicted time-averaged k profiles at the different cross-shore locations before, on the top of, and after the bar together with the corresponding measurements. Compared with the measurements, it is seen that using 4 σ levels the model predicts fairly reasonably the cross-shore variation of the breaking-induced turbulence as in the regular case S1.

5.6 Steepness-limited Unsteady Breaking Waves

The data sets of Rapp & Melville (1990) and Tian et al. (2012) are considered to study the model capability and accuracy for breaking-induced processes in steepness-limited unsteady breaking waves. Here, the model results for the two unsteady plunging breakers of Rapp & Melville (1990), hereafter referred as RM1 and RM2, in an intermediate depth regime with $k_c d \approx 1.9$ and one of the plunging cases of Tian et al. (2012), hereafter referred as T1, in a deep water regime with $k_c d \approx 6.9$ are presented, where k_c is the wave number of the center frequency wave of the input packet defined below. The evolution of the free surface, mean velocity field and large mean vortex under isolated breaking case RM1 are compared to the corresponding measurements and the results of the VOF-based simulation of Derakhti & Kirby (2014a). Integral breaking-induced energy dissipation under an isolated steepness-limited unsteady breaking wave is examined for RM2. In addition, the power spectral density evolution as well as integral breaking-induced energy dissipation under multiple steepness-limited unsteady breaking waves are examined for T1.

In both experiments, breaking waves were generated using the dispersive focusing technique, in which an input packet propagates over an constant depth and breaks at a predefined time, t_b , and location, x_b . The input wave packet was composed of N sinusoidal components of steepness $a_i k_i$ where the a_i and k_i are the amplitude and wave number of the i th component. Based on linear superposition and by imposing that the

maximum $\langle \eta \rangle$ occurs at x_b and t_b , the total surface displacement at the incident wave boundary can be obtained as (Rapp & Melville 1990, §2.3)

$$\langle \eta \rangle(0, t) = \sum_{i=1}^N a_i \cos[2\pi f_i(t - t_b) + k_i x_b], \quad (5.1)$$

where f_i is the frequency of the i th component. The discrete frequencies f_i were uniformly spaced over the band $\Delta f = f_N - f_1$ with a central frequency defined by $f_c = \frac{1}{2}(f_N - f_1)$. Different global steepnesses $S = \sum_{i=1}^N a_i k_i$ and normalized band-widths $\Delta f / f_c$ lead to spilling or plunging breaking, where increasing S and/or decreasing $\Delta f / f_c$ increases the breaking intensity (See Drazen et al. (2008) for more details). In the numerical wavemaker, free surface and velocities of each component are calculated using linear theory and then superimposed at $x = 0$. Sponge levels are used at the right boundary to minimize reflected waves. The input wave parameters for different cases are summarized in table 5.4.

The normalized time and locations are defined as

$$x^* = \frac{x - x_{ob}}{L_c}, \quad z^* = \frac{z}{L_c}, \quad t^* = \frac{t - t_{ob}}{T_c}, \quad (5.2)$$

where T_c and L_c are the period and wavelength of the center frequency wave of the input packet, respectively. Here, t_{ob} and x_{ob} are the time and location at which the forward jet hits the free surface, obtained from corresponding VOF simulations of Derakhti & Kirby (2016).

5.6.1 Time-dependent Free Surface Evolution

Figure 5.35 shows the free surface evolution in the breaking region for RM1 using 8 σ levels. Figure 5.36 shows the free surface time series at locations before and after the break point, showing that the model captures the free surface evolution up to the break point fairly accurately. The overall wave height decay is also predicted reasonably well. However, the sudden drop of the crest during active breaking is not

Table 5.4: Input parameters for the simulated focused wave packets. d is the still water depth, $S = \sum_{i=1}^N a_i k_i$ is the global steepness, N is the number of components in the packet, $a_i k_i$ is the component steepness which is the same for the all components, and the discrete frequencies f_i were uniformly spaced over the band $\Delta f = f_N - f_1$ with a central frequency defined by $f_c = \frac{1}{2}(f_N - f_1)$.

Case no.	d (m)	S	f_c (1/s)	$\Delta f/f_c$	N	breaking type
<i>RM1</i>	0.60	0.352	0.88	0.73	32	plunging
<i>RM2</i>	0.60	0.388	0.88	0.73	32	plunging
<i>T1</i>	0.62	0.576	1.70	0.824	128	plunging

resolved.

Figure 5.37 shows the water surface elevations at different x locations for T1 using 8 σ levels. Nearly all the input wave components are in the deep water regime ($d/L_i > 0.5$), and thus the packet is highly dispersive. Multiple breaking was observed in the experiment between $x^* \approx -1$ and $x^* \approx 1$, where $x^* = 0$ is the x location of the main breaking event in the packet. The model captures the packet propagation and evolution accurately. The focusing of dispersive waves before the break point can be seen at panels (a) through (c) with decrease in the number of waves and increase of the maximum crest elevation. Downstream of the breaking region (Figure 5.37e and f), the results indicate that the wave height decay due to multiple unsteady breaking events, as well as dispersive properties of the packet, are captured by the model reasonably well.

5.6.2 Integral Breaking-Induced Dissipation

In this section, the predicted integral breaking-induced dissipation is compared to the corresponding measurements by looking at the evolution of the time-integrated energy density, $\overline{\rho g \eta^2}$, as well as the power spectral density. In this section, $\overline{(\quad)}$ refers to long-time integration over the entire wave packet.

Strictly speaking, $\overline{\rho g \eta^2}$ is twice the time-integrated potential energy density, $\overline{E_p}$, and, to a good approximation, can be considered as the time-integrated total energy density far from the breaking region. By choosing an appropriate characteristic group velocity, $C_g \overline{\rho g \eta^2}$ is then used as an estimation of the time-integrated total horizontal energy flux, \overline{F} . Thus, the spatial variation of $\overline{\rho g \eta^2}$ is related to total breaking-induced dissipation for unsteady breaking waves, as explained by [Derakhti & Kirby \(2016\)](#) in detail. Figure 5.38 shows the variation of $\overline{\eta^2}/\overline{\eta_1^2}$ for the intermediate depth unsteady breaking case, RM2, using different horizontal and vertical resolutions. The predicted integral dissipation is underestimated comparing with the measurements. In addition, the predicted decay of $\overline{E_p}$ occurs at a larger down wave distance compared with the measurements, and the sudden drop of the potential energy density is not resolved.

Here, the entire dissipation is imposed by the shock-capturing TVD scheme in these cases. In other words, the turbulence model has not been triggered, and ν_t is approximately zero. It is well known that the numerical dissipation applied by TVD schemes decreases as the grid resolution increases. In breaking waves, the large gradient in a velocity field occurs near the sharp wave front and in the horizontal direction. As expected, by decreasing the horizontal resolution from $\Delta x = 23\text{mm}$ to $\Delta x = 10\text{mm}$ the total decay of $\overline{E_p}$ becomes smaller, whereas the associated change in $\overline{E_p}$ due to further decrease of Δx from 10 mm to 5 mm is negligibly small. Increasing the vertical resolution, on the other hand, improves the results. Similar behavior is observed in other cases (not shown).

Figure 5.39 shows the evolution of different spectral components in the wave packet for T1, and the corresponding measurements of [Tian et al. \(2012\)](#). The measured spectrum is obtained by ensemble averaging over 5 runs and then band averaging over three neighboring bands (30 degrees of freedom) with a spectral resolution of $\Delta f = 0.075\text{Hz}$, where the signal length is 40 s, and the sampling rate is 100 Hz. The computed spectrum is based on a single realization with the same length and sampling rate. In general, the energy of the high frequency ($f/f_c > 2$) part of the spectrum is underestimated due to a relatively coarse vertical resolution of the model which can not

resolved fast decay of short-waves orbital velocities with depth. The nonlinear energy transfer into low-frequency components ($f/f_c < 0.5$), however, is fairly reasonably resolved. Energy is dissipated mostly in the frequency range $0.75 < f/f_c < 1.5$, as shown in panels (e) and (f). Close to the break point, the model does not capture the sudden dissipation of energy, especially for larger frequencies (Figure 5.39c). The predicted spectrum becomes more similar to the measured spectrum as the packet propagates away from the breaking region.

5.6.3 Velocity Field

Comprehensive experimental work by Rapp & Melville (1990) and Drazen & Melville (2009) has revealed the main characteristics of the ensemble-averaged flow field under unsteady breaking waves, especially after active breaking. Rapp & Melville (1990) measured the velocity field using LDV at seven elevations and seven x locations in the breaking region. Figure 5.40 shows the normalized horizontal and vertical velocities at $x^* = 0.60$, $z^* = -0.025$ for RM1 using 10 σ levels versus the corresponding unfiltered measured ensemble-averaged signals. After breaking, the larger velocities compared with the measurements also demonstrates the underprediction of the breaking-induced dissipation shown in Figure 5.38.

The ensemble-averaged velocity field can be decomposed into

$$\langle \mathbf{u} \rangle = \mathbf{u}_w + \mathbf{u}_{fw} + \mathbf{u}_c, \quad (5.3)$$

where \mathbf{u}_w is the orbital velocity of the surface waves, \mathbf{u}_{fw} is the velocity of the forced long-waves induced by breaking, and \mathbf{u}_c is the current stemming from the momentum loss during the breaking and/or Stokes drift. The rest of the available measured velocity signals are low-pass filtered using the threshold frequency of 0.3 Hz, to remove the surface waves as in Rapp & Melville (1990), where the frequency range of the input surface waves is $0.56 < f_i < 1.20$. Figure 5.41 shows the low-pass filtered results and the corresponding measurements for RM1 at $x^* = 0.15$ and $x^* = 0.60$, from very close

to the free surface to $z^* = -0.15$ ($\approx z = -d/2$). The smaller low-passed filtered velocity field is due to the smaller wave dissipation and smaller wave forcing, predicted by the model.

The mean current can be calculated by time averaging of the ensemble-averaged velocity signal,

$$\mathbf{u}_c = \bar{\mathbf{u}} = \frac{1}{t_2^* - t_1^*} \int_{t_1^*}^{t_2^*} \langle \mathbf{u} \rangle dt^*, \quad (5.4)$$

where t_1^* and t_2^* cover the entire wave packet. During time integration for each grid point, when the point is above the free surface the velocity signal is zero. Figure 5.42 shows the spatial distribution of the normalized mean current and its horizontal-averaged between $x^* = 0$ and 1.5, as well as the normalized horizontal-averaged mass flux below the depth z^* , $\widehat{M}^*(z^*) = \int_{z_1^*}^{z^*} \widehat{u}_c^* dz^*$ where $z_1^* = -0.31$ is the bottom elevation, for RM1 using 8 σ levels (top panels) together with the LES/VOF results by Derakhti & Kirby (2014a) (bottom panels). The positive current near the surface, the return negative current at lower depths and the two distinct circulation cells are captured by the model as in the LES/VOF results. Comparing with the measurements of (Rapp & Melville 1990, Figure 43) and the LES/VOF simulation, we can see that the model generated a large mean vortex with relatively stronger velocity field. We believe this is due to the absence of an enhanced eddy viscosity that would be present as a result of the turbulence, which was not captured by NHWAVE in unsteady breaking cases. In addition, the model predicts relatively larger cells than those predicted by the LES/VOF simulation, especially in the x direction. The predicted patch of persistent vorticity (not shown) is consistent with Drazen & Melville (2009, Figure 4) and the LES/VOF simulation of Derakhti & Kirby (2014a, Figure 4.16), having larger vorticity values due to underestimation of effective viscosity in the absence of turbulence.

5.7 Conclusions

In this paper, we examined wave-breaking predictions ranging from shallow- to deep-water conditions using a surface-following, shock-capturing 3D non-hydrostatic

model, NHWAVE (Ma et al. 2012), comparing results both with corresponding experiments and with outcomes of a VOF/Navier-Stokes solver (Ma et al. 2011, Derakhti & Kirby 2014b,a). The new version of NHWAVE has been described in Derakhti et al. (2016a), including the new governing equations and exact surface and bottom boundary conditions. We considered regular and irregular depth-limited breaking waves on planar and barred beaches as well as steepness-limited unsteady breaking waves in intermediate and deep depths. The same equations and numerical methods are used for the various depth regimes and involve no ad-hoc treatment. Vertical grid resolution in all simulated cases is at least an order of magnitude coarser than that of typical VOF-based simulations. The main conclusions can be categorized as follows.

(a) Depth-limited breaking waves: using as few as 4 σ levels, the model was shown to accurately predict depth-limited breaking wave properties in terms of (1) time-dependent free-surface and mean velocity field evolution, (2) integral breaking-induced dissipation, (3) second- and third-order bulk statistics, and (4) breaking-induced organized motion both on a planar and barred beaches. In addition, the model is shown to predict k distributions under troughs as accurate as those predicted by typical VOF-based simulations without bubble effects. As it was explained by Derakhti et al. (2016a), the new boundary conditions significantly improve the predicted velocity and turbulence fields under depth-limited breaking waves compared with the commonly used simplified stress boundary conditions, ignoring the effects of surface and bottom slopes in the transformation of stress terms. The k prediction above the troughs may be further improved by replacing the zero gradient boundary condition for k and/or the zero-stress tangential stress boundary with a physics-based model such as the model proposed by Brocchini & Peregrine (2001), Brocchini (2002). Under strong plunging breakers, the rapid advection of high k to lower depths can not be captured by the model due to the unresolved jet impact and subsequent splash processes. It was found that this turbulence underprediction, and thus the underprediction of the turbulent eddy viscosity, can not be improved by increasing the number of σ levels. As a result, the amount of the curvature of undertow profiles are overpredicted in the

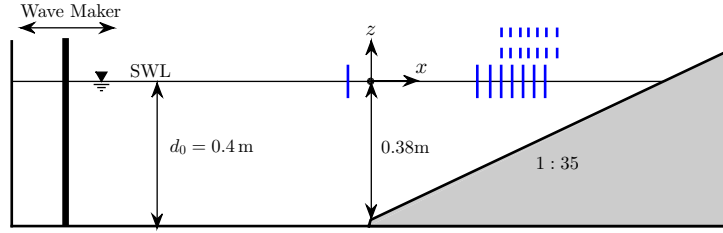


Figure 5.1: Experimental layout of [Ting & Kirby \(1994\)](#). Vertical solid lines: the cross-shore locations of the velocity measurements for TK1. Vertical dashed lines: the cross-shore locations of the velocity measurements for TK2.

events where the breaking is characterized as strong plunging.

(b) Steepness-limited breaking waves: it was shown that all the dissipation was imposed indirectly by only the TVD shock-capturing scheme, and the turbulence model had not been triggered. Although the absence of turbulence in deep water breaking waves predictions led to the underestimation of the total breaking-induced dissipation, and, thus, the overprediction of the velocity and vorticity field in the breaking region, the model was shown to predict (1) the dispersive and nonlinear properties of different wave packet components before and after the break point, (2) the overall wave height decay and spectral evolutions, and (3) the structures of the mean velocity and vorticity fields including large breaking-induced coherent vortices. The near-surface turbulence model for whitecap events, e.g., the model proposed by [Brocchini \(2002\)](#) to set boundary condition for k , is needed to provide sufficient k levels during active breaking, with which the model will produce the turbulence field, leading to an enhance eddy viscosity and an appropriate amount of breaking-induced dissipation in the breaking region.

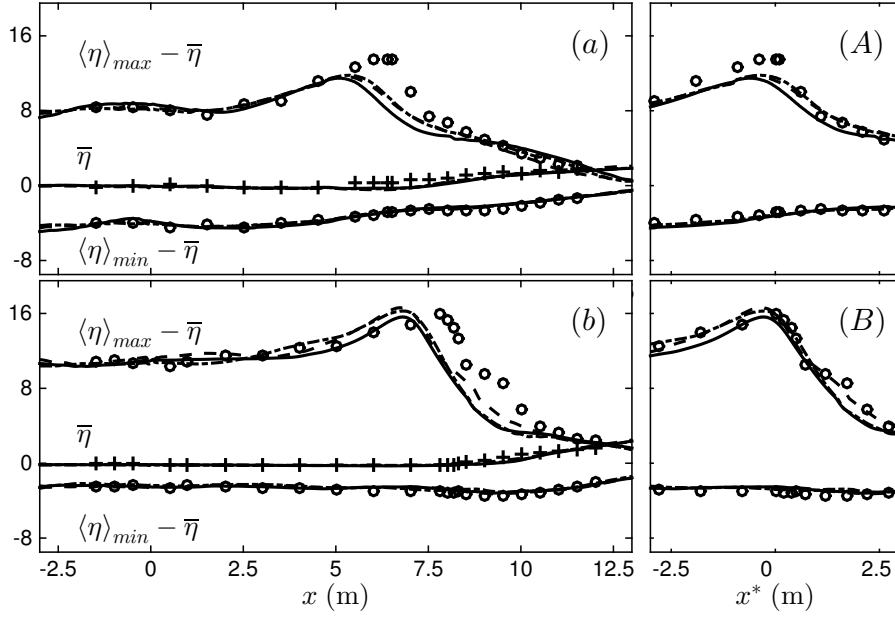


Figure 5.2: Cross-shore distribution of crest and trough elevations as well as mean water level for the surf zone (a,A) spilling breaking case TK1 and (b,B) plunging breaking case TK2. Comparison between NHWAVE results with 4 σ levels (dashed lines), 8 σ levels (dotted-dashed lines), 16 σ levels (solid lines) and the measurements of [Ting & Kirby \(1994\)](#) (circle markers). In panels (A) and (B), $x^* = x - x_b$ represents the horizontal distance from the break point.

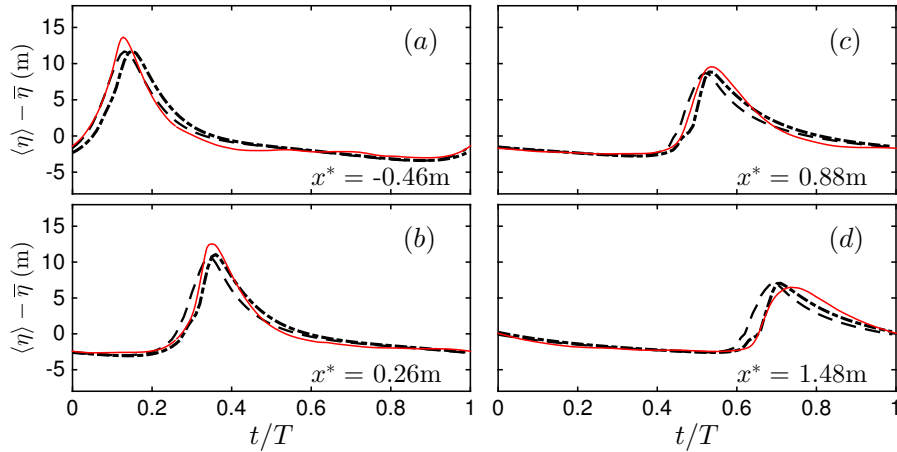


Figure 5.3: Phase-averaged free surface elevations for the surf zone spilling breaking case TK1 at different cross-shore locations before and after the initial break point $x^* = 0$. Comparison between NHWAVE results with 4 σ levels (dashed lines), 8 σ levels (dotted-dashed lines) and the measurement (thin red solid lines).

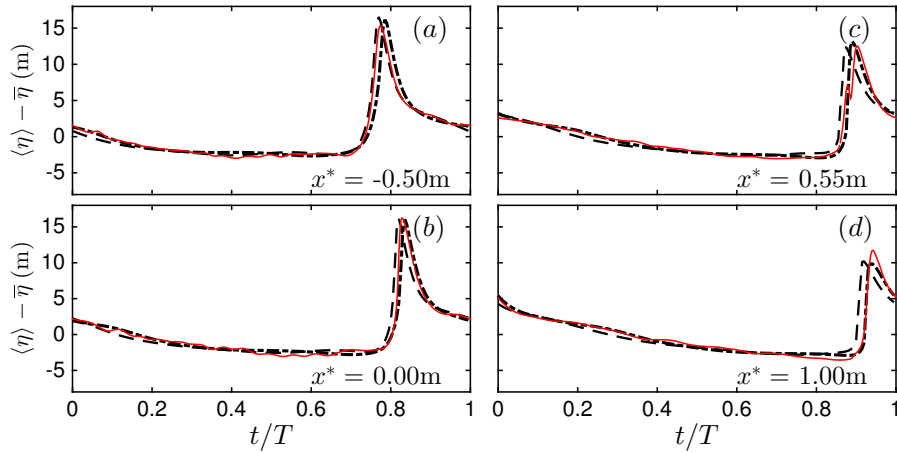


Figure 5.4: Phase-averaged free surface elevations for the surf zone plunging breaking case TK2 at different cross-shore locations before and after the initial break point $x^* = 0$. Comparison between NHWAVE results with 4 σ levels (dashed lines), 8 σ levels (dotted-dashed lines) and the measurement (thin red solid lines).

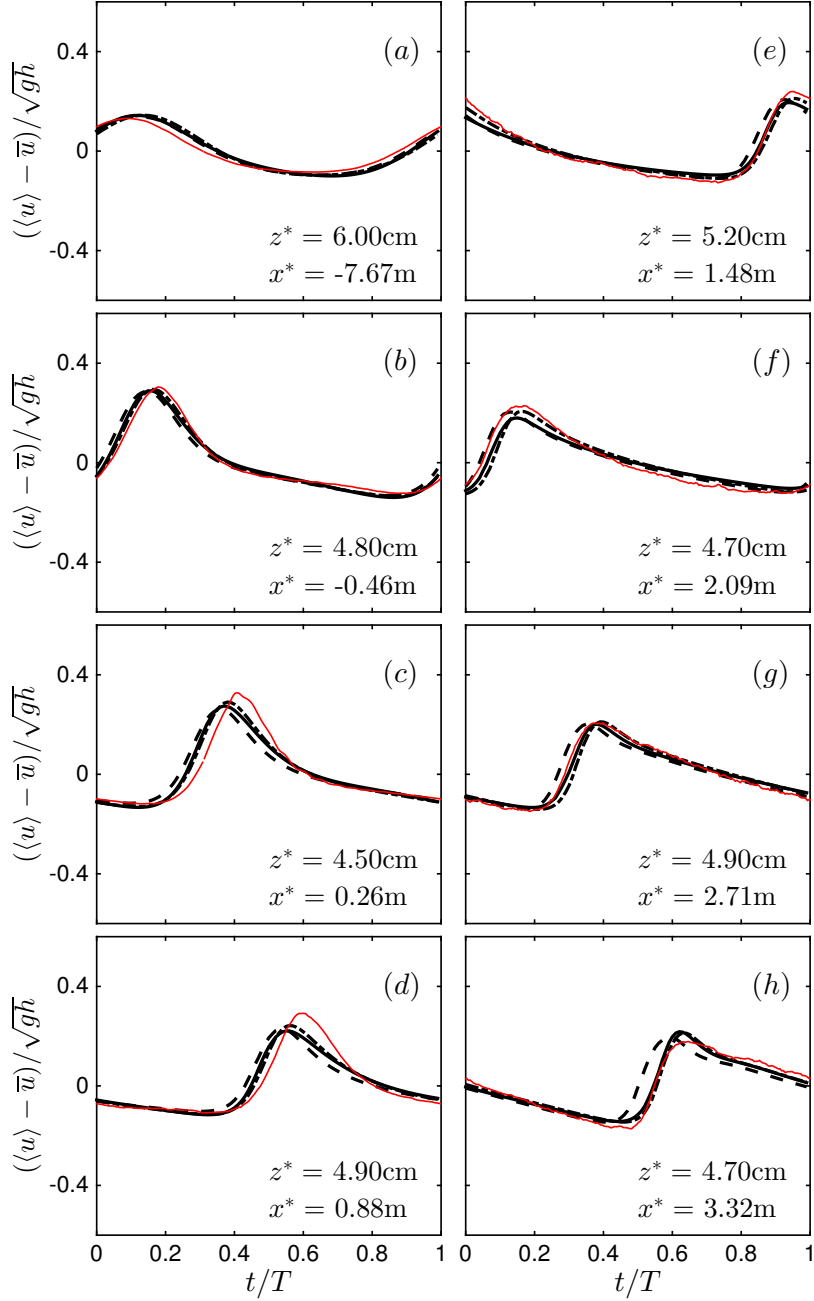


Figure 5.5: Phase-averaged normalized horizontal velocities for the surf zone spilling breaking case TK1 at about 5 cm above the bed (z^* is the distance from the bed), at different cross-shore locations before and after the initial break point $x^* = 0$. Comparison between NHWAVE results with 4 σ levels (dashed lines), 8 σ levels (dotted-dashed lines), 16 σ levels (thick solid lines) and measurements (thin red solid lines).

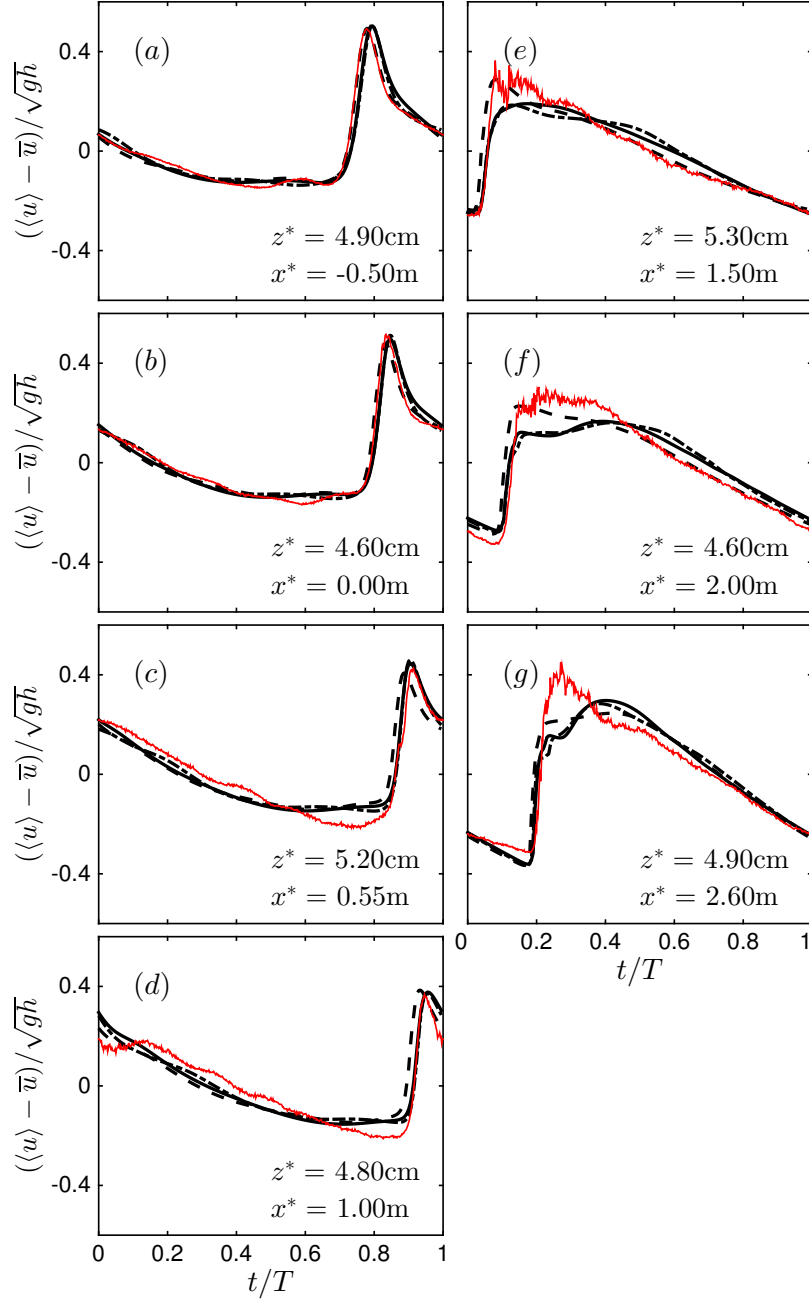


Figure 5.6: Phase-averaged normalized horizontal velocities for the surf zone plunging breaking case TK2 at about 5 cm above the bed (z^* is the distance from the bed), at different cross-shore locations before and after the initial break point $x^* = 0$. Comparison between NHWAVE results with 4 σ levels (dashed lines), 8 σ levels (dotted-dashed lines), 16 σ levels (thick solid lines) and measurements (thin red solid lines).

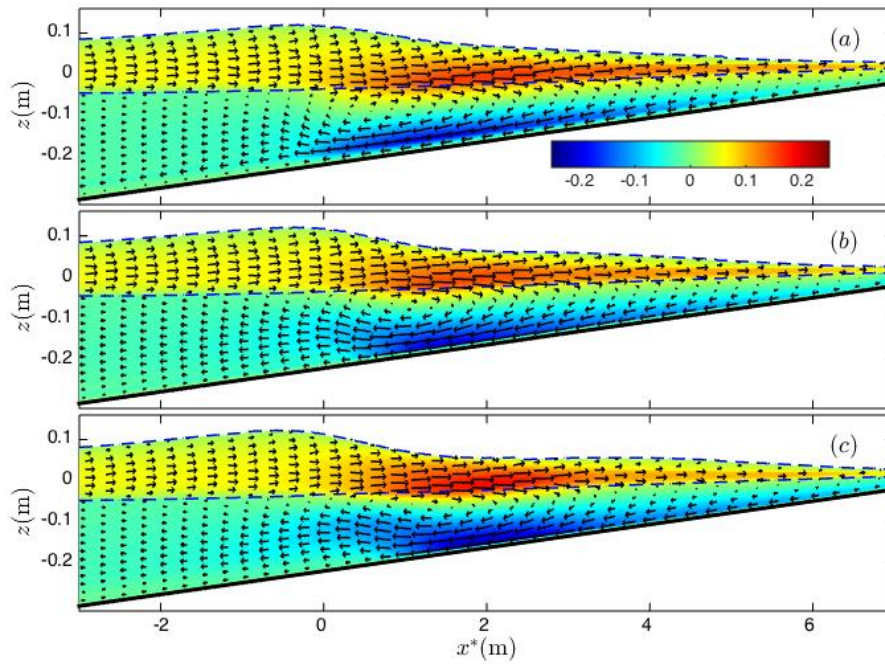


Figure 5.7: Time-averaged velocity field, $\bar{\mathbf{u}}$, for the surf zone spilling breaking case TK1. NHWAVE results with (a) 4 σ levels, (b) 8 σ levels, and (c) 16 σ levels. Dash lines show the crest $\langle \eta \rangle_{max}$ and trough $\langle \eta \rangle_{min}$ elevations. Colors show \bar{u}/\sqrt{gh} .

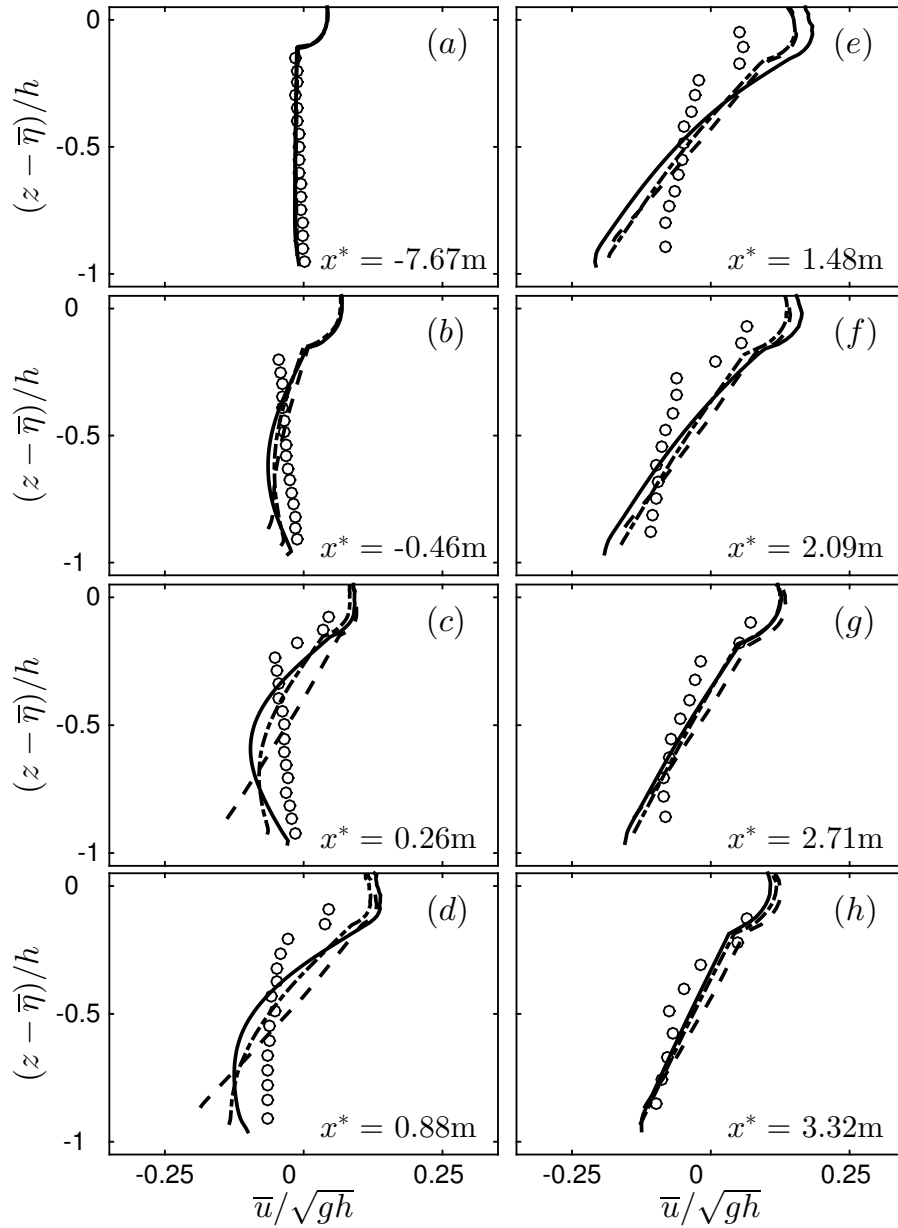


Figure 5.8: Time-averaged normalized horizontal velocity (undertow) profiles for the surf zone spilling breaking case TK1 at different cross-shore locations before and after the initial break point, $x^* = 0$. Comparison between NHWAVE results with 4 σ levels (dashed lines), 8 σ levels (dotted-dashed lines), 16 σ levels (solid lines) and the measurements (circle markers).

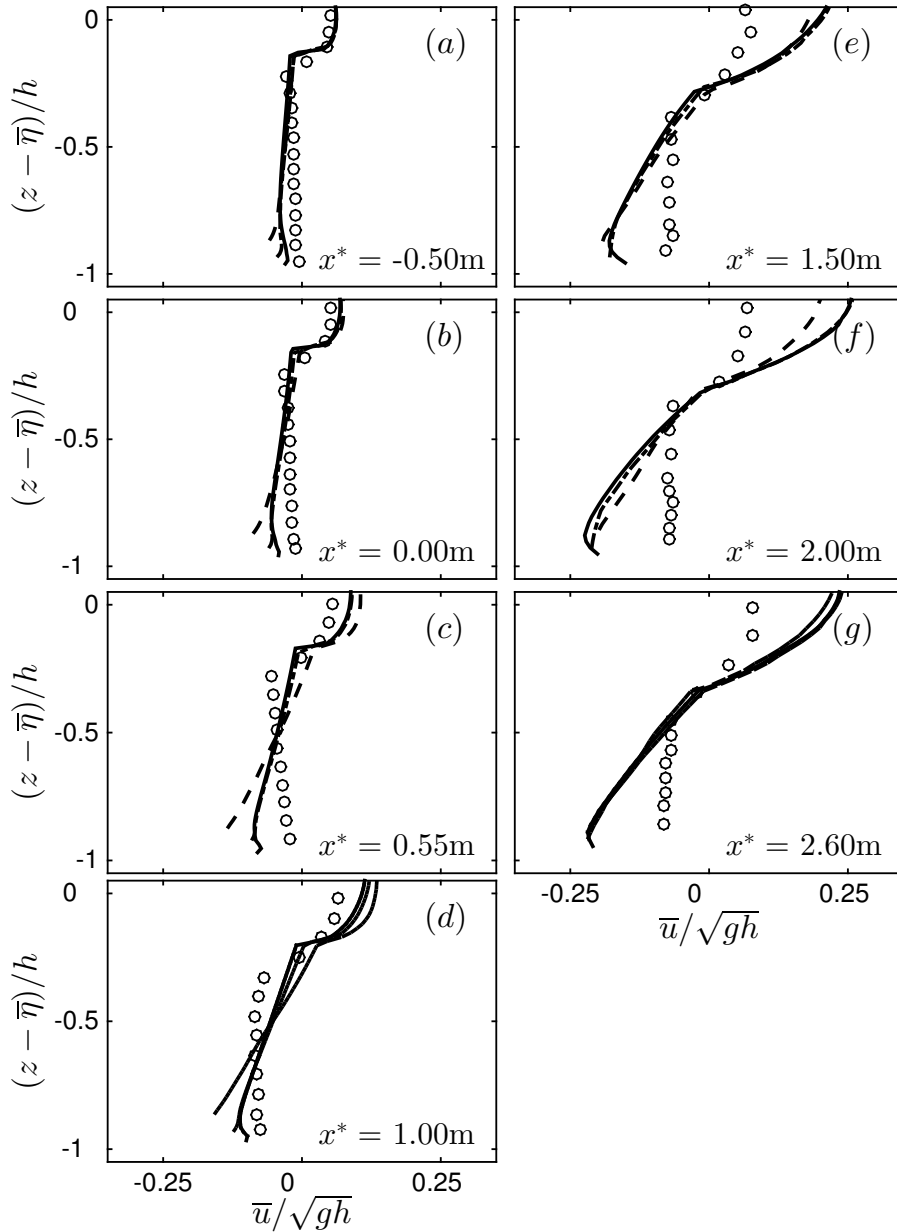


Figure 5.9: Time-averaged normalized horizontal velocity (undertow) profiles for the surf zone plunging breaking case TK2 at different cross-shore locations before and after the initial break point, $x^* = 0$. Comparison between NHWAVE results with 4 σ levels (dashed lines), 8 σ levels (dotted-dashed lines), 16 σ levels (solid lines) and the measurements (circle markers).

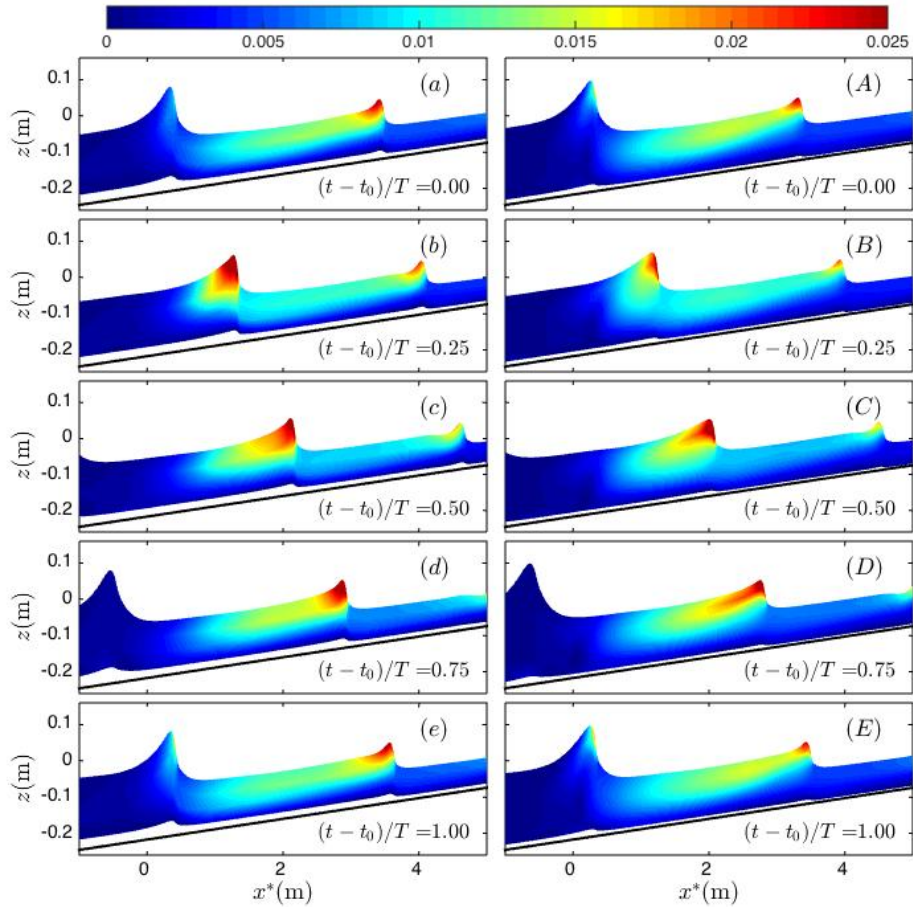


Figure 5.10: Snapshots of the turbulent kinetic energy, $k(\text{m}^2/\text{s}^2)$, distribution for the surf zone spilling breaking case TK1. NHWAVE results with (a – e) 4 σ levels and (A – E) 8 σ levels.

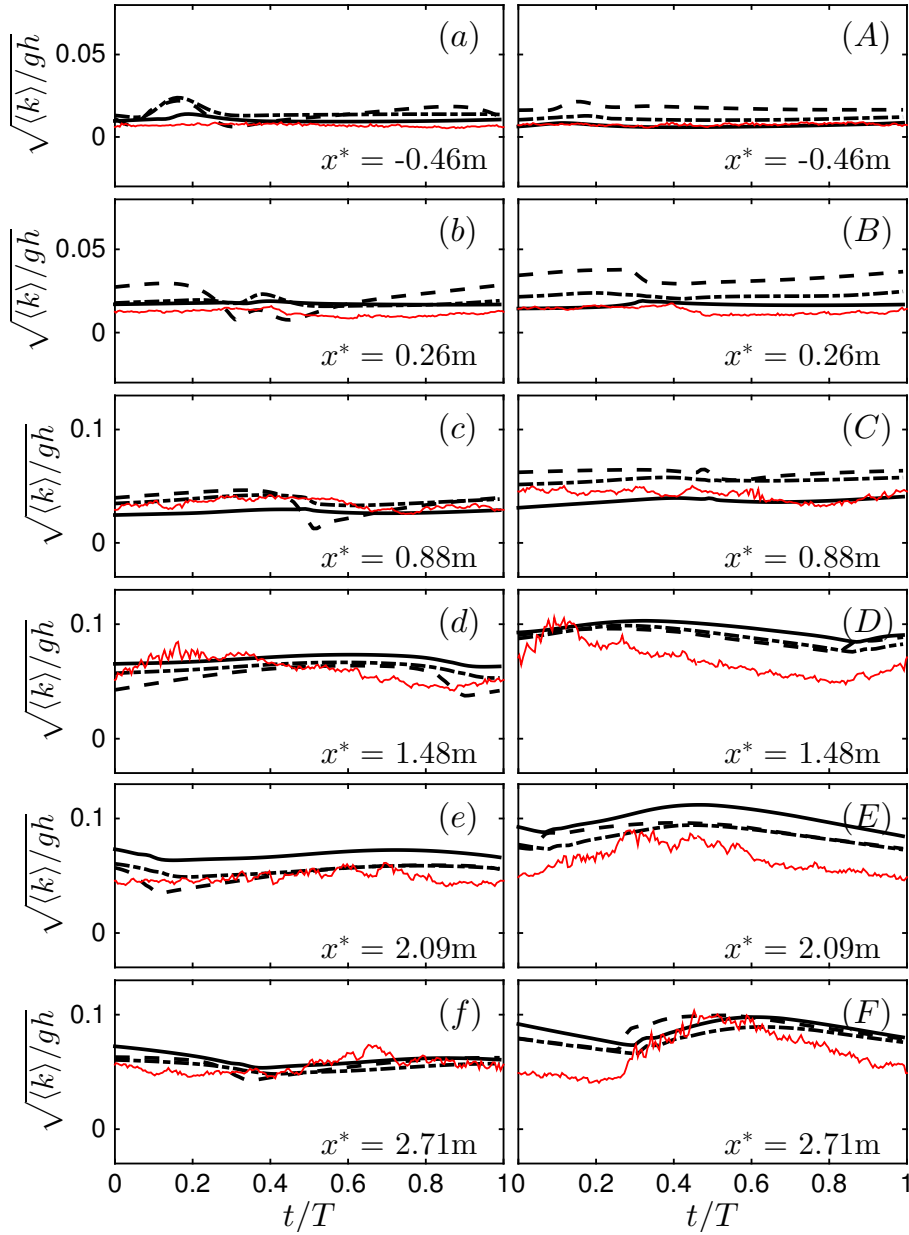


Figure 5.11: Phase-averaged k time series for the surf zone spilling breaking case TK1 at (a – f) ~ 4 cm and (A – F) ~ 9 cm above the bed at different cross-shore locations before and after the initial break point, $x^* = 0$. Comparison between NHWAVE results with 4 σ levels (dashed lines), 8 σ levels (dotted-dashed lines), 16 σ levels (thick solid lines) and the measurement (thin red solid lines)

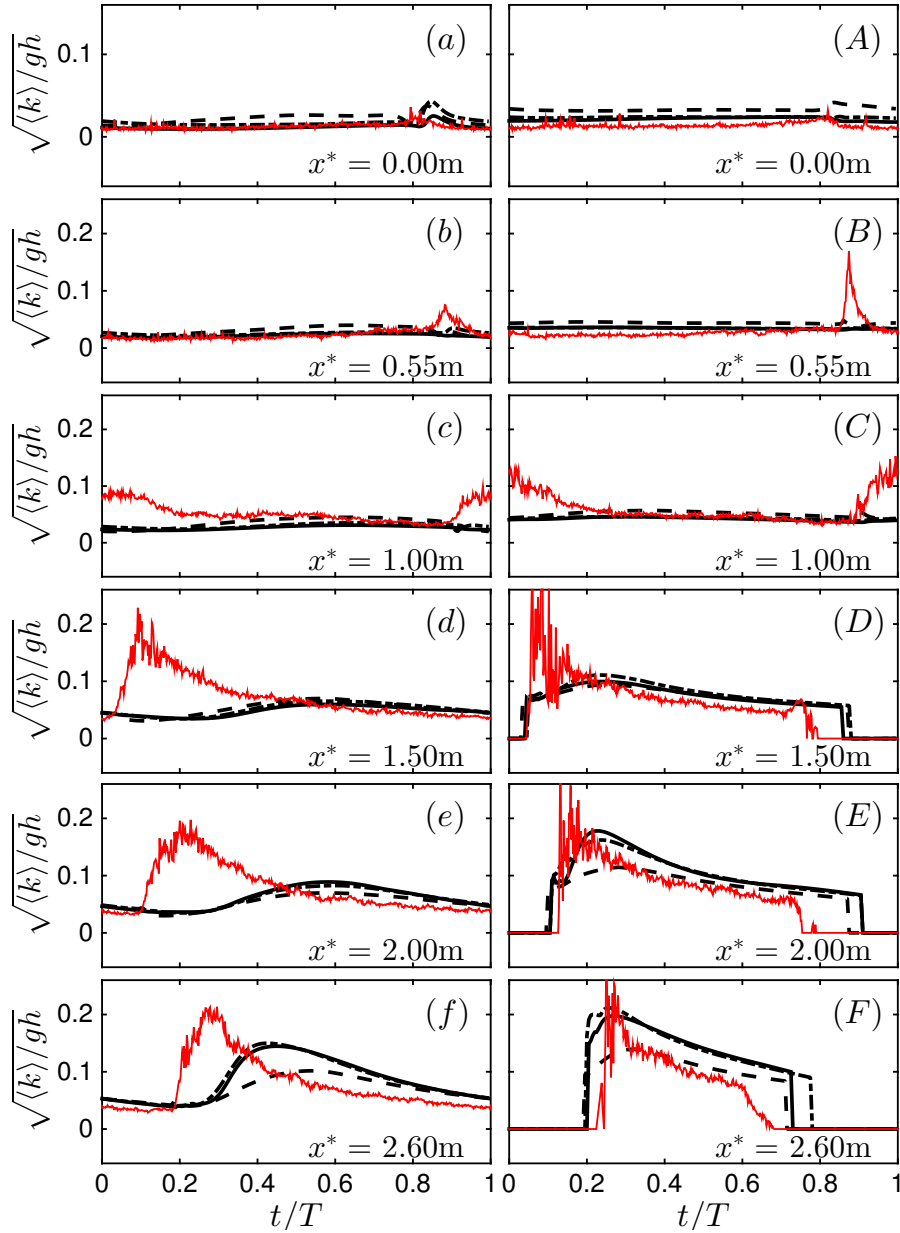


Figure 5.12: Phase-averaged k time series for the surf zone plunging breaking case TK2 at $(a - f) \sim 4$ cm and $(A - F) \sim 9$ cm above the bed at different cross-shore locations after the initial break point, $x^* = 0$. Comparison between NHWAVE results with 4σ levels (dashed lines), 8σ levels (dotted-dashed lines), 16σ levels (thick solid lines) and the measurement (thin red solid lines)

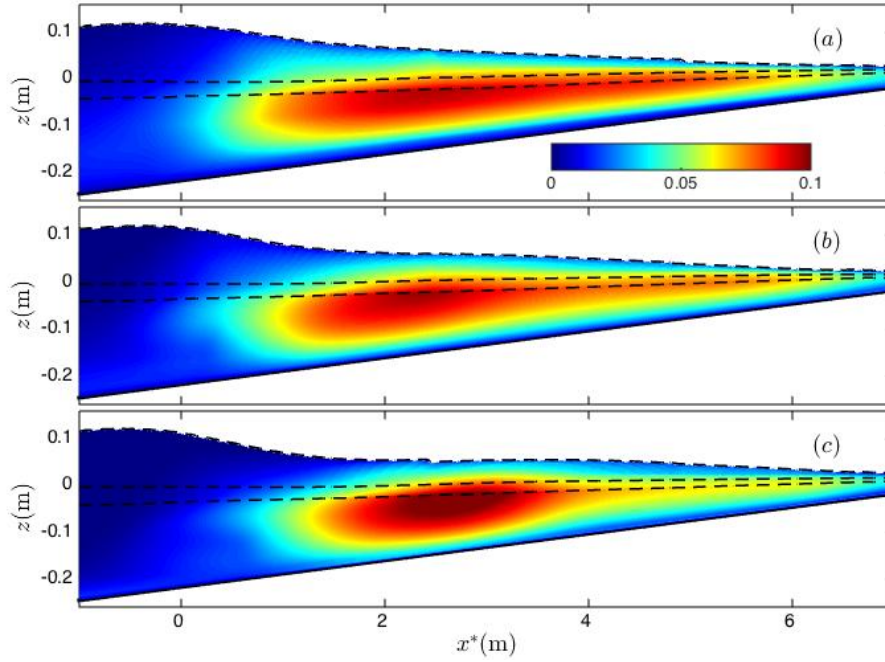


Figure 5.13: Time-averaged normalized k field, \sqrt{k}/gh , for the surf zone spilling breaking case TK1. NHWAVE results with (a) 4 σ levels, (b) 8 σ levels, and (c) 16 σ levels. Dash lines show the crest $\langle \eta \rangle_{max}$, mean $\bar{\eta}$ and trough $\langle \eta \rangle_{min}$ elevations.

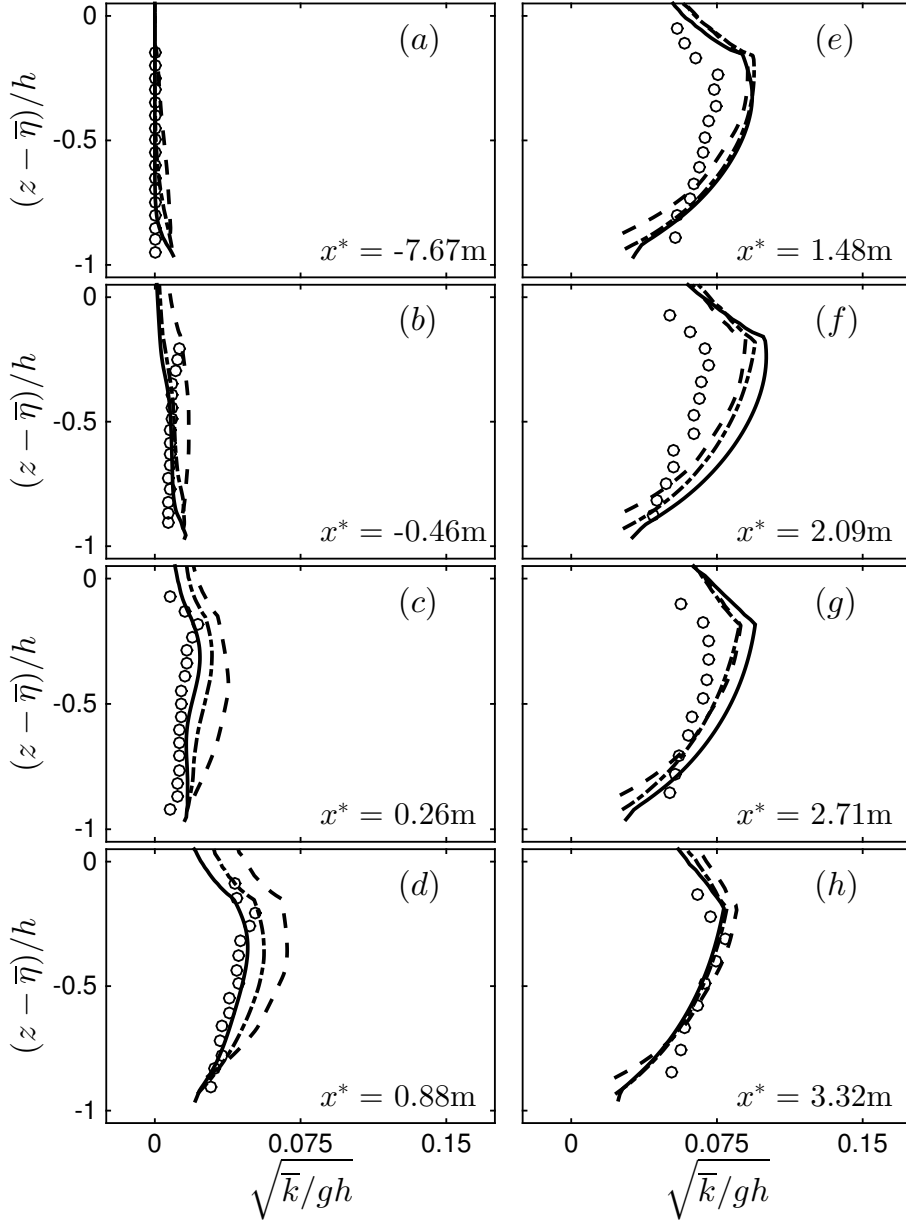


Figure 5.14: Time-averaged normalized k profiles for the surf zone spilling breaking case TK1 at different cross-shore locations before and after the initial break point, $x^* = 0$. Comparison between NHWAVE results with 4σ levels (dashed lines), 8σ levels (dotted-dashed lines), 16σ levels (solid lines) and the measurements (circle markers).

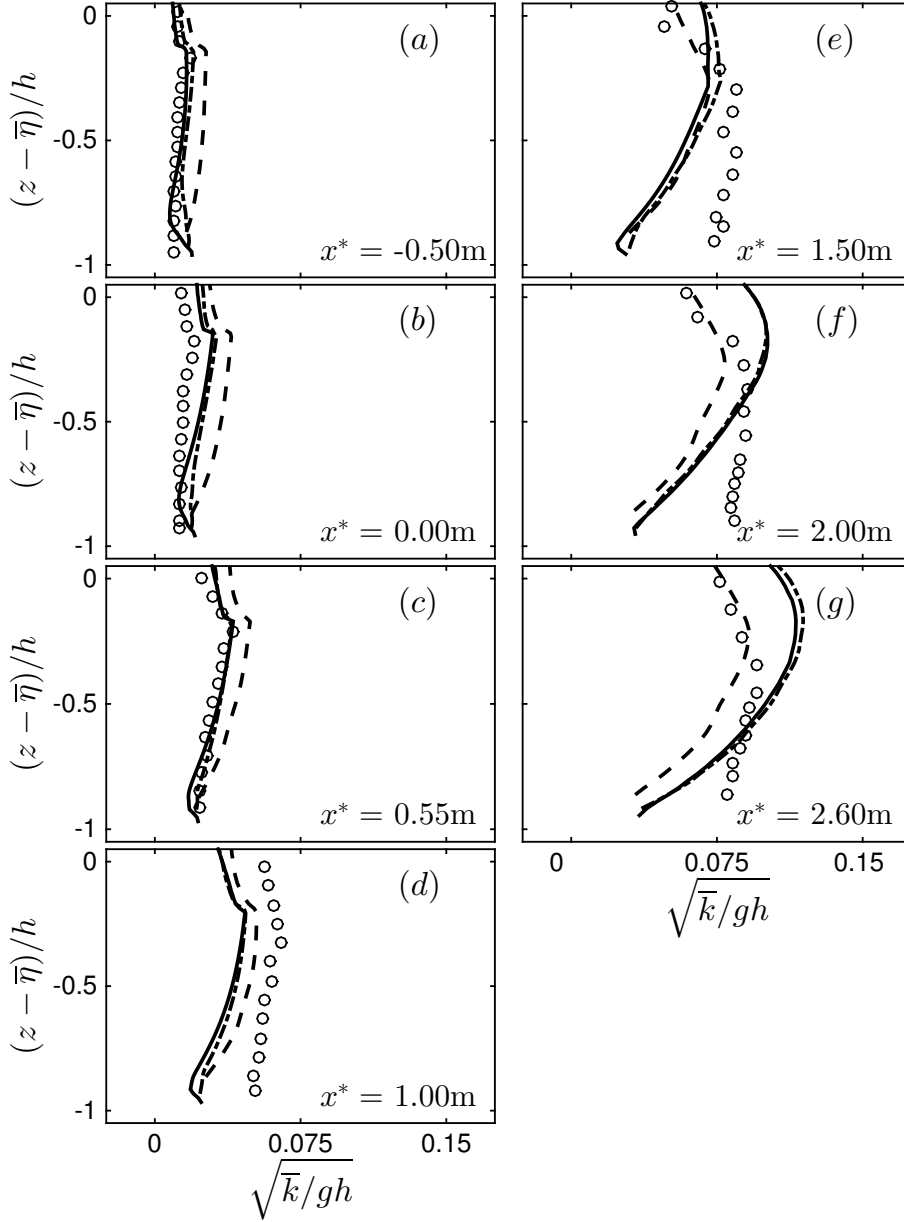


Figure 5.15: Time-averaged normalized k profiles for the surf zone plunging breaking case TK2 at different cross-shore locations before and after the initial break point, $x^* = 0$. Comparison between NHWAVE results with 4 σ levels (dashed lines), 8 σ levels (dotted-dashed lines), 16 σ levels (solid lines) and the measurements (circle markers).

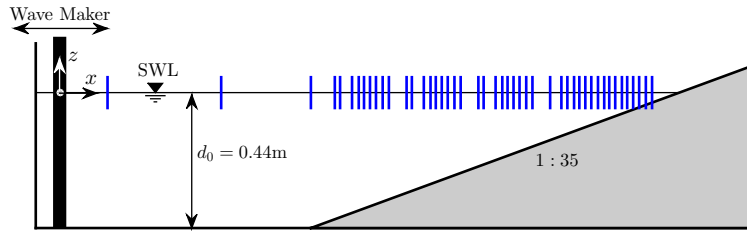


Figure 5.16: Experimental layout of [Bowen & Kirby \(1994\)](#). Vertical solid lines: the cross-shore locations of the free surface measurements.

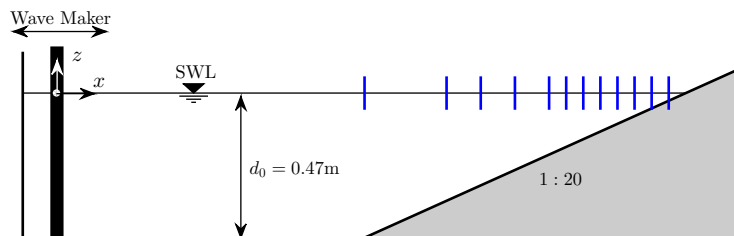


Figure 5.17: Experimental layout of [Mase & Kirby \(1992\)](#). Vertical solid lines: the cross-shore locations of the free surface measurements.

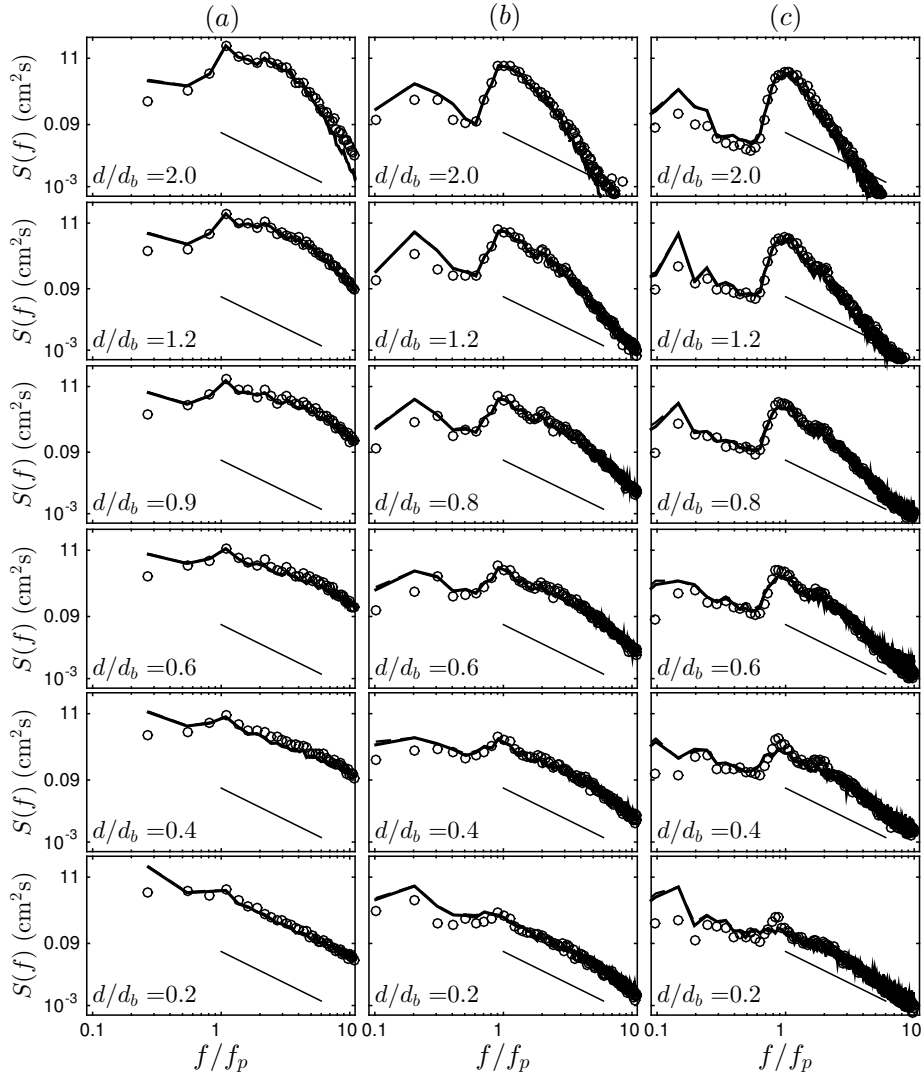


Figure 5.18: Power spectral density evolution, $S(f)$ ($\text{cm}^2.\text{s}$), for the random breaking cases, (a) BK with $f_p = 0.225\text{Hz}$, (b) MK1 with $f_p = 0.6\text{Hz}$, and (c) MK2 with $f_p = 1.0\text{Hz}$ at different cross-shore locations. Comparison between NHWAVE results with 4σ levels (dashed lines), 8σ levels (thick solid lines) and the corresponding measurements (circles). Here, d is the still water depth, and d_b is the still water depth at $x = x_b$ ($d_b \sim 20.5\text{cm}$ for BK and $d_b \sim 12.5\text{cm}$ for MK1 and MK2). The solid lines show an f^{-2} frequency dependence.

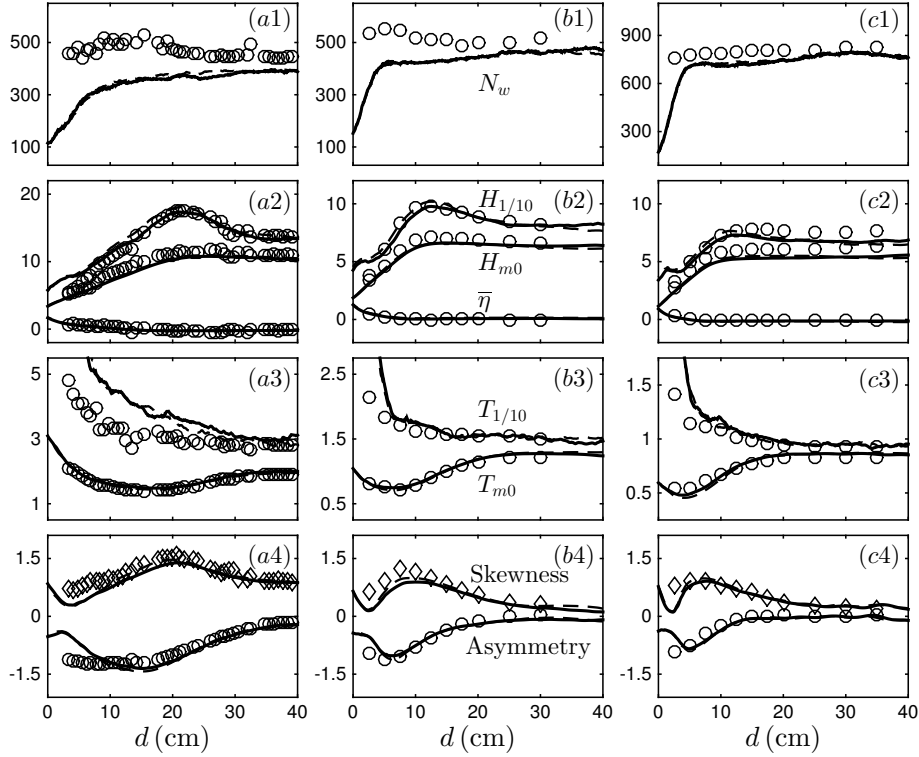


Figure 5.19: Cross-shore variation of different Second- and third-order wave statistics for (a) BK, (b) MK1 and (c) MK2. Comparison between NHWAVE results with 4 σ levels (dashed lines), 8 σ levels (solid lines) and the corresponding measurements (circles). Here, N_w is the number of waves detected by the zero-up crossing method, $H_{0.1}$ and $T_{0.1}$ are the averaged height and period of the one-tenth highest waves in the signal, H_{m0} , T_{m02} are the characteristic wave height and period based on the power spectra of the signal, $\text{Skewness} = \overline{\eta^3} / (\overline{\eta^2})^{3/2} > 0$ is the normalized wave skewness, and $\text{Asymmetry} = \overline{\mathcal{H}(\eta)^3} / (\overline{\eta^2})^{3/2} < 0$ is the normalized wave asymmetry. The results shown in (a) and (c) has the same label as in (b).

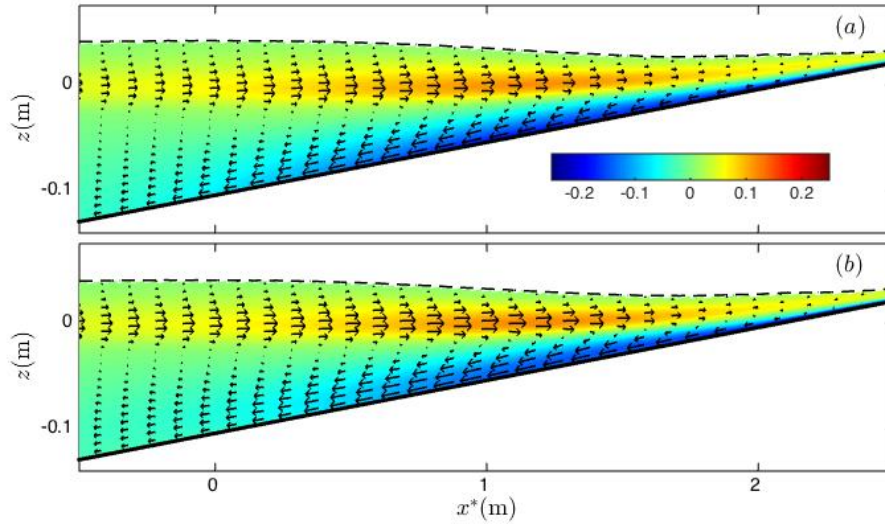


Figure 5.20: Time-averaged velocity field, \bar{u} , for the surf zone irregular breaking case MK2. NHWAVE results with (a) 4 σ levels and (b) 8 σ levels. Dash lines show $H_{rms} + \bar{\eta}$. Colors show \bar{u}/\sqrt{gh} .

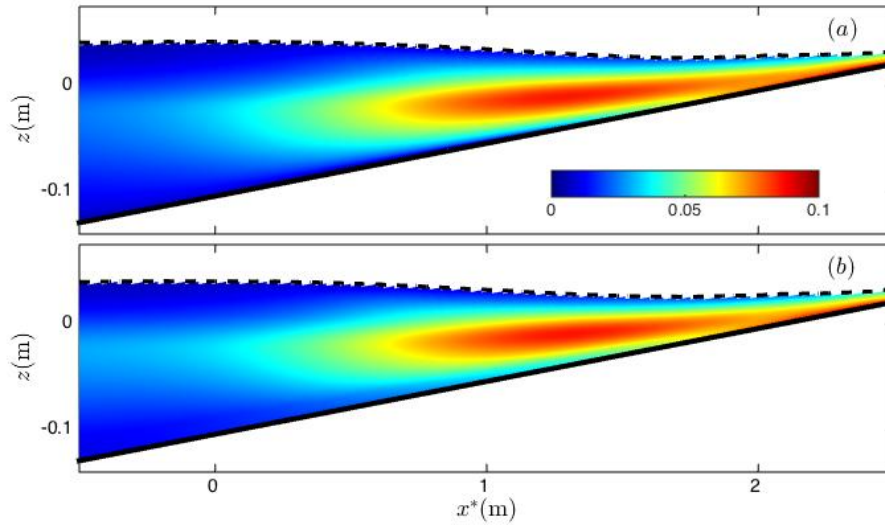


Figure 5.21: Time-averaged normalized k field, \sqrt{k}/gh , for the surf zone irregular breaking case MK2. NHWAVE results with (a) 4 σ levels and (b) 8 σ levels. Dash lines show $H_{rms} + \bar{\eta}$.

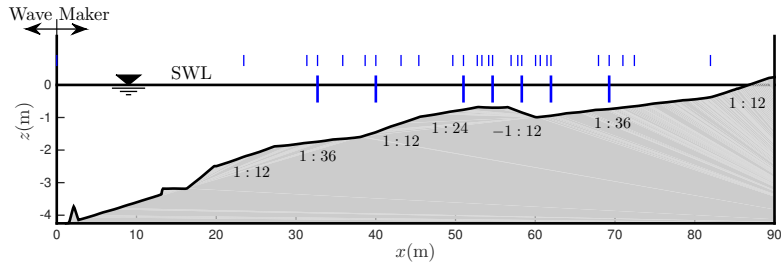


Figure 5.22: Experimental layout of [Scott et al. \(2004\)](#). Vertical thick solid lines: the cross-shore locations of the velocity measurements. Vertical thin solid lines: the cross-shore locations of the free surface measurements.

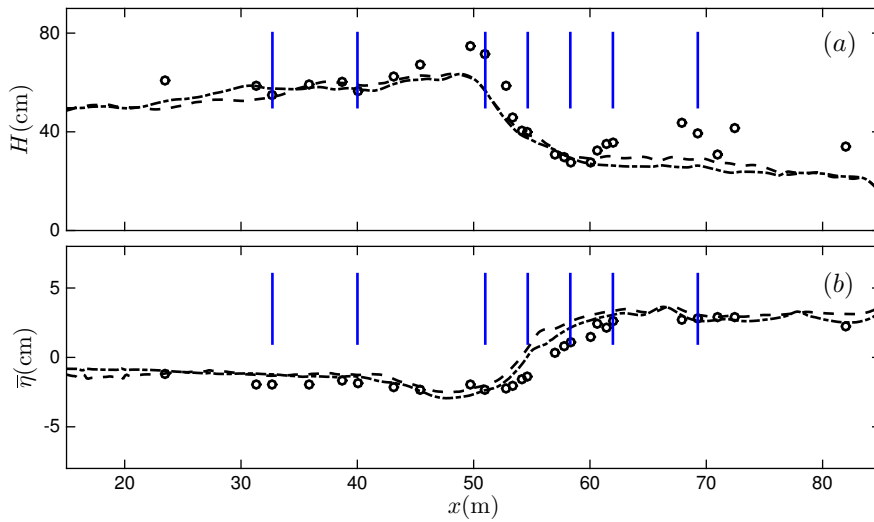


Figure 5.23: (a) Cross-shore distribution of the wave height, $H = \langle \eta \rangle_{max} - \langle \eta \rangle_{min}$, and (b) mean water level, $\bar{\eta}$, for the surf zone regular breaking waves on a barred beach case S1. Comparison between NHWAVE results with 4 σ levels (dashed lines), 8 σ levels (dotted-dashed lines) and the measurements of [Scott et al. \(2004\)](#) (circle markers). Vertical lines: the cross-shore locations of the velocity measurements shown in Figure 5.22.

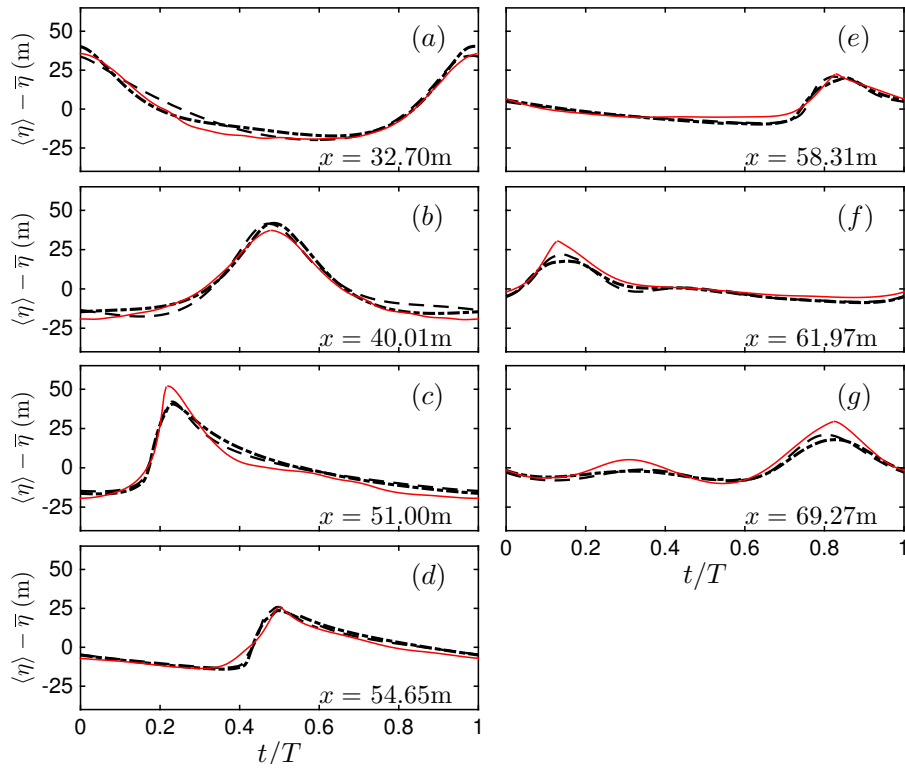


Figure 5.24: Phase-averaged free surface elevations for the surf zone regular breaking waves on a barred beach case S1 at different cross-shore locations before and after the bar. Comparison between NHWAVE results with 4 σ levels (dashed lines), 8 σ levels (dotted-dashed lines) and the measurement (thin red solid lines).

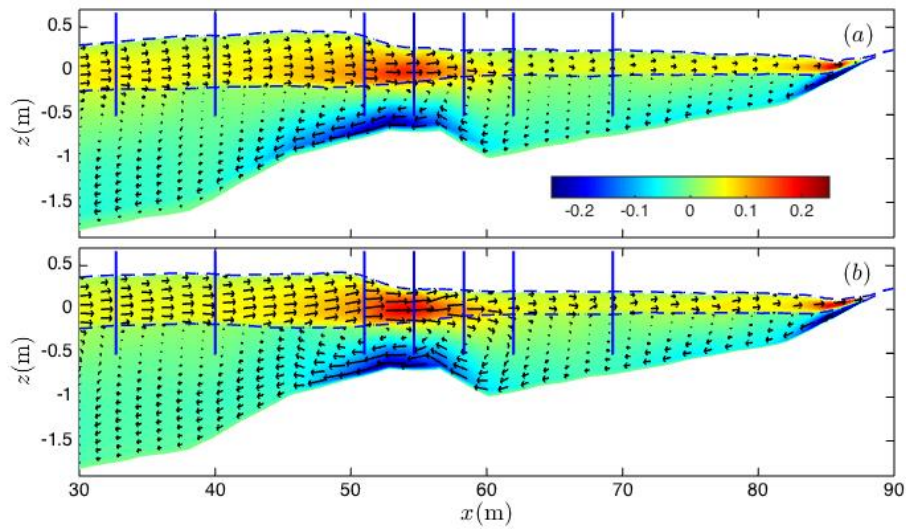


Figure 5.25: Time-averaged velocity field, $\bar{\mathbf{u}}$, for the surf zone regular breaking waves on a barred beach case S1. NHWAVE results with (a) 4 σ levels, and (b) 8 σ levels. Dash lines show the crest $\langle \eta \rangle_{max}$ and trough $\langle \eta \rangle_{min}$ elevations. Colors show \bar{u}/\sqrt{gh} . Vertical lines: the cross-shore locations of the velocity measurements shown in Figure 5.22.

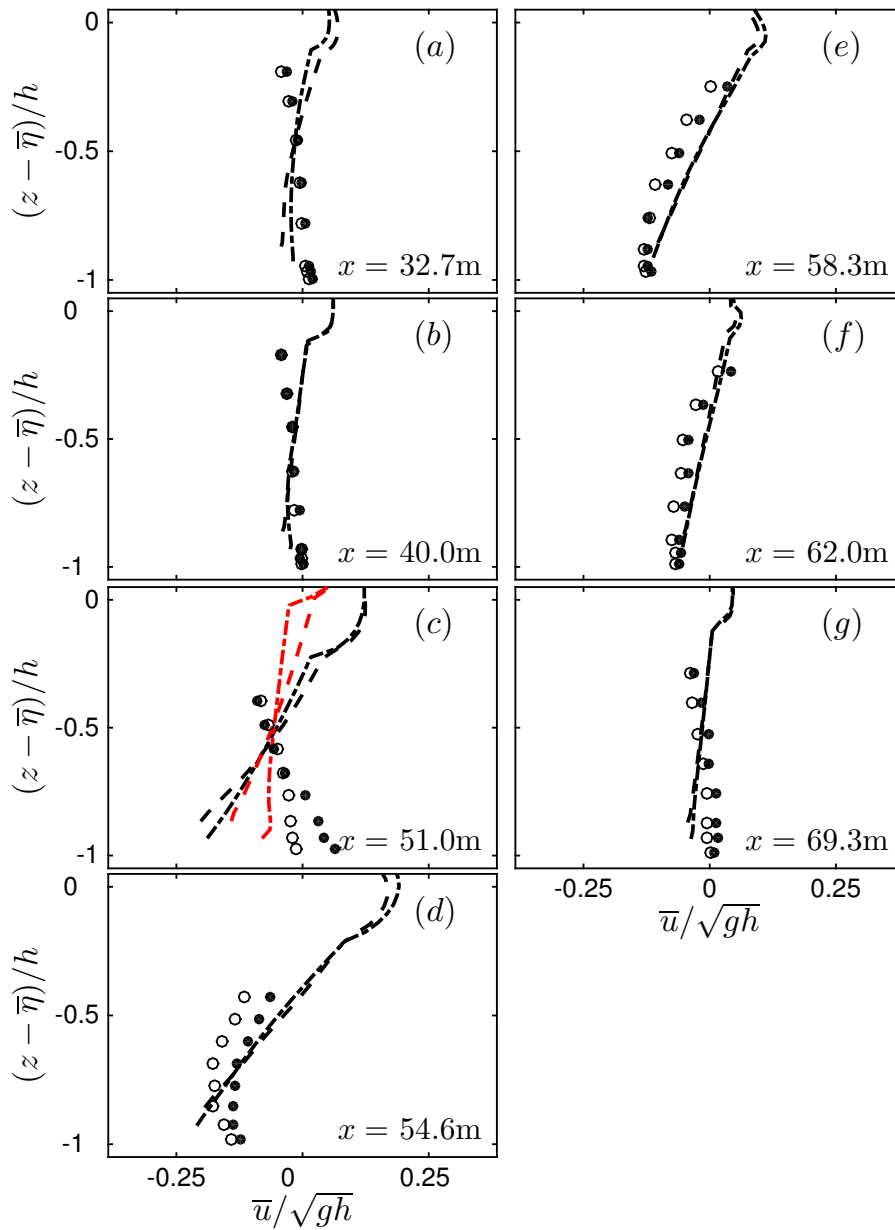


Figure 5.26: Time-averaged normalized horizontal velocity (undertow) profiles for the surf zone regular breaking waves on a barred beach case S1 at different cross-shore locations before and after the bar. Comparison between NHWAVE results with 4 σ levels (dashed lines), 8 σ levels (dotted-dashed lines), and the measurements at two different longshore locations (open and solid circle markers). Red lines at (c) show the results 3m seaward of the corresponding measurement location.

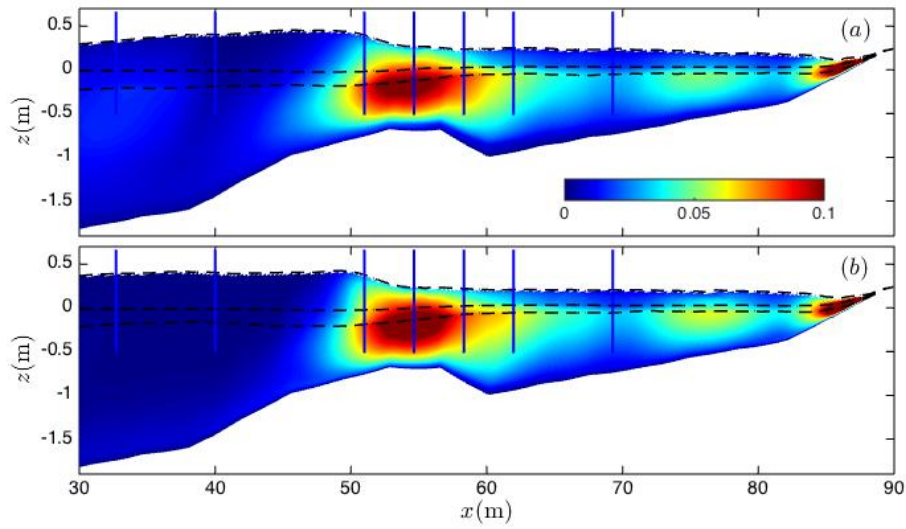


Figure 5.27: Time-averaged normalized k field, $\sqrt{k/gh}$, for the surf zone regular breaking waves on a barred beach case S1. NHWAVE results with (a) 4 σ levels, and (b) 8 σ levels. Dash lines show the crest $\langle\eta\rangle_{max}$, mean $\bar{\eta}$ and trough $\langle\eta\rangle_{min}$ elevations. Vertical lines: the cross-shore locations of the velocity measurements shown in Figure 5.22.

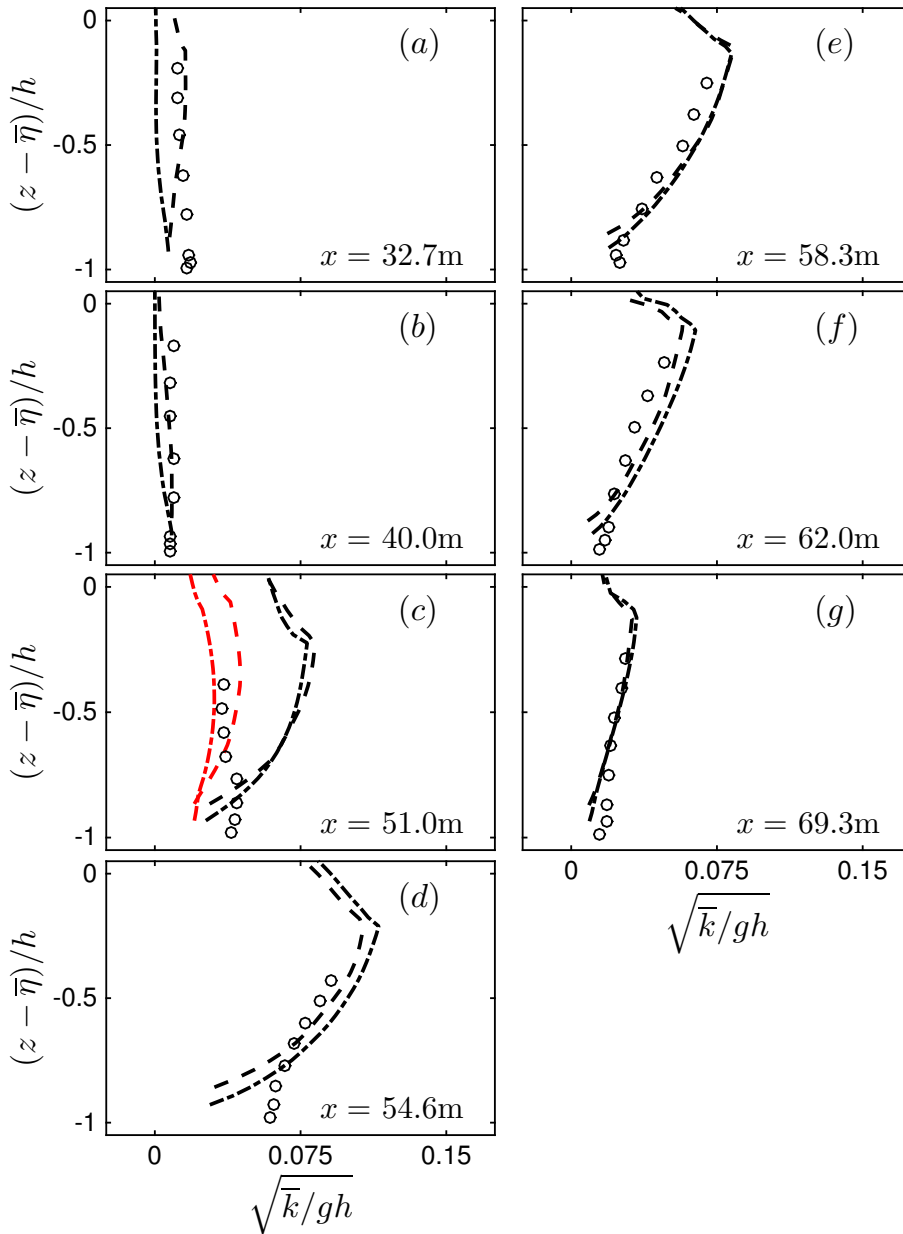


Figure 5.28: Time-averaged normalized k profiles for the surf zone regular breaking waves on a barred beach case S1 at different cross-shore locations before and after the bar. Comparison between NHWAVE results with 4σ levels (dashed lines), 8σ levels (dotted-dashed lines), and the measurements (circle markers). Red lines at (c) show the results 3m seaward of the corresponding measurement location.

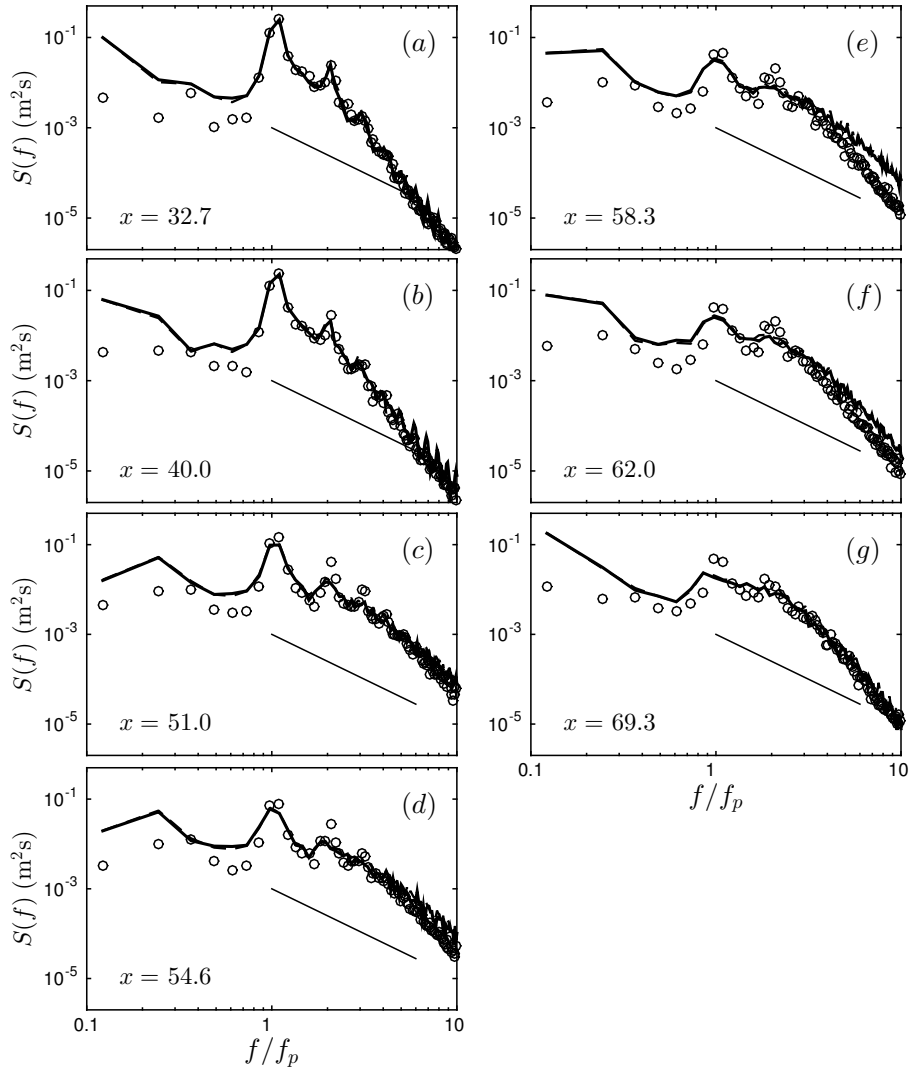


Figure 5.29: Power spectral density evolution, $S(f)$ ($\text{m}^2 \cdot \text{s}$), for the random breaking on a barred beach case S2 at different cross-shore locations. Comparison between NHWAVE results with 4 σ levels (dashed lines), 8 σ levels (thick solid lines) and the corresponding measurements (circles). The solid lines show f^{-2} .

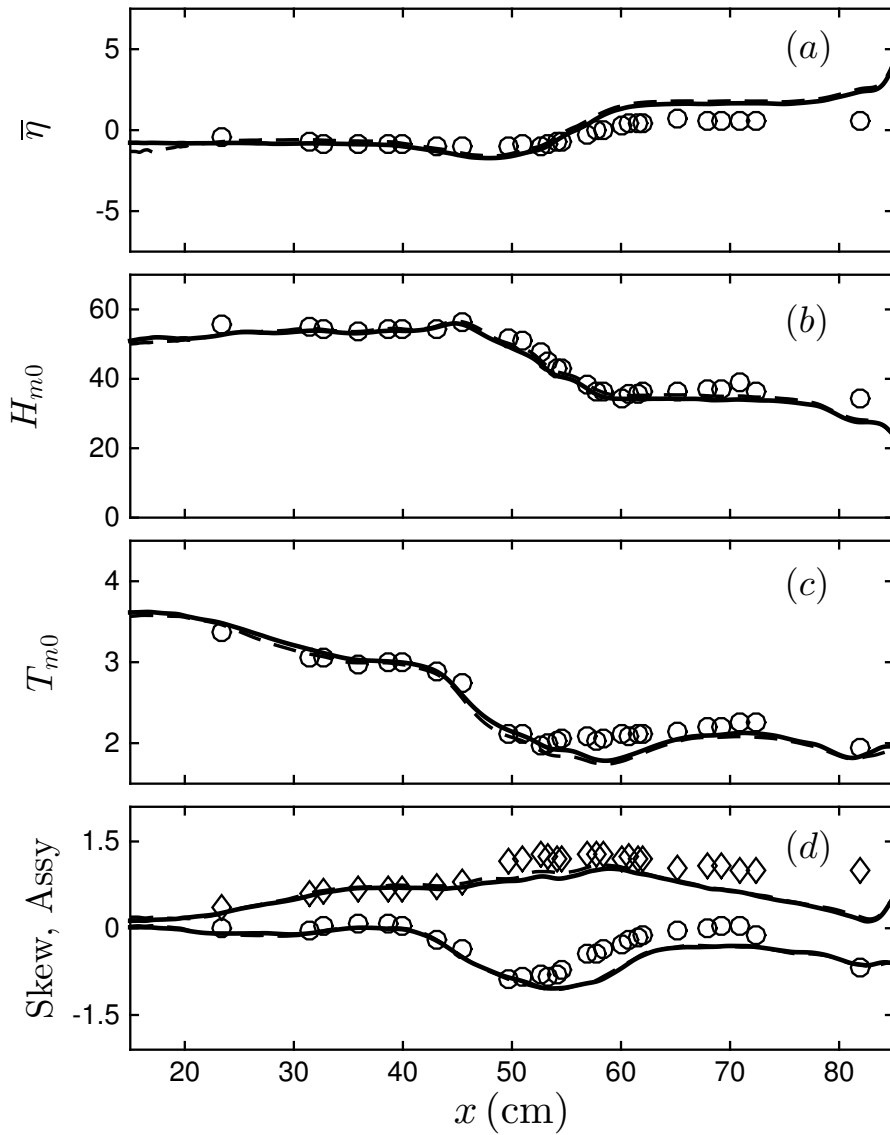


Figure 5.30: Cross-shore variation of different Second- and third-order wave statistics for the random breaking on a barred beach case S2. Comparison between NHWAVE results with 4 σ levels (dashed lines), 8 σ levels (solid lines) and the corresponding measurements (circles). The definitions are the same as in Figure 5.19.

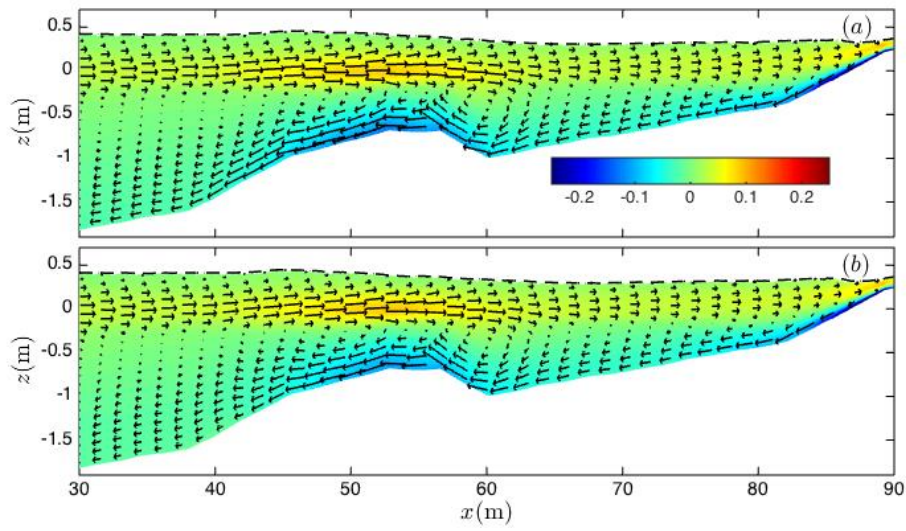


Figure 5.31: Time-averaged velocity field, $\bar{\mathbf{u}}$, for the random breaking on a barred beach case S2. NHWAVE results with (a) 4 σ levels and (b) 8 σ levels. Dash lines show $H_{rms} + \bar{\eta}$. Colors show \bar{u}/\sqrt{gh} .

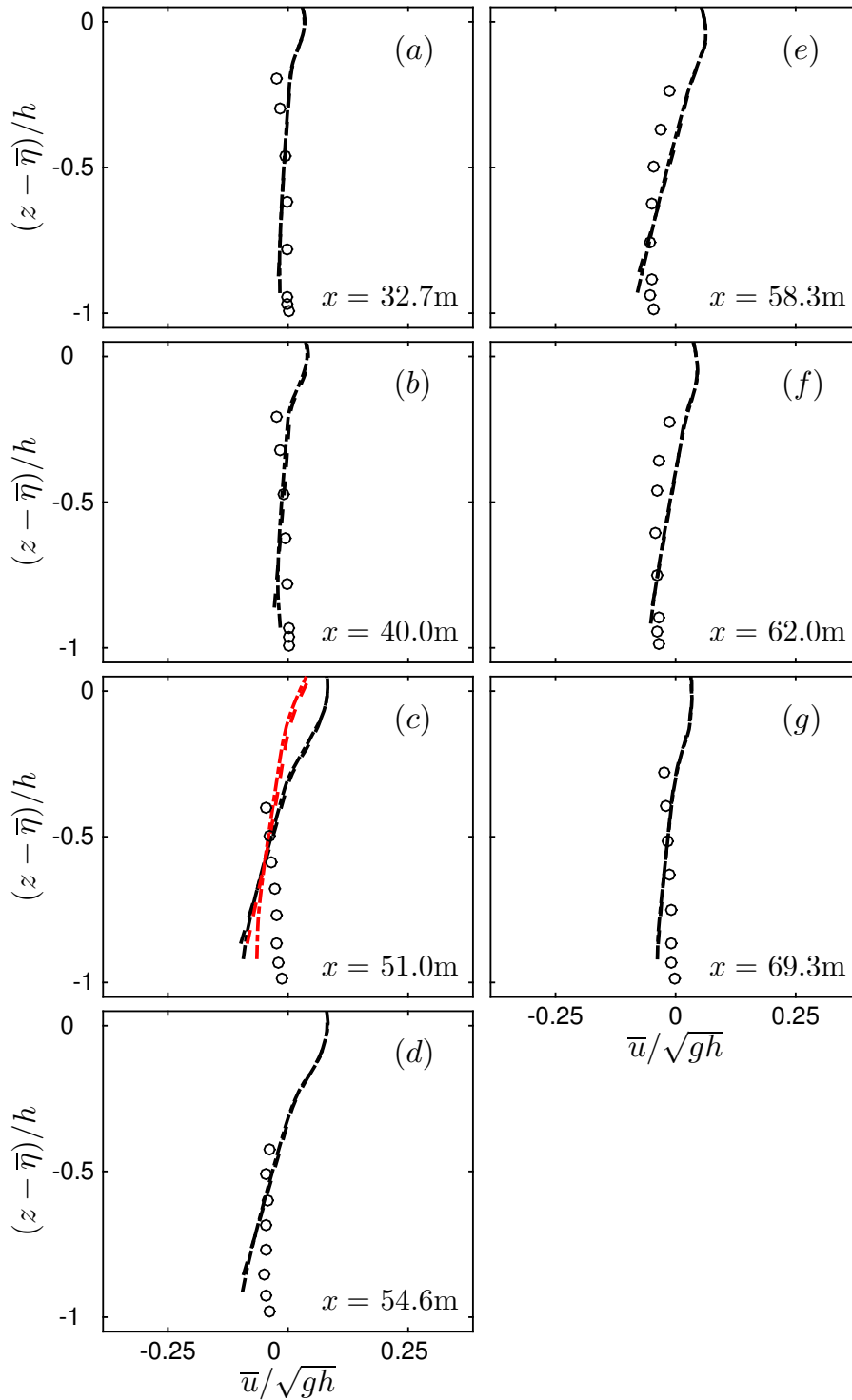


Figure 5.32: Time-averaged normalized horizontal velocity (undertow) profiles for the random breaking on a barred beach case S2 at different cross-shore locations before and after the bar. Comparison between NHWAVE results with 4σ levels (dashed lines), 8σ levels (dotted-dashed lines), and the measurements (circle markers). Red lines at (c) show the results 3m seaward of the corresponding measurement location.

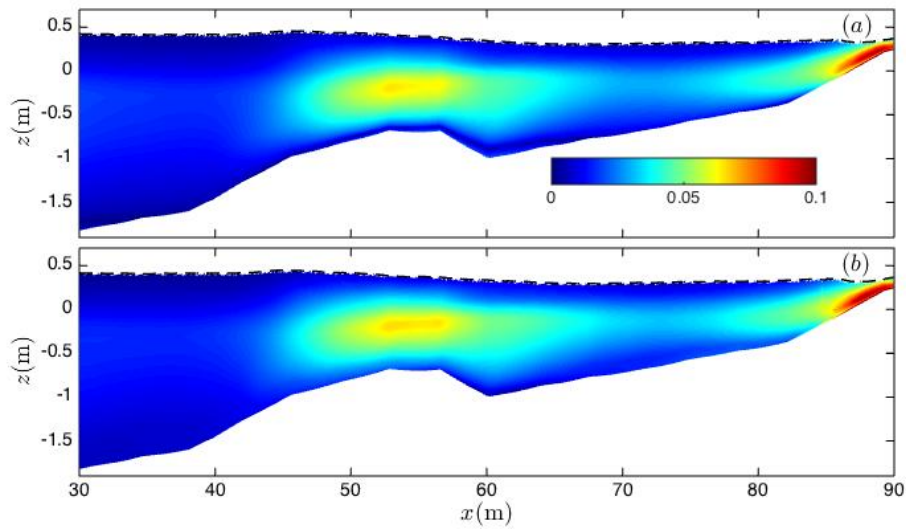


Figure 5.33: Time-averaged normalized k field, \sqrt{k}/gh , for the random breaking on a barred beach case S2. NHWAVE results with (a) 4 σ levels and (b) 8 σ levels. Dash lines show $H_{rms} + \bar{\eta}$.

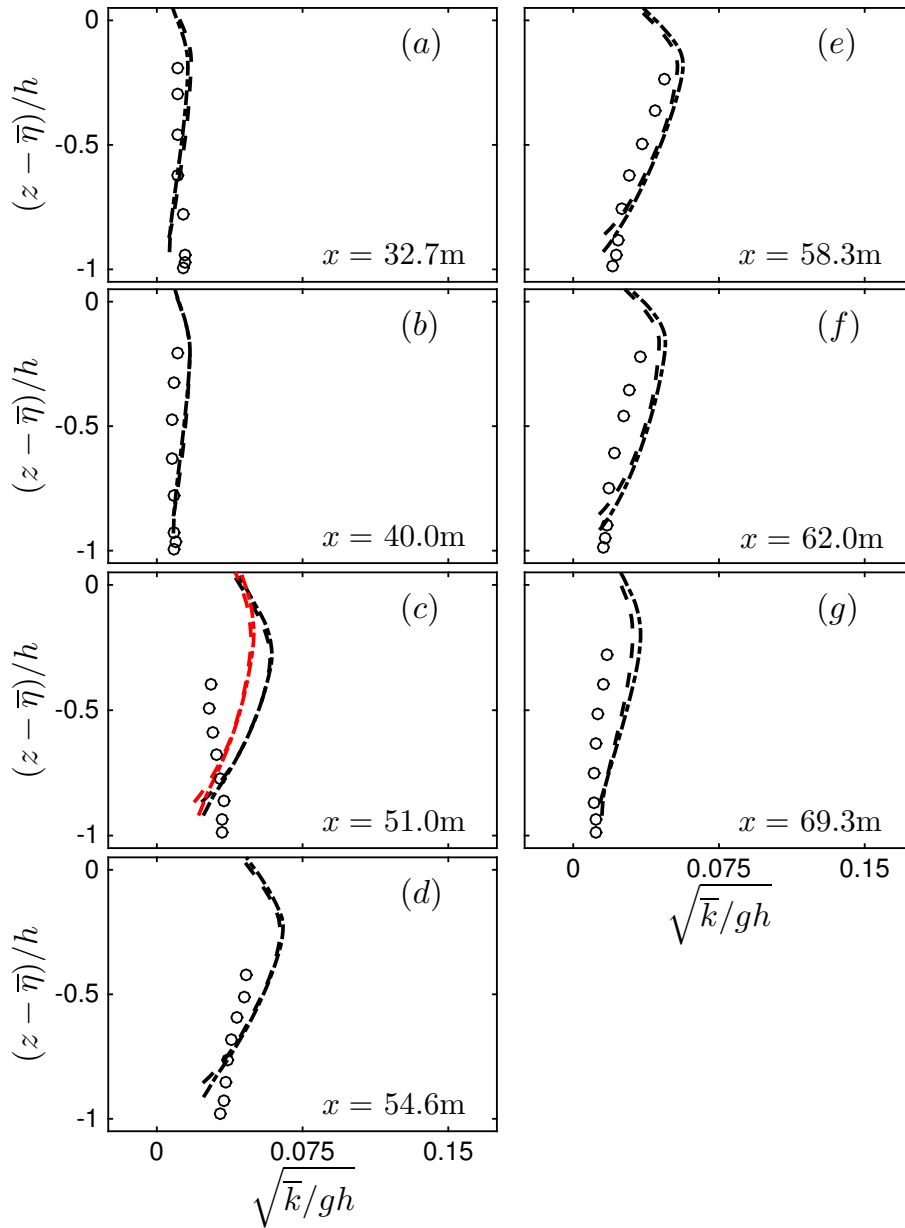


Figure 5.34: Time-averaged normalized k profiles for the random breaking on a barred beach case S2 at different cross-shore locations before and after the bar. Comparison between NHWAVE results with 4σ levels (dashed lines), 8σ levels (dotted-dashed lines), and the measurements (circle markers). Red lines at (c) show the results 3m seaward of the corresponding measurement location.

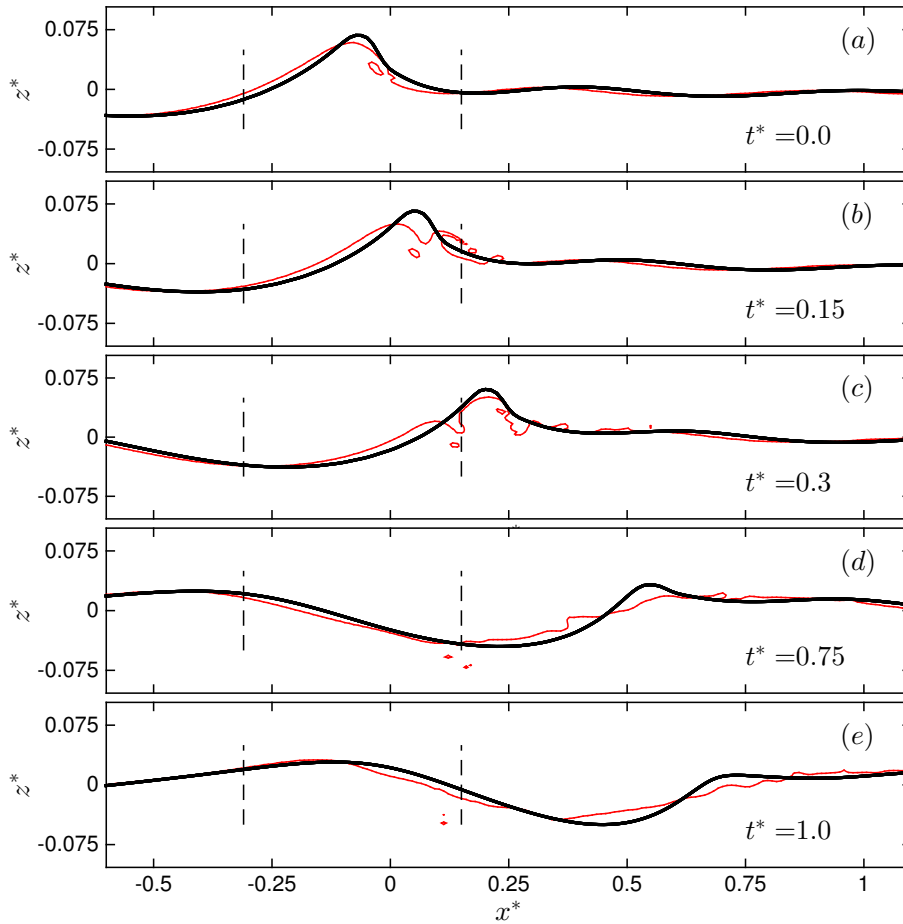


Figure 5.35: Snapshots of the free surface evolution during active breaking for the intermediate depth breaking case, RM1. Comparison between NHWAVE results with 8 σ levels (thick solid lines) and the VOF-based model (thin solid lines). The free surface time series at the locations indicated by vertical dashed lines are shown in Figure 5.36.

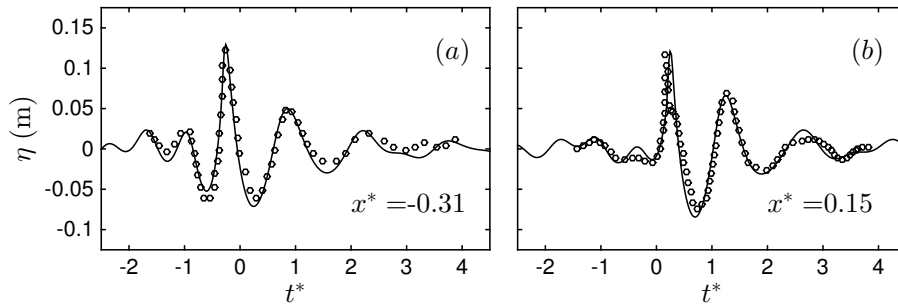


Figure 5.36: Time series of the free surface evolution for the intermediate depth breaking case, RM1 at (a) before and (b) after the break point ($x^* = 0$). Comparison between NHWAVE results with 8 σ levels (solid lines) and the corresponding measurements of [Rapp & Melville \(1990\)](#) (circles).

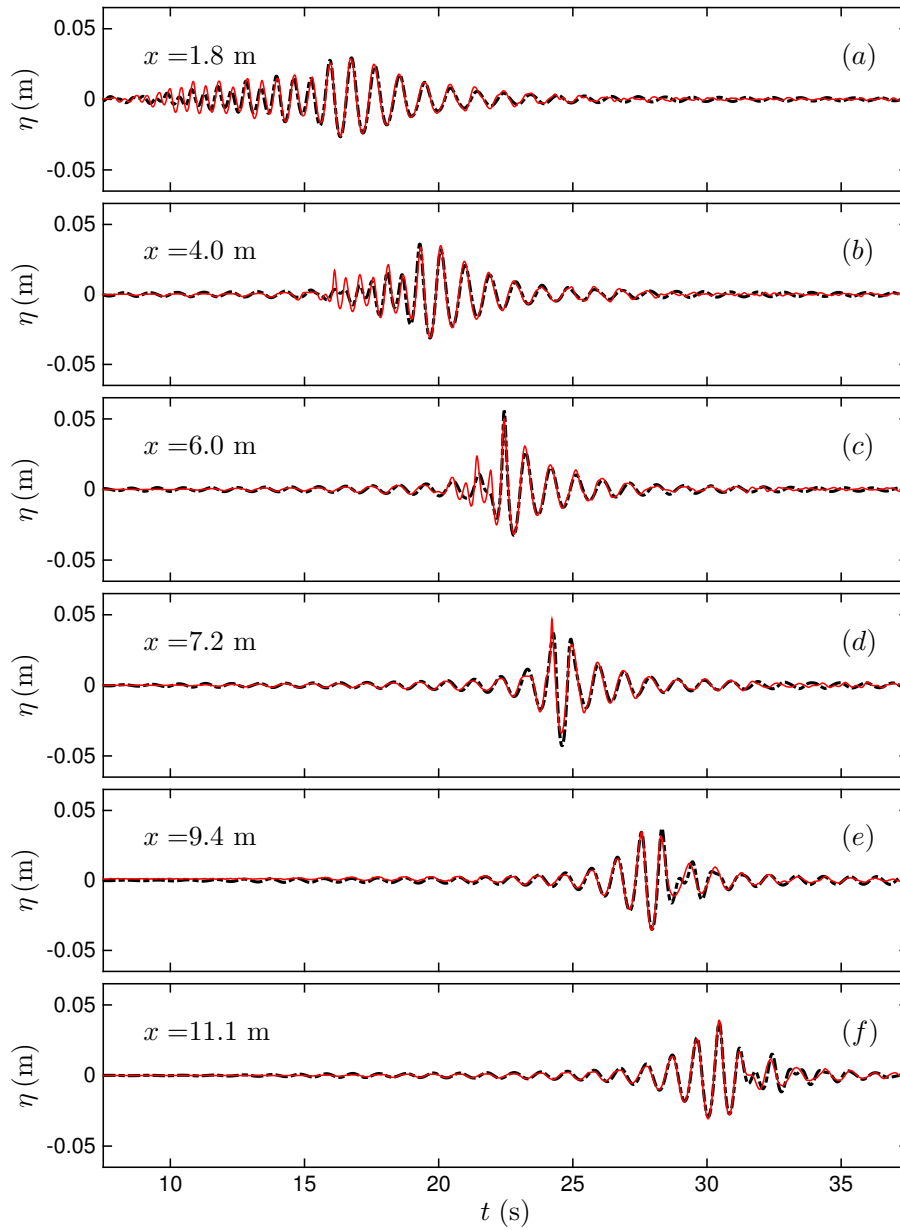


Figure 5.37: Time series of the free surface evolution at different x locations for the deep water breaking case, T1. Comparison between NHWAVE results with 8σ levels and the horizontal resolution of $\Delta x = 10\text{mm}$ (dotted dashed lines) and the measurement of [Tian et al. \(2012\)](#) (solid lines).

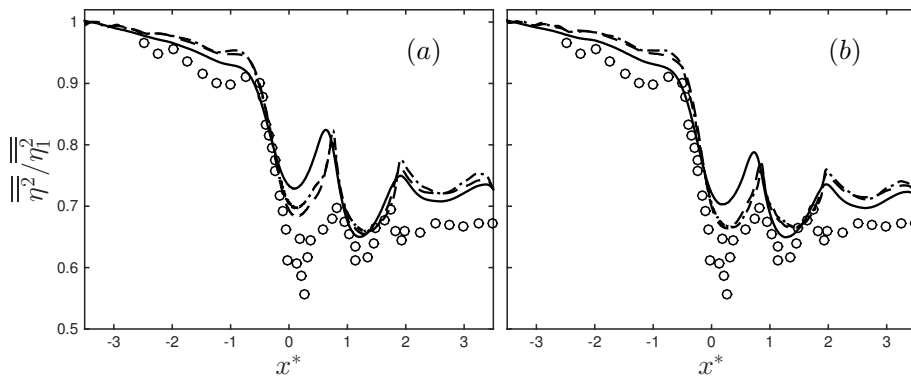


Figure 5.38: Normalized time-integrated potential energy density, $\overline{\overline{E_p}}$, for the intermediate depth breaking case, RM2. Comparison between the corresponding measurements (circles) and NHWAVE results with (a) 8 σ levels and (b) 16 σ levels, using different horizontal resolutions of $\Delta x = 23\text{mm}$ (solid lines), $\Delta x = 10\text{mm}$ (dashed lines) and $\Delta x = 5\text{mm}$ (dashed-dotted lines).

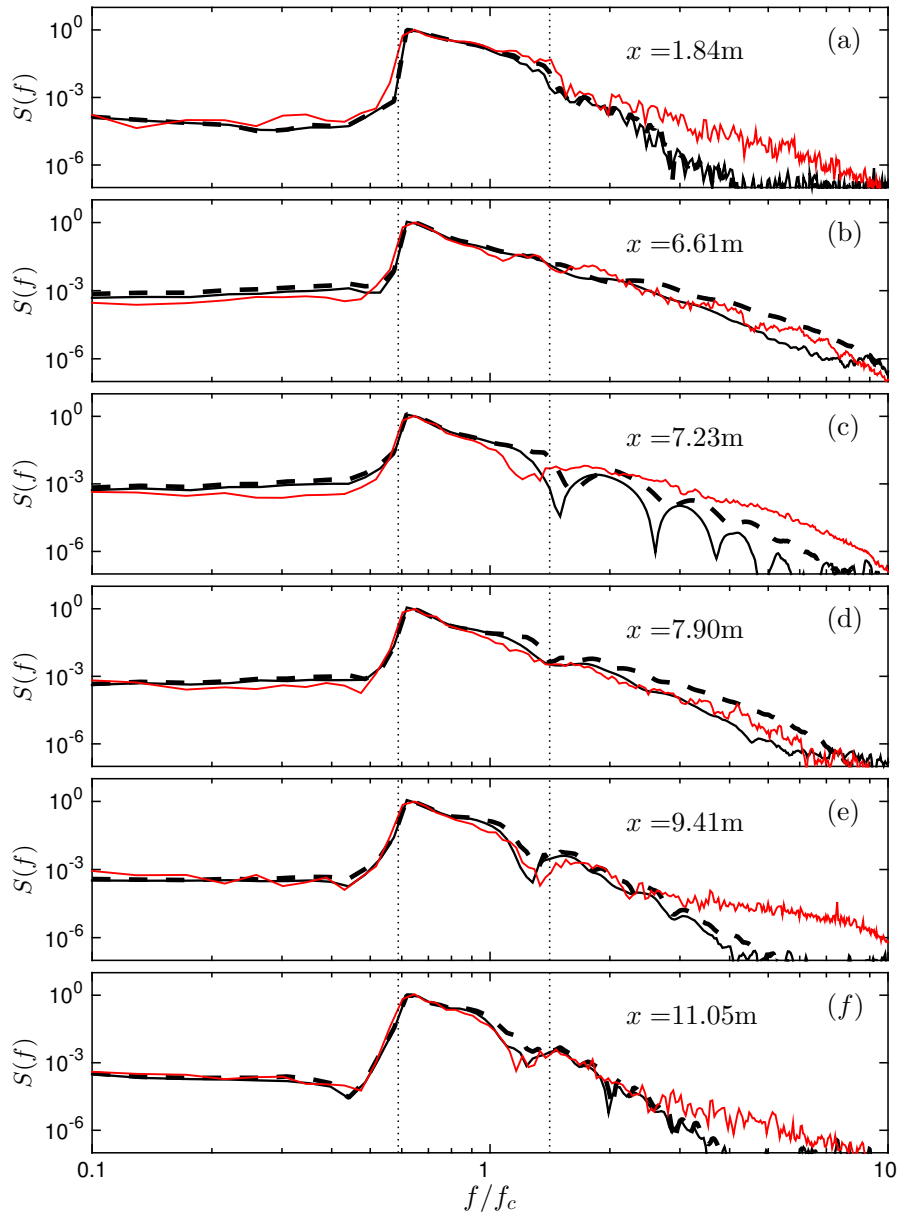


Figure 5.39: Energy density spectrum evolution, $S(f)$ ($\text{cm}^2 \cdot \text{s}$) for the deep water breaking case, T1. Comparison between NHWAVE results with 8σ levels using $\Delta x = 10\text{mm}$ (thick solid lines) and $\Delta x = 5\text{mm}$ (dashed lines) as well as the measurements of [Tian et al. \(2012\)](#) (solid lines). Vertical dotted lines indicate the frequency range of the input packet.

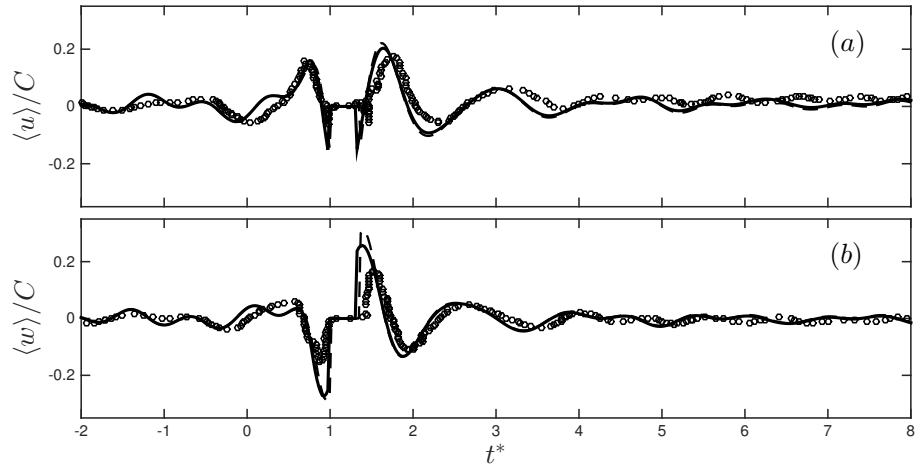


Figure 5.40: Normalized ensemble-averaged velocities for RM1 using 8 σ levels (dashed lines) and 16 σ levels (solid lines) at $x^* = 0.6$, $z^* = -0.025$. The circles are the measurements of the corresponding case adopted from [Rapp & Melville \(1990\)](#), Figure 41.

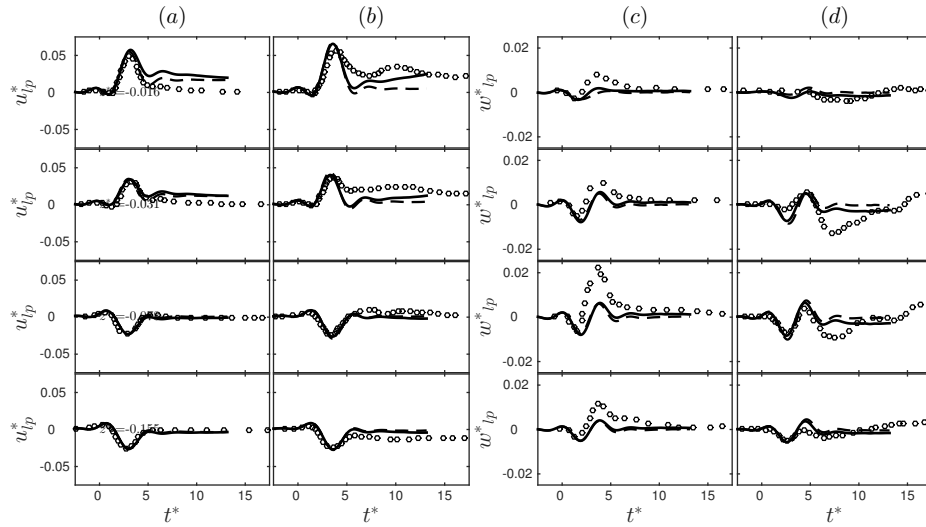


Figure 5.41: Normalized low-pass filtered velocities for RM1 using 8 σ levels (dashed lines) and 16 σ levels (solid lines), at (a,c) $x^* = 0.15$ and (b,d) $x^* = 0.60$ at different elevations. The circles are the measurements of the corresponding case adopted from [Rapp & Melville \(1990\)](#), Figure 42.

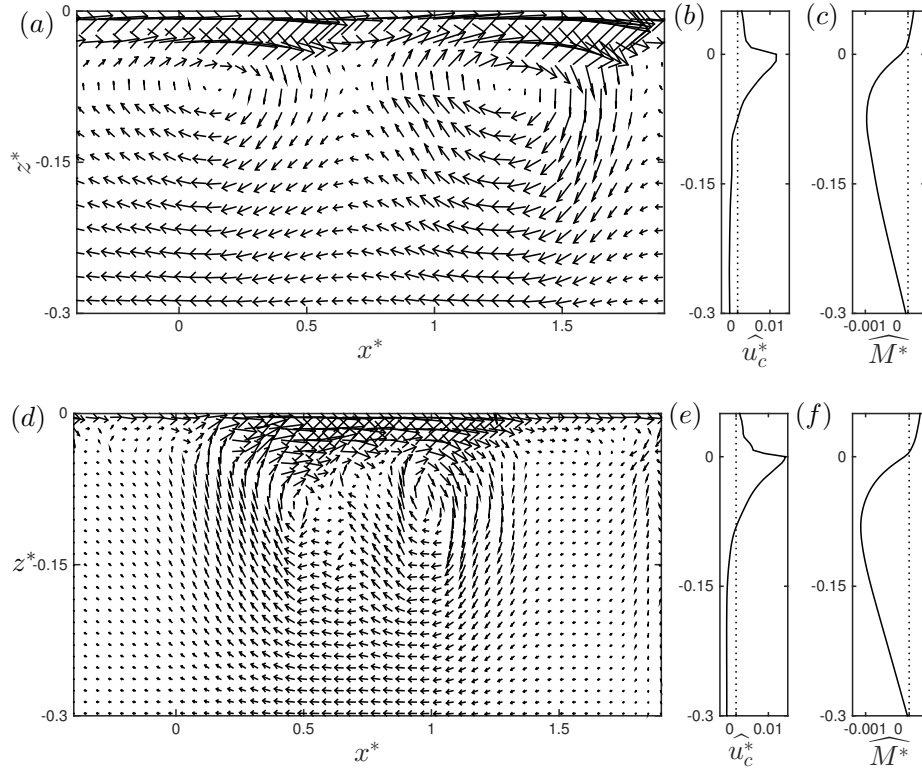


Figure 5.42: (a, d) Spatial distribution of the normalized mean current, \mathbf{u}_c^* ; (b, e) normalized horizontal-averaged mean current in the streamwise direction, \hat{u}_c^* and (c, f) normalized accumulative horizontal-averaged mass flux, \widehat{M}^* , in the breaking region for RM1. (a-c) NHWAVE results with 8 σ levels and (d-f) LES/VOF results by Derakhti & Kirby (2014a).

BIBLIOGRAPHY

- Ai, C., Ding, W. & Jin, S. (2014), ‘A general boundary-fitted 3d non-hydrostatic model for nonlinear focusing wave groups’, *Ocean Eng.* **89**, 134–145.
- Allis, M. J. (2013), The Speed, Breaking Onset and Energy Dissipation of 3D Deep-Water Waves, PhD thesis, U. New South Wales.
- Balachandar, S. & Eaton, J. K. (2010), ‘Turbulent dispersed multiphase flow’, *Ann. Rev. Fluid Mech.* **42**, 111–133.
- Baldy, S. (1988), ‘Bubbles in the close vicinity of breaking waves: Statistical characteristics of the generation and dispersion mechanism’, *J. Geophys. Res.* **93**, 8239–8248.
- Banner, M. L. & Peirson, W. L. (2007), ‘Wave breaking onset and strength for two-dimensional deep-water wave groups’, *J. Fluid Mech.* **585**, 93–115.
- Banner, M. L. & Peregrine, D. H. (1993), ‘Wave breaking in deep water’, *Ann. Rev. Fluid Mech.* **25**, 373–397.
- Benjamin, T. B. & Feir, J. (1967), ‘The disintegration of wave trains on deep water part 1. theory’, *J. Fluid Mech.* **27**, 417–430.
- Blenkinsopp, C. E. & Chaplin, J. R. (2007), ‘Void fraction measurements in breaking waves’, *Proc. Roy. Soc. A* **463**, 3151–3170.
- Bowen, G. D. & Kirby, J. T. (1994), Shoaling and breaking random waves on a 1: 35 laboratory beach, Technical report, Tech. Rep. CACR-94-14.
- Bradford, S. F. (2000), ‘Numerical simulation of surf zone dynamics’, *J. Waterway, Port, Coastal, and Ocean Eng.* **126**, 1–13.
- Bradford, S. F. (2011), ‘Nonhydrostatic model for surf zone simulation’, *J. Waterway, Port, Coastal, and Ocean Eng.* **137**, 163–174.
- Bradford, S. F. (2012), ‘Improving the efficiency and accuracy of a nonhydrostatic surf zone model’, *Coastal Eng.* **65**, 1–10.
- Brocchini, M. (2002), ‘Free surface boundary conditions at a bubbly/weakly splashing air–water interface’, *Phys. Fluids* **14**, 1834–1840.

- Brocchini, M. & Peregrine, D. (2001), ‘The dynamics of strong turbulence at free surfaces. part 2. free-surface boundary conditions’, *J. Fluid Mech.* **449**, 255–290.
- Carrica, P. M., Drew, D., Bonetto, F. & Lahey, R. T. (1999), ‘A polydisperse model for bubbly two-phase flow around a surface ship’, *Int. J Multiphase Flow* **25**, 257–305.
- Chakraborty, P., Balachandar, S. & Adrian, R. J. (2005), ‘On the relationships between local vortex identification schemes’, *J. Fluid Mech.* **535**, 189–214.
- Chen, G., Kharif, C., Zaleski, S. & Li, J. (1999), ‘Two-dimensional navier-stokes simulation of breaking waves’, *Phys. Fluids* **11**, 121–133.
- Christensen, E. D. (2006), ‘Large eddy simulation of spilling and plunging breakers’, *Coastal Eng.* **53**, 463–485.
- Christensen, E. D. & Deigaard, R. (2001), ‘Large eddy simulation of breaking waves’, *Coastal Eng.* **42**, 53–86.
- Clift, R., Grace, J. R. & Weber, M. E. (1978), *Bubbles, Drops and Particles*, *Academic Press, New York*.
- Cox, D. & Shin, S. (2003), ‘Laboratory measurements of void fraction and turbulence in the bore region of surf zone waves’, *J. Eng. Mech.* **129**, 1197–1205.
- Deane, G. B. & Stokes, M. D. (2002), ‘Scale dependence of bubble creation mechanisms in breaking waves’, *Nature* **418**, 839–844.
- Derakhti, M. & Kirby, J. T. (2014*a*), Bubble entrainment and liquid-bubble interaction under unsteady breaking waves, Technical Report CACR-14-06, Center for Applied Coastal Research, University of Delaware, available at <http://www.udel.edu/kirby/papers/derakhti-kirby-cacr-14-06.pdf>.
- Derakhti, M. & Kirby, J. T. (2014*b*), ‘Bubble entrainment and liquid-bubble interaction under unsteady breaking waves’, *J. Fluid Mech.* **761**, 464–506.
- Derakhti, M. & Kirby, J. T. (2016), ‘Breaking-onset, energy and momentum flux in unsteady focused wave packets’, *J. Fluid Mech.*, *in press*.
- Derakhti, M., Kirby, J. T., Shi, F. & Ma, G. (2016*a*), ‘NHWAVE: Governing equations, consistent boundary conditions and turbulence modeling’, *Ocean Mod.*, *under review*.
- Derakhti, M., Kirby, J. T., Shi, F. & Ma, G. (2016*b*), ‘Wave breaking in the surf zone and deep water in a non-hydrostatic model’, *Ocean Mod.*, *under review*.
- Drazen, D. A. & Melville, W. K. (2009), ‘Turbulence and mixing in unsteady breaking surface waves’, *J. Fluid Mech.* **628**, 85.

- Drazen, D. A., Melville, W. K. & Lenain, L. (2008), ‘Inertial scaling of dissipation in unsteady breaking waves’, *J. Fluid Mech.* **611**, 307–332.
- Drew, D. (1983), ‘Mathematical modeling of two-phase flow’, *Ann. Rev. Fluid Mech.* **15**, 261–291.
- Drew, D. A. & Passman, S. L. (1999), *Theory of multicomponent fluids*, Springer.
- Duncan, J. H. (1983), ‘The breaking and non-breaking wave resistance of a two-dimensional hydrofoil.’, *J. Fluid Mech.* **126**, 507–520.
- Duncan, J. H. (2001), ‘Spilling breakers’, *Ann. Rev. Fluid Mech.* **33**, 519–547.
- Elgar, S. & Guza, R. (1985), ‘Observations of bispectra of shoaling surface gravity waves’, *J. Fluid Mech.* **161**, 425–448.
- Farahani, R. J. & Dalrymple, R. A. (2014), ‘Three-dimensional reversed horseshoe vortex structures under broken solitary waves’, *Coastal Eng.* **91**, 261–279.
- Farge, M. (1992), ‘Wavelet transforms and their applications to turbulence’, *Ann. Rev. Fluid Mech.* **24**, 395–458.
- Fox, R. (2012), ‘Large-eddy-simulation tools for multiphase flows’, *Ann. Rev. Fluid Mech.* **44**, 47–76.
- Garcez Faria, A. F., Thornton, E. B., Lippmann, T. C. & Stanton, T. P. (2000), ‘Undertow over a barred beach’, *J. Geophys. Res.* **105**, 16999–17010.
- Garrett, C., Li, M. & Farmer, D. (2000), ‘The connection between bubble size spectra and energy dissipation rates in the upper ocean’, *J. Phys. Oceanogr.* **30**, 2163–2171.
- Gemmrich, J. R., Banner, M. L. & Garrett, C. (2008), ‘Spectrally resolved energy dissipation rate and momentum flux of breaking waves’, *J. Phys. Oceanogr.* **38**, 1296–1312.
- Gemmrich, J. R. & Farmer, D. M. (2004), ‘Near-surface turbulence in the presence of breaking waves’, *J. Phys. Oceanogr.* **34**, 1067–1086.
- Gemmrich, J., Zappa, C. J., Banner, M. L. & Morison, R. P. (2013), ‘Wave breaking in developing and mature seas’, *J. Geophys. Res.* **118**, 4542–4552.
- Germano, M., Piomelli, U., Moin, P. & Cabot, W. H. (1991), ‘A dynamic subgrid-scale eddy viscosity model’, *Phys. Fluids* **3**, 1760–1765.
- Goulet, A. & Choi, W. (2011), ‘Nonlinear evolution of irregular surface waves: Comparison of numerical solutions with laboratory experiments for long crested waves’, *Phys. Fluids* p. 016601.

- Grare, L., Peirson, W. L., Branger, H., Walker, J. W., Giovanangeli, J. & Makin, V. (2013), ‘Growth and dissipation of wind-forced, deep-water waves’, *J. Fluid Mech.* **722**, 5–50.
- Hoque, A. & Aoki, S. (2005), ‘Distributions of void fraction under breaking waves in the surf zone’, *Ocean Eng.* **32**, 1829–1840.
- Hunt, J. C. R., Wray, A. A. & Moin, P. (1988), Eddies, streams, and convergence zones in turbulent flows, *in* ‘Center for Turbulence Research, CTR-S88’, Vol. 1, pp. 193–208.
- Hwang, P. A., Hsu, Y. H. L. & Wu, J. (1990), ‘Air bubbles produced by breaking wind waves: A laboratory study’, *J. Phys. Oceanogr.* **20**, 19–28.
- Iafrati, A. (2009), ‘Numerical study of the effects of the breaking intensity on wave breaking flows’, *J. Fluid Mech.* **622**, 371–411.
- Iafrati, A. (2011), ‘Energy dissipation mechanisms in wave breaking processes: Spilling and highly aerated plunging breaking events’, *J. Geophys. Res.* **116**, C07024, doi:10.1029/2011JC007038.
- Jacobsen, N. G., Fredsoe, J. & Jensen, J. H. (2014), ‘Formation and development of a breaker bar under regular waves. part 1: Model description and hydrodynamics’, *Coastal Eng.* **88**, 182–193.
- Jeong, J. & Hussain, F. (1995), ‘On the identification of a vortex’, *J. Fluid Mech.* **285**, 69–94.
- Kaihatu, J. M., Veeramony, J., Edwards, K. L. & Kirby, J. T. (2007), ‘Asymptotic behavior of frequency and wave number spectra of nearshore shoaling and breaking waves’, *J. Geophys. Res.* **112**, C06016.
- Kiger, K. T. & Duncan, J. H. (2012), ‘Air-entrainment mechanisms in plunging jets and breaking waves’, *Ann. Rev. Fluid Mech.* **44**, 563–596.
- Kim, D., Lynett, P. J. & Socolofsky, S. A. (2009), ‘A depth-integrated model for weakly dispersive, turbulent, and rotational fluid flows’, *Ocean Mod.* **27**, 198–214.
- Kirby, J. T., Ma, G., Derakhti, M. & Shi, F. (2012), Numerical investigation of turbulent bubbly flow under breaking waves, *in* ‘Proc. 33d Int. Conf. Coastal Eng.’, Santander, pp. waves–66.
- Lakehal, D. & Liovic, P. (2011), ‘Turbulence structure and interaction with steep breaking waves’, *J. Fluid Mech.* **674**, 522–577.
- Lakehal, D., Smith, B. L. & Milelli, M. (2002), ‘Large-eddy simulation of bubbly turbulent shear flows’, *J. Turbulence* **3**, N25.

- Lamarre, E. & Melville, W. K. (1991), ‘Air entrainment and dissipation in breaking waves’, *Nature* **351**, 469–472.
- Lamarre, E. & Melville, W. K. (1994), ‘Void-fraction measurements and sound-speed fields in bubble plumes generated by breaking waves’, *J. Acoust. Soc. Am.* **95**, 1317–1328.
- Lance, M. & Bataille, J. (1991), ‘Turbulence in the liquid phase of a uniform bubbly air-water flow’, *J. Fluid Mech.* **222**, 95–118.
- Lanckriet, T. & Puleo, J. A. (2013), ‘Near-bed turbulence dissipation measurements in the inner surf and swash zone’, *J. Geophys. Res.* **118**, 6634–6647.
- Leifer, I., Caulliez, G. & De Leeuw, G. (2006), ‘Bubbles generated from wind-steepened breaking waves: 2. bubble plumes, bubbles, and wave characteristics’, *J. Geophys. Res.* **111**, C06021.
- Leifer, I. & De Leeuw, G. (2006), ‘Bubbles generated from wind-steepened breaking waves: 1. bubble plume bubbles’, *J. Geophys. Res.* **111**, C06020.
- Lilly, D. K. (1992), ‘A proposed modification of the germano subgrid-scale closure method’, *Phys. Fluids* **4**, 633–635.
- Lin, P. & Liu, P.-F. (1998), ‘A numerical study of breaking waves in the surf zone’, *J. Fluid Mech.* **359**, 239–264.
- Loewen, M., O’Dor, M. & Skafel, M. (1996), ‘Bubbles entrained by mechanically generated breaking waves’, *J. Geophys. Res.* **101**, 20759–20769.
- Longuet-Higgins, M. S. (1953), ‘Mass transport in water waves’, *Phil. Trans. Roy. Soc. London, A* **245**, 535–581.
- Longuet-Higgins, M. S. (1970), ‘Longshore currents generated by obliquely incident sea waves: 1’, *J. Geophys. Res.* **75**, 6778–6789.
- Lubin, P. & Glockner, S. (2013), ‘Numerical simulations of three-dimensional plunging breaking waves: generation and evolution of aerated vortex filaments’, *J. Fluid Mech.* *Submitted.* .
- Lubin, P. & Glockner, S. (2015), ‘Numerical simulations of three-dimensional plunging breaking waves: generation and evolution of aerated vortex filaments’, *J. Fluid Mech.* **767**, 364–393.
- Lubin, P., Vincent, S., Abadie, S. & Caltagirone, J. (2006), ‘Three-dimensional large eddy simulation of air entrainment under plunging breaking waves’, *Coastal Eng.* **53**(8), 631–655.

- Ma, G. (2012), Multiscale numerical study of turbulent flow and bubble entrainment in the surf zone, PhD thesis, University of Delaware, Newark DE.
- Ma, G., Chou, Y. & Shi, F. (2014), ‘A wave-resolving model for nearshore suspended sediment transport’, *Ocean Mod.* **77**, 33–49.
- Ma, G., Kirby, J. T. & Shi, F. (2013), ‘Numerical simulation of tsunami waves generated by deformable submarine landslides’, *Ocean Mod.* **69**, 146–165.
- Ma, G., Kirby, J. T., Su, S., Figlus, J. & Shi, F. (2013), ‘Numerical study of turbulence and wave damping induced by vegetation canopies’, *Coastal Eng.* **80**, 68–78.
- Ma, G., Shi, F., Hsiao, S. & Wu, Y. (2014), ‘Non-hydrostatic modeling of wave interactions with porous structures’, *Coastal Eng.* **91**, 84–98.
- Ma, G., Shi, F. & Kirby, J. T. (2011), ‘A polydisperse two-fluid model for surf zone bubble simulation’, *J. Geophys. Res.* **116**, C05010, doi:10.1029/2010JC006667.
- Ma, G., Shi, F. & Kirby, J. T. (2012), ‘Shock-capturing non-hydrostatic model for fully dispersive surface wave processes’, *Ocean Mod.* **43**, 22–35.
- Martínez-Bazán, C., Montañés, J. L. & Lasheras, J. C. (1999*a*), ‘On the breakup of an air bubble injected into a fully developed turbulent flow. part 1. breakup frequency’, *J. Fluid Mech* **401**, 157–182.
- Martínez-Bazán, C., Montañés, J. L. & Lasheras, J. C. (1999*b*), ‘On the breakup of an air bubble injected into a fully developed turbulent flow. part 2. size pdf of the resulting daughter bubbles’, *J. Fluid Mech.* **401**, 183–207.
- Martínez-Bazán, C., Rodríguez-Rodríguez, J., Deane, G. B., Montañés, J. L. M. & Lasheras, J. C. (2010), ‘Considerations on bubble fragmentation models’, *J. Fluid Mech* **661**, 159–177.
- Mase, H. & Kirby, J. T. (1992), Hybrid frequency-domain KdV equation for random wave transformation, *in* ‘Proc. 23d Int. Conf. Coastal Eng.’, Venice, pp. 474–487.
- Maxey, M. R. & Riley, J. J. (1983), ‘Equation of motion for a small rigid sphere in a nonuniform flow’, *Phys. Fluids* **26**, 883.
- Melville, W. K. (1982), ‘The instability and breaking of deep-water waves’, *J. Fluid Mech.* **115**, 165–185.
- Melville, W. K. (1994), ‘Energy dissipation by breaking waves’, *J. Phys. Oceanogr.* **24**, 2041–2049.
- Melville, W. K. (1996), ‘The role of surface-wave breaking in air-sea interaction’, *Ann. Rev. Fluid Mech.* **28**, 279–321.

- Moraga, F. J., Carrica, P. M., Drew, D. A. & Lahey Jr, R. T. (2008), ‘A sub-grid air entrainment model for breaking bow waves and naval surface ships’, *Comp. Fluids* **37**, 281–298.
- Mori, N., Suzuki, T. & Kakuno, S. (2007), ‘Experimental study of air bubbles and turbulence characteristics in the surf zone’, *J. Geophys. Res* **112**, C05014.
- Nadaoka, K., Hino, M. & Koyano, Y. (1989), ‘Structure of the turbulent flow field under breaking waves in the surf zone’, *J. Fluid Mech* **204**, 359–387.
- Perlin, M., Choi, W. & Tian, Z. (2013), ‘Breaking waves in deep and intermediate waters’, *Ann. Rev. Fluid Mech.* **45**, 115–145.
- Phillips, O. (1977), *The dynamics of the upper ocean*, Cambridge University Press, London.
- Phillips, O., Posner, F. & Hansen, J. (2001), ‘High range resolution radar measurements of the speed distribution of breaking events in wind-generated ocean waves: Surface impulse and wave energy dissipation rates’, *J. Phys. Oceanogr.* **31**, 450–460.
- Pizzo, N. E. & Melville, W. K. (2013), ‘Vortex generation by deep-water breaking waves’, *J. Fluid Mech.* **734**, 198–218.
- Rapp, R. J. & Melville, W. K. (1990), ‘Laboratory measurements of deep-water breaking waves’, *Phil. Trans. Roy. Soc. A*, **331**, 735–800.
- Rider, W. J. & Kothe, D. B. (1998), ‘Reconstructing volume tracking’, *J. Comp. Phys.* **141**, 112–152.
- Robinson, S. K. (1991), ‘Coherent motions in the turbulent boundary layer’, *Ann. Rev. Fluid Mech.* **23**, 601–639.
- Rodi, W. (1980), ‘Turbulent models and their application in hydraulics—a state of the art review’, *Int. Assoc. for Hydraul Res., Delft* .
- Rogers, B. D., Borthwick, A. & Taylor, P. H. (2003), ‘Mathematical balancing of flux gradient and source terms prior to using roe’s approximate riemann solver’, *J. Comp. Phys.* **192**, 422–451.
- Rojas, G. & Loewen, M. R. (2007), ‘Fiber-optic probe measurements of void fraction and bubble size distributions beneath breaking waves’, *Exp. Fluids* **43**, 895–906.
- Romero, L., Melville, W. K. & Kleiss, J. M. (2012), ‘Spectral energy dissipation due to surface wave breaking’, *J. Phys. Oceanogr.* **42**, 1421–1444.
- Sato, Y. & Sekoguchi, K. (1975), ‘Liquid velocity distribution in two-phase bubble flow’, *Int. J. Multiphase Flow* **2**, 79–95.

- Scott, C. P., Cox, D. T., Shin, S. & Clayton, N. (2004), Estimates of surf zone turbulence in a large-scale laboratory flume, *in* ‘Proc. 29th Int. Conf. Coastal Eng.’, pp. 379–391.
- Shen, L. & Yue, D. K. P. (2001), ‘Large-eddy simulation of free-surface turbulence’, *J. Fluid Mech.* **440**, 75–116.
- Shi, F., Kirby, J. T., Harris, J. C., Geiman, J. D. & Grilli, S. T. (2012), ‘A high-order adaptive time-stepping TVD solver for Boussinesq modeling of breaking waves and coastal inundation’, *Ocean Modelling* **43**, 36–51.
- Shi, F., Kirby, J. T. & Ma, G. (2010), ‘Modeling quiescent phase transport of air bubbles induced by breaking waves’, *Ocean Modelling* **35**, 105–117.
- Shirkavand, A. & Badiiei, P. (2014), ‘The application of a godunov-type shock capturing scheme for the simulation of waves from deep water up to the swash zone’, *Coastal Eng.* **94**, 1–9.
- Smagorinsky, J. (1963), ‘General circulation experiments with the primitive equations’, *Monthly Weather Review* **91**, 99–164.
- Smit, P., Janssen, T., Holthuijsen, L. & Smith, J. (2014), ‘Non-hydrostatic modeling of surf zone wave dynamics’, *Coastal Eng.* **83**, 36–48.
- Smit, P., Zijlema, M. & Stelling, G. (2013), ‘Depth-induced wave breaking in a non-hydrostatic, near-shore wave model’, *Coastal Eng.* **76**, 1–16.
- Song, C. & Sirviente, A. (2004), ‘A numerical study of breaking waves’, *Phys. Fluids* **16**, 2649–2667.
- Song, J. & Banner, M. L. (2002), ‘On determining the onset and strength of breaking for deep water waves. part i: Unforced irrotational wave groups’, *J. Phys. Oceanogr.* **32**, 2541–2558.
- Svendsen, I. A. (1984), ‘Mass flux and undertow in a surf zone’, *Coastal Eng.* **8**, 347–365.
- Tappin, D. R., Grilli, S. T., Harris, J. C., Geller, R. J., Masterlark, T., Kirby, J. T., Shi, F., Ma, G., Thingbaijam, K. K. S. & Mai, P. M. (2014), ‘Did a submarine landslide contribute to the 2011 tohoku tsunami?’, *Marine Geology* **357**, 344–361.
- Thomson, J., Gemmrich, J. R. & Jessup, A. T. (2009), ‘Energy dissipation and the spectral distribution of whitecaps’, *Geophys. Res. Lett.* **36**.
- Thorpe, S. (1982), ‘On the clouds of bubbles formed by breaking wind-waves in deep water, and their role in air–sea gas transfer’, *Philos. Trans. R. Soc. London, Ser. A.* **304**, 155–210.

- Thorpe, S. A. (1995), ‘Dynamical processes of transfer at the sea surface’, *Prog. Oceanogr.* **35**, 315–352.
- Thorpe, S. & Humphries, P. (1980), ‘Bubbles and breaking waves’, *Nature* **283**, 463–465.
- Tian, Z., Perlin, M. & Choi, W. (2008), ‘Evaluation of a deep-water wave breaking criterion’, *Phys. Fluids* **20**, 066604.
- Tian, Z., Perlin, M. & Choi, W. (2010), ‘Energy dissipation in two-dimensional unsteady plunging breakers and an eddy viscosity model’, *J. Fluid Mech.* **655**, 217–257.
- Tian, Z., Perlin, M. & Choi, W. (2012), ‘An eddy viscosity model for two-dimensional breaking waves and its validation with laboratory experiments’, *Phys. of Fluids* **24**, 036601.
- Ting, F. C. K. (2001), ‘Laboratory study of wave and turbulence velocities in a broad-banded irregular wave surf zone’, *Coastal Eng.* **43**, 183–208.
- Ting, F. C. K. (2008), ‘Large-scale turbulence under a solitary wave: Part 2: Forms and evolution of coherent structures’, *Coastal Eng.* **55**, 522–536.
- Ting, F. C. K. & Kirby, J. T. (1994), ‘Observation of undertow and turbulence in a laboratory surf zone’, *Coastal Eng.* **24**, 51–80.
- Ting, F. C. K. & Nelson, J. R. (2011), ‘Laboratory measurements of large-scale near-bed turbulent flow structures under spilling regular waves’, *Coastal Eng.* **58**, 151–172.
- Ting, F. C. K. & Reimnitz, J. (2015), ‘Volumetric velocity measurements of turbulent coherent structures induced by plunging regular waves’, *Coastal Eng.* **104**, 93–112.
- Ting, F., Reimnitz, J., Auch, M. & Lai, W. (2013), Volumetric three-component velocimetry measurements of turbulent flow under breaking waves, in ‘10TH Int. Sym. Particle Image Velocimetry’.
- Toro, E. F. (2009), *Riemann solvers and numerical methods for fluid dynamics: a practical introduction*, Springer.
- Trowbridge, J. & Madsen, O. S. (1984), ‘Turbulent wave boundary layers: 2. second-order theory and mass transport’, *J. Geophys. Res.* **89**, 7999–8007.
- Van Milligen, B. P., Hidalgo, C. & Sanchez, E. (1995), ‘Nonlinear phenomena and intermittency in plasma turbulence’, *Physical review letters* **74**, 395.
- Vremen, B., Geurts, B. & Kuerten, H. (1997), ‘Large-eddy simulation of the turbulent mixing layer’, *J. Fluid Mech.* **339**, 357–390.

- Watanabe, Y., Saeki, H. & Hosking, R. J. (2005), ‘Three-dimensional vortex structures under breaking waves’, *J. Fluid Mech.* **545**, 291–328.
- Wei, G., Kirby, J. T., Grilli, S. T. & Subramanya, R. (1995), ‘A fully nonlinear Boussinesq model for surface waves. Part 1. Highly nonlinear unsteady waves’, *J. Fluid Mech.* **294**, 71–92.
- West, B. J., Brueckner, K. A., Janda, R. S., Milder, D. M. & Milton, R. L. (1987), ‘A new numerical method for surface hydrodynamics’, *J. Geophys. Res.* **92**, 11803–11824.
- Wiegel, R. (1960), ‘A presentation of cnoidal wave theory for practical application’, *J. Fluid Mech.* **7**, 273–286.
- Wu, C. H. & Nepf, H. M. (2002), ‘Breaking criteria and energy losses for three-dimensional wave breaking’, *J. Geophys. Res.* **107**, C10, 41–1 41–18.
- Yakhot, V., Orszag, S., Thangam, S., Gatski, T. & Speziale, C. (1992), ‘Development of turbulence models for shear flows by a double expansion technique’, *Phys. Fluids* **4**, 1510–1520.
- Young, C. & Wu, C. H. (2010), ‘Nonhydrostatic modeling of nonlinear deep-water wave groups’, *J. Eng. Mech.* **136**, 155–167.
- Zang, Y., Street, R. L. & Koseff, J. R. (1993), ‘A dynamic mixed subgrid-scale model and its application to turbulent recirculating flows’, *Phys. Fluids A* **5**, 3186–3196.
- Zhou, Z., Sangermano, J., Hsu, T. & Ting, F. C. K. (2014), ‘A numerical investigation of wave-breaking-induced turbulent coherent structure under a solitary wave’, *J. Geophys. Res.: Oceans* **119**, 6952–6973.
- Zijlema, M., Stelling, G. & Smit, P. (2011), ‘SWASH: An operational public domain code for simulating wave fields and rapidly varied flows in coastal waters’, *Coastal Eng.* **58**, 992–1012.

Appendix A

EULERIAN-EULERIAN MULTIPHASE MODELS

A.1 Different Numerical Approaches to Turbulent Multiphase Flows

[Balachandar & Eaton \(2010\)](#) reviewed computational approaches for turbulent dispersed multiphase flows. In dispersed multiphase flows, the evolution of the interface between the phases is considered of secondary importance. As they pointed out: (1) the phenomenon of preferential accumulation, and (2) turbulence modulation by particles are the most important features of turbulent multiphase flows.

Considering bubble and sediment phases as continuous dispersed phases is a reasonable assumption. The possible exception is during the entrainment stage near the free surface, at which time a large air cavity is entrained and breaks down to some extent, and can not be described as dispersed bubbles. The key factors to choose an appropriate numerical framework are the relative particle size and the volumetric concentration of the dispersed phase. [Figure A.1](#) shows the applicability of different approaches to turbulent multiphase flow proposed by [Balachandar & Eaton \(2010\)](#). The horizontal axis is the volumetric concentration, Φ_v , of a dispersed phase. They proposed the upper limit of $\Phi_v \approx 0.1\%$ for considering dilute suspension regime and ignoring inter-particle momentum transfer and collision processes. However, the dilute suspension regime is typically assumed to be valid for Φ_v values up to $1 \sim 10\%$ for sediment modeling. In the present study, we have always ignored particle-particle interaction for dispersed bubbles. We will also ignore this interaction for suspended sediment phases. In other words, we have used one- or two-way coupled frameworks. The vertical axis refers to particle stokes number, $S_t = \tau_p/\tau_k$ or τ_p/τ_ξ , where $\tau_p = d^2\rho_r/[18\nu\phi(Re)]$ is the particle time scale, $\tau_k = (\nu/\varepsilon)^{(1/2)}$ is the Kolmogorov timescale,

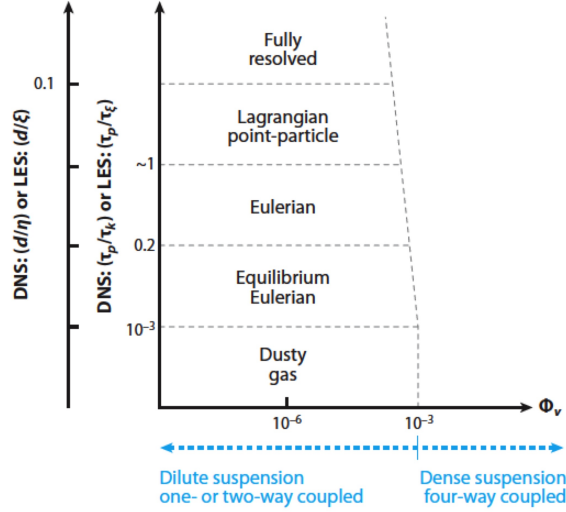


Figure A.1: Different approaches to turbulent multiphase flows. Their applicability is separated in terms of timescale and length-scale ratios. Figure taken from [Balachandar & Eaton \(2010\)](#) figure 1.

and $\tau_\xi = \tau_k(\xi/\eta)^{(2/3)}$ is the smallest resolved eddy timescale. ξ is the smallest resolved LES length scale, $\eta = (\nu^3/\varepsilon)^{(1/4)}$ is the Kolmogorov length scale, ν is the kinematic viscosity of the fluid, ε is turbulence dissipation rate, $\rho_r = \rho_p/\rho_f$ is particle-to-fluid density ratio, and d is the particle diameter. Finally, $\phi(Re) = 1 + 0.15Re^{0.687}$, where $Re = |\mathbf{v} - \mathbf{u}|d/\nu$ is the particle Reynolds number, and \mathbf{v}, \mathbf{u} are the particle and carrier phase velocities, respectively. In case of LES of the carrier phase, S_t can be written as ([Balachandar & Eaton 2010](#))

$$St = \frac{\tau_p}{\tau_\xi} = \frac{2\rho_r + 1}{36} \frac{1}{\phi(Re)} \left(\frac{d}{\xi}\right)^2 \left(\frac{\xi}{\eta}\right)^{\frac{4}{3}}. \quad (\text{A.1})$$

The turbulence dissipation rate, ε (m^2s^{-3}), in breaking waves has a wide range from $O(0.1 \sim 1.0)$ at the initial stage of active breaking near the free surface to $O(10^{-5} \sim 10^{-4})$ after active breaking and/or in deeper depths (see for example, [Lanckriet & Puleo 2013](#), [Gemmrich & Farmer 2004](#), among others).

Table A.1: Bubble Stokes number for different bubble diameters and turbulence dissipation rates. w_b is the rise velocity of a bubble.

d_b (mm)	w_b (m/s)	$St(\varepsilon = 0.01)$	$St(\varepsilon = 0.1)$	$St(\varepsilon = 1.0)$
1	0.15	0.014	0.031	0.066
3	0.23	0.051	0.110	0.236
5	0.23	0.102	0.219	0.472
8	0.23	0.191	0.412	0.887
10	0.23	0.258	0.555	1.196

Table A.1 summarizes the corresponding bubble stokes number for different bubble diameters, d_b , and turbulence dissipation rates. In this study, we have used 20 different groups with characteristic bubble diameters increased by a constant spacing in a logarithmic scale, from 0.1 to 8 mm with the Hinze scale equals to 1 mm. Based on table A.1, we conclude that the Equilibrium Eulerian approach can be used for bubble groups with the maximum diameter of 3 mm during active breaking. For larger bubble diameters ($3 < d_b < 8$ mm), St is still smaller than 1.0, and thus the Eulerian-Eulerian framework will be appropriate.

In general, we can divide Eulerian-Eulerian numerical models of bubbly flows into discrete and continuous models. In the discrete models, the interface between an individual bubble and the liquid is resolved. Obviously, the possible bubble diameter which can be resolved is limited to the grid resolution. To account for the bubble size distribution under breaking waves, we need to have a very fine grid resolution about two orders of magnitude smaller than typical LES resolution. In the continuous models, instead, the interface between an individual bubble and the liquid is not resolved, and the interfacial momentum transfers are considered using closure models. A critical issue in this approach, especially under breaking waves, is accurately introducing air bubbles into a model using a bubble entrainment formulation (Moraga et al. 2008, Shi et al. 2010, Ma et al. 2011).

As summarized by Perlin et al. (2013), most of the numerical simulations for

deep water breaking waves are limited to the evolution of a periodic unstable wave train with relatively low-Reynolds numbers ($\sim 10^4$) and short wave lengths ($< 0.3m$) (Chen et al. 1999, Song & Sirviente 2004, Lubin et al. 2006, Iafrati 2009, 2011, Lubin & Glockner 2013). This artificial way of leading a wave train to breaking has an advantage in that it represents a more compact computational problem. However, it is not possible to do comparisons with experimental data, except in a qualitative sense. In addition, it is well known that, at such a short scale, surface tension significantly affects the breaking process and fragmentation of the air cavity. Furthermore, although wave breaking is initially a fairly 2D event, the entrainment process is highly 3D even in the case of a small scale plunger where surface tension appears to be playing a strong role (Kiger & Duncan 2012). Thus, 2D frameworks can not accurately account for bubble transport and vorticity evolution during and after breaking. In these discrete numerical studies, the Navier-Stokes equations are solved both in air and water with a relatively fine spatial resolution that can resolve cavity fragmentation to some extent. Although the density and viscosity of the gas is not equal to real air in most of the previous simulations, consideration of the gas phase considerably increases the computational effort. To study periodic breaking waves in laboratory scale with 3D LES VOF-based models, the common practice is to neglect the computations in the air side by replacing the air by void (Christensen & Deigaard 2001, Watanabe et al. 2005, Christensen 2006, Ma 2012). An exception is Lakehal & Liovic (2011) where actual air density and viscosity was considered. Lakehal & Liovic (2011) carried out 3D LES of the filtered two-fluid Navier-Stokes equations combined with the VOF method. The Smagorinsky sub-grid scale model is coupled with a new damping formula similar to a solid wall function that has several input parameters and needs the so called air-side interfacial shear/friction velocity to estimate the "interface turbulence units" length scale. They analyzed the energy transfer between the mean flow and the wave modes, and studied wave-turbulence interaction. They found that wave breaking is accompanied by intermittent generation of local vortices and increased surface wrinkling. The turbulent kinetic energy budget and energy decay are linked to the localized incidence

of coherent structures in the liquid. The mesh resolution in the stream-wise direction is much coarser than the other two directions, $\frac{\Delta x}{\Delta y} = \frac{\Delta x}{\Delta z} \sim 5$. With this grid resolution, bubble entrainment and transport as well as liquid-bubble interactions can not be resolved properly.

The first attempt to use a continuous model for studying bubbly flow under breaking waves was done by [Shi et al. \(2010\)](#). They used a 2D VOF-based mixture model, with a $k - \varepsilon$ turbulence closure, to study air bubble evolution in an isolated unsteady breaking wave in a laboratory scale event. They used an air bubble entrainment formula which connected shear production at the air-water interface and the bubble number density with the bubble size distributions suggested by [Deane & Stokes \(2002\)](#). The bubble velocities were calculated directly by adding the rise velocities to the liquid velocity, and the additional terms were used both in k and ε transport equations to account for the bubble-induced turbulence. They argued that, with an appropriate parameter in the bubble entrainment formula, the model is able to predict the main features of bubbly flows as evidenced by reasonable agreement with measured void fraction. [Ma et al. \(2011\)](#) incorporated a polydisperse two-fluid model ([Carrica et al. 1999](#)) into the VOF-based Navier-Stokes solver TRUCHAS. They proposed an entrainment model that connected bubble entrainment with turbulent dissipation rate, ε , at the air-water interface. The model was tested against laboratory experimental data for an oscillatory bubble plume and the bubbly flow under a laboratory periodic breaking wave using 2D simulations with a $k - \varepsilon$ turbulence closure, in conjunction with the additional terms to account for bubble-induced turbulence. The exponential decay in time of void fraction observed in the laboratory experiments was captured by the model. The kinematics of the bubble plume, as well as the evolution of the bubble size spectrum over depth, were investigated. They employed a bubble breakup model proposed by [Martínez-Bazán et al. \(1999a,b\)](#) and showed that the model reproduced the $-10/3$ dependence for bubbles greater than the Hinze scale in the bubble size spectrum, consistent with the observation of [Deane & Stokes \(2002\)](#). [Ma \(2012\)](#) and [Kirby et al. \(2012\)](#) extended the model to a LES framework with a constant Smagorinsky

subgrid formulation for turbulence closure. They investigated surf zone breaking and found that the integrated void fraction has a linear growth and exponential decay in time. They showed that, as the vortices move downward, bubbles are transported to the lower part of the water column and concluded that the turbulent coherent structures tend to transport bubbles more deeply into the water column. Based on both 2D and 3D simulations, they found that the presence of bubbles suppresses liquid phase turbulence and enstrophy.

A.2 Polydisperse Two-fluid Model

Using the multi-group approach explained by Carrica et al. (1999), bubbles are divided into N_G groups with a characteristic diameter, and the filtered polydisperse two-fluid model is derived based on the filtered monodisperse two-fluid model of Lakehal et al. (2002). In this section, we quickly review the traditional two-fluid model as well as work by Lakehal et al. (2002), and then the extension to the polydisperse two-fluid model and the corresponding main assumptions are discussed.

A.2.1 The filtered two-fluid equations

The filtered two-fluid model is obtained by applying a certain averaging process on the microscopic instantaneous equations governing each phase evolving in the mixture. The conservation laws for each phase can be written using the phase indicator function $\chi(\mathbf{x}, t)$ at time t and point \mathbf{x} , defined by (Drew 1983),

$$\chi^k(\mathbf{x}, t) = \begin{cases} 1 & \text{if } \mathbf{x} \text{ lies in phase } k \text{ at time } t \\ 0 & \text{otherwise} \end{cases} \quad (\text{A.2})$$

to determine the volumes occupied by each phase. Here, k refers either to the gas phase or to the liquid phase. In the absence of heat and mass transfer, the continuity

and momentum equations for each phase can be written as

$$\frac{\partial}{\partial t}(\chi^k \rho^k) + \frac{\partial}{\partial x_j}(\chi^k \rho^k u_j^k) = 0, \quad (\text{A.3})$$

$$\frac{\partial}{\partial t}(\chi^k \rho^k u_i^k) + \frac{\partial}{\partial x_j}(\chi^k \rho^k u_i^k u_j^k) = \chi^k \frac{\partial}{\partial x_j} \Pi_{ij}^k + \chi^k \rho^k g_i, \quad (\text{A.4})$$

where ρ^k is the phase density, u^k is the phase velocity and g is the gravitational acceleration. The phase net stress, composed of the pressure contribution, p^k , and the viscous stress σ_{ij}^k , is defined by $\Pi_{ij}^k = -p^k \delta_{ij} + \sigma_{ij}^k$. In a Newtonian fluid,

$$\sigma_{ij}^k = \rho^k \nu^k \left(\frac{\partial u_i^k}{\partial x_j} + \frac{\partial u_j^k}{\partial x_i} \right) \quad (\text{A.5})$$

where ν^k is the phase kinematic viscosity. Within the LES framework, a filtering process is utilized which is defined by

$$\overline{f(\mathbf{x})} = \int_D G(\mathbf{x} - \mathbf{x}'; \Delta) f(\mathbf{x}') d^3 \mathbf{x}', \quad (\text{A.6})$$

where D is the domain of the flow, $G(\mathbf{x} - \mathbf{x}'; \Delta)$ represents a spatial filter and Δ is the filter width which should strictly be larger than the characteristic length scale of the dispersed phase. On the other hand, Δ should be small enough to resolve mean flow and at least 80% of the TKE. To meet the latter in LES of small-scale breaking events, as in the present study, we need to have $\Delta \sim \text{O}(1\text{cm})$, which is close to the bubble diameters of the upper range of the typical observed bubble size distribution. At larger-scale breaking events, however, larger values for the filtered width may be chosen, and thus the whole range of bubble diameters can be considered using the polydisperse approach. With this operator, the volume fraction of phase k can be defined by

$$\alpha^k(\mathbf{x}) = \overline{\chi^k(\mathbf{x})}. \quad (\text{A.7})$$

As carried out by [Lakehal et al. \(2002\)](#), the filtered equations are obtained by adopting a component-weighted volume-averaging procedure, in which

$$\tilde{f}^k = \frac{\overline{\chi^k f^k}}{\overline{\chi^k}} = \frac{\overline{\chi^k f^k}}{\alpha^k}. \quad (\text{A.8})$$

By applying the above definition to (A.3) and (A.4) and ignoring surface tension effects, the filtered Eulerian-Eulerian equations are obtained ([Lakehal et al. 2002](#)),

$$\frac{\partial}{\partial t}(\alpha^k \rho^k) + \frac{\partial}{\partial x_j}(\alpha^k \rho^k \tilde{u}_j^k) = 0 \quad (\text{A.9})$$

$$\frac{\partial}{\partial t}(\alpha^k \rho^k \tilde{u}_i^k) + \frac{\partial}{\partial x_j}(\alpha^k \rho^k \tilde{u}_i^k \tilde{u}_j^k) = \frac{\partial}{\partial x_j} \alpha^k [\tilde{\Pi}_{ij}^k - \rho^k \tau_{ij}^k] + \alpha^k \rho^k g_i + \mathbf{M}^k, \quad (\text{A.10})$$

where $\tilde{(\cdot)}$ is the filter operation (A.8), $\mathbf{M}^k = \overline{\Pi_{ij}^k n_j^k \delta(x - x_I)}$ are the pure interfacial forces resulting from filtering, where n_j^k is the normal unit vector pointing outward of phase k , δ is the Dirac distribution identifying the interface location with x_I and

$$\tau_{ij}^k = \widetilde{u_i u_j^k} - \tilde{u}_i^k \tilde{u}_j^k, \quad (\text{A.11})$$

is the subgrid-scale (SGS) stress. Interphase momentum exchange \mathbf{M}^k and SGS stress τ_{ij}^k are the two unresolved terms in (A.10); our treatment of them will be explained in the following sections. Equations (A.9) and (A.10) can be easily extended for the polydisperse two-fluid model by neglecting the momentum exchange between bubble groups as in [Carrica et al. \(1999\)](#) and [Ma et al. \(2011\)](#). To simulate polydisperse bubbly flow, the dispersed bubble phase is separated into N_G groups. Each group has a characteristic bubble diameter d_k^b , $k = 1, 2, \dots, N_G$, and a corresponding volume fraction α_k^b . By definition, the volume fraction of all of the phases must sum to one:

$$\alpha^l + \sum_{k=1}^{N_G} \alpha_k^b = 1, \quad (\text{A.12})$$

where the superscripts l and b refer to the liquid and bubble phases respectively. The volume fraction of the k th bubble group is related to the bubble number density N_k^b by

$$\alpha_k^b = \frac{m_k^b N_k^b}{\rho^b}, \quad (\text{A.13})$$

where m_k^b is the mass of the k th bubble group, N_k^b is the number density of the k th bubble group and ρ^b is the bubble density, which is assumed to be constant. The governing equations consist of mass conservation for the liquid phase,

$$\frac{\partial(\alpha^l \rho^l)}{\partial t} + \frac{\partial}{\partial x_j}(\alpha^l \rho^l \tilde{u}_j^l) = 0, \quad (\text{A.14})$$

momentum conservation for the liquid phase,

$$\frac{\partial(\alpha^l \rho^l \tilde{u}_i^l)}{\partial t} + \frac{\partial}{\partial x_j}(\alpha^l \rho^l \tilde{u}_i^l \tilde{u}_j^l) = -\frac{\partial}{\partial x_j}(\alpha^l \tilde{p}) \delta_{ij} + \alpha^l \rho^l g_i + \frac{\partial}{\partial x_j} [\alpha^l (\tilde{\sigma}_{ij}^l - \rho \tau_{ij}^l)] + \mathbf{M}^{gl}, \quad (\text{A.15})$$

the bubble number density equation for each bubble group,

$$\frac{\partial N_k^b}{\partial t} + \frac{\partial}{\partial x_j}(\tilde{u}_{k,j}^b N_k^b) = B_k^b + S_k^b + D_k^b, \quad k = 1, \dots, N_G \quad (\text{A.16})$$

and the momentum conservation for each bubble group,

$$0 = -\frac{\partial}{\partial x_j}(\alpha_k^b \tilde{p}) \delta_{ij} + \alpha_k^b \rho^b g_i + \mathbf{M}_k^{lg}, \quad k = 1, \dots, N_G \quad (\text{A.17})$$

in which we neglect the inertia and shear stress terms in the gas phase following [Carrica et al. \(1999\)](#) and [Ma et al. \(2011\)](#). Here, ρ^l is assumed to be constant; \tilde{p} is the filtered pressure, which is identical in each phase due to the neglect of interfacial surface tension; B_k^b is the source for the k th bubble group due to air entrainment, and S_k^b is the intergroup mass transfer, which only accounts for bubble breakup in the present study ([Moraga et al. 2008](#), [Ma et al. 2011](#)). The bubble breakup model proposed by [Martínez-Bazán et al. \(2010\)](#) is employed. Here, $D_k^b = \nu^b (\partial N_k^b / \partial x_j)$ stems from filtering the exact bubble number density equation and represents the SGS diffusion for the k th

bubble group with bubble diffusivity, ν^b , given by (A.32) below; \mathbf{M}^{gl} and \mathbf{M}_k^{lg} are the momentum transfers between phases, which satisfy the following relationship:

$$\mathbf{M}^{gl} + \sum_{k=1}^{N_G} \mathbf{M}_k^{lg} = 0. \quad (\text{A.18})$$

A.2.2 Interfacial Momentum Exchange

For a single particle moving in a fluid, the force exerted by the continuous phase on the particle includes drag, lift, virtual mass and Basset history forces. These forces are well established in the literature for both laminar and turbulent flows (Clift et al. (1978) and Maxey & Riley (1983), among many others). By neglecting the Basset history force, the filtered interfacial forces can be formulated as follows:

$$\mathbf{M}_k^{lg} = \tilde{\mathbf{f}}_k^{VM} + \tilde{\mathbf{f}}_k^L + \tilde{\mathbf{f}}_k^D, \quad (\text{A.19})$$

where the filtered virtual mass force $\tilde{\mathbf{f}}_k^{VM}$, the filtered lift force $\tilde{\mathbf{f}}_k^L$ and the filtered drag force $\tilde{\mathbf{f}}_k^D$ are approximated as (Lakehal et al. 2002)

$$\begin{aligned} \tilde{\mathbf{f}}_k^{VM} &\approx \alpha_k^b \rho^l C_{VM} \left(\frac{D\tilde{\mathbf{u}}^l}{Dt} - \frac{D\tilde{\mathbf{u}}_k^b}{Dt} \right), \\ \tilde{\mathbf{f}}_k^L &\approx \alpha_k^b \rho^l C_L (\tilde{\mathbf{u}}^l - \tilde{\mathbf{u}}_k^b) \times (\nabla \times \tilde{\mathbf{u}}^l), \\ \tilde{\mathbf{f}}_k^D &\approx \alpha_k^b \rho^l \frac{3}{4} \frac{C_D}{d_k^b} (\tilde{\mathbf{u}}^l - \tilde{\mathbf{u}}_k^b) | \tilde{\mathbf{u}}^l - \tilde{\mathbf{u}}_k^b |, \end{aligned} \quad (\text{A.20})$$

where $\frac{D}{Dt}$ is the material derivative defined in terms of the Eulerian velocity field, C_{VM} is the virtual mass coefficient with a constant value of 0.5, C_L is the lift force coefficient chosen as 0.5 and C_D is the drag coefficient given by (Clift et al. 1978)

$$C_D = \begin{cases} \frac{24}{Re_k} (1 + 0.15 Re_k^{0.687}) & \text{for } Re_k < 1000, \\ 0.44 & \text{for } Re_k \geq 1000, \end{cases} \quad (\text{A.21})$$

where $Re_k = (d_k^b | \tilde{\mathbf{u}}^l - \tilde{\mathbf{u}}_k^b |) / \nu^l$ is the bubble Reynolds number of the k th group. It should be noted that in pure water, with no contamination, the bubble drag coefficient

is smaller than that in (A.21). As explained by Clift et al. (1978), the presence of surfactants, which is usually the case in laboratory conditions and the real world, increases the drag force so that the drag corresponds frequently to that of a solid sphere of the same size as given by (A.21). Finally, an inherent assumption in (A.20) is that SGS effects on the interfacial forces are assumed to be negligibly small.

A.2.3 Bubble Entrainment Model

Kiger & Duncan (2012) reviewed the mechanisms of air entrainment in plunging jets and breaking waves. As already mentioned, a detailed examination of the process of bubble entrainment needs much more computational resolution than we are employing. Instead, dispersed bubbles are introduced into the water column using an entrainment model. Ma et al. (2011) correlated the bubble entrainment rate with the shear-induced turbulence dissipation rate, ε^l , which is available in the Reynolds-averaged Navier-Stokes (RANS) framework. In the present LES framework, we use the formulation of Ma et al. (2011) but change ε^l to the shear-induced production rate of SGS kinetic energy, $\varepsilon_{sgs,SI}^l$ (sometimes called the SGS dissipation rate) which represents the rate of transfer of energy from the resolved to the SGS motions, given by (A.31). For polydisperse bubbles, the formulation is

$$B_k^b = \frac{c_{en}}{4\pi} \left(\frac{\sigma}{\rho^l}\right)^{-1} \alpha^l \left(\frac{f(a_k) \Delta a_k}{\sum_{k=1}^{N_G} a_k^2 f(a_k) \Delta a_k} \right) \varepsilon_{sgs,SI}^l, \quad (\text{A.22})$$

where c_{en} is the bubble entrainment parameter and has to be calibrated in the simulation. σ is the surface tension coefficient, a_k is the characteristic radius of each bubble group, Δa_k is the width of each bubble group and $f(a_k)$ is the bubble size spectrum. Deane & Stokes (2002) used a high-speed video camera to measure the bubble size distribution under the laboratory-scale breaking imposed by the focused wave method in seawater. They divided the entrainment process into two distinct mechanisms controlling the bubble size distribution. The first is turbulent fragmentation of the entrapped cavity, which is largely responsible for bubbles larger than the Hinze scale, leading

to a bubble number density proportional to a^{α_1} , where a is the bubble radius. The second is jet interaction and drop impact on the wave face, resulting in smaller bubbles with a number density proportional to a^{α_2} . Their results showed that initially the size spectrum slopes are $\alpha_1 = -10/3$ and $\alpha_2 = -3/2$, with considerable decrease at later times in the quiescent phase. The initial bubble size spectrum (A.23) directly affects the size-dependent liquid-bubble interaction. Bubbles with radii smaller than the Hinze scale contribute approximately a few percent of the total entrained bubbles with smaller dynamical effects due to relatively smaller diameter and rising velocity. Thus, the size spectrum slope for the larger bubbles, α_1 , is more important and need to be chosen accurately. Different experimental studies under laboratory-scale unsteady breaking waves (Loewen et al. 1996, Rojas & Loewen 2007) found similar values for α_1 in both freshwater and saltwater. In addition, Ma et al. (2011) employed a bubble breakup model proposed by Martínez-Bazán et al. (2010) and showed that the model reproduced the $-10/3$ dependence for bubbles greater than the Hinze scale, consistent with the observation of Deane & Stokes (2002). As in Ma et al. (2011), we use the size spectrum suggested by Deane & Stokes (2002),

$$f(a) \propto \begin{cases} a^{-10/3} & \text{if } a > a_h \\ a^{-3/2} & \text{if } a \leq a_h \end{cases} \quad (\text{A.23})$$

where $a_h = 1.0\text{mm}$ is taken to be the Hinze scale, to initially distribute the generated bubbles across the N_G bubble groups. This initial distribution is merely a convenience in that the bubble break-up model of Martínez-Bazán et al. (2010) rapidly redistributes large bubbles to fit this distribution, as shown by Ma et al. (2011). Bubbles are entrained at the free surface cells if $\varepsilon_{sgs,SI}^l$ is larger than a critical value, ε_c^l , which is set to $0.01 \text{ m}^2 \text{ s}^{-3}$. The threshold value, ε_c^l , is imposed to avoid unphysical bubble entrainment, especially after active breaking. We note that if we change ε_c^l by a factor of 2 or so, the change of entrained bubbles during active breaking is negligibly small.

A.2.4 Subgrid-scale Model

The turbulent velocities in the continuous phase can arise from (a) bubble agitations, e.g. turbulent wakes behind individual bubbles, and (b) large-scale flow instabilities, e.g. shear-induced instability (Fox 2012). In a continuum LES framework in which individual bubbles are not resolved and the filter width is in the inertial subrange, the main dissipative scales of motions are not resolved, and then transfer of the energy from the resolved to subgrid scales through shear- and bubble-induced dissipation should be modeled appropriately. The most widely used and simplest SGS model is the Smagorinsky model (Smagorinsky 1963), in which the anisotropic part of the SGS stress $\tau_{ij}^{l,d}$ is related to the resolved rate of strain,

$$\tau_{ij}^{l,d} \equiv \tau_{ij}^l - \frac{\delta_{ij}}{3} \tau_{kk}^l = -2\nu_{sgs}^l \tilde{\mathcal{S}}_{ij}^l, \quad (\text{A.24})$$

where $\tilde{\mathcal{S}}_{ij}^l = \frac{1}{2}(\partial\tilde{u}_i^l/\partial x_j + \partial\tilde{u}_j^l/\partial x_i)$ is the resolved rate of strain and $\nu_{sgs}^l = \nu_{SI}^l + \nu_{BI}^l$ is the eddy viscosity of the SGS motions calculated using linear superposition of both the shear-induced, ν_{SI}^l , and bubble-induced, ν_{BI}^l , viscosities (Lance & Bataille 1991). As in single-phase flow, we take

$$\nu_{SI}^l = (C_s \tilde{\Delta})^2 |\tilde{\mathcal{S}}|, \quad (\text{A.25})$$

where C_s is the Smagorinsky coefficient, $\tilde{\Delta} = (\Delta x \Delta y \Delta z)^{1/3}$ is the width of the grid filter and $|\tilde{\mathcal{S}}| = \sqrt{2\tilde{\mathcal{S}}_{ij}^l \tilde{\mathcal{S}}_{ij}^l}$ is the norm of the resolved strain rate tensor.

The C_s can be chosen as a constant (0.1 \sim 0.2) or determined dynamically. Although the constant Smagorinsky model (CSM) is fairly good at fully turbulent flows with simple geometries (e.g. turbulent channel flow), it is too dissipative near the wall as well as in laminar and transition flows. A near-wall function can be used to give better behavior close to walls, but the extra dissipation can not be removed in transitional turbulence generated under breaking waves. In the case of deep water unsteady breaking, this is more important because we have a localized unsteady TKE

plume with relatively high intensity at the initial stage of the breaking, which gradually becomes more uniform and is mixed down to a greater depth. Shen & Yue (2001) studied the interaction between a turbulent shear flow and a free surface at low Froude numbers using single-phase Navier-Stokes equations. The DNS results showed that the amount of energy transferred from the grid scales to the SGS reduced significantly as the free surface was approached. As a result, the coefficient C_s should decrease towards the free surface (Shen & Yue 2001, Figure 6a), which is not captured in the CSM and leads to excessive dissipation near the free surface. The dynamic Smagorinsky models (DSMs), on the other hand, provide a methodology for determining an appropriate local value for C_s , where the turbulent viscosity converges to zero when the flow is not turbulent and no special treatment is needed near the wall or in laminar and transitional regions. In addition, the DSM is able to capture the anisotropy and the decrease of C_s near the free surface as seen in DNS results. In the present study, we use the dynamic procedure of Germano et al. (1991) with a least-square approach suggested by Lilly (1992) to compute $(C_s)^2$ based on double filtered velocities as

$$(C_s)^2 = -\frac{L_{ij}M_{ij}}{2\tilde{\Delta}^2 M_{ij}M_{ij}}, \quad (\text{A.26})$$

where

$$L_{ij} = \widehat{\tilde{u}_i^l \tilde{u}_j^l} - \widehat{\tilde{u}_i^l} \widehat{\tilde{u}_j^l} \quad \text{and} \quad M_{ij} = \alpha^2 |\widehat{\tilde{\mathcal{S}}}| \widehat{\tilde{\mathcal{S}}}_{ij} - |\widehat{\tilde{\mathcal{S}}}| \widehat{\tilde{\mathcal{S}}}_{ij}. \quad (\text{A.27})$$

Here, $\widehat{}$ represents the test scale filter with $\alpha = \widehat{\Delta}/\tilde{\Delta} > 1$. We use the box filter given in Zang et al. (1993, Appendix A) with $\alpha = 2$. As pointed out by Zang et al. (1993) and others, the locally computed values from (A.26) have large fluctuations and cause numerical instability especially in the case of negative diffusivity. To cope with this problem, averaging in a homogeneous direction (Germano et al. 1991, Vremen et al. 1997) or, in a more general case, local averaging (Zang et al. 1993) should be applied. We perform local averaging and set negative values to zero as in Vremen et al. (1997).

The effect of SGS bubble-induced turbulence is added in the form of a bubble-induced viscosity, ν_{BI}^l (Lance & Bataille 1991, Fox 2012). We use the well-known model

proposed by [Sato & Sekoguchi \(1975\)](#), given by

$$\nu_{BI}^l = C_{\mu,BI} \sum_{k=1}^{N_G} \alpha_k^b d_k^b |\tilde{\mathbf{u}}_{r,k}|, \quad (\text{A.28})$$

where the model constant $C_{\mu,BI}$ is equal to 0.6 and $\tilde{\mathbf{u}}_{r,k}$ is the resolved relative velocity between the k th bubble group and the liquid phase. It should be noted that in regions of high void fraction, (A.28) may underestimate the bubble-induced viscosity due to bubble-bubble interactions, and then SGS pseudo-turbulent kinetic energy. Using (A.5) and (A.24), the $\tilde{\sigma}_{ij}^l - \rho^l \tau_{ij}^l$ term in (A.15) can be written in the form of effective viscosity as

$$\tilde{\sigma}_{ij}^l - \rho^l \tau_{ij}^l = \tilde{\sigma}_{ij}^l - \rho^l \left(\tau_{ij}^{l,d} + \frac{\delta_{ij}}{3} \tau_{kk}^l \right), \quad \tilde{\sigma}_{ij}^l - \rho^l \tau_{ij}^{l,d} = 2\rho^l \nu_{eff}^l \tilde{\mathcal{S}}_{ij}, \quad (\text{A.29})$$

where

$$\nu_{eff}^l = \nu^l + \nu_{sgs}^l = \nu^l + \nu_{SI}^l + \nu_{BI}^l. \quad (\text{A.30})$$

The $\rho^l \frac{\delta_{ij}}{3} \tau_{kk}^l$ term can be absorbed in the pressure term. We write $\varepsilon_{sgs,SI}^l$ in (A.22) as

$$\varepsilon_{sgs,SI}^l = 2\nu_{SI}^l \tilde{\mathcal{S}}_{ij} \tilde{\mathcal{S}}_{ij} = \nu_{SI}^l |\tilde{\mathcal{S}}|^2. \quad (\text{A.31})$$

To compute D_k^b in (A.16), the bubble diffusivity, ν^b , is given by

$$\nu^b = \frac{\nu_{sgs}^l}{Sc^b}, \quad (\text{A.32})$$

where Sc^b is the Schmidt number for the bubble phase, taken equal to 0.7.

A.2.5 Free Surface Tracking

The VOF method with the second-order piecewise linear interface calculation (PLIC) scheme ([Rider & Kothe 1998](#)) is employed to track the free surface location. A linearity-preserving piecewise linear interface geometry approximation ensures that the generated solutions retain second-order spatial accuracy. Second-order temporal

accuracy is achieved by virtue of a multidimensional unsplit time integration scheme. In the VOF approach, an additional equation for the fluid volume fraction ψ is solved,

$$\frac{\partial \psi}{\partial t} + \nabla \cdot (\tilde{\mathbf{u}}^l \psi) = 0, \quad (\text{A.33})$$

where ψ is the volume fraction of the water within a computational cell. If $\psi = 1$, the cell is inside the water, while if $\psi = 0$, the cell is outside the water; otherwise, the cell is at the air(or void)-water interface, and $\psi = 0.5$ determines the position of the free surface.

A.2.6 Boundary Conditions

We do not solve the Navier-Stokes equations in any cell where $\psi = 0$ and treat it as a void with zero density. Instead, the pressure remains unchanged and all of the velocity components are set to zero, which implies zero stress at the void-water interface. Due to the zero-stress assumption, the energy transfer between water and air is ignored. At the top boundary, the pressure is set to zero and then the whole void area has zero pressure. As in [Watanabe et al. \(2005\)](#) and [Christensen \(2006\)](#), we ignore surface tension, which leads to homogeneous boundary conditions for shear and pressure at the free surface. To correctly account for the actual flume geometry, a no-slip condition is imposed along the solid side walls and bottom. The DSM gives zero turbulent viscosity near the wall and does not need any special treatment such as a near-wall damping function. A sponge layer is used to reduce wave reflection from the downstream boundary. At the upstream boundary, the appropriate inflow condition is imposed. The input wave packet is composed of 32 sinusoidal components of steepness $a_i k_i$, where the a_i and k_i are the amplitude and wave number of the i th component. Based on linear superposition and by imposing that the maximum η occurs at x_b and t_b , the total surface displacement at the inlet is given by (see **RM** §2.3)

$$\eta(0, t) = \sum_{i=1}^{N=32} a_i \cos[2\pi f_i(t - t_b) + k_i x_b], \quad (\text{A.34})$$

where f_i is the frequency of the i th component. Here, x_b and t_b are the predefined location and time of breaking respectively. The discrete frequencies f_i were uniformly spaced over the band $\Delta f = f_N - f_1$ with a central frequency defined by $f_c = \frac{1}{2}(f_N - f_1)$. Different global steepnesses, $S = \sum_{i=1}^{N=32} a_i k_i$, and bandwidths, $\Delta f / f_c$, lead to spilling or plunging breaking, where increasing S and/or decreasing $\Delta f / f_c$ increases the breaking intensity (See [Drazen et al. \(2008\)](#) for more details). The free surface and velocities of each component are calculated using linear theory and then superimposed at $x = 0$.

A.2.7 Numerical Method

The 3D VOF unstructured finite volume code TRUCHAS ([Rider & Kothe 1998](#)) was extended to incorporate the polydisperse bubble phase ([Ma et al. 2011](#)) and different turbulent closures. The details of the numerical method are given in [Ma et al. \(2011\)](#). To summarize, the algorithm involves the following steps.

1. Material advection (the VOF model): The material interfaces are reconstructed using PLIC and interface normals are determined. The movement of the material between cells is based on combining the reconstructed geometry obtained from the PLIC algorithm with the normal component of the fluid velocities located on the faces of all mesh cells.
2. Solve the bubble number density and update the volume fractions: we use the bubble velocity at the previous time step to solve (A.16) and then update the volume fractions obtained from (A.12) and (A.13).
3. Velocity prediction: The intermediate predicted velocities are calculated with updated volume fractions by a forward Euler step in time. This step incorporates an explicit approximation to the momentum advection, body force and pressure gradient. These are updated in the correction step. Viscous forces are treated implicitly and then are averaged between the previous time step and the predicted step.
4. Pressure solution and velocity correction: The Poisson equation for pressure correction is solved using the preconditioned generalized minimal residual (GMRES) algorithm to satisfy the solenoidal condition.
5. bubble velocity calculation: Using (A.17), the bubble velocities are calculated based on the updated fluid velocities.

A.2.8 Reynolds Decomposition of the Resolved Fields

The Reynolds decomposition of any field variable, ϕ , can be written as $\phi = \langle \phi \rangle + \phi'$, where $\langle . \rangle$ represents the ensemble-averaged or organized flow and ϕ' is the turbulent fluctuation about this average. Similarly, for the resolved field variable, $\tilde{\phi} = \phi - \phi_{sgs}$, we can define $\tilde{\phi} = \langle \tilde{\phi} \rangle + \tilde{\phi}'$, then

$$\phi' = \phi - \langle \phi \rangle = \tilde{\phi} + \phi_{sgs} - \langle \tilde{\phi} + \phi_{sgs} \rangle = \tilde{\phi}' + \phi_{sgs} - \langle \phi_{sgs} \rangle, \quad (\text{A.35})$$

where the SGS part is unresolved and its magnitude can only be estimated. Although ensemble averaging is practical in experimental studies, it is tedious in the numerical simulation due to the long computational times involved. The averaged variable in the homogenous direction (here the y -direction) can be interpreted as an organized motion and the deviation from this average as the turbulent fluctuation. By this assumption, the ensemble averaging is approximated by the spanwise averaging, and enough grid points in the spanwise direction are needed to obtain a stable statistic. [Christensen & Deigaard \(2001\)](#) and [Lakehal & Liovic \(2011\)](#) used averaging on about 40 grid points in the spanwise direction to study turbulence under surf zone breaking waves, where the lateral boundary condition were periodic. We use a no-slip boundary condition for the side walls and, because of wall effects, we should not perform the averaging through the entire grid. We ignore 20 grid points near each wall, and then averaging is performed on the remaining grid points,

$$\langle \tilde{\phi}(i, k) \rangle \approx \bar{\tilde{\phi}}(i, k) = \sum_{j=21}^{N_y-20} \frac{1}{N_y - 40} \tilde{\phi}(i, j, k), \quad (\text{A.36})$$

where N_y is the number of grid points in the spanwise direction and $\bar{(\)}$ represents the spanwise averaging. Then we can write

$$\tilde{\phi}' = \tilde{\phi} - \bar{\tilde{\phi}} \quad \text{and} \quad \tilde{\phi}'_{r.m.s.} = [\overline{\tilde{\phi}'^2}]^{1/2}, \quad (\text{A.37})$$

where $\tilde{\phi}_{r.m.s.}$ is the resolved r.m.s. of the turbulent fluctuations.

Appendix B

FREE SURFACE DEFINITION CLOSE TO THE BREAK POINT

The free surface location $\eta(x, t)$ defined as the top air/water interface location if $\alpha^l > 0.5$ is satisfied in the three adjacent computational cells below that interfacial cell. By doing this we avoid the small splashes and low void fraction regions to be considered as a free surface. Figure B.1 shows snapshots of the spatial variations of the air-water interface and its associated calculated $\eta(x, t)$ (black lines) for the intermediate-depth plunging breaking case DP1. Figure B.2 shows that the approximated time-averaged potential energy density, $\frac{1}{2}\rho^l \overline{g\eta^2}$, based on our choice of the free surface location, has more pronounced oscillations during the jet formation between $-0.2 < x^* < 0$ compared with the exact values $\overline{E_p}$. For $x^* < -0.2$ and $0.5 < x^*$, the difference between $\overline{E_p}$ and $\frac{1}{2}\rho^l \overline{g\eta^2}$ are negligibly small.

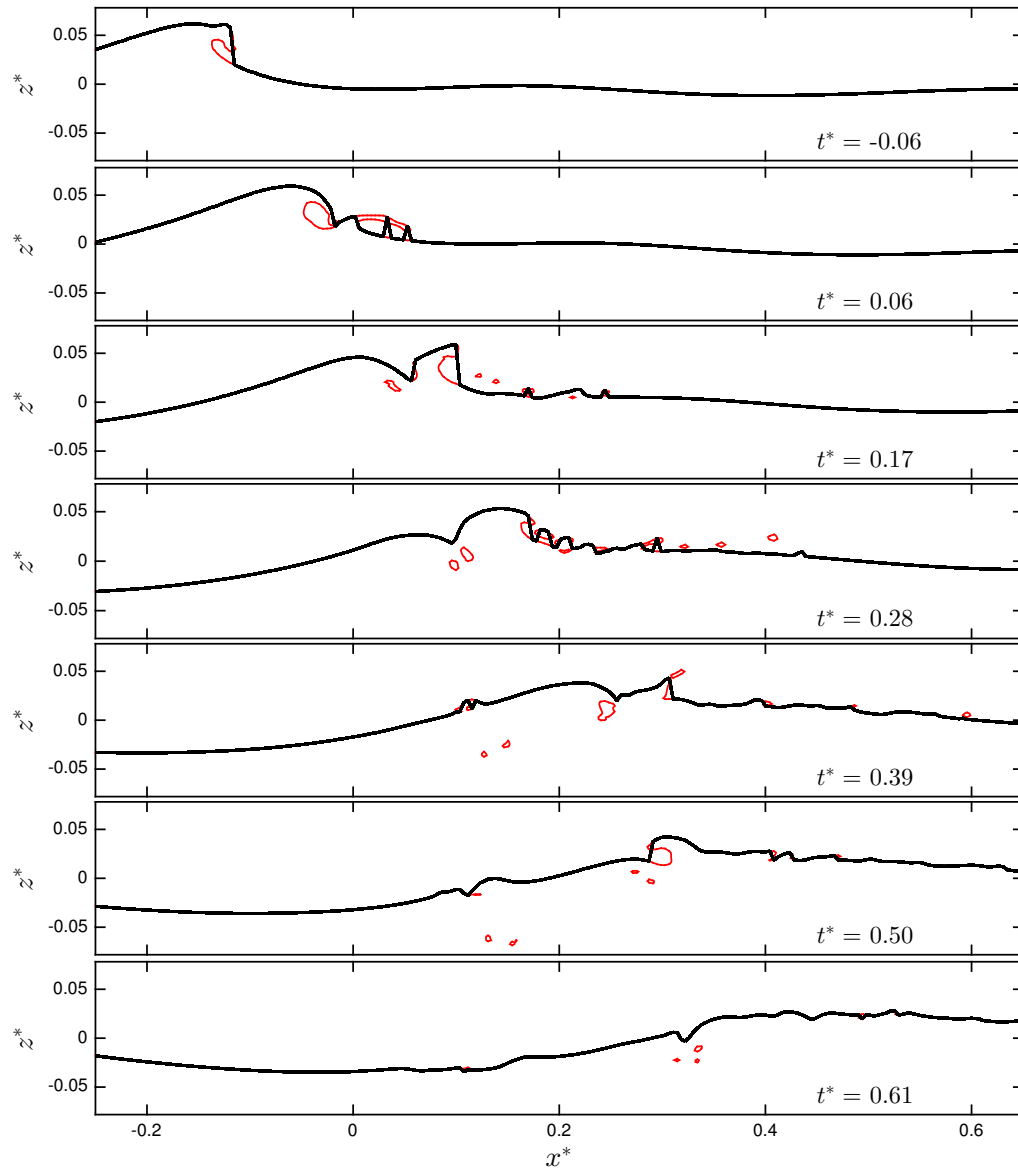


Figure B.1: Snapshots of the spatial variations of the air-water interface (—) and the calculated $\eta(t, x)$ (---) for the intermediate-depth plunging breaker DP1. The resolution density is $G3 = (\Delta x = 10.0, \Delta z = 5.0)$ mm.

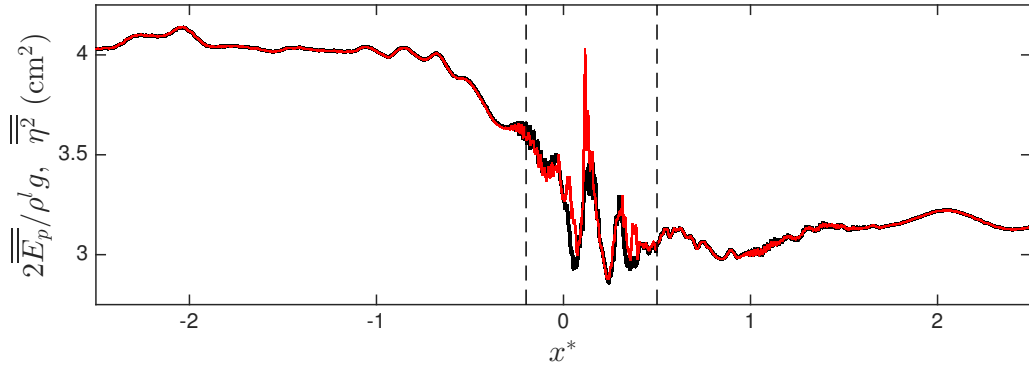


Figure B.2: Spatial variations of the normalized exact, $2\overline{\overline{E_p}}/\rho^l g$, (—) and approximated, $\overline{\overline{\eta^2}}$, (—) time-averaged potential energy density for the intermediate-depth plunging breaker DP1. The resolution density is G3 = ($\Delta x = 10.0, \Delta z = 5.0$)mm. Vertical dashed lines show $x^* = -0.2$ and $x^* = 0.5$.

Appendix C

ESTIMATION OF WAVE ENERGY DISSIPATION DUE TO BREAKING AND NON-BREAKING PROCESSES

The total loss of the horizontal wave energy flux $\int_t \overline{\Delta F^E}$ given by (2.9) includes both non-breaking, e.g. , viscous dissipation due to boundaries and inside the water body, and breaking processes. In any model simulation, numerical dissipation always contributes to some of the energy loss in the system. Here, we consider the numerical dissipation as a non-breaking dissipation. To estimate the total non-breaking wave energy dissipation, we fit a line to $\int_t \overline{F^E}$ upstream of the break point, we observed that this line also represents a linear fit to $\int_t \overline{F^E}$ downstream of the break point. Then, we assume that $\int_t \overline{\Delta F_{nb}^E}(x^* \rightarrow x^* + 1)$ which is the slope of the fitted line is constant over the whole numerical domain, including the breaking region. Thus the total non-breaking loss of the horizontal wave energy flux between x_1 and x_2 can be estimated as

$$\int_t \overline{\Delta F_{nb}^E}(x_1 \rightarrow x_2) = (x_2 - x_1) \int_t \overline{\Delta F_{nb}^E}(x^* \rightarrow x^* + 1), \quad (\text{C.1})$$

and thus $\int_t \overline{\Delta F_{br}^E} = \int_t \overline{\Delta F^E} - \int_t \overline{\Delta F_{nb}^E}$. The values of $\int_t \overline{\Delta F_{br}^E}$ for the considered focused wave packets are given in table 2.3. The ratio of $\int_t \overline{\Delta F_{nb}^E}(x^* \rightarrow x^* + 1) / \int_t \overline{\Delta F_{br}^E}$ ranges from ≈ 0.01 up to 0.04 in our focused plunging and spilling breaking wave packets. In most of the considered cases, the decrease of the mesh resolution results in the increase of $\int_t \overline{\Delta F_{br}^E}$ and thus the increase of the breaking strength parameter b . Table C.1 summarizes the estimated b using different mesh resolution for our focused breaking wave packets.

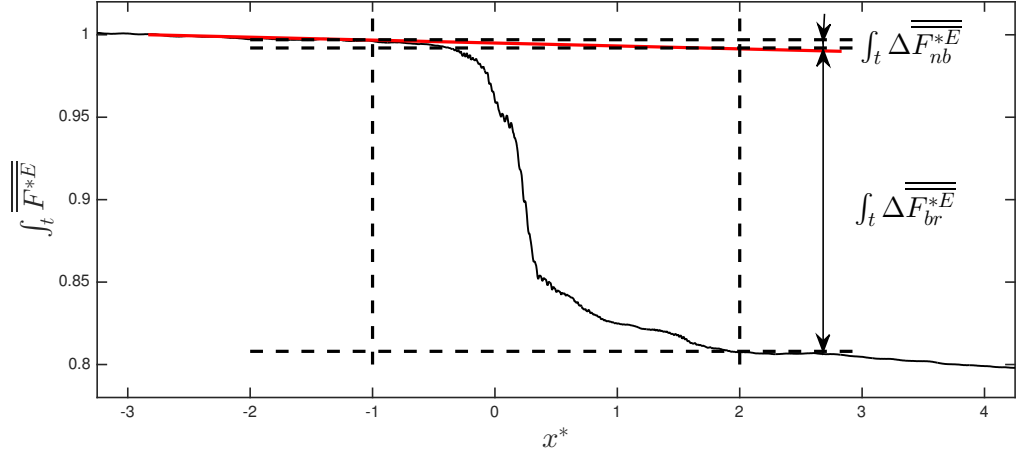


Figure C.1: Calculation of the total loss of the horizontal wave energy flux due to breaking and non-breaking processes. The reference value is the total horizontal wave energy flux far upstream of the break point, $\int_t \overline{F_1^E}$.

Table C.1: Variation of the breaking strength parameter b given by (2.18) with respect to different grid densities for simulated focused packets. Different mesh grid densities are: G2 = ($\Delta x = 18.3, \Delta z = 5.0$)mm, G3 = ($\Delta x = 10.0, \Delta z = 5.0$)mm, and G4 = ($\Delta x = 5.0, \Delta z = 5.0$)mm.

Case no.	Mesh resolution	b	Mesh resolution	b
RS1	G3	9.1×10^{-3}	G2	13.1×10^{-3}
RP1	G3	40.0×10^{-3}	G2	41.0×10^{-3}
RP2	G3	34.7×10^{-3}	G2	35.0×10^{-3}
DS1	G3	7.3×10^{-3}	G2	8.8×10^{-3}
DP1	G3	37.3×10^{-3}	G2	36.6×10^{-3}
DP2	G3	60.0×10^{-3}	G2	60.2×10^{-3}
TP1	G4	6.8×10^{-3}	G3	9.1×10^{-3}
TP2	G4	29.3×10^{-3}	G3	31.4×10^{-3}
TP3	G4	52.0×10^{-3}	G3	51.0×10^{-3}

Appendix D

INPUT PARAMETERS FOR THE BREAKING WAVES DUE TO MODULATIONAL INSTABILITY

For the generation of wave packets due to modulational instability, wave packets composed of a carrier wave and one- or two side-band perturbation components are produced. Here, we follow the set up of the bimodal initial spectrum, case II, wave packets in [Allis \(2013\)](#), which is similar to case II in [Banner & Peirson \(2007\)](#). The surface displacement at the incident boundary $x = 0$ is given by

$$\eta(0, t) = a_0 \cos(\omega_0 t) + a_1 \cos(\omega_1 t - \frac{\pi}{18}), \quad (\text{D.1})$$

where $\omega_0 = 8.985(\text{s}^{-1})$, $\omega_1 = \omega_0 + \Delta\omega$. Table [D.1](#) gives the rest of input parameters for the three simulated cases. The two-dimensional numerical domain of (50.0,0.64)m is discretized by a uniform grid of $\Delta x = 7.8\text{mm}$ and $\Delta z = 4\text{mm}$.

Table D.1: Input parameters for the simulated breaking packets due to modulational instability. Here, $k_0 = 8.23(\text{m}^{-1})$ and $d = 0.55\text{m}$ is the still water depth.

Case no.	$a_0 k_0$	$\Delta\omega/\omega_0$	a_1/a_0
S1	0.107	0.0954	0.3
S2	0.119	0.0954	0.3
S3	0.121	0.100	0.3

Appendix E

THREE-POINTS FINITE-DIFFERENCE APPROXIMATION IN A NON-UNIFORM GRID

For a continuous function Φ , with the given values $\Phi(x_1)$, $\Phi(x_2)$, and $\Phi(x_3)$, using the Taylor expansion formula it can be shown that,

$$\begin{aligned}
 \Phi(x) &= \alpha^{(0)}\Phi(x_1) + \beta^{(0)}\Phi(x_2) + \gamma^{(0)}\Phi(x_3) - \frac{e_3}{6}\Phi'''(x) - \frac{e_1e_3}{24}\Phi''''(x) + O(e_1^2e_3, e_2e_3), \\
 \Phi'(x) &= \alpha^{(1)}\Phi(x_1) + \beta^{(1)}\Phi(x_2) + \gamma^{(1)}\Phi(x_3) + \frac{e_2}{6}\Phi'''(x) + \frac{e_1e_2 - e_3}{24}\Phi''''(x) + O(e_1^2e_2, e_1e_3, e_2^2), \\
 \Phi''(x) &= \alpha^{(2)}\Phi(x_1) + \beta^{(2)}\Phi(x_2) + \gamma^{(2)}\Phi(x_3) - \frac{e_1}{3}\Phi'''(x) - \frac{e_1^2 - e_2}{12}\Phi''''(x) + O(e_1^3, e_1e_2, e_3),
 \end{aligned} \tag{E.1}$$

where

$$\begin{aligned}
 \alpha^{(0)} &= \frac{(x_2 - x)(x_3 - x)}{(x_1 - x_2)(x_1 - x_3)} \quad \beta^{(0)} = \frac{(x_1 - x)(x_3 - x)}{(x_2 - x_1)(x_2 - x_3)} \quad \gamma^{(0)} = \frac{(x_1 - x)(x_2 - x)}{(x_3 - x_1)(x_3 - x_2)}, \\
 \alpha^{(1)} &= -\frac{(x_2 - x) + (x_3 - x)}{(x_1 - x_2)(x_1 - x_3)} \quad \beta^{(1)} = -\frac{(x_1 - x) + (x_3 - x)}{(x_2 - x_1)(x_2 - x_3)} \quad \gamma^{(1)} = -\frac{(x_1 - x) + (x_2 - x)}{(x_3 - x_1)(x_3 - x_2)}, \\
 \alpha^{(2)} &= \frac{2}{(x_1 - x_2)(x_1 - x_3)} \quad \beta^{(2)} = \frac{2}{(x_2 - x_1)(x_2 - x_3)} \quad \gamma^{(2)} = \frac{2}{(x_3 - x_1)(x_3 - x_2)},
 \end{aligned} \tag{E.2}$$

and

$$\begin{aligned}
 e_1 &= (x_1 - x) + (x_2 - x) + (x_3 - x) \\
 e_2 &= (x_1 - x)(x_2 - x) + (x_1 - x)(x_3 - x) + (x_2 - x)(x_3 - x) \\
 e_3 &= (x_1 - x)(x_2 - x)(x_3 - x).
 \end{aligned} \tag{E.3}$$

Appendix F

SECOND-ORDER FINITE-DIFFERENCE APPROXIMATION FOR THE PRESSURE AND VELOCITY GRADIENTS IN A NON-UNIFORM GRID

In the current NHWAVE formulation, we used uniform grid in the horizontal directions. For the vertical direction, however, we may have a non-uniform arbitrary grid $\sigma_1, \sigma_2, \dots, \sigma_K, \sigma_{K+1}$, where K is the number of the vertical levels, and, $\sigma_1 = 0$ and $\sigma_{K+1} = 1$ represent the bottom and free surface respectively.

Because the pressure field, $\mathcal{P}_{i,j,k}$ is defined at the σ levels, $\{\frac{\partial \psi \mathcal{P}}{\partial \sigma}\}_{i,j,k}$ can be estimated using $\mathcal{P}_{i,j,k-1}$, $\mathcal{P}_{i,j,k}$ and $\mathcal{P}_{i,j,k+1}$ using (E.1), with $x_1 = \sigma_{k-1}$, $x = x_2 = \sigma_k$, $x_3 = \sigma_{k+1}$, as

$$\left\{ \frac{\partial \psi \mathcal{P}}{\partial \sigma} \right\}_{i,j,k} = \alpha \{ \psi \mathcal{P} \}_{i,j,k-1} + \beta \{ \psi \mathcal{P} \}_{i,j,k} + \gamma \{ \psi \mathcal{P} \}_{i,j,k+1} + E^{(1)} \quad (\text{F.1})$$

where $\Delta\sigma_{k-1} = \sigma_k - \sigma_{k-1}$, $\Delta\sigma_k = \sigma_{k+1} - \sigma_k$, and

$$\begin{aligned} \alpha &= \frac{-\Delta\sigma_k}{\Delta\sigma_{k-1}(\Delta\sigma_{k-1} + \Delta\sigma_k)} \\ \beta &= \frac{\Delta\sigma_k - \Delta\sigma_{k-1}}{\Delta\sigma_{k-1}\Delta\sigma_k} \\ \gamma &= \frac{\Delta\sigma_{k-1}}{\Delta\sigma_k(\Delta\sigma_{k-1} + \Delta\sigma_k)} \\ E^{(1)} &= -\frac{\Delta\sigma_{k-1}\Delta\sigma_k}{6} \left\{ \frac{\partial^3 \psi \mathcal{P}}{\partial \sigma^3} \right\}_{i,j,k} + O(\Delta\sigma_{k-1}^{1+m} \Delta\sigma_k^{3-m}), \quad m = 0, 1, 2 \end{aligned} \quad (\text{F.2})$$

which is second-order accurate in a sense that $E^{(1)} \approx \Delta\sigma_{k-1}\Delta\sigma_k$.

In addition, we can write

$$\begin{aligned} \left\{ \frac{\partial}{\partial \sigma} \left(\phi \frac{\partial \psi \mathcal{P}}{\partial \sigma} \right) \right\}_{i,j,k} &= 2\alpha \left\{ \phi \frac{\partial \psi \mathcal{P}}{\partial \sigma} \right\}_{i,j,k-\frac{1}{2}} + 2\beta \left\{ \phi \frac{\partial \psi \mathcal{P}}{\partial \sigma} \right\}_{i,j,k} \\ &\quad + 2\gamma \left\{ \phi \frac{\partial \psi \mathcal{P}}{\partial \sigma} \right\}_{i,j,k+\frac{1}{2}} - \frac{\sigma_{k-1} \Delta \sigma_k}{24} \left\{ \frac{\partial^3}{\partial \sigma^3} \left(\phi \frac{\partial \psi \mathcal{P}}{\partial \sigma} \right) \right\}_{i,j,k} \end{aligned} \quad (\text{F.3})$$

where

$$\begin{aligned} \left\{ \phi \frac{\partial \psi \mathcal{P}}{\partial \sigma} \right\}_{i,j,k-\frac{1}{2}} &= \phi_{i,j,k-\frac{1}{2}} \frac{\{\psi \mathcal{P}\}_{i,j,k} - \{\psi \mathcal{P}\}_{i,j,k-1}}{\Delta \sigma_{k-1}} \\ &\quad - \phi_{i,j,k-\frac{1}{2}} \frac{[\Delta \sigma_{k-1}]^2}{24} \left\{ \frac{\partial^3 \psi \mathcal{P}}{\partial \sigma^3} \right\}_{i,j,k-\frac{1}{2}} + O(\Delta \sigma_{k-1}^4), \\ \left\{ \phi \frac{\partial \psi \mathcal{P}}{\partial \sigma} \right\}_{i,j,k} &= \phi_{i,j,k} \left(\alpha \{\psi \mathcal{P}\}_{i,j,k-1} + \beta \{\psi \mathcal{P}\}_{i,j,k} + \gamma \{\psi \mathcal{P}\}_{i,j,k+1} \right) \\ &\quad - \phi_{i,j,k} \frac{\Delta \sigma_{k-1} \Delta \sigma_k}{6} \left\{ \frac{\partial^3}{\partial \sigma^3} \left(\phi \frac{\partial \psi \mathcal{P}}{\partial \sigma} \right) \right\}_{i,j,k} \\ \left\{ \phi \frac{\partial \psi \mathcal{P}}{\partial \sigma} \right\}_{i,j,k+\frac{1}{2}} &= \phi_{i,j,k+\frac{1}{2}} \frac{\{\psi \mathcal{P}\}_{i,j,k+1} - \{\psi \mathcal{P}\}_{i,j,k}}{\Delta \sigma_k} \\ &\quad - \phi_{i,j,k+\frac{1}{2}} \frac{[\Delta \sigma_k]^2}{24} \left\{ \frac{\partial^3 \psi \mathcal{P}}{\partial \sigma^3} \right\}_{i,j,k+\frac{1}{2}} + O(\Delta \sigma_k^4), \end{aligned} \quad (\text{F.4})$$

and, thus,

$$\begin{aligned} \left\{ \frac{\partial \phi \frac{\partial \psi \mathcal{P}}{\partial \sigma}}{\partial \sigma} \right\}_{i,j,k} &= 2\alpha \left(\frac{-1}{\Delta \sigma_{k-1}} \phi_{i,j,k-\frac{1}{2}} + \beta \phi_{i,j,k} \right) \{\psi \mathcal{P}\}_{i,j,k-1} \\ &\quad + \left(\frac{2\alpha}{\Delta \sigma_{k-1}} \phi_{i,j,k-\frac{1}{2}} + 2\beta^2 \phi_{i,j,k} - \frac{2\gamma}{\Delta \sigma_k} \phi_{i,j,k+\frac{1}{2}} \right) \{\psi \mathcal{P}\}_{i,j,k} \\ &\quad + 2\gamma \left(\beta \phi_{i,j,k} + \frac{1}{\Delta \sigma_k} \phi_{i,j,k+\frac{1}{2}} \right) \{\psi \mathcal{P}\}_{i,j,k+1} + E^{(2)}. \end{aligned} \quad (\text{F.5})$$

where

$$\begin{aligned} E^{(2)} &= -\frac{\Delta \sigma_{k-1} \Delta \sigma_k}{24} \left\{ \frac{\partial \phi \frac{\partial^3 \psi \mathcal{P}}{\partial \sigma^3}}{\partial \sigma} + \frac{\partial^3 \phi \frac{\partial \psi \mathcal{P}}{\partial \sigma}}{\partial \sigma^3} \right\}_{i,j,k} - \frac{\Delta \sigma_k - \Delta \sigma_{k-1}}{3} \phi_{i,j,k} \left\{ \frac{\partial^3 \psi \mathcal{P}}{\partial \sigma^3} \right\}_{i,j,k} \\ &\quad + O(\Delta \sigma_{k-1}^{1+m} \Delta \sigma_k^{2-m}, \Delta \sigma_k^3, \Delta \sigma_{k-1}^4 / \Delta \sigma_k), \quad m = 0, 1, 2 \end{aligned} \quad (\text{F.6})$$

Because $E^{(2)} \approx \Delta \sigma_k - \Delta \sigma_{k-1}$, (F.5) is a first-order scheme. As $\Delta \sigma_k - \Delta \sigma_{k-1}$ becomes on the order of $\Delta \sigma_{k-1} \Delta \sigma_k$, however, it becomes a second order scheme.

The velocity field is defined at the center of each vertical levels, where $U_{i,j,k-1}$, $U_{i,j,k}$ and $U_{i,j,k+1}$ are defined at $x_1 = \sigma_{k-1} + \Delta\sigma_{k-1}/2$, $x_2 = \sigma_k + \Delta\sigma_k/2$, $x_3 = \sigma_{k+1} + \Delta\sigma_{k+1}/2$ respectively. Using (E.1) we have

$$\left\{ \frac{\partial\psi U}{\partial\sigma} \right\}_{i,j,k} = \alpha^c \{\psi U\}_{i,j,k-1} + \beta^c \{\psi U\}_{i,j,k} + \gamma^c \{\psi U\}_{i,j,k+1} + E^{(3)}, \quad (\text{F.7})$$

where $\Delta\sigma_{k-1}^c = (\Delta\sigma_k + \Delta\sigma_{k-1})/2$, $\Delta\sigma_k^c = (\Delta\sigma_{k+1} + \Delta\sigma_k)/2$, and

$$\begin{aligned} \alpha^c &= \frac{-\Delta\sigma_k^c}{\Delta\sigma_{k-1}^c(\Delta\sigma_{k-1}^c + \Delta\sigma_k^c)} \\ \beta^c &= \frac{\Delta\sigma_k^c - \Delta\sigma_{k-1}^c}{\Delta\sigma_{k-1}^c \Delta\sigma_k^c} \\ \gamma^c &= \frac{\Delta\sigma_{k-1}^c}{\Delta\sigma_k^c(\Delta\sigma_{k-1}^c + \Delta\sigma_k^c)}. \end{aligned} \quad (\text{F.8})$$

$$E^{(3)} = -\frac{\Delta\sigma_{k-1}^c \Delta\sigma_k^c}{6} \left\{ \frac{\partial^3 \psi U}{\partial \sigma^3} \right\}_{i,j,k} + O([\Delta\sigma_{k-1}^c]^{1+m} [\Delta\sigma_k^c]^{3-m}), \quad m = 0, 1, 2,$$

In addition, we have

$$\begin{aligned} \left\{ \frac{\partial\phi}{\partial\sigma} \frac{\partial\psi U}{\partial\sigma} \right\}_{i,j,k} &= \frac{\left\{ \phi \frac{\partial\psi U}{\partial\sigma} \right\}_{i,j,k+\frac{1}{2}} - \left\{ \phi \frac{\partial\psi U}{\partial\sigma} \right\}_{i,j,k-\frac{1}{2}}}{\Delta\sigma_k} \\ &\quad - \frac{[\Delta\sigma_k]^2}{24} \left\{ \frac{\partial^3 \phi \frac{\partial\psi U}{\partial\sigma}}{\partial\sigma^3} \right\}_{i,j,k} + O(\Delta\sigma_k^4), \end{aligned} \quad (\text{F.9})$$

where

$$\begin{aligned}
\left\{ \phi \frac{\partial \psi U}{\partial \sigma} \right\}_{i,j,k-\frac{1}{2}} &= \phi_{i,j,k-\frac{1}{2}} \left\{ \left(\alpha^c - \frac{\Delta \sigma_k}{\Delta \sigma_{k-1}^c (\Delta \sigma_{k-1}^c + \Delta \sigma_k^c)} \right) \{\psi U\}_{i,j,k-1} \right. \\
&+ \left. \left(\beta^c + \frac{\Delta \sigma_k}{\Delta \sigma_{k-1}^c \Delta \sigma_k^c} \right) \{\psi U\}_{i,j,k} + \left(\gamma^c - \frac{\Delta \sigma_k}{\Delta \sigma_k^c (\Delta \sigma_{k-1}^c + \Delta \sigma_k^c)} \right) \{\psi U\}_{i,j,k+1} \right\} \\
&+ \frac{\Delta \sigma_k (\Delta \sigma_k^c - \Delta \sigma_{k-1}^c) + 3/4 [\Delta \sigma_k]^2 - \Delta \sigma_{k-1}^c \Delta \sigma_k^c}{6} \left\{ \phi \frac{\partial^3 \psi U}{\partial \sigma^3} \right\}_{i,j,k-\frac{1}{2}} + HOT
\end{aligned} \tag{F.10}$$

$$\begin{aligned}
\left\{ \phi \frac{\partial \psi U}{\partial \sigma} \right\}_{i,j,k+\frac{1}{2}} &= \phi_{i,j,k+\frac{1}{2}} \left\{ \left(\alpha^c + \frac{\Delta \sigma_k}{\Delta \sigma_{k-1}^c (\Delta \sigma_{k-1}^c + \Delta \sigma_k^c)} \right) \{\psi U\}_{i,j,k-1} \right. \\
&+ \left. \left(\beta^c - \frac{\Delta \sigma_k}{\Delta \sigma_{k-1}^c \Delta \sigma_k^c} \right) \{\psi U\}_{i,j,k} + \left(\gamma^c + \frac{\Delta \sigma_k}{\Delta \sigma_k^c (\Delta \sigma_{k-1}^c + \Delta \sigma_k^c)} \right) \{\psi U\}_{i,j,k+1} \right\} \\
&+ \frac{-\Delta \sigma_k (\Delta \sigma_k^c - \Delta \sigma_{k-1}^c) + 3/4 [\Delta \sigma_k]^2 - \Delta \sigma_{k-1}^c \Delta \sigma_k^c}{6} \left\{ \phi \frac{\partial^3 \psi U}{\partial \sigma^3} \right\}_{i,j,k+\frac{1}{2}} + HOT,
\end{aligned}$$

and, thus,

$$\begin{aligned}
\left\{ \frac{\partial \phi \frac{\partial \psi U}{\partial \sigma}}{\partial \sigma} \right\}_{i,j,k} &= \left(\frac{\alpha^c [\phi_{i,j,k+\frac{1}{2}} - \phi_{i,j,k-\frac{1}{2}}]}{\Delta \sigma_k} + \frac{[\phi_{i,j,k+\frac{1}{2}} + \phi_{i,j,k-\frac{1}{2}}]}{\Delta \sigma_{k-1}^c (\Delta \sigma_{k-1}^c + \Delta \sigma_k^c)} \right) \{\psi U\}_{i,j,k-1} \\
&+ \left(\frac{\beta^c [\phi_{i,j,k+\frac{1}{2}} - \phi_{i,j,k-\frac{1}{2}}]}{\Delta \sigma_k} - \frac{[\phi_{i,j,k+\frac{1}{2}} + \phi_{i,j,k-\frac{1}{2}}]}{\Delta \sigma_{k-1}^c \Delta \sigma_k^c} \right) \{\psi U\}_{i,j,k} \\
&+ \left(\frac{\gamma^c [\phi_{i,j,k+\frac{1}{2}} - \phi_{i,j,k-\frac{1}{2}}]}{\Delta \sigma_k} + \frac{[\phi_{i,j,k+\frac{1}{2}} + \phi_{i,j,k-\frac{1}{2}}]}{\Delta \sigma_k^c (\Delta \sigma_{k-1}^c + \Delta \sigma_k^c)} \right) \{\psi U\}_{i,j,k+1} \\
&+ E^{(4)}
\end{aligned} \tag{F.11}$$

where

$$\begin{aligned}
E^{(4)} &= -\frac{[\Delta \sigma_k]^2}{24} \left\{ \frac{\partial^3 \phi \frac{\partial \psi U}{\partial \sigma}}{\partial \sigma^3} \right\}_{i,j,k} + \left(\frac{3[\Delta \sigma_k]^2}{24} - \frac{\Delta \sigma_{k-1}^c \Delta \sigma_k^c}{6} \right) \left\{ \frac{\partial \phi \frac{\partial^3 \psi U}{\partial \sigma^3}}{\partial \sigma} \right\}_{i,j,k} \\
&- (\Delta \sigma_k^c - \Delta \sigma_{k-1}^c) \left(\left\{ \phi \frac{\partial^3 \psi U}{\partial \sigma^3} \right\}_{i,j,k+\frac{1}{2}} + \left\{ \phi \frac{\partial^3 \psi U}{\partial \sigma^3} \right\}_{i,j,k-\frac{1}{2}} \right) \\
&+ O([\Delta \sigma_{k-1}^c]^{1+m} [\Delta \sigma_k^c]^{3-m} / \Delta \sigma_k, [\Delta \sigma_k^c]^4 // \Delta \sigma_k, [\Delta \sigma_{k-1}^c]^4 / \Delta \sigma_k), \quad m = 0, 1, 2,
\end{aligned} \tag{F.12}$$

Equations (F.7) and (F.11) are a second-order and a first-order scheme respectively. As $\Delta \sigma_k^c - \Delta \sigma_{k-1}^c = (\Delta \sigma_{k+1} - \Delta \sigma_{k-1})/2$ becomes on the order of $\Delta \sigma_{k-1}^c \Delta \sigma_k^c$, however, (F.11) becomes a second order scheme in a sense that $E^{(4)} \approx \Delta \sigma_{k-1}^c \Delta \sigma_k^c$.